Laser diagnostics of soot in hydrocarbon diffusion flames

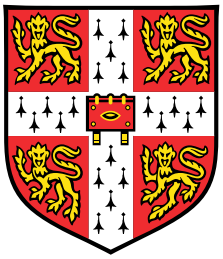

Bo Tian

Department of Engineering

University of Cambridge

This dissertation is submitted for the degree of

Doctor of Philosophy

St Edmund's College

November 2016

Declaration

I hereby declare that except where specific reference is made to the work of others, the contents of this dissertation are original and have not been submitted in whole or in part for consideration for any other degree or qualification in this, or any other university. This dissertation is my own work and contains nothing which is the outcome of work done in collaboration with others, except as specified in the text and acknowledgements. This dissertation contains fewer than 65,000 words including appendices, bibliography, footnotes, tables and equations and has fewer than 150 figures.

Bo Tian

November 2016

Acknowledgements

Firstly, I would like to express my deepest gratitude to my supervisor, Professor Simone Hochgreb, for her continuous support of my PhD study. Her guidance, patience, motivation, and immense knowledge have helped me during my research and writing of this thesis. Her enthusiasm for research has also encouraged me to stay in academia after my PhD.

I would like to thank my advisor, Dr. Adam Boies, for his help during my PhD study and especially in the first year assessment. His insightful comments and encouragement have motivated me to widen the scope of my research.

My sincere thanks also go to Dr. Yi Gao, who provided me with an opportunity to learn about lasers and optics. Without her precious support it would not have been possible to conduct this research.

I thank my colleagues for their stimulating discussions, for the days and nights we worked together before deadlines, and for all the fun we have had in the last four years. Also, I thank my friends in the Department of Chemical Engineering and Shanghai Jiao Tong University. In particular, I am grateful to Dr. Weiwei Cai for his advice on the development of the laser cavity extinction measurement system.

Last but not the least, I would like to thank my family for supporting me unconditionally in everything I do.

List of Publications

Journal papers

B. Guan, H. Lin, L. Zhu, B. Tian, and Z. Huang. Effect of ignition temperature for combustion synthesis on the selective catalytic reduction of NO_x with NH_3 over $Ti_{0.9}Ce_{0.05}V_{0.05}O_2$ nanocomposites catalysts prepared by solution combustion route. Chem. Eng. J. 181182, 307 (2012).

B. Tian, Y. Gao, S. Balusamy, and S. Hochgreb, High Spatial Resolution Laser Cavity Extinction and Laser Induced Incandescence in Low Soot Producing Flames, Appl. Phys. B Lasers Opt. 120, 469487 (2015).

B. Tian, Y. Gao, C. Zhang, and S. Hochgreb, 2D 2-Color Time-Resolved Laser Induced Incandescence Sizing of Ultra-fine Soot Particles in a Methane Diffusion Flame, Exp. Fluid. (under review).

T. Yu, B. Tian, and W. Cai, Development of a beam optimization method for absorption-based tomography. Optics Express, (under review).

S. Balusamy, M. M. Kamal, S. M. Lowe, B. Tian, Y. Gao, and S. Hochgreb, "Laser diagnostics of pulverized coal combustion in O2/N2 and O2/CO2 conditions: velocity and scalar field measurements," Exp. Fluids 56, (2015).

B. Tian, Y. Gao, C. Zhang, and S. Hochgreb, Soot measurement by combining continuous wave multipass extinction and laser-induced incandescence in diluted methane flames, (In preparation).

B. Tian, C. Zhang, Y. Gao and S. Hochgreb, Planar 2-Colour Time-Resolved Laser Induced Incandescence and Laser Cavity Extinction Measurements of Soot in a Diffusion Flame, (In preparation).

Conference proceedings

B. Tian, S. Balusamy, and S. Hochgreb, High Spatial Resolution Laser Cavity Extinction Measurements of Soot in Low Soot Producing Flames, in Proceedings of British and Scandinavian-Nordic Section Combustion Meeting (2014), pp. 7980. (Accepted for oral presentation)

B. Tian, Y. Gao, and S. Hochgreb, High Spatial Resolution and Sensitivity Laser Cavity Extinction Measurements of Soot Volume Fraction in Nitrogen Diluted Methane Flames, in Proceedings of European Combustion Meeting (2015).

Abstract

Driven by the demand for soot-free combustion, laser-based diagnostic techniques on soot have been developing since the late 1980s. One of these techniques is line-of-sight extinction, which is a fast, low-cost, and quantitative method to investigate the soot volume fraction in flames. However, the extinction-based technique suffers from relatively high measurement uncertainty due to a low signal-to-noise ratio, as the single-pass attenuation of the laser beam intensity is often insufficient. Multipass techniques can increase the sensitivity, but may suffer from a low spatial resolution. To overcome this problem, in the present study, we have developed a high spatial resolution continuous wave laser-cavity extinction (CW-LCE) technique to measure the soot volume fraction from low-soot producing flames. A laser beam cavity is realised by placing two partially reflective concave mirrors on either side of the laminar diffusion flame under investigation. This configuration makes the beam convergent inside the cavity, allowing a spatial resolution within 200 μm, whilst increasing the absorption by an order of magnitude. Three different hydrocarbon fuels are tested: methane, propane and ethylene. The measurements of soot distribution across the flame show good agreement with results using laser-induced incandescence (LII) in the range of the soot volume fraction from 20 ppb to 15 ppm. The system is further applied to the measurement of soot volume fraction profiles of a series of nitrogen-diluted methane diffusion flames. The results of CW-LCE agree well with LII. The effect of fuel dilution on soot is interpreted by using a numerically calculated flow velocity and temperature field. It is found that a previous one-step model for soot formation may underestimate

the suppression effect by dilution. This is because diluent addition may shift the location of the sooting region away from the high temperature region, shortening the residence time for surface growth of soot particles. The effect of each factor (thermal, dilution, residence time) responsible for soot reduction is isolated and quantitatively compared.

The size of soot particles is another important aspect of comprehensive soot measurement, and to address this aspect, a planar two-dimensional two-colour time-resolved laser-induced incandescence (2D-2C-TiRe-LII) method is developed and employed to investigate the soot formation in a series of standard ethylene and methane laminar diffusion flame. The time resolution of the 2D-LII signal is realised by shifting the delay time of the ICCD cameras. A two-colour configuration is applied to measure the peak temperature of soot particles after the laser pulse, rather than use the energy balance equations to compute the peak temperature, which may introduce significant uncertainty. By combining with the CW-LCE technique, both a soot particle volume fraction and a particle size distribution map of the flame are obtained, using a minimum error approach.

Table of contents

List of figures

List of tables

Nomenclature

Roman Symbols

A_p	proportion coefficient for soot formation rate
B_p	proportion coefficient for soot formation rate
c	speed of light
C_{det}	detector constant
C_{det}	constant of detection system
C_{em}	LII emission constant
c_p	heat capacity of gas
C_s	Sutherland's constant
c_{s}	specific heat of soot particles
D	particle diameter
D_f	diffusivity
D_{ij}	function of linear Abel transform operators $I_{ij}(0)$ and $I_{ij}(1)$
E	radiation power per unit solid angle and area
E_a	global activation energy for soot formation

f	Eucken correction to the thermal conductivity
f^*	non-dimensional value $Y_F - \frac{Y_O}{S}$
f_v	local soot volume fraction
G	heat-transfer factor
h	Planck constant
h^*	non-dimensional enthalpy across flame
h_c	absolute enthalpy of reaction mixture
I_0	incident laser beam intensity before entering cavity
i_0	photocurrent due to incident laser
i_1	current from photodiode 1
i_2	current from photodiode 2
i_{B1}	photocurrent in photodiode 1 with ambient luminosity
i_{B2}	photocurrent in photodiode 1 with ambient luminosity
i_F	photocurrent in photodiode 1 with laser and flame on
i_{F1}	photocurrent in photodiode 1 with flame on
i_{F2}	photocurrent in photodiode 2 with flame on
I_i	incident laser intensity
I_{ij}	operator in Abel transform
I_{ij}	The deconvolution operators of Abel transform
i_{ref}	steady reference current

I_T	total transmitted laser power
I_t	transmitted laser intensity through a extinction volume
I_{tn}	transmitted intensity after n times transmission by mirror 2
J_{cal}	predicted temporal LII signal
J_{exp}	experimentally measured temporal LII signal
$J_{\text{L}II}$	total collected LII signal
K_a	local absorption coefficient
k_{a}	thermal conductivity of the surrounding gases
k_B	Boltzmann constant
K_e	local extinction coefficient
Kn	Knudsen number
L	mean free path
K_{LII}	LII calibration coefficient
m	complex refractive index
N	number density of soot particles
n_0	The subscript of deconvolution operators $I_{ij}(n_0)$
N_{p}	particle number concentration
P_0	single pass laser extinction projection
P_{ref}	reference pressure to calculate P_{v}
P_t	total laser extinction projection

P_{v}	partial pressure of sublimed carbon clusters
Q	combustion enthalpy of methane
$\dot{Q}_{\mathrm{a}}$	rate of energy absorption from the laser pulse
$\dot{Q}_{\mathrm{c}}$	rate of heat lost by heat conduction
$\dot{Q}_{\mathrm{r}}$	rate of heat lost by radiation
$\dot{Q}_{\mathrm{s}}$	rate of heat lost by soot sublimation
r	radial coordinate
r_0	inner radius of fuel tube
r_1	reflectance of mirror 1
r_2	reflectance of mirror 2
R_{g}	universal gas constant
R_m	product of the reflectivity of the two cavity mirrors
r_p	inner diameter of fuel port
r_P	radius of the burner central tube
s	molar ratio of air and fuel of complete combustion
S_D	LII signal intensity for single soot particle
S_{LII}	integrated LII signal intensity with probe volume
S_{LII}	LII signal intensity
T	temperature
t_1	transmittance of mirror 1

t_2	transmittance of mirror 2
T_{act}	activiation temperature of methane
$T_{F,0}$	temperature of methane in fuel flow
Tl	local temperature for soot formation
T_m	product of the transmittance of the two cavity mirrors
$T_{O,0}$	temperature of oxygen in co-flow
T_p	temperature of soot particle
$T_{\mathrm{p,0}}$	peak temperature of soot particle
t_r	residence time for soot formation
T_{ref}	reference temperature of cold mixture
T_{ref}	reference temperature to calculate P_{v}
$\dot{U}_{\mathrm{in}}$	internal energy of soot particle
u_r	radial velocity
u_x	uncertainty in variable x
u_z	axial velocity
V	probe volume
$\dot{v}_F$	mass flow rate of fuel
$\dot{v}_n$	mass flow rate of co-flow air
$\dot{v}_O$	mass flow rate of co-flow air
V_{out}	output voltage of logarithmic amplifier

W molecular weight

W_{s} molecular weight of solid carbon

W_{v} molecular weight of C3 carbon vapour

x running integration variable

y chord position

Y_O mass fraction of oxygen

Y_F mass fraction of fuel

$Y_{O,0}$ mass fraction of oxygen in co-flow

Greek Symbols

α_M mass accommodation coefficient

α_{T} thermal accommodation coefficient

ΔV probe volume of LII

Δy horizontal distance between two measured positions

η_o optical efficiency

λ_c heat conductivity

λ_e extinction laser wavelength

λ_s LII signal wavelength

μ_v viscosity

Ω solid angle

Ω_c detector collection solid angle

ω chemical reaction rate

ϕ_d detector sensitivity

γ heat-capacity ratio for air

ρ density

ρ_{v} density of carbon vapour

σ standard deviation

τ character residence time for soot formation

ε emissivity

ξ mixture fraction

Subscripts

0 initial condition

ad adiabatic

F fuel

l local

O oxidiser

ref reference

s soot

st stoichiometric

Other Symbols

$E(m)$ absorption function of soot particle, $E(m) = -\mathrm{Im}\left(\frac{m^2-1}{m^2+2}\right)$, where Im means the imaginary part

Acronyms / Abbreviations

CPPs condensed phase particles

CRDS cavity ring-down spectroscopy

CW condensed phase particles

HACA hydrogen-abstraction-carbon-addition

IDFs inverted diffusion flames

LIE laser induced emissions

LII laser induced incandescense

LOSE line of sight extinction

PAHs polycyclic aromatic hydrocarbons

RDG-FA RayleighDebyeGans theory for fractal aggregates

SNR singal to Noise Ratio

TDLAS tunable diode laser absorption spectroscopy

TiRe time resolved

UV ultraviolet

Chapter 1

Introduction

Since the 1960s, the power generation and vehicle industries have been developing rapidly worldwide. Accompanying this development, global exhaust emissions from combustion have increased dramatically, leading to detrimental environmental effects [16–19].

Soot (particulate matter) is one of the main exhaust emissions produced from the combustion processes of fossil fuels [20, 21], and there has been an enormous effort in understanding the formation of soot in a variety of flames and systems, but the problem is very complex, as it involves a very long chain from hydrocarbons to the building blocks of soot, with many possible pathways [1, 22]. Moreover, the research methods have been extremely limited until the 1980s [23–25], when laser based diagnostics and particle sizing techniques were introduced to the research field.

The present study primarily focuses on laser-based diagnostics of soot, including volume fraction and particle size distribution measurements. Several new techniques have been developed and tested on hydrocarbon flames.

1.1 Soot and its impacts

1.1.1 What is soot?

Almost every combustion process of carbon-based fuel can produce particles, even if most of the particles produced are invisible [26]. Soot is one of the particles that can be seen by the naked eye, in the form of black smoke from power plants or vehicles.

Soot is defined as a carbon-rich residue of combustion of any carbonaceous material, including solid, gaseous or liquid hydrocarbons, and other materials. In the present study, soot is defined as carbon particles produced from the incomplete combustion of carbon-containing fuels.

1.1.2 The formation of soot

Many existing soot formation models are based on the hydrogen-abstraction-carbon-addition (HACA) model (shown in Fig. 1.1) proposed by Frenklach and colleagues [1, 27, 28]. The model can be described as starting with the initial formation of benzene or polycyclic aromatic hydrocarbons (PAHs), producing an aryl radical by abstraction of H atoms, which become open to other radicals or activated PAHs. In this model, acetylene plays a vital role for producing aromatics, and the H atom abstracted from fuel molecules gives the driving force to allow the reaction to continue.

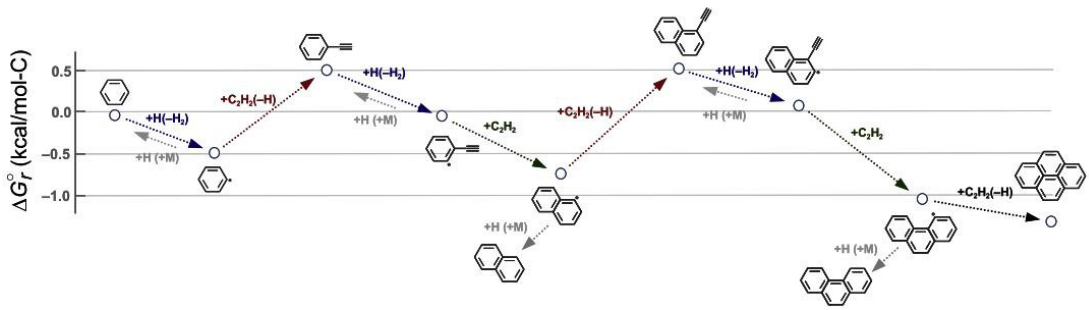

Fig. 1.1 Diagram of the HACA mechanism [1].

The formation of benzene provides the building block to generate PAHs, before the process of nucleation starts. There have been three potential pathways from PAHs to soot (as shown in Fig. 1.2). The first assumption raised by Homann [29] (path A in Fig. 1.2) indicated that the nascent soot had a structure like a fullerene, or Buckminsterfullerenes.

This theory was challenged by the HACA mechanism, as the former mechanism was determined to be slower than the rates observed experimentally for soot nucleation [22]. Two alternative paths involve the physical aggregation of middle-sized PAHs into stacked structures (path B shown in Fig. 1.2) [30] and the reaction or chemical coalescence of PAHs into cross-linked three-dimensional clusters (path C in Fig. 1.2) [31, 32] are more widely accepted since there are some experimental results supporting their assertions [1].

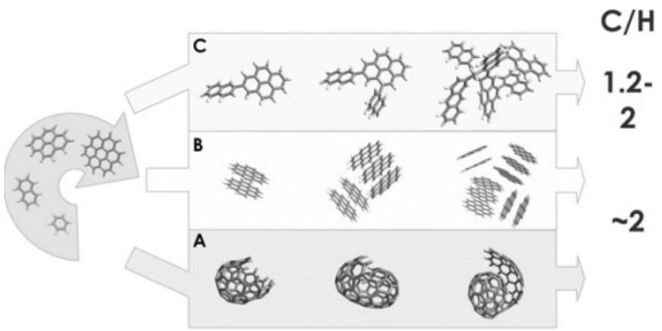

Fig. 1.2 Three conceptual mechanisms of soot particle nucleation from PAHs [1].

After nucleation, nascent soot particles begin to grow both in mass and size. According to HACA theory [27, 28], the nucleus surface could provide an aryl radical site while losing an H atom; the site is then occupied by another acetylene molecule. This reaction is the dominant reaction in the process of nascent soot growth. Thus, acetylene is the main mass growth reactant. While surface reactions determine the ultimate mass of soot, simultaneous particle-to-particle coagulation determines the ultimate size of the soot particles [1]. Nascent soot particles gradually become spherical as a result of the combination of soot particles and acetylene. The process of soot mass growth is illustrated in Fig. 1.3.

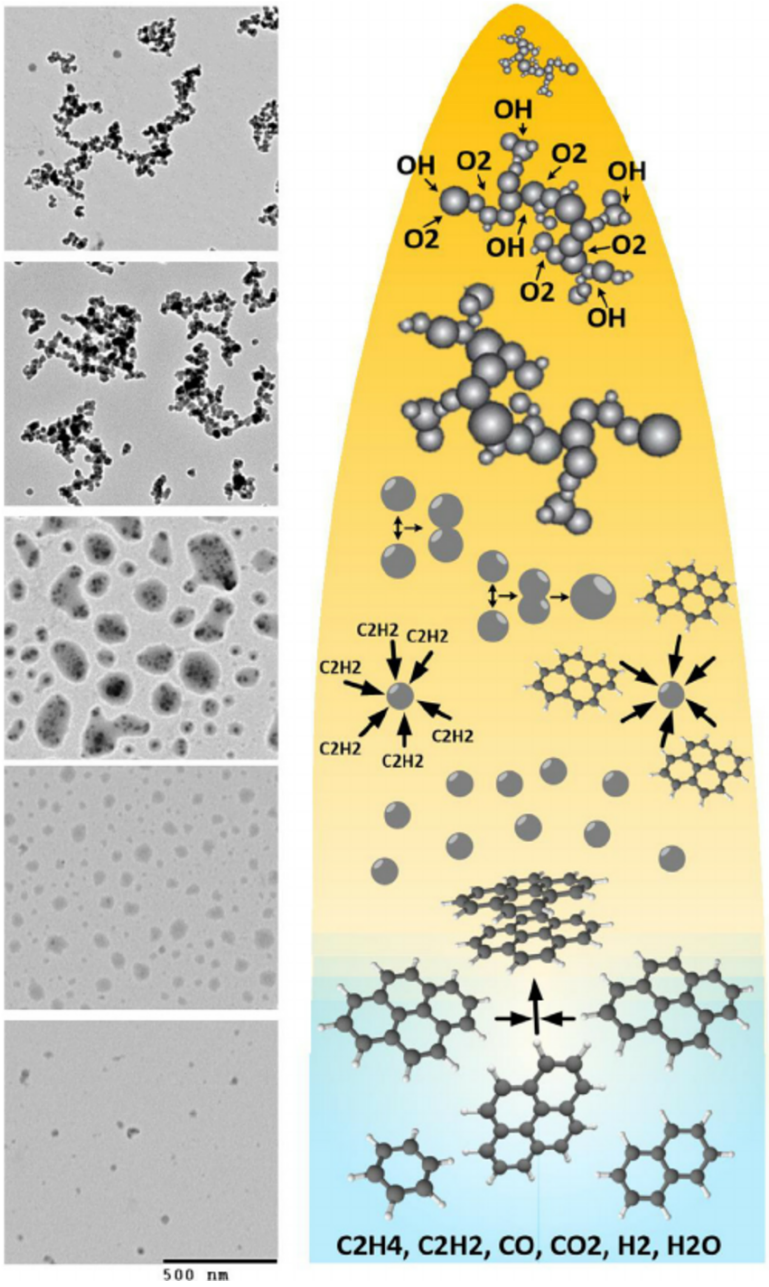

Fig. 1.3 Mass growth model of soot particles (M. R. Kholghy *et al.* [2]).

1.1.3 The impacts of soot

As a product of the incomplete combustion of hydrocarbon fuel (such as for some fossil fuels with a high carbon/hydrogen ratio, like diesel and kerosene), soot has a significant negative impact on the environment and mankind. Soot particles

are considered as one of the most important pollutants with regards to air clarity in cities and global climate change [16, 33].

Environmental and atmospheric scientists often refer to soot as black carbon [25, 34, 35]. In this thesis, when soot particles are referred to without further explanation, the reference is to the solid particles or soot as defined by combustion scientists and black carbon as defined by the atmospheric community.

According to a well-known study conducted by Bond *et al.* [34], global emissions of black carbon soot were estimated at 7.5×10^6 metric tons in the year 2000. They also quantitatively evaluated the role of soot in global climate change and found that the emission of black carbon increased the average absorption of the solar radiation by the Earth by 1.1 Wm^{-2}, and concluded that carbon black is the second most important human emission, after carbon dioxider, in terms of its climate forcing in the present-day atmosphere [34].

Soot is also harmful to the human body. In the United States, the well-known Six Cities Study [35] showed early indications of health effects of human exposure to ambient particles. The results show that mortality was most strongly associated with air pollution with fine particulates. This is because the fine particles (whose diameter is smaller than 2.5 μm, $\mathrm{PM}_{2.5}$) and ultrafine particles (whose diameter is smaller than 0.1 μm, $\mathrm{PM}_{0.1}$) are more likely to penetrate lung cells when breathing or adhere to skin and become absorbed into the human body. Whilst soot particles are not the dominant component of coarse PM (whose diameter is 2.5-10 μm) in atmospheric aerosols, soot (in organic or elemental carbon) consists of significant and even dominant parts of fine and ultrafine particles. A study conducted at the University of Southern California (USC) [4] provides data of the variation on composition between coarse aerosol particles and fine and ultrafine particles (as shown in Fig. 1.4).

The results from the USC study show that organic and elemental carbon (soot) dominates ultrafine aerosols but they are less important in coarse particles [3]. These fine and ultrafine particles, once inside, can be transported within

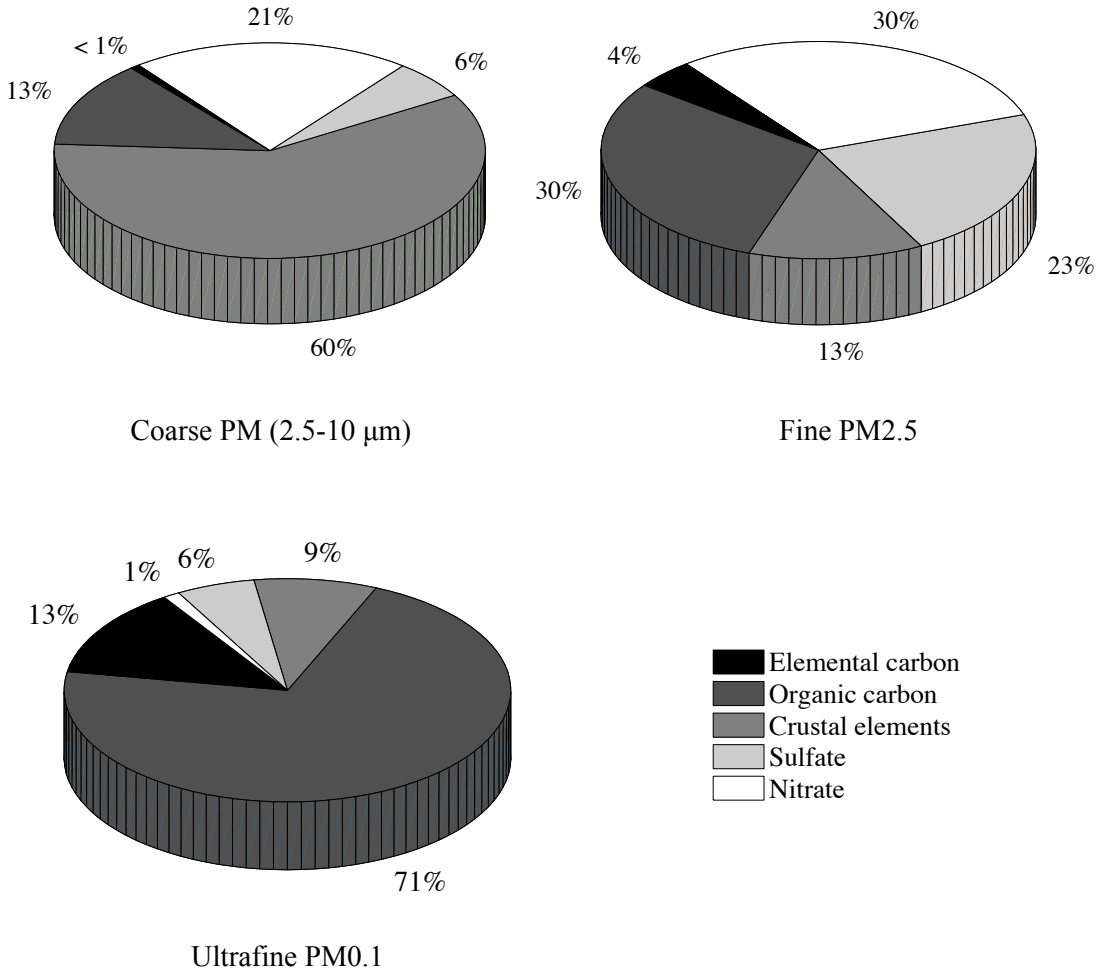

Fig. 1.4 Average composition of ambient aerosol particles in different size ranges during 2002-2003 at the USC EPA Supersite in Los Angeles. Carbon becomes more and more important as the particle size decreases. Adapted from [3], based on data of Sardar *et al.* [4].

the human body, eventually interacting with organs and cells due to their high carbon composition and the active site on the carbon particle's surface [3].

Paticulate matter may also exacerbate underlying health problems such as congestive heart failure [36, 37], as opposed to just being responsible for acute respiratory problems. A variety of detrimental symptoms may be linked to exposure to $PM_{2.5}$ and $PM_{0.1}$, including a reduction in heart rate variability. One's susceptibility to fine particles may also be exacerbated by underlying health conditions, with diabetes [38] having been recently implicated as one of these conditions.

Now that fine particles have been shown to be a more significant health hazard than coarse particles, the previous mass-based emission regulation may not constitute a sufficiently effective standard. The E.U. has already enacted a size-based emissions standards for fossil fuel engines from July 2015 [39]. These developments in emissions regulations will certainly require more accurate and low-cost soot particle diagnostic techniques.

1.1.4 Soot used in industry

In industry, soot particles are often termed 'carbon black'. In the prehistoric period, carbon black was used as a pigment for cave paintings, and even today it is still the main functional component in toners and printing inks. From the early 20th century, carbon became widely utilised in the rubber industry as a colourant [1]. The carbon black in the rubber can significantly increase the strength and toughness of rubber [40–43]. In addition to applications in the tyre industry, carbon black has also been utilised in plastics such as for conductive packaging, films, fibres, mouldings, pipes and semiconductive cable compounds.

1.2 Research background

Mature soot particles are good optical absorbers in the ultraviolet (UV), visible, and infrared (IR) wavelength regimes [25]. Thus, absorption/extinction based measurement technique to determine the concentration are possible. Moreover, soot is also a refractory material with a sublimation point of about 4000 K [25, 44], and when heated up to a temperature close to the sublimation point, the soot particles will emit a strong wide-band incandescence signal. The intensity and decay rate can be markers of the concentration and particle size of soot. Based on this property of soot, laser induced incandescence (LII) has been developed.

In this section, current progresses of the two most popular laser-based soot diagnostics methods (extinction and LII) is breifly reviewed as the background

of the present study.

1.2.1 Extinction measurement

Since the 1970s, a number of diagnostic methods for the measurement of soot in a flame have been developed. Optical methods, and particularly laser-based methods, have led to the most important developments because they provide non-intrusive measurements with the potential for *in-situ* data in flames. Therefore, laser diagnostics, *e.g.* laser extinction/scattering and laser induced incandescence, have been applied to soot measurements in a variety of different flames, such as laminar premixed flames [45–52], laminar diffusion flames [52–60] and turbulent diffusion flames. [47, 55, 61–65].

Line-of-sight extinction (LOSE) measurement is one of the *in-situ* and quantified soot volume fraction measurement techniques, and can be used as long as the complex refractive index is known. It quantitatively describes the proportional relationship between the ratio of the differential of light intensity to the incident light intensity and the differential of the path length. By assuming the extinction coefficient is independent of light intensity, the value of the soot volume fraction can be calculated using the results from the electromagnetic theory of spherical particles [23] (the detailed theory of the extinction can be found in Chapter 2). Thus, extinction measurements can be employed to obtain the quantified soot volume fraction [66] and, as a result, are often used as the calibration method for LII and other optical diagnostics [7, 67, 68].

The main advantage of the extinction measurements technique is its low cost. This is a result of its modest requirements for setup, namely low power lasers and detectors [69]. A continuous wave (CW) 10 mW laser has been used as a light source in some extinction measurements [70]. Furthermore, photodiodes can be used as detectors for some extinction measurement because of the small diameter of the laser beam required [63, 70, 71]. Therefore, it is possible to develop an integrated apparatus for extinction measurement that is highly portable and has

a short response time.

However, extinction measurements do suffer from several significant disadvantages: (a) It is a line of sight measurement, so its interpretation depends on symmetry. (b) It is only a point measurement unless calibrated measurements using cameras are used [72]. (c) It is difficult to apply them to low-soot producing flames due to low signal-to-noise ratio (SNR). However, the low-soot production is in particular need of exploration. At present, many vehicle engines are operated under relatively lean conditions and produce low soot. Hence, to explore the low-soot production region using extinction measurements can be meaningful to the development of a diagnostic technique for soot particles.

In the present study, it is assumed the signal measured in extinction is proportional to the fraction absorbed or scattered by soot (detailed in Chapter 2). The extinction coefficient is proportional to the concentration, so when the concentrations are small, so is the signal. One way to increase the signal is to increase the path length thus the extinction. The multipass configuration is a popular method used to increase the path length. A handful of multipass cells have been developed to be used in the low SNR conditions [6, 66, 73–77].

However, the lack of spatial resolution in these cells is still a problem. A method can avoid this limitation while keeping the high measurement sensitivity is cavity ring-down spectroscopy (CRDS), which was developed by O'Keefe *et al.* [78]. In the CRDS configuration, the laser beam is confined to remain along a single line in multipass cell, leading to a higher spatial resolution (depends on the size of the beam). Many researchers have followed this configuration and applied it to soot detection [51, 79–84]. However, the laser source required for the CRDS technique is a pulsed laser rather than a CW laser, thus eliminating the possibility of continuous measurement in time, but because the power can be higher instantaneously, it is possible to obtain higher SNR (normally several orders of magnitude higher) for low concentrations. Moreover, the cost of CRDS is high due to the requirement of fast response, highly sensitive optical detectors and

signal receivers. Therefore, a low-cost technique that can maintain the advantages of a highly sensitive and spatially resolved measurement system is still needed.

1.2.2 LII measurement

LII measurements have long been used in the determination of soot particle mass/volume concentration [7, 8, 23, 24, 51, 55, 61–63, 67, 83, 85–92] and size [45, 50, 52, 52, 53, 93–98].

The basic idea behind the LII technique starts with the use of a high-power laser to heat the particle close to its sublimation temperature (around 4000 K). At this temperature, the soot particle emits wide band incandescence radiation. Santoro *et al.* first proposed a linear relationship between the soot volume fraction (f_v) and its incandescence emission intensity [23]. The proportional relationship between f_v and the LII signal is based on the radiation calculation of small particles within the Raleigh Regime, which is valid for most flame-generated soot particles whose diameter is less than 100 nm. After Santoro *et al.*'s study [23], due to its non-intrusive nature and simplicity in both theory and application, the LII technique has become a popular method to determine f_v in flames [7, 8, 89]. Shaddix *et al.* [7] made a significant contribution to the development of the technique by detailing some important experimental parameters, such as the appropriate choice of the excitation laser energy/fluence, the collection wavelengths, the width of the collection time window of ICCD cameras and line-of-sight laser power correction, *etc.* However, it is difficult to make LII measurement of soot f_v independently and absolutely quantitative, because even if the LII signal is quantitatively linearly proportional to the soot volume fraction (see Section 2.3.6), the proportionality coefficient between f_v and the LII signal is difficult to be evaluated merely by LII experiment, since it highly depends on many factors in the experiments, such as the intensification of ICCD cameras, the space angle of the collecting lens, and the laser intensity profile in the excitation laser beam/sheet. Therefore, the extinction technique is often used separately to quantitatively cal-

ibrate LII results [7, 8, 68, 83, 88, 89]. As an alternative calibration technique, Snelling *et al.* [87] developed the technique of auto-compensating LII, which enabled quantitative measurements of volume fraction without the need for calibration via another soot measurement technique, by using the absolute LII signal intensity from soot particles. However, the data interpretation process involves many assumptions in Planck's radiation calculation, which introduce a level of uncertainty to the calibration constants. Nevertheless, LII measurements with *ex-situ* or *in-situ* extinction calibration are still the mainstream for LII based soot f_v measurements.

The time-resolved LII (TiRe-LII) technique can be used to determine the size of soot particles.

The concept TiRe-LII technique was first published by Weeks *et al.* [99], in which a TEA CO_2 laser was used to heat submicron powder of carbon black (soot particles). The time-resolved emission from soot particles after the laser pulse showed that the decay time may be related to particle size. Weeks' work was followed by Eckbreth *et al.* [135] and Burakov *et al.* [136], who developed energy and mass balance equations to model the processes of laser-induced heating, incandescence emission, and saturation of the LII signal from soot due to sublimation of the particle. Some flames were measured and the models were subsequently validated.

Melton [85] then expanded the model to include other heating and cooling processes, such as surface heat conduction and heat radiation of the particles. Will *et al.* [100, 101] developed a model of TiRe-LII based on the earlier work. This model is widely referred to and is used under various studies [45, 47, 49, 50, 52–54, 57, 64, 65, 93, 94, 94, 95, 95–98, 101–109].

Since the 1990s, some researchers attempting to apply it to some non-soot nanoparticles or nanostructures. Vander Wal *et al.* first applied the technique to carbon nanotubes and several metal materials [110]. He found that the LII signal intensity from metals can be related to their particle concentration, and

the nature of the signal decay was similar to that of soot particles.

After 2005, a number of works have been published about using LII for detecting non-soot particles. Maffi *et al.* [111] investigated the laser-induced spectrum of titanium dioxide (TiO_2) particles. His results provided criteria for others to choose suitable collection wavelengths for LII measurements of TiO_2 particles. Cignoli *et al.* [15] conducted TiRe-LII measurements for titania nanoparticles in a flame reactor during its synthesis process, and qualitatively established a relationship between the size of titania nanoparticles and the decay timescale. Daun *et al.* [112] examined the thermal accommodation coefficients for TiRe-LII of nickel nanoparticles in argon.

However, there are still many gaps in our knowledge relating to the non-soot LII measurements that need further research, since the optical properties of soot particles may be quite different to those of other materials. This is also a future research direction of the present study (as discribed in Chapter 6)

1.3 Objectives

The main objectives of the present study are to:

1) Develop a highly-sensitive, high spatial resolution but low-cost CW laser extinction system for *in-situ* soot volume fraction measurements, based on the multipass configuration.

2) Apply and test the system on a series of standard low-soot producing flames and perform an appropriate uncertainty analysis, and compare the measured soot volume fraction with the results obtained from other authors.

3) Produce a soot volume fraction database for the standard flames tested.

4) Develop a new 2-dimensional 2-colour time-resolved LII (2D2C-TiRe-LII) measurement method for determining soot particle size, and test the system with standard diffusion ethylene flames.

5) Test the TiRe-LII measurement system with ultrafine soot particles pro-

duced in a diffusion methane flame.

1.4 Thesis organisation

The thesis consists of six chapters.

Chapter 1 begins with an introduction to the research background and the objectives of this research.

Chapter 2 introduces a high-spatial resolution laser-cavity extinction technique. This newly developed technique is described in detail and tested with a standard laminar diffusion flame. A comparison between the laser-cavity extinction technique and LII technique is also shown in Chapter 2.

In order to investigate the soot formation mechanism in nitrogen diluted diffusion flames, and further test the limit of the laser-cavity extinction system, a series of nitrogen diluted, low-soot producing laminar methane-air diffusion flames are tested in Chapter 3.

Chapter 4 introduces the 2C-2D-TiRe-LII technique, which is a combination of the 2D-TiRe-LII technique and the 2C-LII technique. The LII configuration allows both peak temperature and soot primary particle sizes to be determined in an ethylene diffusion flame. The results of the 2C-2D-TiRe-LII technique are compared with others TEM results.

The ultrafine soot particles (diameter$<$30 nm) in a standard diffusion methane flame are measured with the 2C-2D-TiRe-LII technique in Chapter 5 and finally a summary of conclusions and suggestions for future research is provided in Chapter 6.

Chapter 2

Continuous Wave Laser Cavity Extinction and Laser-Induced Incandescence in Methane, Ethylene and Propane Flames

2.1 Introduction

2.1.1 Line-of-sight extinction (LOSE) and LII technique

As discussed in Chapter 1, soot is not only a significant atmospheric pollutant, but also a contributor to climate change [1, 16, 33, 113]. Many techniques have been developed to measure soot particles from a variety of sources, both via sampling and non-intrusive techniques. Over the last few decades, LII has become the main non-intrusive method for *in situ* soot volume fraction measurement in flames, given its ability to resolve soot concentrations quantitatively and with good spatial resolution. Nevertheless, LII requires independent calibration, typically via LOSE measurements [68], and unsteady measurements are only possi-

ble with high-power, high repetition rate lasers. Shaddix *et al.* [7, 8] exploited these combined measurements to produce a popular database of quantitative soot measurements in laminar hydrocarbon diffusion flames. The same technique was also applied by other researchers in the investigations of laminar diffusion flames [53, 114, 115], laminar premixed flames [45, 51, 116] and turbulent diffusion flames [61, 63–65].

As discussed in Chapter 1, LOSE measurements have some intrinsic advantages: They (a) provide close to absolute measurements of soot mass fraction, (b) are easily adapted to unsteady measurements, and (c) are relatively simple and inexpensive to set up. The key disadvantages of LOSE are: (a) as line-of-sight measurements, they provide an integrated measurement of the soot attenuation, which can only be deconvoluted for symmetric paths or by multi-path tomography, (b) a limited signal-to-noise ratio (SNR) due to low extinction in single-pass configurations, and (c) poor spatial resolution in the cross-path direction, particularly when multipass configurations are adopted. The cross-path spatial resolution can be improved, for example, by using CCDs rather than point detectors for measurements such as those used by Thomson and Johnson [117], but which require sources with high power stability and spectral selectivity. Solutions for the limitations of low SNR can be mitigated by adding a beam stabiliser [7, 118], but this cannot eliminate other instrumental noise. SNR issues can be improved by using multipass cells, often at the expense of spatial resolution [74, 76, 77, 119]. Several examples of multipass systems in low SNR conditions are briefly introduced and compared in the next section.

2.1.2 Several examples of multipass systems in low SNR conditions

The three mainstream types of multipass system used by researchers are the White [66, 73, 74], Herriott [75, 76] and Circular (compact) [6, 77] systems.

The White system is shown in Fig. 2.1. It consists of three mirrors with the same radius of curvature: the larger mirror A, and two smaller mirrors B and B'. The center of curvature of A is located between B and B', while the centres of curvature of B and B' fall on the surface of A. According to the geometric optics, the light beam emitted from A will be reflected back to A after reflecting off B and B', and the distances from the two points to the curvature centres of B and B' are equal. If the curvature centres of B and B' are symmetric about A's centre of curvature, the desired positions of the centre of curvature of B and B', as well as the incidence angles, can be calculated from the required optical path length. If there is some deviation in the vertical position of B and B', then the image on the point A will be scattered up and down.

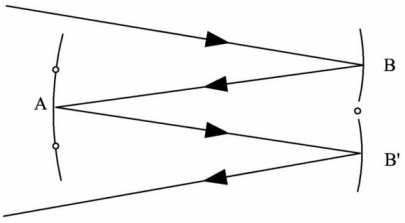

Fig. 2.1 Schematic of the White multipass system

The Herriott is another type of multipass system. Figure 2.2 shows the schematic of a typical Herriott multipass system. The system is made up of two opposing spherical mirrors. A hole is machined into one of the mirrors to allow the input and output beams to enter and exit the cavity. Alternatively, the beam may exit through a hole in the opposite mirror. In this fashion the Herriott system can support multiple light sources by providing multiple entrance and exit holes in either of the mirrors. Unlike the White system, the number of traversals is controlled by adjusting the separation distance between the two mirrors.

The Circular system was developed in recent years [6]. The development of this new type of multipass system was driven by the demands for compactness, robustness, low volume, and ease of use in practice. As showed in Fig. 2.3, a single piece of reflective toroidal surface forms a circular cavity for the laser beam

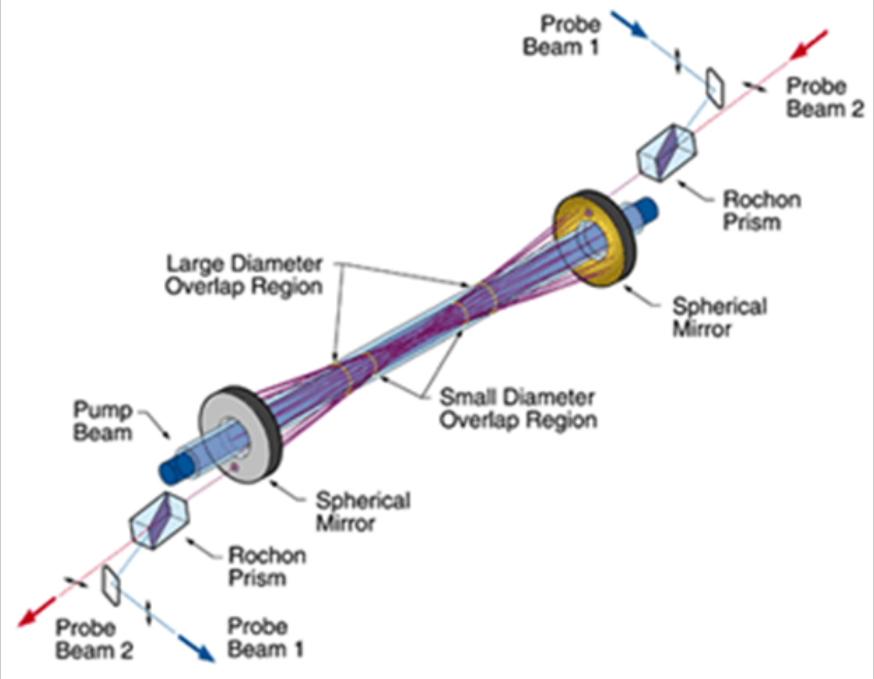

Fig. 2.2 Schematic of the Herriott multipass system [5].

to interact with the measured medium many times and hence increase the optical depth of the system.

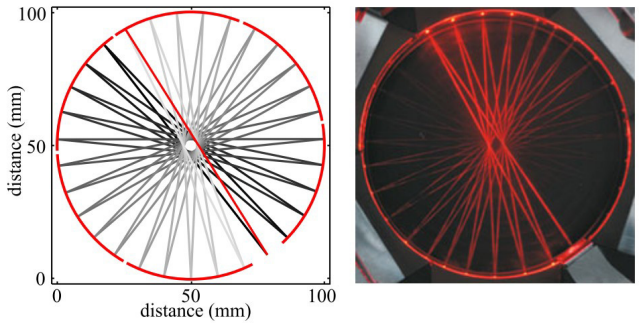

Fig. 2.3 Schematic of the Circular multipass system [6]

The pros and cons of the three multipass systems are compared in Table 2.1

From Table 2.1 we can see that all of these systems are closed optical cells and are mainly used in the diagnostic of homogeneous environments. Spatial resolution is not primary aim. Futhermore, they are closed cells, which allow gases trapped in the cells to be measured, however, this is not applicable to the

Table 2.1 Advantages and disadvantages of the three multipass systems

System	Advantages	Disadvantages
White	Number of traversals easily controlled. Allows for high numerical aperture.	Cannot be used in systems where high spatial resolution is required. Misalignment may be a problem.
Herriott	Simpler than the White cell. Less susceptible to mechanical disturbance of the cell. More stable than the White system.	Requires machining of special mirrors. Very expensive.
Circular	Allows flexible path length adjustments by simply changing the angle of the laser beam at the entrance window.	Poor spatial resolution. Toroidal mirror required.

current experiment because the present study needs an open environment. Cost is also a consideration as the price of each cell can be as high as thousands of GBPs, due to the cost of specially shaped mirrors. The high cost of the multipass cell may be a barrier to the development of a portable and low-cost particle detection device.

The idea of placing two opposite mirrors to form a laser cavity (a device to enable the light beam to reflect back and forth) from the Herriot multipass system can be adapted in the present study, since it is easy to achieve and can be used in an open environment when removing the outer cell. However the spatial resolution is still a problem since the laser path is non-collinear in the laser cavity. To overcome this problem, the cavity mirror alignment used in cavity ring-down spectrometry (CRDS) [51, 79–84] and the multipass tunable diode laser absorption spectroscopy (TDLAS) absorption method [120–128] is adopted. In both techniques, the laser beam travels in the cavity. This configuration allows a multipass measurement while retaining a good spatial resolution. However, there is the need for symmetry for deconvolution of the LOSE system, which is

a disadvantage.

By combining the advantages of the CW multipass cell (Herriott cell) and the collinear cavity absorption technique (CRDS and TDLAS), a novel CW cavity LOSE technique is developed in this study. This improves the SNR by two orders of magnitude over a single pass system, whilst maintaining a spatial resolution of the order of 200 μm in measurements of low-sooting laminar diffusion flames. The primary distinction between the present technique and previous efforts in soot detection via CRDS [51, 82] is that the present technique does not rely on pulsed, shot-to-shot measurements, but rather a low-power, low-cost CW laser. This allows for a much simpler, less expensive system, which does not require a fast response detector and signal receiver capable of nanosecond time resolution. Moreover, it becomes possible to employ the LOSE system in unsteady situations, as demonstrated in engines [70, 129, 130]. Since soot absorption takes place over a wide range of wavelengths, the method does not require a tuneable light source. The results obtained by this CW cavity LOSE system are used to calibrate the LII measurements performed on the same flames. The calibrated LII and deconvoluted LOSE measurements are then compared across the radial dimension. The next sections of this chapter describe the background theory, experimental set-up and results, including a detailed uncertainty analysis.

2.2 Theory of cavity extinction

2.2.1 The extinction coefficient and soot volume fraction

The extinction process consists of the power reduction of an incident laser beam as it passes through a sooting flame, because of the absorption and scattering of soot particles. The Lambert-Beer Law [131, 132] has been considered as the cornerstone of extinction measurement, which can be explained with reference to Fig. 2.4 and Eq. (2.1):

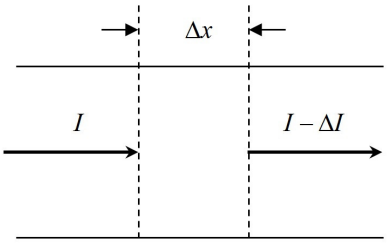

Fig. 2.4 Extinction of a laser beam.

$$\frac{\Delta I}{I} = -K_e \Delta x \tag{2.1}$$

As shown in Fig. 2.4, ΔI is the reduction of the incident laser beam intensity after transmission through a thickness Δx, I is the incident laser beam intensity, and K_e is the extinction coefficient of the medium, which is determined by the local volume fraction and the optical properties of soot. Integrating Eq. (2.1), we get:

$$-\ln \frac{I_t}{I_i} = \int_{I_i}^{I_t} \frac{\mathrm{d}I}{I} = \int_{-\infty}^{+\infty} K_e \mathrm{d}x = P_0 \tag{2.2}$$

where I_t and I_i are the intensities of the transmitted and incident beams respectively when the beams pass once through an extinction volume. The value P_0 represent the value of Eq. (2.2), which is the logarithmic attenuation of the laser intensity when the beams pass through the absorptive volume once.

The extinction of a laser beam can arise from particle absorption and scattering (as shown in Fig. 2.5). Both scattering and absorption can cause the reduction of the incident light beam after it passes through a space filled with particles. The amount of intensity reduction due to scattering or absorption depends on the size of the particles and the wavelength of the incident beam.

In the Rayleigh region, when the incident beam wavelength λ_e is much larger than the particle diameter D, the total scattering can be calculated as the product of the total scattering cross section of soot particles and its relative frequency of

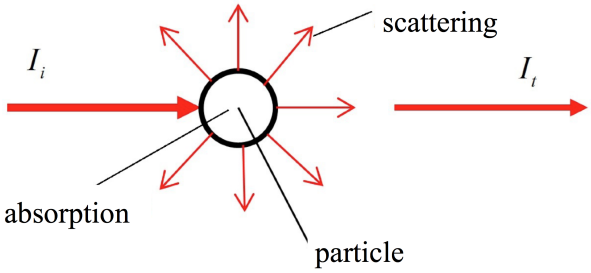

Fig. 2.5 Schematic of scattering and absorption. The light beam was partially scattered in all directions and partially absorbed by particles.

occurrence [23]:

$$K_s = N\frac{8\pi}{3}\left(\frac{\pi}{\lambda_e}\right)^4 \frac{F(m)}{4}\int_0^\infty P(D)D^6 \mathrm{d}D \tag{2.3}$$

where m is the complex refractive index of soot particles, $P(D)$ is the particle diameter probability distribution function, and $F(m)$ is the scattering function of soot particles, and is defined as:

$$F(m) = \left|\frac{m^2-1}{m^2+2}\right|^2 \tag{2.4}$$

The absorption coefficient of soot particles in the Rayleigh region is similar to the scattering function, and the total extinction coefficient K_e can be calculated as the extinction cross section multiplied by the particle number density:

$$K_a = N\frac{\pi^2}{\lambda_e}E(m)\int_0^\infty P(D)D^3 \mathrm{d}D \tag{2.5}$$

where $E(m)$ is the soot absorption function, given by:

$$E(m) = -\mathrm{Im}\left(\frac{m^2-1}{m^2+2}\right) \tag{2.6}$$

The extinction of the incident light beam is due to the linear composition of

absorption and scattering, so that:

$$K_e = K_a + K_s \tag{2.7}$$

From Eqs. (2.3) to (6.4), we can see that the scattering coefficient K_{scat} is proportional to D^6/λ^4 whereas the absorption coefficient is proportional to D^3/λ, thus, the ratio of scattering and absorption scales with D/λ. A non-dimensional size parameter d is introduced in the analysis to indicate the portion of absorption and scattering in total light extinction, which is defined as:

$$d = \frac{\pi D}{\lambda_e} \tag{2.8}$$

When $d < 0.3$, the scattering can be considered negligible compared with absorption [133], which is the Rayleigh approximation. In the present research, the Rayleigh approximation is used to estimate the soot volume fraction, since the soot load in the flames tested is not high and the primary diameter of soot particles is small. In the present study, the $\lambda = 638$ nm is used as the laser source for LOSE measurement, so $d \leq 0.296$ for soot particles whose diameter ≤ 60 nm (which is valid for most of the soot particles produced in tested flame). Hence Eq. (2.7) can be written as:

$$K_e = K_a \tag{2.9}$$

However, soot particles are not uniform spherical particles, and the aggregation effect is more dominant in heavy sooting flames; the Rayleigh-Debye-Gans approximation for the optical cross sections of fractal (GDG-FA) model was used by some researchers [81, 134–136].

Liu *et al.* investigated the effect of beam extinction in a laminar diffusion flame with both the Rayleigh approximation and Rayleigh-Debye-Gans approximation models [137]. They suggested that the contribution of scattering in laminar diffusion flames is negligible and hence the Rayleigh approximation is suitable the

present case. Therefore, by combining Eqs. (6.4) and (2.9), we can relate the soot volume fraction f_v and K_e by:

$$K_e = \frac{6\pi E(m)}{\lambda_e} f_v \tag{2.10}$$

Using Eq. (2.10), f_v can be calculated once the extinction coefficient K_e is known.

In reporting the experimental results, we therefore have two options: (a) neglect the contribution of scattering and choose a value for the refraction coefficient to extract the soot value fraction, and (b) report the experimentally obtained values of K_e, so that the results are useful even though the controversy regarding the contribution of scattering and the value of the refraction coefficient remains. In the present study, we use the same assumptions as Shaddix *et al.* [7, 8], and assume the same value of $E(m)$ in order to compare values for negligible scattering and $E(m)$ with the published values of $E(m)$. The LII results of the present study are thus calibrated and compared with extinction data. Meanwhile, the values of K_e are also reported, which are independent of any assumptions about $E(m)$, and can be useful in the validation of future models. The values are available in the form of numerical data (see in Appendix F.1).

2.2.2 Mathematical model of laser cavity extinction

A typical collinear multipass system can be organised as shown in Fig. 2.6.

In Fig. 2.6, the medium is confined between two partial reflective mirrors of high reflectivity, r_1 and r_2, and low transmissivity, t_1 and t_2, whose values are carefully measured (see Appendix A). The output power of the laser is I_0 and the total laser beam intensity is $I_t(n)$, where $(n = 1, 2, ..., n)$ is the transmitted intensity at n order transmission by partial reflective mirror 2; with the flame on,

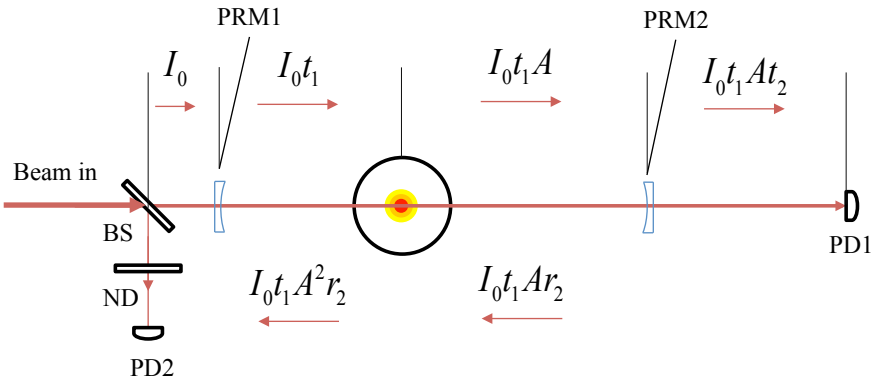

Fig. 2.6 Schematic of the cavity ($A = e^{-P_0}$; BS: beam splitter; ND: neutral density filter; PD: photodiode; PRM: partial reflective mirror).

we have:

$$\begin{aligned} I_t(1) &= I_0 t_1 A t_2 \\ I_t(2) &= I_0 A^3 r_1 r_2 t_1 t_2 \\ I_t(3) &= I_0 A^5 (r_1 r_2)^2 t_1 t_2 \\ &\cdots\cdots \\ I_t(n) &= I_0 A^{2n-1} (r_1 r_2)^{n-1} t_1 t_2 \end{aligned} \tag{2.11}$$

The total transmitted intensity I_T after adding up an infinite number of passes through the mirrors is:

$$I_T = \sum_{n=1}^{\infty} I_t(n) = \frac{I_0 T_m A}{1 - A^2 R_m} \tag{2.12}$$

where $R_m = r_1 r_2$, $T_m = t_1 t_2$, and A is the ratio of intensities across the flame, where $A = \exp(-P_0)$. The ratio of transmitted to incident power across the cavity system is:

$$\frac{I_T}{I_0} = \frac{T_m A}{1 - A^2 R_m} \tag{2.13}$$

and the logarithmic loss of intensity across the cavity P_t is:

$$P_t = -\ln \frac{I_T}{I_0} = -\ln \frac{I_T}{I_0} = -\ln \frac{T_m A}{1 - A^2 R_m} \tag{2.14}$$

Assuming we can measure the total ratio $\frac{I_T}{I_0} = B = \exp(-P_t)$, we can solve for A and thus P_0 by solving the quadratic equation (2.14):

$$A = \frac{T_m}{2R_m B}\left[\sqrt{1 + \frac{4R_m B^2}{T_m^2}} - 1\right] \tag{2.15}$$

$$-P_0 = \ln A = \ln\left(\frac{T_m}{2R_m}\right) - \ln B + \ln\left[\sqrt{1 + \frac{4R_m B^2}{T_m^2}} - 1\right] \tag{2.16}$$

$$P_0 = -P_t - \ln\left(\frac{T_m}{2R_m}\right) - \ln\left[\sqrt{1 + \frac{4R_m \exp^2(-P_t)}{T_m^2}} - 1\right] \tag{2.17}$$

In Eq. (2.17), the value of P_t is measurable; R_m and T_m are carefully calibrated (see Appendix A), and hence the value of P_0 can be obtained.

2.2.3 Abel transform

Once the value of P_0 is known for each chord location across the flame, it is possible to invert the function to obtain the extinction coefficient using the Abel transform, by assuming radial symmetry. We define our coordinate system with radius, r, the distance to the chord from the origin, y, and the running integration variable, x. The projection of the line-of-sight extinction coefficient along the chord coordinate y from the centreline is:

$$P_0(y) = 2\int_0^{+\infty} K_e(x)\, dx \tag{2.18}$$

Taking $x^2 + y^2 = r^2$, and substituting for dx at fixed y, we have:

$$P_0(y) = 2\int_y^{\infty} \frac{rK_e(r)}{\sqrt{r^2 - y^2}}\, dr \tag{2.19}$$

which admits the inverse Abel transform:

$$K_e(r) = -\frac{1}{\pi}\int_r^{\infty} \frac{P_0'(y)}{\sqrt{y^2 - r^2}}\, dy \tag{2.20}$$

Since the measurements of $P_0(y)$ are conducted at a discrete point along the y axis, one uses discretisation of the integral in y, which is replaced by the index j for each element separated by the measured point y_j [138]:

$$f(r_i) = -\frac{1}{\pi}\sum_{j=i}^{\infty}\int_{0,j=i;-\frac{\Delta y}{2},j>i}^{\infty} \frac{P_0'(y_j+\delta)}{\sqrt{(y_j+\delta)^2 - {r_i}^2}}\mathrm{d}\delta \tag{2.21}$$

$P_0'(y)$ is approximated by the second order derivative with respect to y, as follows:

$$P_0'(y_j+\delta) = \frac{P_0(y_{j+1}) - P_0(y_{j-1})}{2\Delta y} + \frac{[P_0(y_{j+1}) + P_0(y_{j-1}) - 2P_0(y_j)]\delta}{\Delta y^2} \tag{2.22}$$

Using Eqs. (2.21) and (2.22), $f(r)$, which is the local extinction coefficient K_e can be obtained:

$$\begin{aligned} K_e(r_i) = f(r_i) = -\frac{1}{\Delta y}\sum_{j=i}^{\infty}\{&[I_{ij}(1) - I_{ij}(0)]P_0(y_{j-1}) \\ &-2I_{ij}(1)P_0(y_j) + [I_{ij}(1) + I_{ij}(0)]P_0(y_{j+1})\} \end{aligned} \tag{2.23}$$

in which:

$$I_{ij}(n_0) = \frac{1}{2\pi}\int_{0,j=i;-1,j>i}^{1} \frac{\delta^n}{\sqrt{(2j+\delta)^2 - 4i^2}}\mathrm{d}\delta \tag{2.24}$$

where $I_{ij}(n_0)$ is the linear deconvolution operator of the Abel transform, and $n_0 = 0$ or 1. When $r = 0$ to 6 mm and the step is chosen as 0.25 mm.

2.3 Experiment

2.3.1 Burner and flames

The experiments were performed on a laminar diffusion burner with operating conditions almost identical to those used by Santoro *et al.* [23, 24, 86] and Shaddix *et al.* [7, 8] (Fig. 2.7). The diameter of the inner fuel tube was 10.5 mm, and that for the outer air co-flow tube was 96.8 mm. The mass flow controllers (MFC, Alicat MC20 for fuel, MCR500 for air, accuracy ± 0.8% FS) were used to control the mass flow of fuels and co-flow air. The burner was mounted on a traverse platform to scan the position with a precision of 0.01 mm along the horizontal direction and 0.5 mm along the vertical. Methane, ethylene and propane flames were investigated, with operational conditions listed in Table 2.2, mirroring the prior work of Shaddix *et al.*. Figure 2.8 shows natural light photos of the five flames investigated.

Fig. 2.7 Cross section (left) and top view (right) of the burner used in the present work.

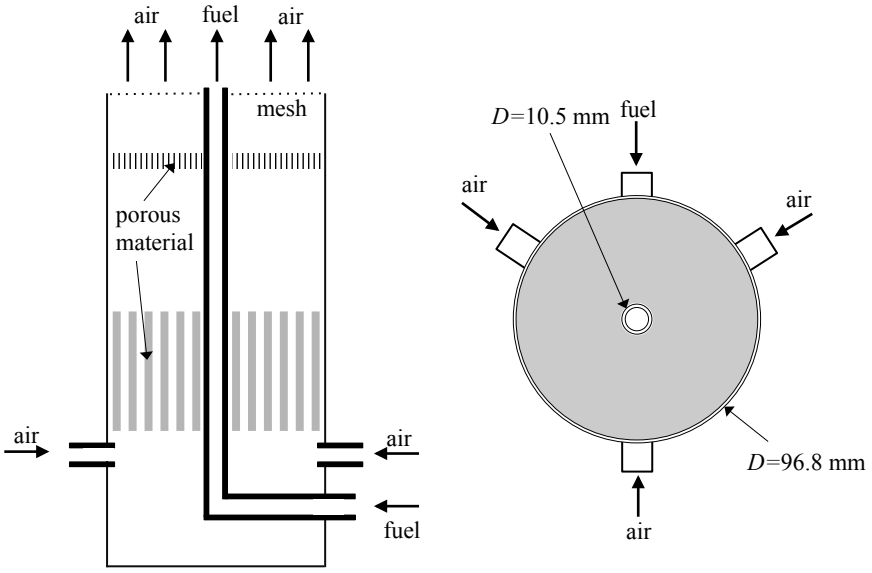

Case	CH_4(A)	CH_4(B)	C_3H_8	C_2H_4(A)	C_2H_4(B)
Fuel flow velocity (cm/s)	7.69	10.08	2.69	3.62	4.43
Air flow velocity (cm/s)	7.92	14.60	8.65	7.92	8.65
Fuel mass flow rate (slpm)	0.40	0.53	0.14	0.18	0.23
Air mass flow rate (slpm)	35.0	65.8	38.2	35.0	38.2
Visible flame height (mm)	75 ± 2	98 ± 2	85 ± 2	65 ± 2	85 ± 2

Table 2.2 Tested conditions for laminar diffusion flames

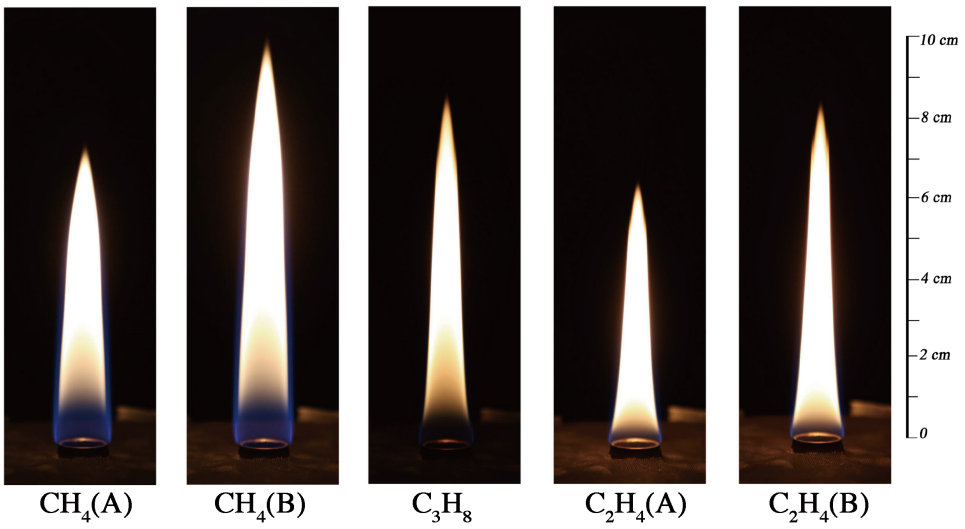

Fig. 2.8 Natural luminosity of the laminar diffusion flames tested (Camera model: Canon EOS 6D DLSR, exposure time = 1/60 s, photographic sensitivity (ISO) = 1250; lens model: Canon EF 24-105 mm f/4L IS, f = 4.0, focal length = 105 mm).

2.3.2 Cavity extinction measurement system

The schematic of the laser cavity measurement system is shown in Fig. 2.9. A diode laser (Omicron $LuxX-638-150$, 638 nm wavelength, 150 mW maximum power) was used as the laser source. Near-infrared light is preferred because visible wavelengths can be absorbed by polycyclic aromatic hydrocarbons (PAHs), creating uncertainties. A longer wavelength also means that the Rayleigh approximation is still valid for larger soot aggregates. The incident laser beam was split via a beam sampler (Thorlabs BSF05-A) into a reference laser beam ($\leq$ 1% of the power) and a probe laser beam. A neutral density filter ND1 (Thor-

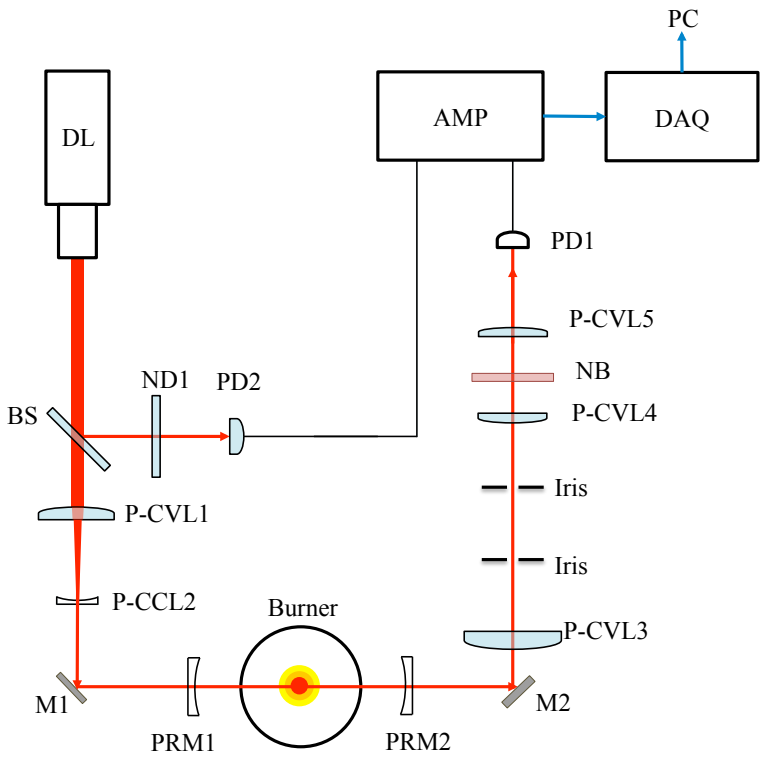

Fig. 2.9 Diagram of the LOSE system (DL: Diode laser; M: mirror; BS: beam sampler; ND: neutral density filter; PD: photodiode; CVL: convex lens; CCL: concave lens; NB: narrow band filter; PRM: partially reflective mirror; AMP: amplifier; DAQ: data acquisition board)

labs NE40A, optical density = 4.0) was used to attenuate the beam density to a range relevant for the reference photodiode. The probe beam was focused by a planar-convex lens P-CVL1 (Thorlabs LA1301-A, 250 mm focal length) and a planar-concave lens P-CCL (Thorlabs LC4888, -100 mm focal length) down to a diameter of 200 μm before entering the cavity. The two mirrors, PRM1 (COMAR Optics customised, 25 mm diameter, 1000 mm focal length, reflectivity: $r_1 = 98.11\% \pm 0.20\%$, transmissivity: $t_1 = 1.53\% \pm 0.15\%$ at 638 nm wavelength), and PRM2 (COMAR Optics customised, 1000 mm focal length, reflectivity: $r_2 = 98.11\% \pm 0.19\%$, transmissivity: $t_2 = 1.54\% \pm 0.16\%$ at 638 nm wavelength) were aligned and separated by 17.5 cm, with the burner in the middle.

The small separation distance and the large radius of curvature of the mir-

ror surfaces ensured that the laser beam diameter was nearly constant between the mirrors. The spatial resolution of the measurements has been characterised by profiling of the laser beam using a sharp blade to block the radial intensity, and differentiating. The results showed that the beam profile was approximately Gaussian, with FWHM $\approx$ 210 μm. The distance selected between two points in the LOSE measurements was 0.25 mm, which was larger than the diameter of the beam. The spatial resolution of the measurements was therefore approximately 200 μm throughout the measurement region. Unlike species with low molecular weight, absorption of soot laser light takes place over a wide range of wavelengths, so that phase matching is not required for maximum light extinction. The detection system consisted of two identical photodiodes, PD1 and PD2 (Thorlabs SM05PD1A Silicon Photodiode, 350-1100 nm, Cathode Grounded) which detect the light sampled from the transmitted and reference beam, respectively. Maximum SNR was ensured by selecting mirror reflectivities close to unity. The photocurrents obtained from the two photodiodes PD1 and PD2 (i_1 and i_2) were determined to be linearly proportional to the respective incident intensities. These are compared using a logarithmic amplifier (Texas Instrument LOG104), which improves the SNR relative to a linear amplifier for this application. The output voltage of the amplifier, V_{out} was obtained as:

$$V_{out} = C \log_{10} \frac{i_1}{i_2} \tag{2.25}$$

where the calibration constant $C = 0.496 \pm 0.0088$ V was obtained using an accurate reference current. A data acquisition board (NI USB-6009) was used to acquire the amplifier signal at a 14-bit resolution and at 2000 Hz for 10 seconds using LabView software. The value of the current ratio is affected by laser intensity fluctuations, flame luminosity and dark noise of the photodetectors.

2.3.3 Calibration of the laser beam

The diameter of the laser beam was approximately constant between the mirrors. The spatial resolution of the measurements was characterised by profiling of the laser beam using a sharp blade to block the radial intensity, and differentiating. The results show that the beam profile is approximately Gaussian (as shown in Fig. 2.10), with full width at half maximum (FWHM) ≈ 210 μm. The distance selected between two points in the LOSE measurements was 0.25 mm. The spatial resolution of the measurements was therefore approximately 200 μm throughout the measurement region.

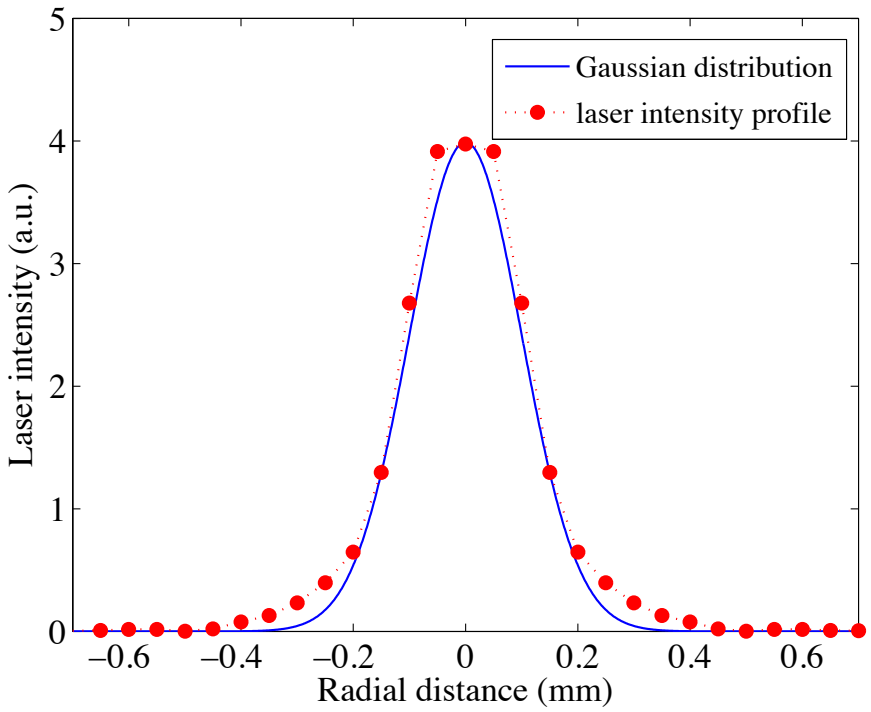

Fig. 2.10 Radial intensity profile of probe laser beam in the cavity, which closely obeys a Gaussian distribution and the width of 2σ is about 180 μm.

2.3.4 Measurement procedure for P_t

In order to precisely measure the value of P_t, a series of output voltages under different conditions were measured, as shown in Table 2.3.

Table 2.3 Definition of variables and case studies for decoupling interferences. Variables are: i_0: photocurrent of incident laser; i_F: photocurrent of PD1, laser on, flame on; i_{F1} and i_{F2}: photocurrent due to flame in PD1 and PD2; i_{B1} and i_{B2}: background ambient luminosity currents in PD1 and PD2; i_1: reference laser currents in PD1 and PD2; i_{ref}: steady reference current used for photocurrent of PD1.

V	Definition	Expression
V_{IN}	incident laser on PD1	$C\log\frac{i_0+i_{B1}}{i_2+i_{B2}}$
V_{LF}	laser on, flame on	$C\log\frac{i_F+i_{F1}+i_{B1}}{i_2+i_{F2}+i_{B2}}$
V_B	laser off, flame off	$C\log\frac{i_{B1}}{i_{B2}}$
V_F	laser off, flame on	$C\log\frac{i_{F1}+i_{B1}}{i_{F2}+i_{B2}}$
V_{ref1}	laser on, flame off PD1 blocked	$C\log\frac{i_{B1}}{i_2+i_{B2}}$
V_{ref2}	laser off, flame on, using stable reference current i_{ref} for PD1	$C\log\frac{i_{ref}}{i_{F2}+i_{B2}}$
V_{ref3}	laser on, flame off, using stable reference current i_{ref} for PD1	$C\log\frac{i_{ref}}{i_2+i_{B2}}$

By combining the equations in Table 2.3 and listing the equation system:

$$\begin{cases} V_{IN} = C\log\dfrac{i_0+i_{B1}}{i_2+i_{B2}} \text{.....}(a) \\ V_{LF} = C\log\dfrac{i_t+i_{F1}+i_{B1}}{i_2+i_{F2}+i_{B2}} \text{.....}(b) \\ V_B = C\log\dfrac{i_{B1}}{i_{B2}} \text{.....}(c) \\ V_F = C\log\dfrac{i_{F1}+i_{B1}}{i_{F2}+i_{B2}} \text{.....}(d) \\ V_{ref1} = C\log\dfrac{i_{B1}}{i_2+i_{B2}} \text{.....}(e) \\ V_{ref2} = C\log\dfrac{i_{ref}}{i_{F2}+i_{B2}} \text{.....}(f) \\ V_{ref3} = C\log\dfrac{i_{ref}}{i_2+i_{B2}} \text{.....}(g) \end{cases} \tag{2.26}$$

We obtain seven equations in Eq. (2.26) and eight unknown variables: i_0, i_t, i_{F1}, i_{F2}, i_{B1}, i_{B2}, i_2, i_{ref}.

From Eqs. (2.26a) and (2.26b), we obtain Eq. (2.27):

$$i_t = 10^{\frac{V_{LF}}{C}}(i_2 + i_{F2} + i_{B2}) - (i_{F1} + i_{B1}) \tag{2.27}$$

and

$$i_0 = 10^{\frac{V_{IN}}{C}}(i_2 + i_{B2}) - i_{B1} \tag{2.28}$$

thus,

$$\frac{i_t}{i_0} = \frac{10^{\frac{V_{LF}}{C}}(i_2 + i_{F2} + i_{B2}) - (i_{F1} + i_{B1})}{10^{\frac{V_{IN}}{C}}(i_2 + i_{B2}) - i_{B1}} \tag{2.29}$$

Dividing by $i_2 + i_{B2}$, we have:

$$\frac{i_t}{i_0} = \frac{10^{\frac{V_{LF}}{C}}\frac{i_2 + i_{F2} + i_{B2}}{i_2 + i_{B2}} - \frac{i_{F1} + i_{B1}}{i_2 + i_{B2}}}{10^{\frac{V_{IN}}{C}} - \frac{i_{B1}}{i_2 + i_{B2}}} \tag{2.30}$$

Using Eqs. (2.26d) and (2.26e) gives:

$$\frac{i_t}{i_0} = \frac{10^{\frac{V_{LF}}{C}}\frac{i_2 + i_{F2} + i_{B2}}{i_2 + i_{B2}} - 10^{\frac{V_F}{C}}\frac{i_{F2} + i_{B2}}{i_2 + i_{B2}}}{10^{\frac{V_{IN}}{C}} - 10^{\frac{V_{ref1}}{C}}} \tag{2.31}$$

and

$$\frac{i_t}{i_0} = \frac{10^{\frac{V_{LF}}{C}}\left(\frac{i_{F2}}{i_2 + i_{B2}} + 1\right) - 10^{\frac{V_F}{C}}\left(\frac{i_{F2}}{i_2 + i_{B2}} + \frac{i_{B2}}{i_2 + i_{B2}}\right)}{10^{\frac{V_{IN}}{C}} - 10^{\frac{V_{ref1}}{C}}} \tag{2.32}$$

Using Eqs. (2.26c) and (2.26e), we obtain:

$$\frac{i_t}{i_0} = \frac{10^{\frac{V_{LF}}{C}}\left(\frac{i_{F2}}{i_2 + i_{B2}} + 1\right) - 10^{\frac{V_F}{C}}\left(\frac{i_{F2}}{i_2 + i_{B2}} + \frac{1}{10^{\frac{V_B}{C}}} \times \frac{i_{B1}}{i_2 + i_{B2}}\right)}{10^{\frac{V_{IN}}{C}} - 10^{\frac{V_{ref1}}{C}}} \tag{2.33}$$

and

$$\frac{i_t}{i_0} = \frac{10^{\frac{V_{LF}}{C}}\left(\frac{i_{F2}}{i_2+i_{B2}}+1\right) - 10^{\frac{V_F}{C}}\left(\frac{i_{F2}}{i_2+i_{B2}} + \frac{10^{\frac{V_{ref1}}{C}}}{10^{\frac{V_B}{C}}}\right)}{10^{\frac{V_{IN}}{C}} - 10^{\frac{V_{ref1}}{C}}} \tag{2.34}$$

The value of $\frac{i_{F2}}{i_2+i_{B2}}$ can be obtained by the following steps:

Equation (2.26f) can be reconstructed as:

$$i_{F2} = \frac{i_{ref}}{10^{\frac{V_{ref2}}{C}}} - i_{B2} \tag{2.35}$$

Thus,

$$\frac{i_{F2}}{i_2+i_{B2}} = \frac{\frac{i_{ref}}{10^{\frac{V_{ref2}}{C}}} - i_{B2}}{i_2+i_{B2}} = \frac{1}{10^{\frac{V_{ref2}}{C}}} \times \frac{i_{ref}}{i_2+i_{B2}} - \frac{i_{B2}}{i_2+i_{B2}} \tag{2.36}$$

Using Eqs. (2.26d) and (2.26g), we have:

$$\frac{i_{F2}}{i_2+i_{B2}} = \frac{1}{10^{\frac{V_{ref2}}{C}}} \times \frac{i_{ref}}{i_2+i_{B2}} - \frac{i_{B2}}{i_2+i_{B2}} = \frac{10^{\frac{V_{ref3}}{C}}}{10^{\frac{V_{ref2}}{C}}} - \frac{10^{\frac{V_{ref1}}{C}}}{10^{\frac{V_B}{C}}} \tag{2.37}$$

By subsituting Eq. (2.37) into Eq. (2.34), we obtain:

$$\frac{i_t}{i_0} = \frac{10^{\frac{V_{LF}}{C}}\left(\frac{10^{\frac{V_{ref3}}{C}}}{10^{\frac{V_{ref2}}{C}}} - \frac{10^{\frac{V_{ref1}}{C}}}{10^{\frac{V_B}{C}}}+1\right) - 10^{\frac{V_F}{C}}\left(\frac{10^{\frac{V_{ref3}}{C}}}{10^{\frac{V_{ref2}}{C}}} - \frac{10^{\frac{V_{ref1}}{C}}}{10^{\frac{V_B}{C}}} + \frac{10^{\frac{V_{ref1}}{C}}}{10^{\frac{V_B}{C}}}\right)}{10^{\frac{V_{IN}}{C}} - 10^{\frac{V_{ref1}}{C}}} \tag{2.38}$$

and simplifing Eq. (2.38) gives:

$$\frac{i_t}{i_0} = \frac{10^{\frac{V_{LF}}{C}}}{10^{\frac{V_{IN}}{C}}} \times \frac{1 + 10^{\frac{V_{ref3}-V_{ref2}}{C}} - 10^{\frac{V_{ref1}-V_B}{C}} - 10^{\frac{V_F+V_{ref3}-V_{ref2}-V_{LF}}{C}}}{1 - 10^{\frac{V_{ref1}-V_{IN}}{C}}} \tag{2.39}$$

A quantitative calibration shows that the response of the the photodiode is linear with the laser intensity, we have:

$$\frac{I_T}{I_0} = \frac{i_t}{i_0} \tag{2.40}$$

So that the value of $P_t = -\ln\frac{I_T}{I_0}$ can be calculated by combining Eqs. (2.38) and (2.40). Now, we have the value of P_t from Eq. (2.41), since all of the voltages are measurable.

$$P_t = f(\mathbf{V}, C) = -\ln\frac{i_t}{i_0} = -\frac{\ln 10}{C}(V_{LF} - V_{IN}) + \ln\left(1 - 10^{\frac{V_{ref1} - V_{IN}}{C}}\right)$$
$$- \ln\left(1 + 10^{\frac{V_{ref3} - V_{ref2}}{C}} - 10^{\frac{V_{ref1} - V_B}{C}} - 10^{\frac{V_F + V_{ref3} - V_{ref2} - V_{LF}}{C}}\right) \tag{2.41}$$

2.3.5 LII measurement

The 2D LII measurements were made using the set-up described in Fig. 2.11. The laser source is a 532 nm Nd:YAG laser (Litron nanoPIV) firing at 10-25 Hz. The laser sheet was collimated into a parallel sheet by a series of beam-shaping optics (Thorlabs cylindrical lenses with focal lengths of 75 mm, -25 mm and 100 mm), followed by an aperture to generate a top-hat profile. The laser beam energy profile was detected using a cuvette filled with fluorescent dye (Rhodamine 6G in ethanol solvent) using an unintensified CCD camera (LaVision Imager Pro X 4M, 1 μs gate width, 1024 $\times$ 1024 pixels) equipped with a Nikon AF Micro Nikkor 60 mm lens (f/5.6) and a narrow band filter (Thorlabs FB600-10, central wavelength = 600 $\pm$ 2 nm, FWHM = 10 $\pm$ 2 nm). The laser power was verified to be top-hat from dye imaging measurements. The LII signal induced by the laser sheet was captured by an ICCD camera (LaVision Intensified Relay Optics and Imager Pro X 4M, 1024 $\times$ 1024 pixels) through a Nikon AF Micro Nikkor 60 mm lens 175

(f/2.8) and band filter (Thorlabs FB400-10, central wavelength = 400 ± 2 nm, FWHM = 10 ± 2 nm) to minimise luminosity from PAH fluorescence, C_2 radiation and the flame. A gate width of 100 ns was used to maximise the signal-to-noise ratio. The relatively long gate width may bias the f_v measurements towards larger particles [68] but since focus of the study is on comparisons between the multipass method and LII, this effect is relatively unimportant.

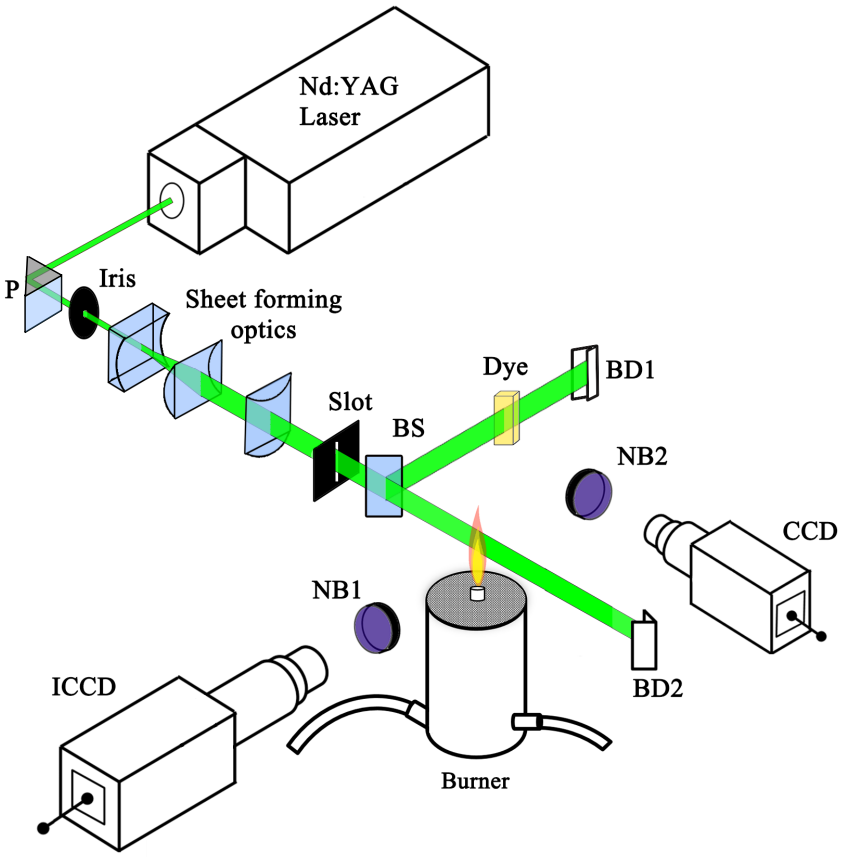

Fig. 2.11 Schematic of LII measurement set-up (P: prism; BS: beam splitter; NB1: 400 ± 20 nm band filter; NB2: 600 ± 5 nm band filter; BD: beam dump).

Figure 2.12 shows the dependence of the LII signal on the fluence of the laser sheet. The LII signal at each fluence is an average value of all pixels of the LII signal (100 ns gate width) from HAB = 34 mm to 66 mm for ethylene flame case B. In the low laser fluence region ($\sim$ 0.1 J/cm^2), the LII signal rises rapidly with increasing laser fluence, since the radiation intensity scales with T^4. As the

fluence increases, the sublimation of soot particles becomes significant, so that the LII signal reaches a maximum around 0.1-0.2 J/cm^2), as indicated in the marked rectangle. In this region, the LII signal is less sensitive to local laser fluence. In this work it is assumed that the fluence dependence of the LII signal is similar in the CH_4 and C_2H_4 flames, even though the soot particle sizes in these two flames are likely to be significantly different, as discussed by Shaddix and Smyth [7]. Figure 2.13 shows the beam profile and variance over 500 shots, as characterised by the resulting fluorescence in a cuvette containing Rhodamine 6G dye. The local intensity fluctuation of the laser sheet was as small as 2.5% in 500 shots as shown in Fig. 2.13; the error introduced by either laser shot fluctuations and spatial fluency was smaller than 1%. A total of 250 LII images were acquired for each condition, at an acquisition rate of 25 Hz. All images were averaged, with the background noise subtracted. The nominal spatial resolution was 33 μm/pixel for an imaging area of 34.1×34.1 mm^2.

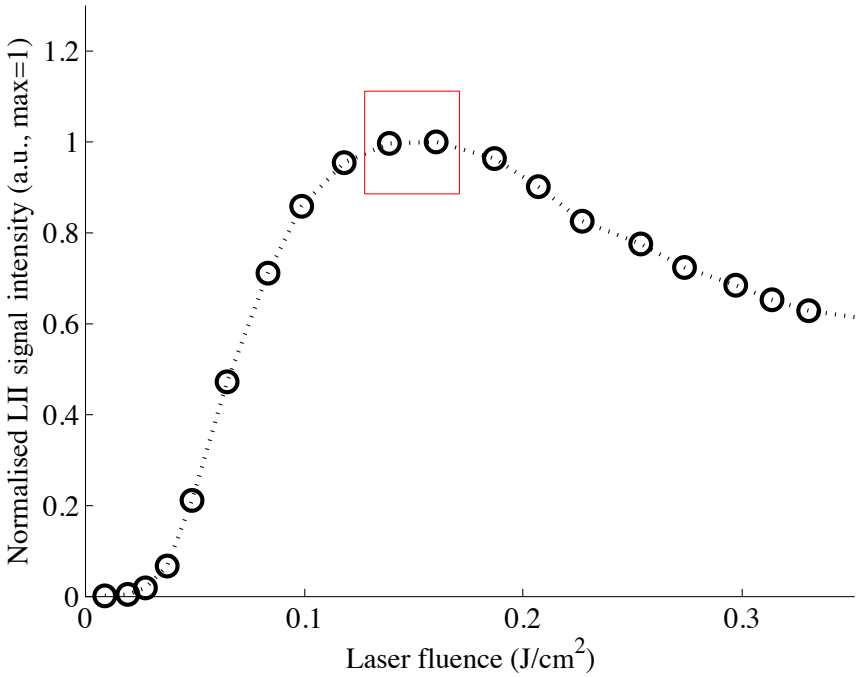

Fig. 2.12 Fluence dependence of the LII signal as a function of the fluence of the laser sheet; the plateau region (in the marked rectangle) was selected to conduct LII measurements.

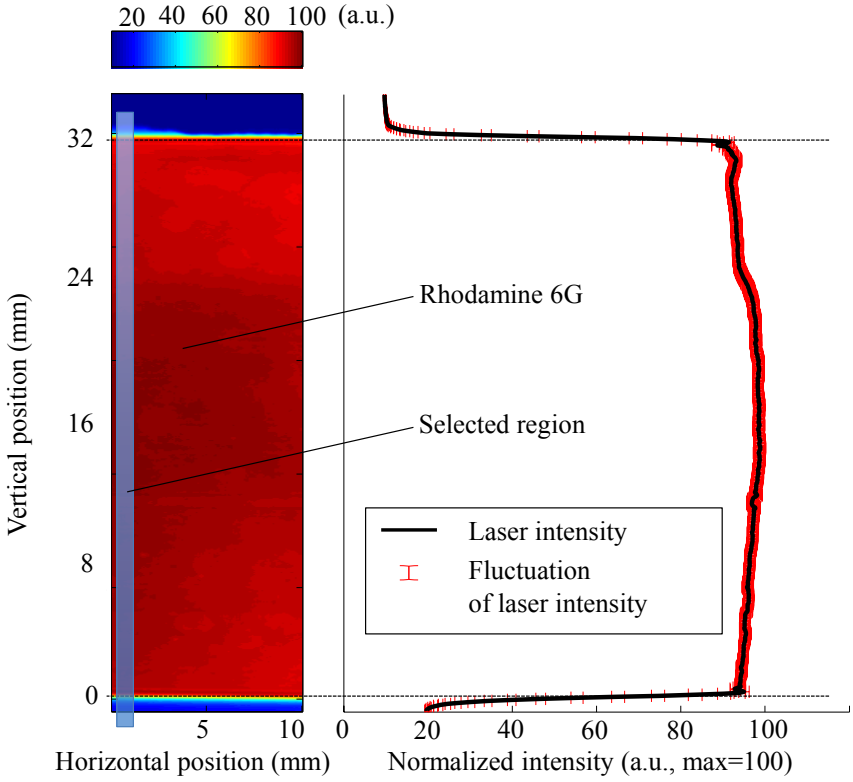

Fig. 2.13 Normalized laser beam intensity profile used for LII excitation. Left: Rhodamine 6G fluorescence excited by laser sheet in cuvette; Right: integrated fluorescent light intensity profile over the region shown in the highlighted rectangle.

2.3.6 LII calibration

According to Planck's law, the power per unit area and solid angle emitted by an object with emissivity of ε_{λ_s} at the respective wavelength equals:

$$E = \varepsilon_{\lambda_s} \frac{2hc^2}{\lambda_s^5 \left[\exp\left(\frac{hc}{\lambda_s k_B T}\right) - 1\right]} \tag{2.42}$$

where h is Planck's constant, c is the speed of light, k_B is Boltzmann's constant, λ_s is the emission signal wavelength and T is the surface temperature, often taken to be the sublimation temperature of the soot. The total solid angle for a grey element of surface $\mathrm{d}A_P$ is the hemispherical 2π, and the total area of a spherical

particle of diameter D is $A_P = \pi D^2$, so that the total emitted power is:

$$S_D = \varepsilon_{\lambda_s} \frac{2\pi^2 D^2 h c^2}{{\lambda_s}^5 \left[\exp\left(\frac{hc}{\lambda_s k_B T}\right) - 1\right]} \tag{2.43}$$

According to Kirchhoff's law [91, 139, 140], absorptivity is equal to emissivity, thus the spectral emissivity is assumed to be:

$$\varepsilon_{\lambda_s} = \frac{4\pi D E(m)}{\lambda_s} \tag{2.44}$$

By substituting Eq. (2.44) into Eq. (2.43), we obtain:

$$S_D = \frac{48\pi^2 h c^2 E(m)}{{\lambda_s}^6 \left[\exp\left(\frac{hc}{\lambda_s k_B T}\right) - 1\right]} \frac{\pi D^3}{6} = C_{em} \frac{\pi D^3}{6} \tag{2.45}$$

where C_{em} depends on λ_s, T and the index of refraction of the particle at the emitting wavelength. The LII signal from a collection of particles in the sample region is obtained as the integrated signal from each particle over the probe volume ΔV, and accounting for the mean collection angle Ω_c, optical efficiency η_o, detector sensitivity ϕ_d, number of particles per unit volume n, particle size probability distribution function $p(D)$, we have:

$$S_{\mathrm{LII}} = C_{em} \frac{\Omega_c}{4\pi} \eta_o \phi_d \Delta V n \int_0^\infty p(D) \frac{\pi D^3}{6}\, dD = C_{det} C_{em} f_v = K_{\mathrm{LII}} f_v \tag{2.46}$$

where $C_{det} = \dfrac{\Omega_c}{4\pi} \eta_o \phi_d \Delta V$, and $K_{\mathrm{LII}} = C_{det} C_{em}$ is the calibration constant connecting the LII signal to the soot volume fraction. K_{LII} was obtained by connecting the measured extinction to the corresponding integrated soot volume fraction, as follows:

$$P_0(0) = \int_{-\infty}^{+\infty} K_e(r)\, \mathrm{d}r = \frac{6\pi E(m)}{\lambda_{\mathrm{e}}} \int_{-\infty}^{+\infty} f_v(r)\, \mathrm{d}r \tag{2.47}$$

$$= \frac{6\pi E(m)}{\lambda_{\mathrm{e}}} \frac{1}{K_{\mathrm{LII}}} \int_{-\infty}^{+\infty} S_{\mathrm{LII}}(r)\, \mathrm{d}r \tag{2.48}$$

The calibration constant K_{LII} could therefore be obtained from measurements using:

$$K_{\mathrm{LII}} = \frac{1}{P_0(0)} \frac{6\pi E(m)}{\lambda_{\mathrm{e}}} \int_{-\infty}^{+\infty} S_{\mathrm{LII}}(r)\ \mathrm{dr} \tag{2.49}$$

where C_{det} is only a function of the probe volume and light collection efficiency, and C_{em} is a function of soot emissivity characteristics. Their product, K_{LII} is the ratio of the mean collected LII signal at λ_s per unit soot extinction.

The calibration hinges on the assumption that scattering is unimportant relative to absorption, as has been discussed above. In these particular calibrations, the measurement height was selected to be in the region where the highest soot concentration exists (as determined from extinction measurements). For the calibration of the methane flames, we considered case B at a height of 75 mm above the burner (HAB = 75 mm). For the ethylene and propane flames, we considered the ethylene flame (Case B) at HAB = 50 mm. The calibration constants, calculated via Eq. (2.49), give $K_{\mathrm{LII}} = 8.75 \times 10^8$ for methane flames and $K_{\mathrm{LII}} = 3.33 \times 10^7$ for ethylene and propane flames. The difference in the calibration constants arises due to the difference in the detector sensitivity via the intensifier gain used (the gain value of the ICCD is adjustable from 0 to 99%). Methane soot production is much lower than that of ethylene, requiring a gain of 75% compared to 40% for the other fuels. A linear change in gain setting on the camera changes the actual gain constant exponentially, thus the ratio in calibration constant is not linear. The value of the soot absorption function, $E(m)$, used for comparison with the work of Shaddix *et al.* [7, 8], is assumed to be 0.26, based on an estimated value of the index of refraction $m = 1.57 - 0.56i$ by D'Alessio *et al.* [141]. However, as discussed above, the particular value of the constant is not important for the comparisons, but only for the absolute value obtained of the soot volume fraction.

2.4 Results and discussion

2.4.1 Measured extinction coefficient K_e

Since measurements of soot volume fractions depend on the particular choice of $E(m)$, it is useful to consider the direct, Abel unwrapped measurements of $K_e(r)$ from the light attenuation. Figure 2.14 shows measured extinction coefficient K_e for all tested flames at different HABs. We note that in all cases, the peak extinction moves from the outer to the inner region as the HAB increases, and that values for the extinction coefficient in the case of ethylene and propane are up to two orders of magnitude higher than in the case of methane. The numerical measured values of $K_e(r)$ appear as supplemental material to the study (see Appendix F.1). The measured values of K_e were used to obtain the f_v according to Eq. (2.10) and an $E(m)$ value of 0.26, for calibration of LII and further comparison with other studies, as shown in the next subsection.

2.4.2 Comparison of cavity extinction and LII

Figure 2.15 shows LII images for each case considered. In order to accommodate the length to width ratio of the flames, three different series of images were taken (250 images for each series), with images connecting at heights of 34 and 68 mm. Comparisons with the extinction measurements are provided for one half of the flame, which is symmetric. The methane flame produces significantly less soot (sub-ppm) than the other two fuels.

The present LII measurements are compared with previous measurements by Puri and Santoro *et al.* [86, 89], extracted from NIST's website [9], as shown in Fig. 2.16. The two studies differ slightly in the size of the diffusion jet diameter (10.5 mm for the current study, and 11 mm in [7, 8]). Therefore, the results are compared based on the non-dimensional radius r/r_0, where r_0 is the inner radius of the fuel tube for each burner. The peak concentrations measured in this study are within 20% of those previously measured, for the worst case scenario of low

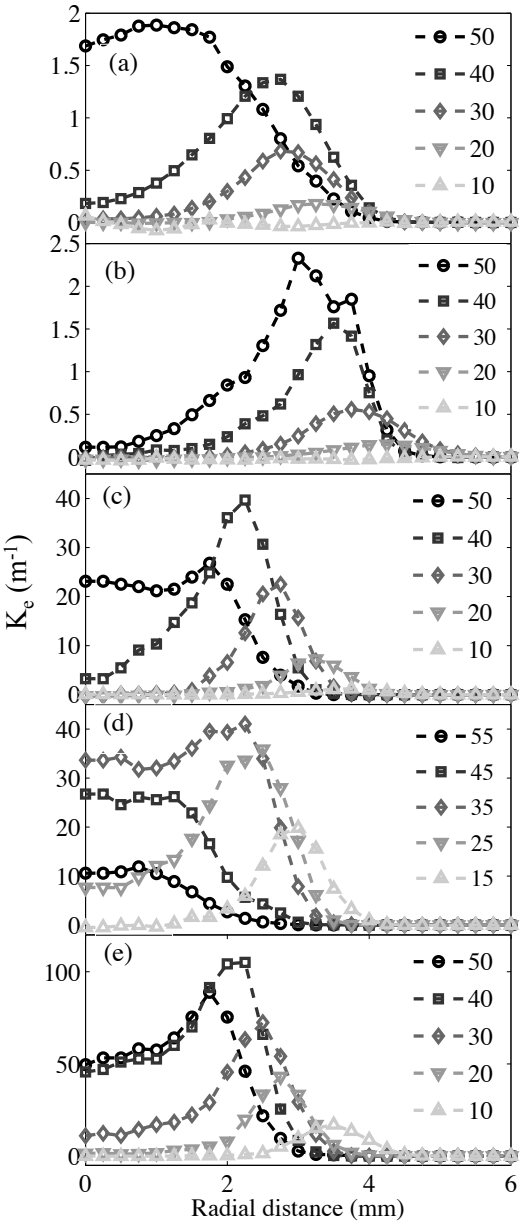

Fig. 2.14 Extinction coefficient K_e measured for various test flames at different HABs. (a) methane case A; (b) methane case B; (c) propane; (d) ethylene case A; (e) ethylene case B. Note that not all HAB data is shown in this figure. The dataset of K_e is available in the supplemental material of this study (see Appendix F.1 to F.5)

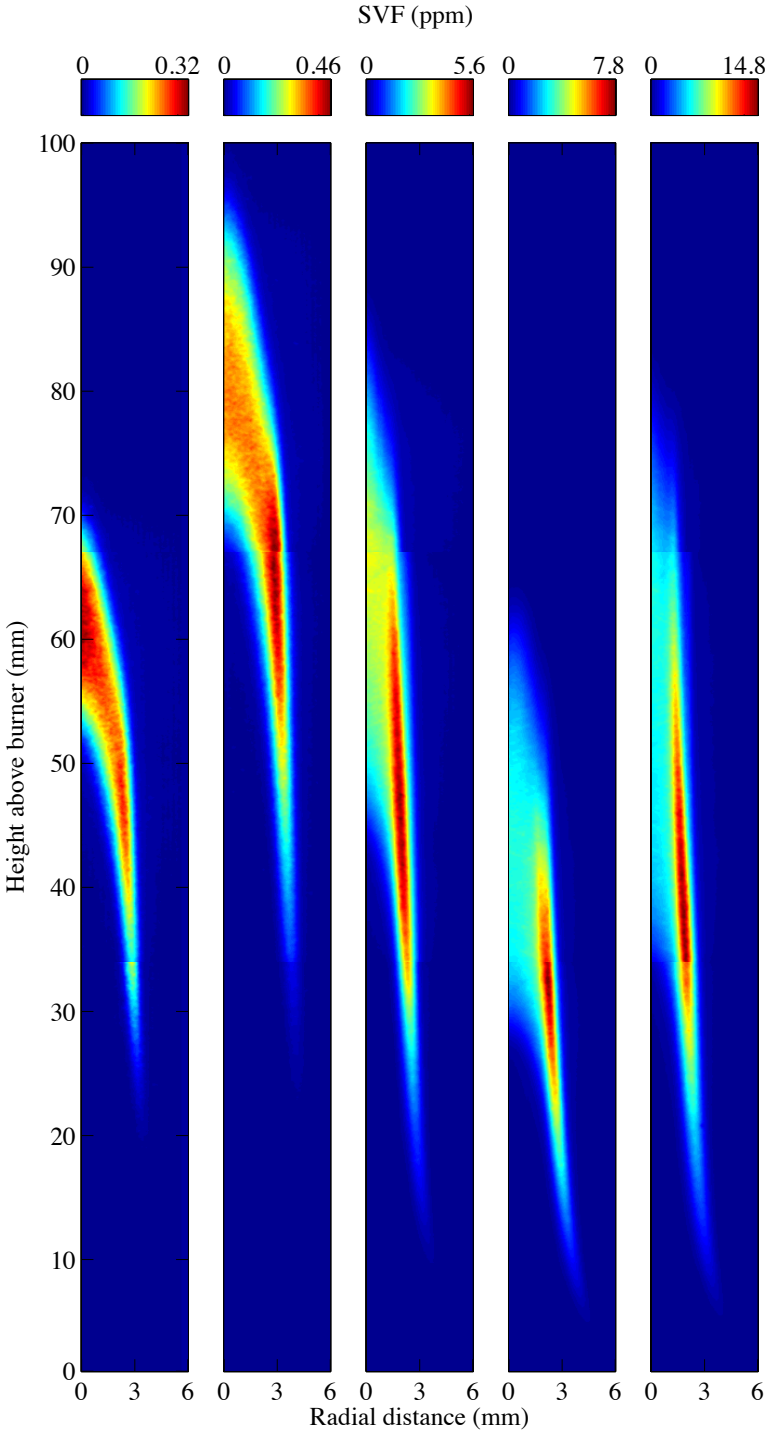

Fig. 2.15 LII images for various test flames (from left to right): methane case A, methane case B, propane, ethylene case A, ethylene case B. Note that there is an order of magnitude difference in scale between the methane cases and other fuels. Images are composites of three separate series, with overlaps at 34 and 68 mm.

soot (methane). Other cases for propane and ethylene differ by around 15%. The tube diameter is different by 0.5 mm between the present study and the references, thus a non-demension radius r/r_0, which is the ratio of r and the inner radius of the fuel tube, is used as horizontal axis, as show in Fig. 2.16.

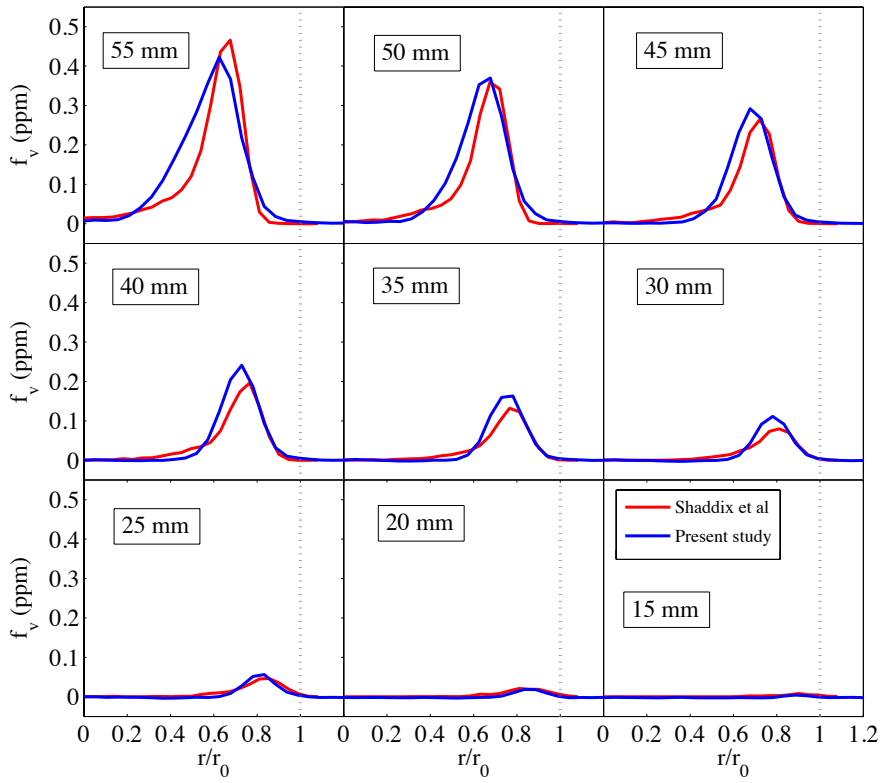

Fig. 2.16 LII measurements in the present work (blue) and from Shaddix *et al.* [7–9] (red) for methane flame case B, plotted against the non-dimensional radial distance r/r_0, for different heights above the burner (HAB).

The LII and cavity extinction measurements obtained are directly compared in Figs. 2.17-2.21 at various flame heights, for methane, propane and ethylene flames. The error bars represent the combined uncertainty associated with estimated instrument error, variances due to flame fluctuations, and the tomographic inversion, as discussed in further on. Since the LII is calibrated from the extinction measurements from the integral of the volume fraction, the absolute uncertainties from the extinction measurements are propagated to the LII measurements, and the error bars on the latter only represent the variances in the

images.

Starting with the measurements with higher concentrations, for propane and ethylene flames shown in Figs. 2.19-2.21, it is clear that the cavity LOSE measurements are in good, if not perfect, agreement with the LII measurements throughout the domain. Measurements in the outer zone are in better agreement than in the inner zone, owing to the compounded uncertainties in the inversion (Section 2.4.4). Nevertheless, the peaks are well resolved, and the agreement is good throughout the flame. In cases where the peak concentrations are of the order of tens of ppm, the resolution of the peak is very good (Case B, Fig. 2.21). As the peak f_v dips below 1 ppm, however (Figs. 2.17-2.18), the uncertainties become larger, and disagreements appear. Nevertheless, the LOSE measurements are able to capture the gradients indicated by the LII images, at values below 1 ppm. To our knowledge, there have been no prior reported CW-extinction measurements of soot volume fraction extending below 0.1 ppm. Further data analysis shows that for a stable measurement target without flickering, the measurement error can be lower than 20 ppb, resulting in a measurement range of down to tens of ppb, but not lower.

The uncertainties attributed to the LOSE measurements arise from three sources: (a) instrumentation error, (b) tomographic inversion via the Abel transform and (c) flame fluctuations. Systematic errors in f_v can also arise from errors in the assumed value for $E(m)$. These uncertainties are discussed in the following sections.

2.4.3 Instrumentation uncertainties

The extinction coefficient and ultimately the volume fraction is extracted from the total extinction measured, to yield P_0 via Eq. (2.17), which is susceptible to uncertainties in P_t, and the smaller uncertainties in R_m and T_m. P_t is obtained from the measurement in the attenuation of light using the photodetectors. The uncertainties are obtained from estimates of the error induced by laser light fluc-

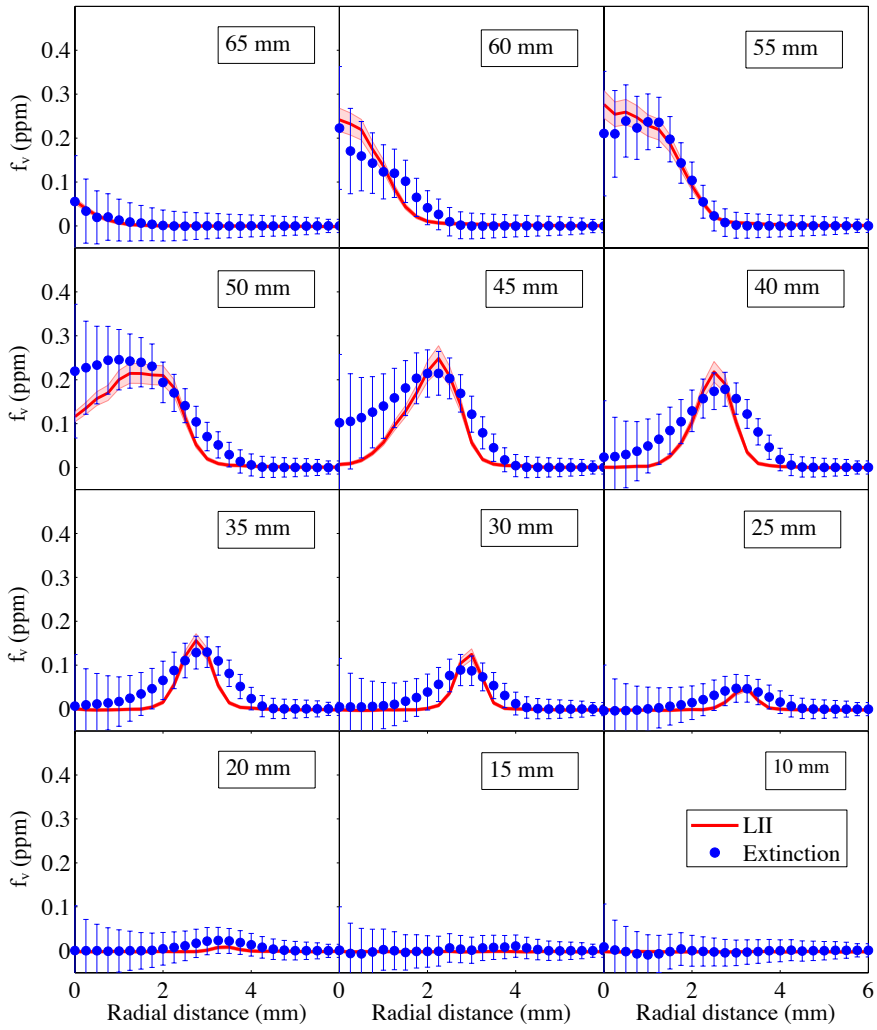

Fig. 2.17 Soot volume fraction f_v measured using cavity extinction (blue circles) and LII (red line) for the methane flame (case A). Error bars for extinction (blue) are discussed in the text, upper and lower limits for LII (light red regions) represent image variances.

tuations, flame intensity interference and background currents, estimated from their respective rms fluctuations. They are collected in expressions using the logarithmic amplifier (base 10) to allow the uncertainties to be calculated from the overall expression in Eq. (2.41).

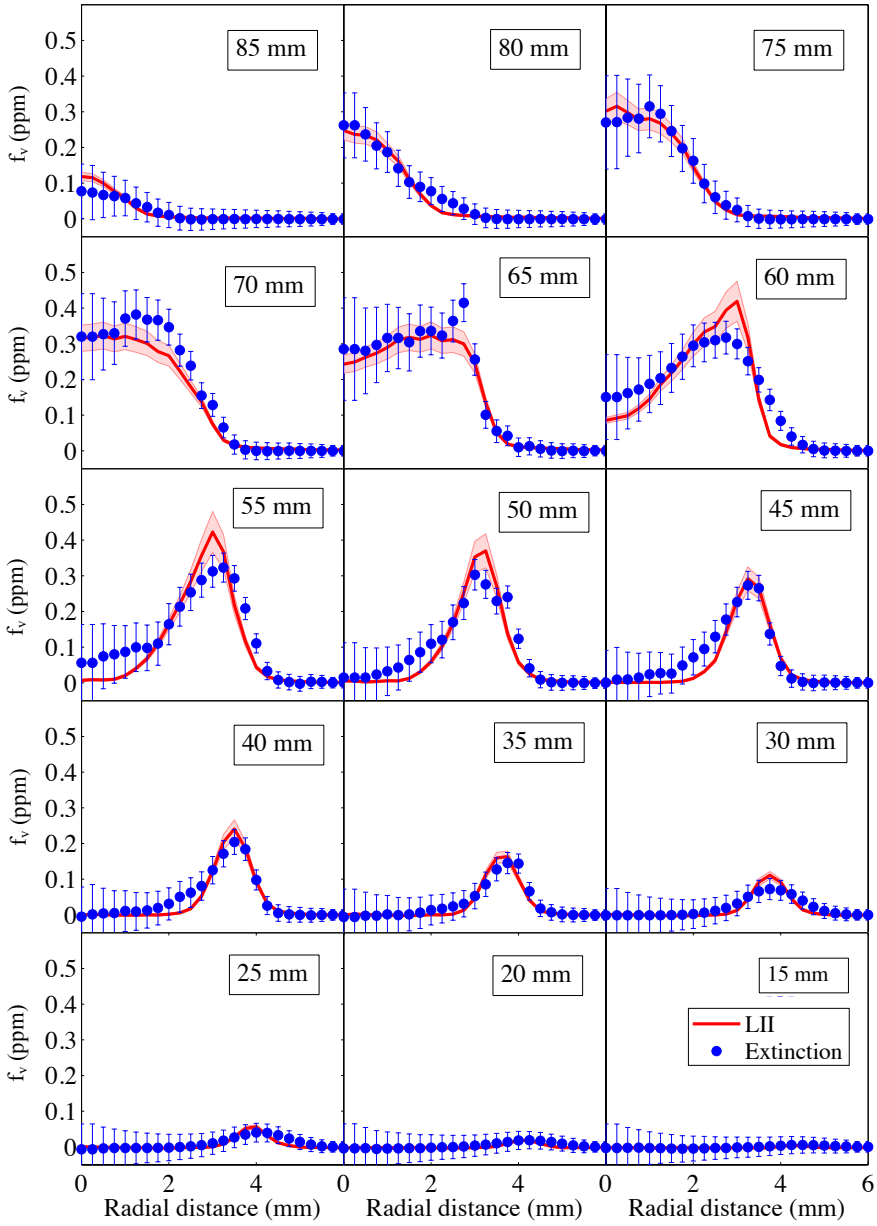

Fig. 2.18 Soot volume fraction f_v measured using cavity extinction (blue circles) and LII (red line) for the methane flame (case B).

The uncertainty in P_0 can be calculated via error propagation as:

$$u_{P_0}^2 = \left(\left(\frac{\partial P_0}{\partial P_t} \cdot \frac{\partial P_t}{\partial \mathbf{V}} \right)^2, \left(\frac{\partial P_0}{\partial P_t} \cdot \frac{\partial P_t}{\partial C} \right)^2, \left(\frac{\partial P_0}{\partial R} \right)^2, \left(\frac{\partial P_0}{\partial T} \right)^2 \right) \begin{pmatrix} \mathbf{U}^2 \\ u_C^2 \\ u_R^2 \\ u_T^2 \end{pmatrix} \tag{2.50}$$

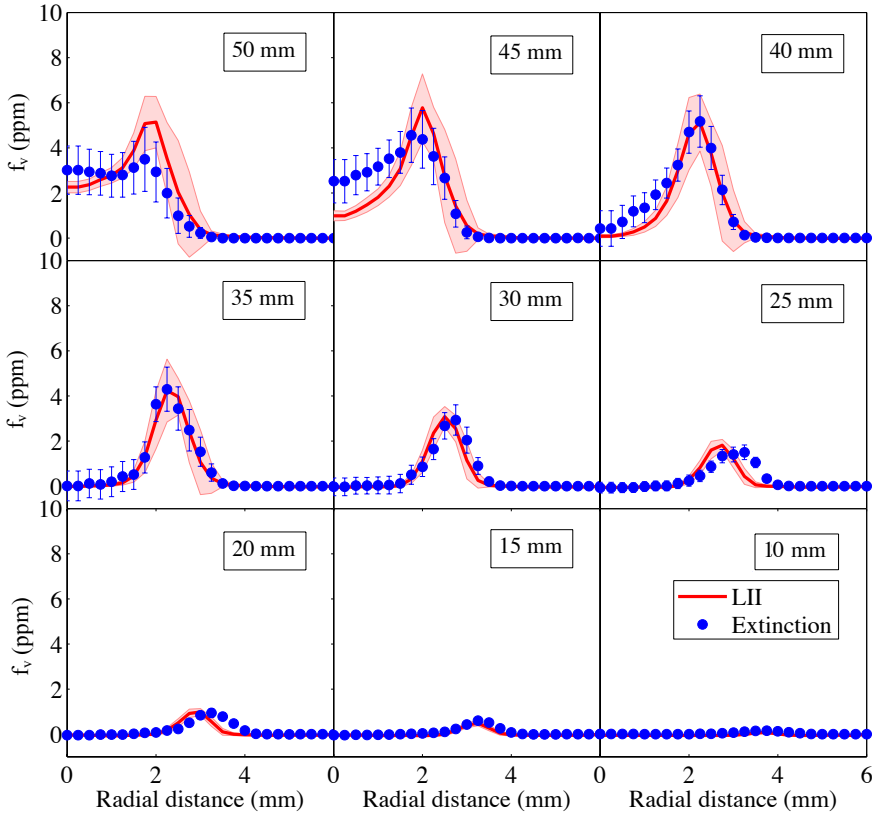

Fig. 2.19 Soot volume fraction f_v measured using cavity extinction (blue circles) and LII (red line) for the propane flame. The blue error bars for the extinction measurements are too small to be displayed at this scale.

where $\mathbf{U} = [u_{V_{IN}}; u_{V_{LF}}; u_{V_F}; u_{V_B}; u_{V_{ref1}}; u_{V_{ref2}}; u_{V_{ref3}}]$ contains the uncertainties in $\mathbf{V}$. The additional uncertainty in the local extinction ratio, u_{K_e}, due to the Abel transform [138] may be expressed as:

$$u_{K_e}^2 = \frac{1}{\Delta y^2} \sum_{j=i}^{\infty} \Big\{ [I_{ij}(1) - I_{ij}(0)]^2 u_{P_0(y_{j-1})}^2 - [2I_{ij}(1)]^2 u_{P_0(y_j)}^2 + [I_{ij}(1) + I_{ij}(0)]^2 u_{P_0(y_{j+1})}^2 \Big\} \tag{2.51}$$

where $I_{ij}(0)$ and $I_{ij}(1)$ are the operators in the Abel transform, and Δy is the horizontal distance between the two measured positions. Then, the uncertainty of K_e can be computed by the Abel transform, and the uncertainty of f_v can be

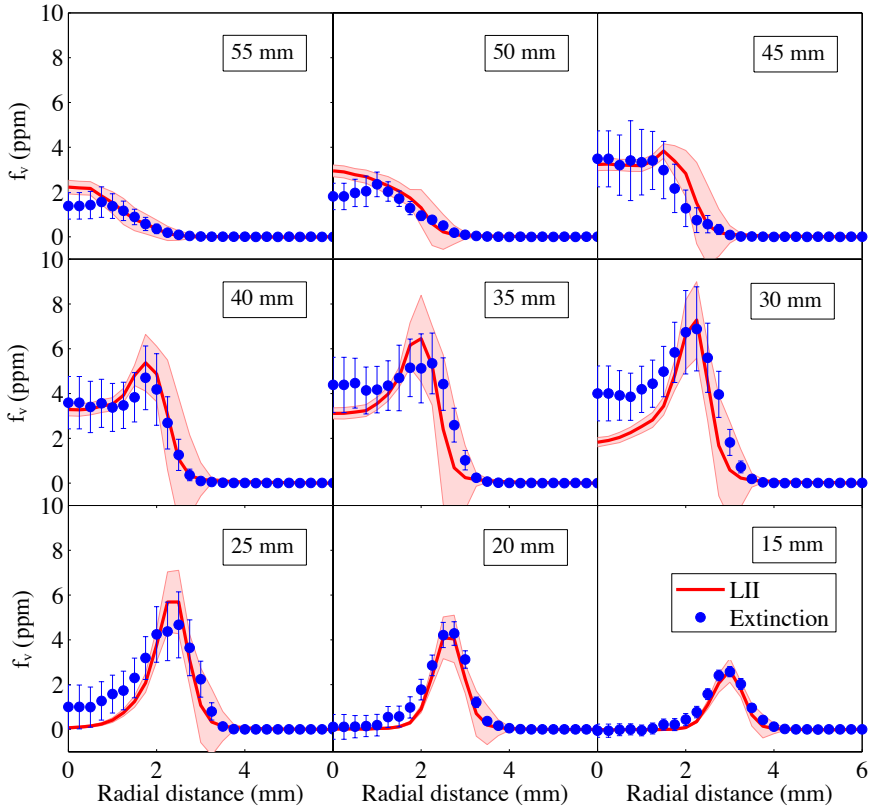

Fig. 2.20 Soot volume fraction f_v measured using cavity extinction (blue circles) and LII (red line) for the ethylene flame (case A)

evaluated from Eq. (2.10).

$$u_{f_v} = \sqrt{\left(\frac{\lambda_e}{6\pi E(m)}\right)^2 u_{K_e}^2} \tag{2.52}$$

The relative importance of instrumentation uncertainty can be considered by selecting a region of the flame where flame fluctuations and Abel transform errors are negligible. This is done by selecting a point sufficiently far upstream from the flame, at an edge position. Figure 2.22 shows the relationship between the instrumentation uncertainty and local soot volume fraction at $r = 3.75$ mm, and the height above burner (HAB) equal to 10 mm and 15 mm, which closely obeys a linear relationship, with a slope of 0.15 and intercept of 0.0171 ppm.

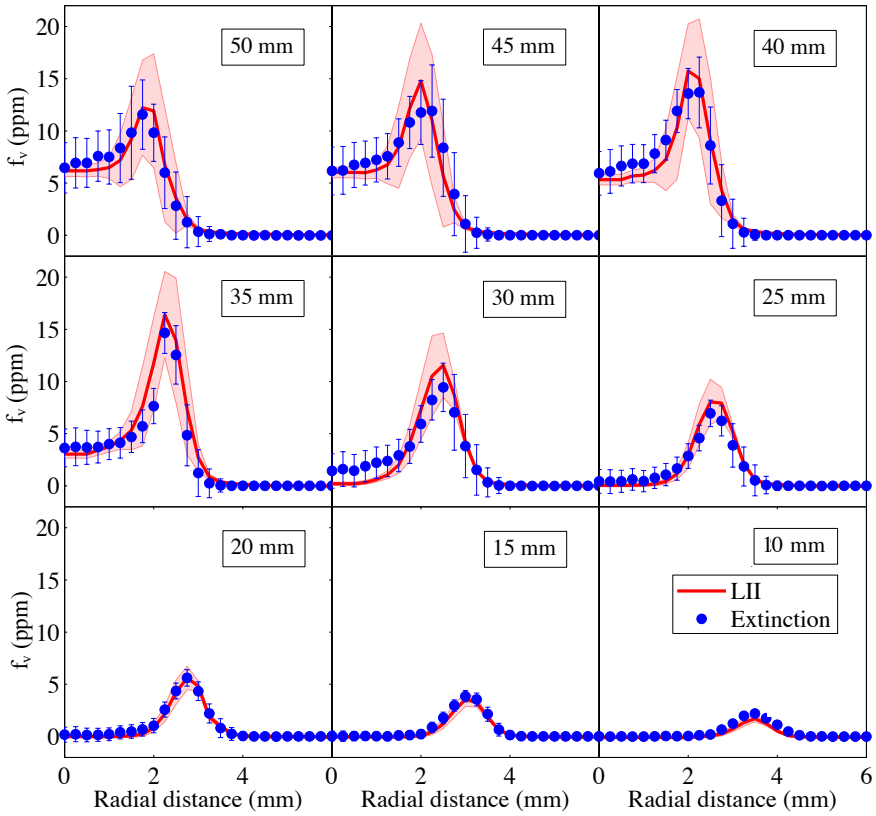

Fig. 2.21 Soot volume fraction f_v measured using cavity extinction (blue circles) and LII (red line) for the ethylene flame (case B)

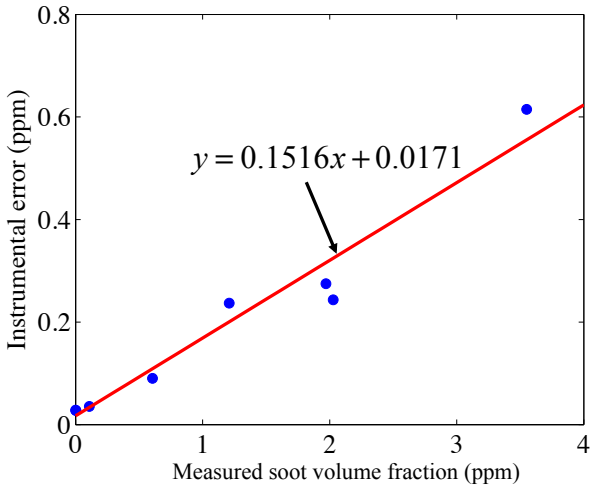

Fig. 2.22 Instrumentation uncertainty as a function of local soot volume fraction at flame edge positions (r = 3.75 mm, HAB=10 mm, 15 mm).

2.4.4 Uncertainty from the Abel transform

The Abel transform leads to cumulative errors between the edge and the centerline of the domain. These errors are a function of the intrinsic fluctuation, convoluted with the discretisation of the field. Dasch [138] investigated the error generated by the three-point Abel transform, and compared it with three other one-dimensional tomographic methods (two-point transform, onion-peeling, and filtered back projection methods), concluding that the three-point Abel transform generated the smallest error. The uncertainty arising from the algorithm depends on the field, so it cannot be quantified in general, but only in reference to a particular field. Here we use a numerical test to bracket the uncertainties, as shown in Figs. 2.23 and 2.24. The smooth Gaussian test distributions in Figs. 2.23 and 2.24 are similar to the distribution of the soot volume fraction in positions downstream and upstream of the flames, respectively. Different sampling intervals (0.125 mm, 0.25 mm and 0.5 mm) are used to test the inversion uncertainties. The projection values are obtained based on the field given, and the three-point Abel transform is utilised to calculate the constructed field value. As expected, the smallest interval resolution offers the lowest error. In the present work, the spatial resolution of the cavity extinction measurements is around 200 μm, so a 0.25 mm interval is representative, yielding a relative error around the peak of 10% for the lower flame height (where we have more soot at the flame edge), and 18% for the greater flame height (more soot in the edge of the flame). For a sample interval of 0.125 mm, the error values are 5% and 12%, respectively. The error due to tomography is therefore relatively large, and the spatial resolution is very important. However, a smaller sampling interval does not always result in a reduction in error. Due to the cumulative effect of the Abel transform, the error at the edge region can be accumulated to the centre. If we simply assume the instrumental error of each projection value P to be the same, the error of each

deconvoluted value (after the Abel transform) can be calculated as:

$$u(r_i) = \frac{u_p}{\Delta r}\left(\sum_{j=0}^{\infty} {D_{ij}}^2\right)^{\frac{1}{2}} \tag{2.53}$$

where $r_i = i\Delta r$ is the distance from the centre of the field, u_p is the error in the projection value, and Δr is the sampling interval [138]. D_{ij} is a function of the linear Abel transform operators $I_{ij}(0)$ and $I_{ij}(1)$:

$$D_{ij} = \begin{cases} 0 & j < i-1 \\ I_{i,j+1}(0) - I_{i,j+1}(1) & j = i-1 \\ I_{i,j+1}(0) - I_{i,j+1}(1) + 2I_{ij}(1) & j = i \\ I_{i,j+1}(0) - I_{i,j+1}(1) + 2I_{ij}(1) - I_{i,j-1}(0) - I_{i,j-1}(1) & j \geq i+1 \\ I_{i,j+1}(0) - I_{i,j+1}(1) + 2I_{ij}(1) - 2I_{i,j-1}(1) & i = 0, j = 1 \end{cases} \tag{2.54}$$

One can define $\left(\sum_{j=0}^{\infty} {D_{ij}}^2\right)^{1/2}\Delta r^{-1}$ as a noise coefficient, which indicates a transfer efficiency from the error of the projection value to the error of the deconvoluted value. Equation (2.53) suggests that the noise is inversely proportional to Δr, which means that smaller sampling steps can yield a larger cumulative error. The noise coefficients for sampling steps of 0.125 mm, 0.25 mm and 0.5 mm are plotted in Fig. 2.25. This suggests that even if the instrumental error in the projection value is constant at each measurement point, deconvolution leads to error accumulation towards the centre.

Figure 2.26 shows representative estimates of uncertainties across the radial distance. For the methane cases ((a) and (b) in Fig. 2.26), the uncertainty increases towards the centre of the flame, due to the cumulative effect of the three-point Abel transform. The flame oscillation causes an increase in uncertainty at the edge of the flame ($\approx$ 4 mm), which is more obvious in ethylene and propane flames ((c) to (e) in Fig. 2.26), because the soot concentrations at the edge of

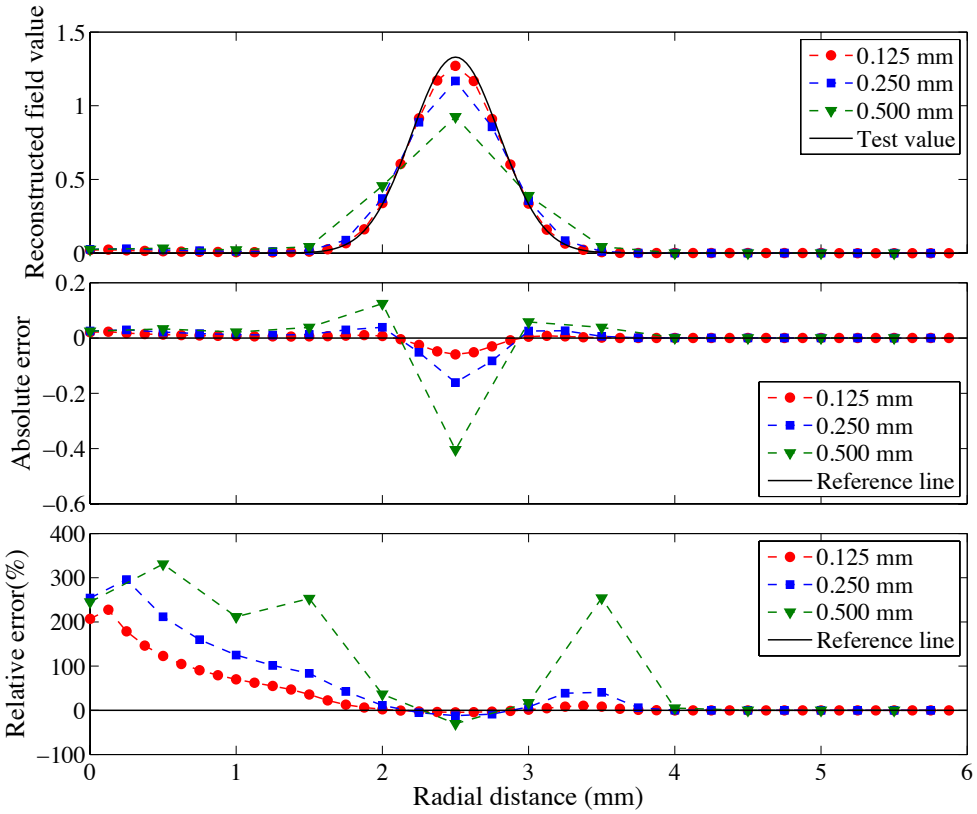

Fig. 2.23 Reconstruction of a given Gaussian field distribution similar to the soot volume fraction distribution at the base of the flame, for different sampling distances (top); absolute error (middle) and relative error (bottom).

those flames are tens of times higher than in methane flames, so that a small oscillation of this region can generate a large uncertainty. The error progressively accumulates towards the centre region of the flame.

Figure 2.27 shows the composition of experimental uncertainties at a 40 mm flame height for two different flames: methane Case A (top) and ethylene Case A (bottom). For the methane flame, the Abel transform uncertainty and instrumental uncertainty play the main roles in the overall uncertainty, as the flame is shorter and experiences lower flame oscillations. For the ethylene flame Case A (bottom), the flame oscillation contributes a significant portion of the total uncertainty because of the high soot concentration at the flame edge.

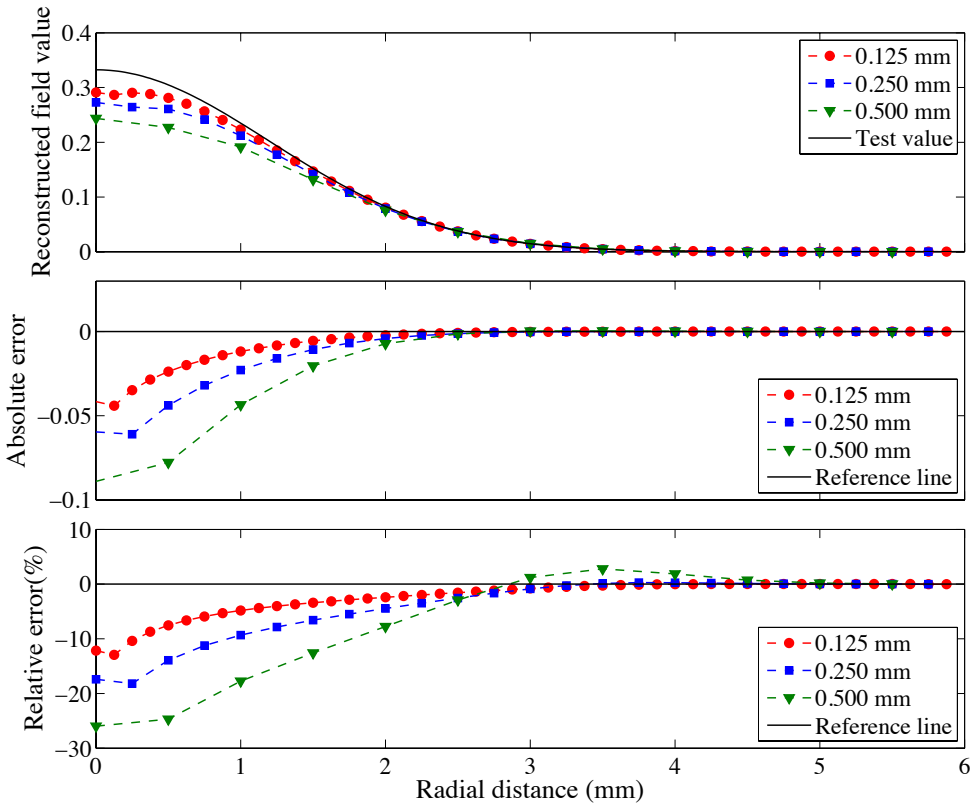

Fig. 2.24 Reconstruction of a given Gaussian field distribution similar to the soot volume fraction distribution at the top of the flame, for different sampling distances (top); absolute error (middle) and relative error (bottom)

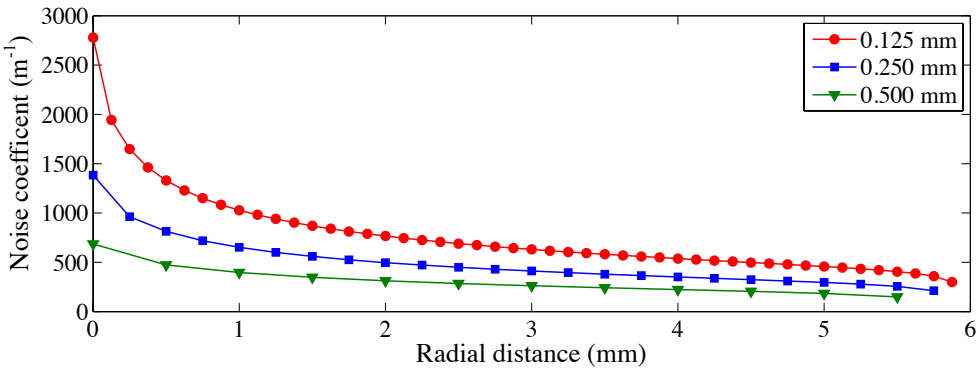

Fig. 2.25 Comparison of noise coefficients using different sampling distances

2.4.5 Uncertainty from E(m)

The absorption function, $E(m)$, is a function of the complex refractive index of soot m (Eq. (2.6)), where m and $E(m)$ are both wavelength and fuel dependent

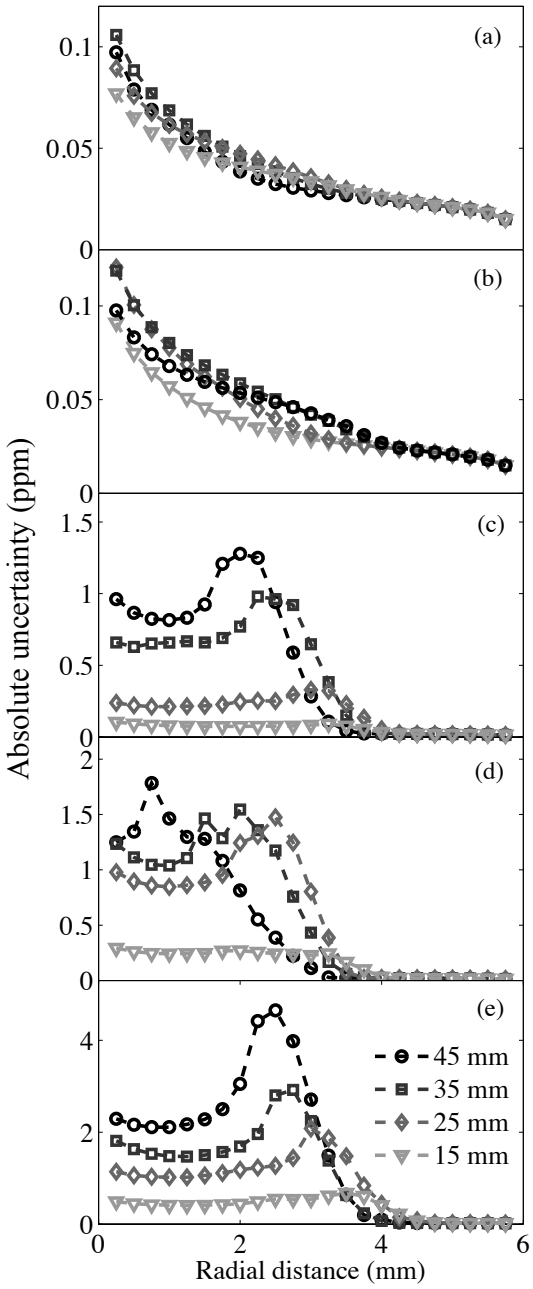

Fig. 2.26 Absolute error in extinction measurement for soot volume fraction of: (a) methane case A; (b) methane case B; (c) propane; (d) ethylene case A; (e) ethylene case B.

[142, 143]. Dalzell *et al.* suggested that within the wavelength range from 435.8 nm to 806.5 nm, the mean value of m is $1.57-0.46i$ for acetylene and $1.57-0.50i$ for propane diffusion flames [143]. In 1973, D'Alessio [141] suggested the value

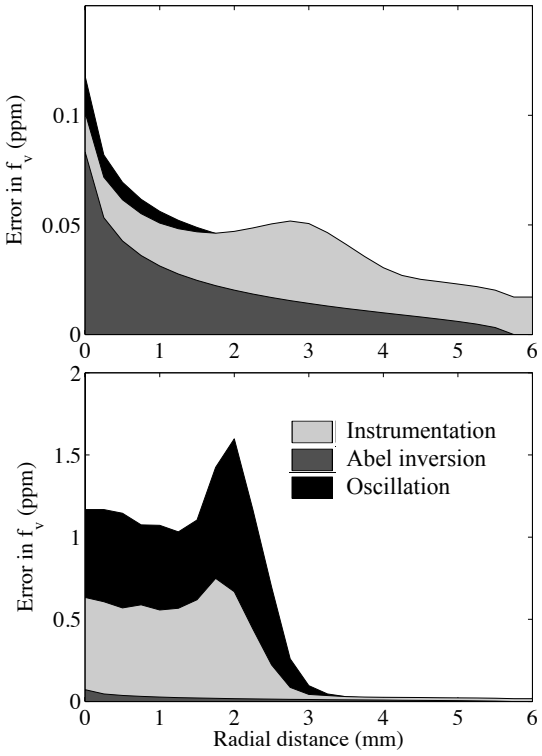

Fig. 2.27 Composition of experimental uncertainties at 40 mm flame height for two different flames, methane case A (top) and ethylene case A (bottom).

$1.57 - 0.56i$ as a mean value in the visible range [144]. Whilst this value has been widely cited for its simplicity, a number of values of m have been also reported by other researchers, as shown in Table 2.4. For a wavelength of around 638 nm, calculations using the values suggested by D'Alessio *et al.* [141] rather than the data of Yon *et al.* [142] ($E(m) = 0.30$ at 632 nm) yield a difference of 15%, however, when compared with Williams' data ($E(m) = 0.37$ at 638 nm) [118], the discrepancy can be as large as 40%. Using the value of 0.26 may is likely to underestimate the f_v deduced by the extinction measurement. However, given the Rayleigh approximation may still overestimate f_v (by neglecting scatter) [144]. Further accurate measurements of $E(m)$ would still directly improve the accuracy of the LOSE method.

Table 2.4 Previously measured complex refractive indices.

Reference	λ_e (nm)	fuel	$m(\lambda_e)$	$E(m)$
Dalzell *et al.* [143]	435.8-806.5	acetylene	$1.57 - 0.46i$	0.21
		propane	$1.57 - 0.50i$	0.23
Williams *et al.* [118]	635	ethylene and nitrogen-diluted kerosene	$1.75 - 1.03i$	0.37
D'Alessio *et al.* [141]	250-650	methane	$1.57 - 0.56i$	0.26
Kohler *et al.* [63]	1064	ethylene	$1.60 - 0.59i$	0.27
Yon *et al.* [142]	266	diesel/rapeseed methyl ester	$1.61 - 0.74i$	0.32
	532		$1.61 - 0.74i$	0.32
	632		$1.68 - 0.73i$	0.30
	1064		$1.81 - 0.76i$	0.28

2.5 Conclusions

A high-spatial resolution laser cavity extinction technique has been developed and implemented to measure soot volume fractions from laminar diffusion flames down to sub-ppm levels. Data analysis shows that for stable measurement targets, the measurement error can be lower than 20 ppb. The high sensitivity is obtained through the multiple reflections of the high reflectivity mirrors, and the fine spatial resolution of the cavity system can be obtained with the use of concave mirrors.

The extinction measurements are used in the absolute calibration of LII measurements. Direct comparisons with LII measurements across the flame, on the same flame, show good agreement and good ability to resolve peaks, particularly in the cases with higher volume fractions. The spatial resolution of around 200 μm compares well with the LII resolution of 33 μm, given the simplicity of the technique. The uncertainty arising due to tomographic inversion and discretisation of the Abel transform is estimated to be around 10% to 20% at the peak f_v position along the flame radials, with a sampling resolution of 0.25 mm. The study shows that the laser cavity extinction technique can be successfully applied even for low-soot concentrations, with uncertainties and spatial resolution similar

to those in LII, but with the significant advantage of an absolute measurement and following unsteady fluctuations.

Chapter 3

Soot measurement with CW-cavity-LOSE and LII in diluted methane flames

3.1 Introduction

In this chapter, the continuous wave line-of-sight extinction (CW-cavity-LOSE) measurement described in Chapter 2 is used to investigate the soot volume fraction (f_v) profiles of a series of nitrogen-diluted methane diffusion flames. The relative measurements of the soot distribution across the flame show good agreement with results using laser-induced incandescence (LII), whilst the absolute measurements provided by absorption are used to calibrate the latter.

In order to interpret the f_v data measured and analyse the effect of temperature, mixture fraction and residence time on soot formation in diluted/undiluted flames, a simplified model of a jet co-flow diffusion flame is implemented numerically. This allows the f_v measurements to be analysed using a local mixture fraction, residence time and temperatures. An exsiting one-step model for soot formation in the diffusion jet flame is modified, and The effect of each factor (thermal, dilution, residence time) responsible for soot reduction is isolated and

quantitatively compared.

3.2 Experiment

3.2.1 Burner and flame

The experiments were performed on a standard laminar diffusion burner, similar to that used by many researchers [7, 8, 23, 24, 86], whose details are available in Chapter 1. The burner is mounted on a traverse platform so as to scan through the flame at various positions with a precision of 0.01 mm along the horizontal direction and 0.5 mm along the vertical. The test conditions are grouped into five categories (from group A to E). In each group, the methane flow rate is kept constant while the nitrogen flow rate is varied. Each flame is labelled using a letter and a digit number, as listed in Table 3.1. Flames D0 and E0 (non-diluted conditions) have been tested by Puri *et al.* [89] in previous work, and are therefore used as a reference. Based on flames D0 and E0, the fuel flow rate is decreased from group E to that of group A, while nitrogen dilution is gradually increased for each flame. Using this method, the total carbon flow rate remains constant, while the mole fraction of fuel in the fuel flow (X_{F0}) changes. The operating conditions are listed in Table 3.1.

Figure 3.1 shows natural light photos of the 16 flames under consideration; the flame height is controlled by the jet flow rate, whilst the natural luminosity decreases with increasing dilution by nitrogen.

3.2.2 CW-cavity-LOSE and LII measurement

The experimental set-up of the CW-cavity-LOSE and LII measurement is the same as the experiment conducted in Chapter 1. However, a higher intensifier gain value was used to obtain a sufficiently high SNR in the cases of extremely low-soot yielding flames (case A1 and B1). Therefore, the calibration constants

Table 3.1 Test conditions for undiluted and nitrogen-diluted laminar CH_4-air diffusion flames.

Case	A		B		C			D			
	A0	A1	B0	B1	C0	C1	C2	D0	D1	D2	D3
CH_4 flow rate (slpm)	0.19		0.24		0.30			0.40			
Air flow rate (slpm)	16.2		20.5		25.6			35.0			
N_2 flow rate (slpm)	0	0.05	0	0.10	0	0.10	0.20	0	0.10	0.20	0.30
$X_{f,in}$ in fuel stream (%)	100	79.2	100	70.6	100	75.0	60.0	100	80.0	66.7	57.1

Case	E				
	E0	E1	E2	E3	E4
CH_4 flow rate (slpm)	0.53				
Air flow rate (slpm)	65.8				
N_2 flow rate (slpm)	0	0.10	0.20	0.30	0.40
$X_{f,in}$ in fuel stream (%)	100	84.1	72.6	63.9	57.0

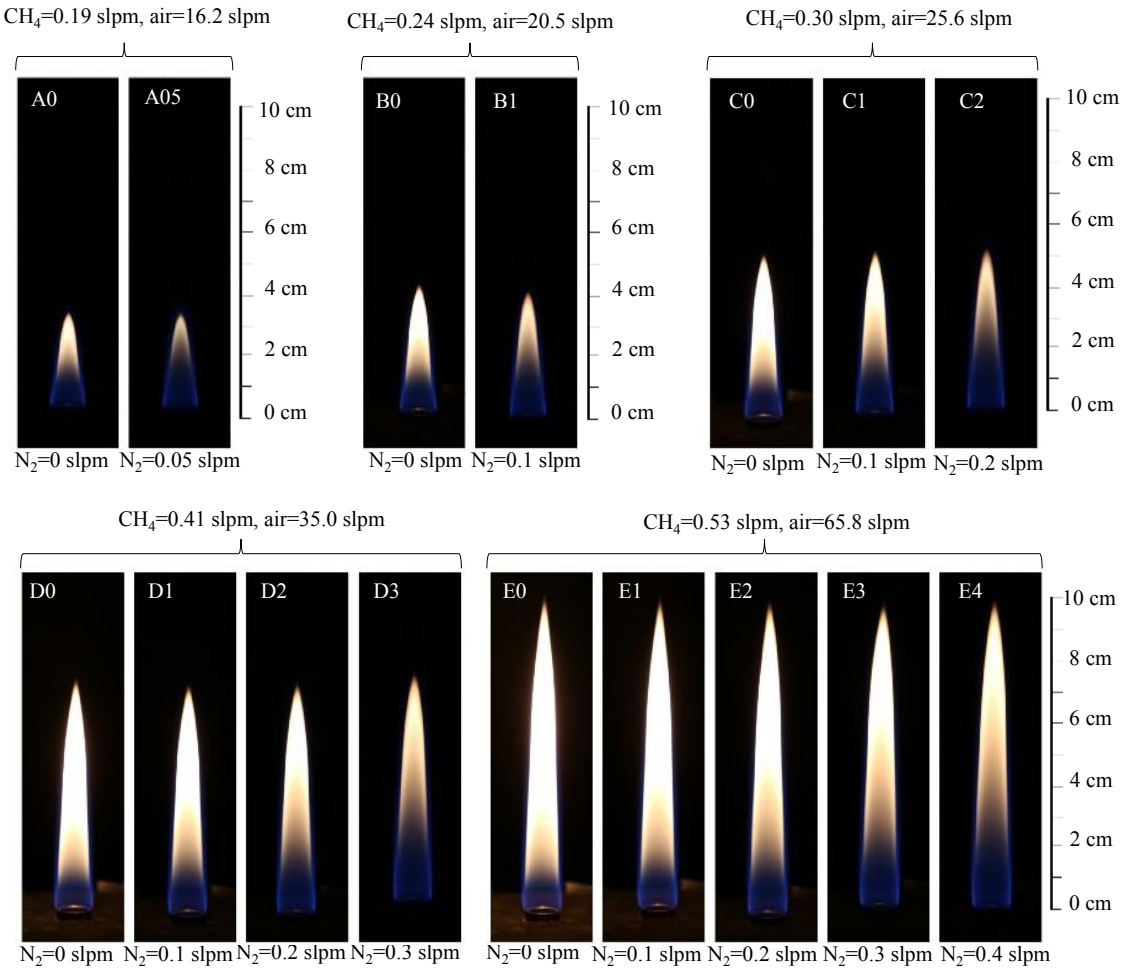

Fig. 3.1 Natural luminosity of laminar diffusion flames tested (camera model: Canon EOS 6D DLSR, exposure time = 1/60 s, photographic sensitivity (ISO) = 1250; lens model: Canon EF 24-105mm f/4L IS, f = 4.0, focal length = 105 mm)

K_{LII} of flame A1 and B1 are different to the other flames. The value of the constant is $K_{\mathrm{LII}} = 8.75 \times 10^8$ (gain = 75%) for all flames except group A and B flames. For flame A1, gain = 85% and $K_{\mathrm{LII}} = 1.05 \times 10^{10}$, and for flame B1, gain = 80%, $K_{\mathrm{LII}} = 2.02 \times 10^9$.

3.3 Numerical model of a flame

3.3.1 Basic assumptions

A simple numerical model of a jet co-flow diffusion flame was established based on the governing equations for mass and momentum for a cylindrically symmetric system. The basic assumptions for the flame simulation are similar to those in [145, 146]:

1) a unity Lewis number, so that the heat diffusivity equals the mass diffusivity;

2) an equal diffusion coefficient and viscosity for all gaseous species in the flame;

3) a one-step reaction between fuel and oxidiser, with negligible reaction time (infinite reaction rate);

4) a variable density, constant pressure, compressible steady-state flow;

5) a negligible axial diffusion; and

6) a zero radiation loss.

3.3.2 Governing equations

Simultaneous equations (3.1) are the governing equations of a typical radially symmetric co-flow diffusion flame (shown in Fig. 3.2).

$$\begin{cases} \rho u_z \dfrac{\partial Y_F}{\partial z} + \rho u_r \dfrac{1}{r}\dfrac{\partial}{\partial r}\left(rY_F\right) = \dfrac{1}{r}\dfrac{\partial}{\partial r}\left(r\rho D_f \dfrac{\partial Y_F}{\partial r}\right) - \dot{w}_F(a) \\ \rho u_z \dfrac{\partial Y_O}{\partial z} + \rho u_r \dfrac{1}{r}\dfrac{\partial}{\partial r}\left(rY_O\right) = \dfrac{1}{r}\dfrac{\partial}{\partial r}\left(r\rho D_f \dfrac{\partial Y_O}{\partial r}\right) - s\dot{w}_F(b) \\ \rho u_z c_p \dfrac{\partial T}{\partial z} + \rho c_p u_r \dfrac{1}{r}\dfrac{\partial}{\partial y}\left(rT\right) = \dfrac{1}{r}\dfrac{\partial}{\partial r}\left(r\lambda_c \dfrac{\partial T}{\partial r}\right) + Q\dot{w}_F(c) \end{cases} \tag{3.1}$$

where ρ is the density of the mixture, D_f is the diffusivity, u_z and u_r are the axial

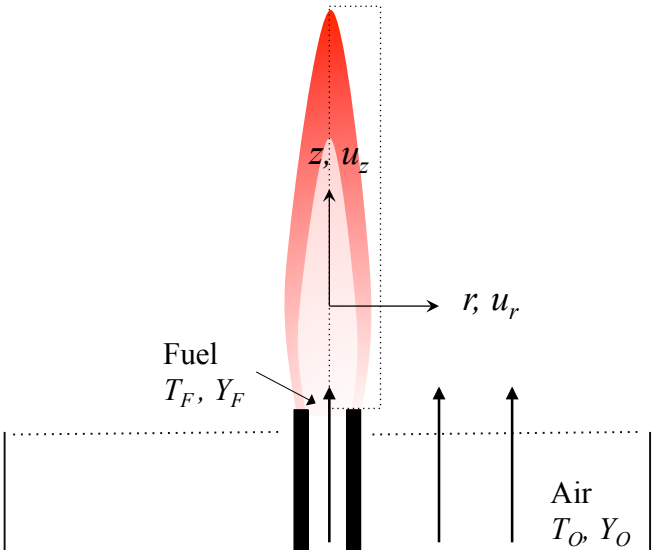

Fig. 3.2 Typical profiles of species mass fractions for a jet non-premixed flame close to the nozzle and further downstream

and radial velocities respectively, and λ_c is the heat conductivity.

Dividing Eq. (3.1b) by s, the mole ratio of air and fuel for complete combustion, and subtracting from Eq. (3.1a), gives:

$$\begin{aligned} \rho u_z \frac{\partial \left(Y_F - \frac{Y_O}{s} \right)}{\partial z} + \rho u_r \frac{1}{r} \frac{\partial}{\partial r} \left(r \left(Y_F - \frac{Y_O}{s} \right) \right) \\ = \frac{1}{r} \frac{\partial}{\partial r} \left(r \rho D_f \frac{\partial \left(Y_F - \frac{Y_O}{s} \right)}{\partial r} \right) \end{aligned} \tag{3.2}$$

Multiplying Eq. (3.1a) by Q, the heating value of fuel, and adding to the Eq. (3.1c), gives:

$$\begin{aligned} \rho u_z \frac{\partial \left(Y_F Q - c_p T \right)}{\partial z} + \rho u_r \frac{1}{r} \frac{\partial}{\partial r} \left(r \left(Y_F Q - c_p T \right) \right) \\ = \frac{1}{r} \frac{\partial}{\partial r} \left(r \rho D_f \frac{\partial (Y_F Q)}{\partial r} \right) - \frac{1}{r} \frac{\partial}{\partial r} \left(r \lambda_c \frac{\partial T}{\partial r} \right) \end{aligned} \tag{3.3}$$

We assume the Lewis number is unity, thus:

$$\rho D_f = \frac{\lambda_c}{c_p} \tag{3.4}$$

On subsituting (3.4) into Eq. (3.3), we obtain:

$$\begin{aligned} \rho u_z \frac{\partial \left(Y_F Q - c_p T\right)}{\partial z} + \rho u_r \frac{1}{r} \frac{\partial}{\partial r} \left(r \left(Y_F Q - c_p T\right)\right) \\ = \frac{1}{r} \frac{\partial}{\partial r} \left(r \rho D_f \frac{\partial \left(Y_F Q - c_p T\right)}{\partial r} \right) \end{aligned} \tag{3.5}$$

In Eq. (3.2), considering the scalar $f^* = Y_F - \frac{Y_O}{s}$, we obtain the mixture fraction:

$$\xi = \frac{f^* - {f^*}_{O,0}}{{f^*}_{F,0} - {f^*}_{O,0}} = \frac{\left(Y_F - \frac{Y_O}{s}\right) - \left(Y_F - \frac{Y_O}{s}\right)_{O,0}}{\left(Y_F - \frac{Y_O}{s}\right)_{F,0} - \left(Y_F - \frac{Y_O}{s}\right)_{O,0}} \tag{3.6}$$

Likewise, to calculate the enthalpy across the flame $h = Y_F Q + c_p T - c_p T_{ref}$ (T_{ref} is the reference temperature of the environment), we can define the non-dimensional enthalpy as:

$$h^* = \frac{h_c - h_{O,0}}{h_{F,0} - h_{O,0}} = \frac{\left(Y_F Q + c_p T\right) - \left(Y_F Q + c_p T\right)_{O,0}}{\left(Y_F Q + c_p T\right)_{F,0} - \left(Y_F Q + c_p T\right)_{O,0}} \tag{3.7}$$

The term $c_p T_{ref}$ is eliminated. Thus, from Eqs. (3.2) to (3.7), we obtain the governing equations for ξ and h^*:

$$\rho u_z \frac{\partial \xi}{\partial z} + \rho u_r \frac{1}{r} \frac{\partial}{\partial r} \left(r \xi\right) = \frac{1}{r} \frac{\partial}{\partial r} \left(r \rho D_f \frac{\partial \xi}{\partial r} \right) \tag{3.8}$$

and

$$\rho u_z \frac{\partial h^*}{\partial z} + \rho u_r \frac{1}{r} \frac{\partial}{\partial r} \left(r h^*\right) = \frac{1}{r} \frac{\partial}{\partial r} \left(r \rho D_f \frac{\partial h^*}{\partial r} \right) \tag{3.9}$$

Both ξ and h^* have an identical form of governing equation as well as boundary

conditions. Thus, they play the same role in their respective governing equations, and we can calcualte a simple relationship:

$$\xi = h^* \tag{3.10}$$

Considering $h_{O,0} = c_p(T_{O,0} - T_{ref})$ and $h_{F,0} = Y_{F,0}Q + c_p(T_{F,0} - T_{ref})$, and substituting the two terms in Eq. (3.7), we have:

$$h^* = \frac{Y_F Y_{F,0} Q + c_p(T - T_{O,0})}{Y_{F,0}Q + c_p(T_{F,0} - T_{O,0})} = \xi \tag{3.11}$$

Solving Eq. (3.11), we obtain an expression for T:

$$T = (\xi - Y_F)\frac{Y_{F,0}Q}{c_p} + \xi(T_{F,0} - T_{O,0}) + T_{O,0} \tag{3.12}$$

Under the assumption of an infinitely fast chemical reaction and equal diffusion coefficient, the flame temperature is linearly related to the mixture fraction according to the state relationship of diffusion combustion. The reaction zone can be seen in Fig. 3.3 [147]. The reaction zone is present at the point where $Y_F = Y_O/s$. Hence, from Eq. (3.6), the stoichiometric mixture fraction is given by:

$$\xi_{st} = \frac{\frac{Y_{O,0}}{s}}{Y_{F,0} + \frac{Y_{O,0}}{s}} \tag{3.13}$$

Moreover, from Fig. 3.3, at the location of the flame, the mole fraction of the fuel is zero due to the fast chemistry model, thus from Eq. (3.12), the temperature of the flame T_f can be obtained:

$$T_f = \xi_{st} Y_{F,0}\frac{Q}{c_p} + \xi_{st}(T_{F,0} - T_{O,0}) + T_{O,0} \tag{3.14}$$

Equation (3.14) can be used to approximate the flame temperature given that $Y_{F,0}$ and Q are known. Combining Eqs. (3.12) and (3.14), we have the final form

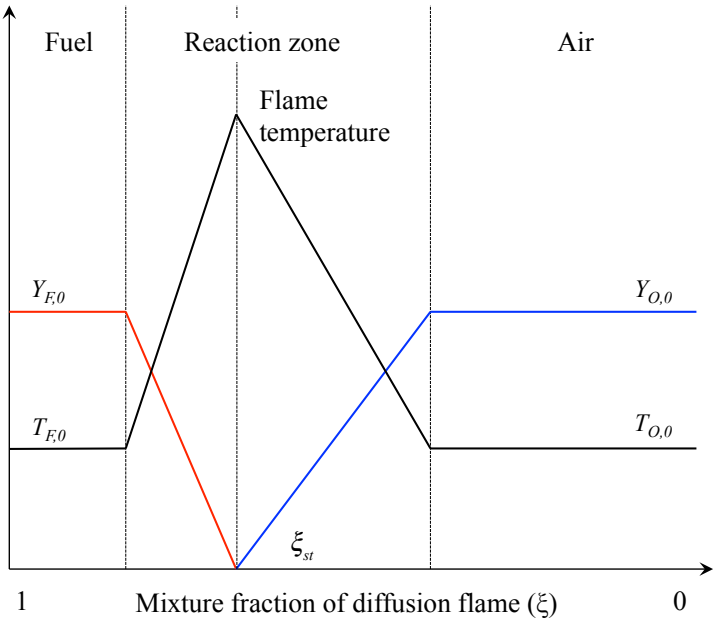

Fig. 3.3 The mass fractions and temperature as a function of the mixture fraction for a typical diffusion flame.

of the expression of temperature T:

$$\begin{cases} T = (T_f - T_{O,0})\,\dfrac{\xi}{\xi_{st}} + T_{O,0}, \;\; \xi \le \xi_{st} \\ \\ T = (T_f - T_{F,0})\,\dfrac{1-\xi}{1-\xi_{st}} + T_0, \;\; \xi > \xi_{st} \end{cases} \tag{3.15}$$

The mass conservation equation for the radially symmetric system is:

$$\frac{\partial}{\partial z}(\rho u_z) + \frac{1}{r}\frac{\partial}{\partial r}(r\rho u_r) = 0 \tag{3.16}$$

The momentum equations in the axial and radial directions are:

$$\rho u_z \frac{\partial u_z}{\partial z} + \rho u_r \frac{\partial u_z}{\partial r} = \frac{1}{r}\frac{\partial}{\partial r}\left(\mu r \frac{\partial u_z}{\partial r}\right) + \rho g \tag{3.17}$$

and

$$\rho u_r \frac{\partial u_r}{\partial r} + \rho u_z \frac{\partial u_r}{\partial z} = \mu \left[\frac{1}{r} \frac{\partial}{\partial r} \left(r \frac{\partial u_r}{\partial r} \right) - \frac{u_r}{r^2} \right] \tag{3.18}$$

3.3.3 Density and transport coefficient

The molecular weight of the mixture is calculated based on the mass fractions of fuel, oxygen and diluent nitrogen as:

$$W = \left(\frac{Y_O}{W_{\mathrm{O}}} + \frac{Y_F}{W_F} + \frac{1 - Y_O - Y_F}{W_{\mathrm{N_2}}} \right)^{-1} \tag{3.19}$$

and the density of the mixture at constant pressure conditions is:

$$\rho = \rho_{ref,0} \frac{T_0}{T} \frac{W}{W_{ref}} \tag{3.20}$$

where the subscript *ref* denotes a reference temperature and molecular weight. The diffusion coefficient of the mixture at ambient temperature (293 K) is assumed to be equal to that of air, $D_{f,0} = 0.2 \times 10^{-4}$ m^2/s [148], and the diffusion coefficient is assumed to vary with temperature according to [149]:

$$D_f = D_{f,0} \left(\frac{T}{T_0} \right)^{1.67} \tag{3.21}$$

The viscosity of the gas mixture is assumed to be equal to that of methane at room temperature and pressure: $\mu_{v,0} = 1.05 \times 10^{-5}$ Pa·s [150], and Sutherland's law [151] is used in the estimation of the dynamic viscosity of the mixture as a function of temperature,

$$\mu_v = \mu_{v,0} \frac{2.78 T_0 + 8 C_s}{2.78 T + 8 C_s} \left(\frac{T}{T_0} \right)^{\frac{3}{2}} \tag{3.22}$$

where C_s is Sutherland's constant. The value of $C_s = 120$ for standard air is obtained from Ref. [152].

The boundary conditions are given as the uniform velocities at the exit of the

jet tube and co-flow tube, and symmetry conditions for the velocity and mixture fraction:

$$\begin{cases} z = 0, & \begin{cases} \xi = 1,\ u_z = u_F,\ u_r = 0,\ \text{for } 0 \leq r \leq r_p \\ \xi = 0,\ u_z = u_O,\ u_r = 0,\ \text{for } r > r \end{cases} \\ z = \infty,\ \xi = 0,\ u_z = 0,\ u_r = 0 \\ r = 0,\ \frac{\partial \xi}{\partial r} = 0,\ \frac{\partial u_z}{\partial r} = 0,\ u_r = 0 \\ r = \infty,\ \xi = 0,\ u_z = 0,\ u_r = 0 \end{cases} \tag{3.23}$$

where r_p is the inner diameter of the fuel port, u_F and u_0 are the flow velocities in the fuel tube and co-flow tube, respectively and velocity does not have an impact on the final temperature and velocity distribution since the flames are highly buoyancy dominated [148, 153]. Combining equations (3.8) to (3.22) with the boundary conditions stated in Eq. (3.23) allows for the mixture fraction ξ and velocity u to be solved numerically. The Matlab code can be found in the Appendix D.

3.4 Results and discussion

3.4.1 Comparison of extinction and LII measurements

Figure 3.4 displays the mean f_v values obtained from 500 LII images for each test case. The signal intensities are converted to the soot volume fraction using the method described in Chapter 2. In order to accommodate the length-to-height ratio of the flames, three different series of images were taken, with images connecting at heights of 34 and 68 mm. For all cases, soot appears at the top and edge regions of the flame where the temperatures are highest, providing a suitable environment for soot particle nucleation, growth and eventual oxidation. Figure 3.4 shows that there is a dramatic decrease in the soot volume fraction with a decrease in the CH_4 mole fraction $X_{F,0}$ in the fuel stream.

Figures 3.5 to 3.9 show the comparison between the results obtained using

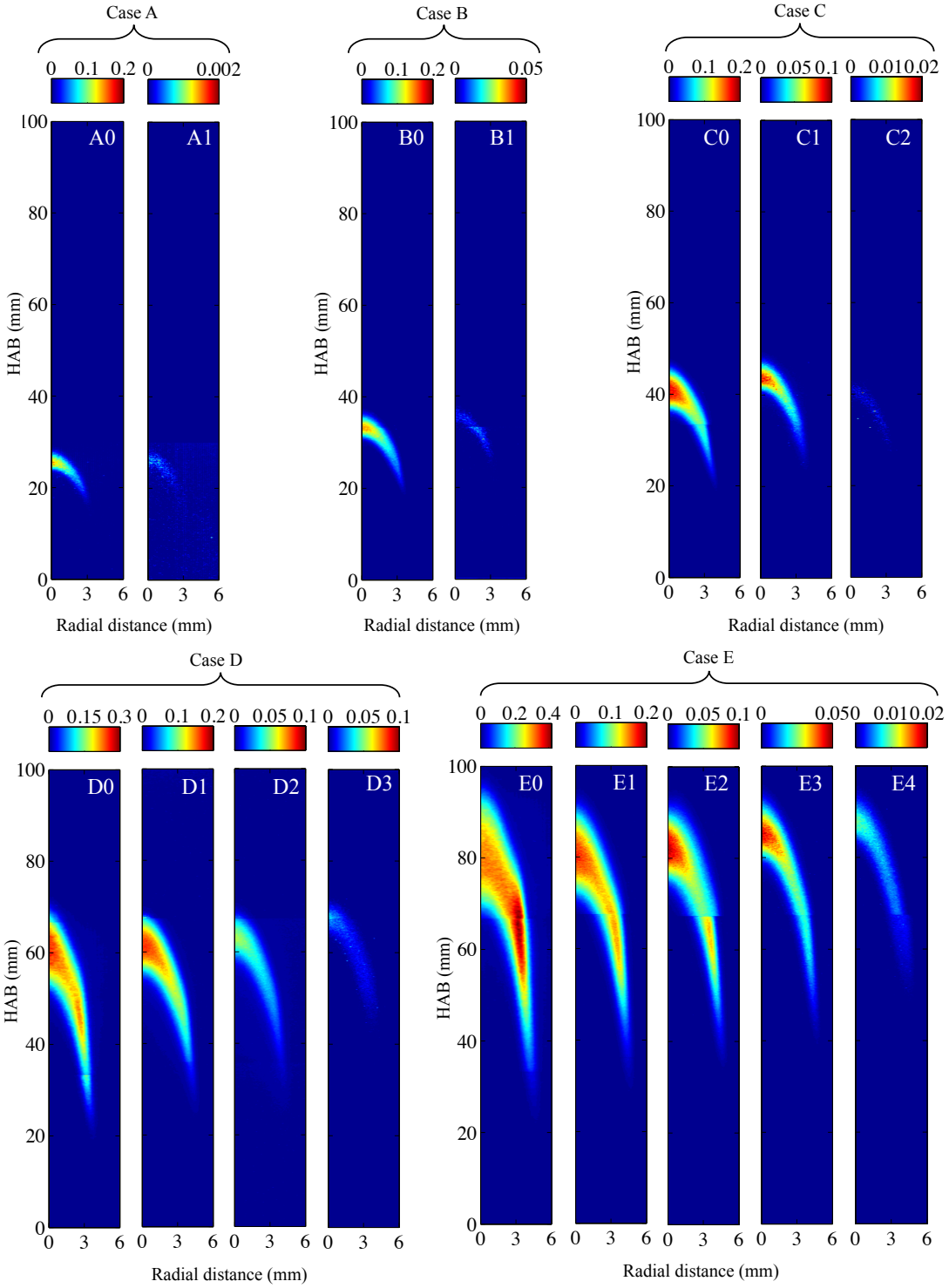

Fig. 3.4 Mean value of 500 images of LII signals for flames A0 to E4. The LII images are calibrated to the soot volume fraction (in ppm).

the LII and extinction measurement techniques for flames A0, B0, C0, D1 and E1 (the results of flames D0 and E0 are not shown here as they are included in Chapter 2). The results for other flames are similar, and K_e for all cases can be found in Appendix F.2. Error bars for the LII measurements are obtained from the standard deviation of LII signals over 500 images, after calibration using the method described in Chapter 2. Error bars for the extinction measurements are directly calculated from the standard deviation of the measured raw data by error propagation (see Section 2.4.3 and 2.4.4). The uncertainty associated with the extinction measurements gradually increases towards the flame centre, due to the cumulative effects of the Abel transform [138]. The detailed analysis of extinction measurement errors shows that stable measurements allow resolution down to 20 ppb, as much of the variance arises due to flame flickering. LII and extinction measurements are in good agreement after a single calibration point for each condition, even in the sub-ppm range. The largest discrepancies appear under conditions in which the soot is negligible at the centre line; the numerical errors tend to accumulate due to the inverse transform, leading to the discrepancies observed.

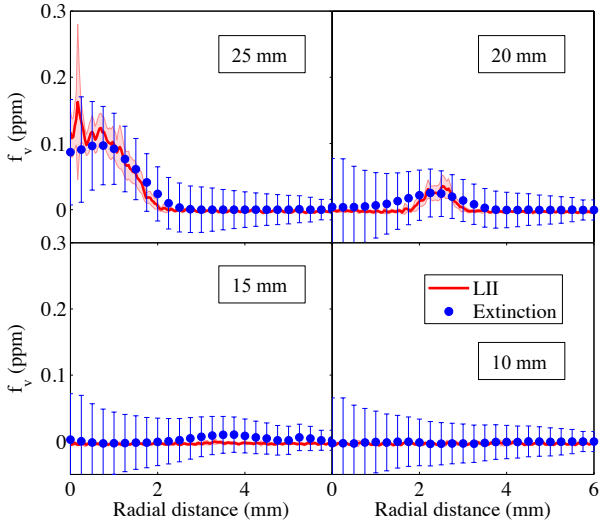

Fig. 3.5 Soot volume fraction f_v measured using cavity extinction (blue circles) and LII (red line) for the flame A0.

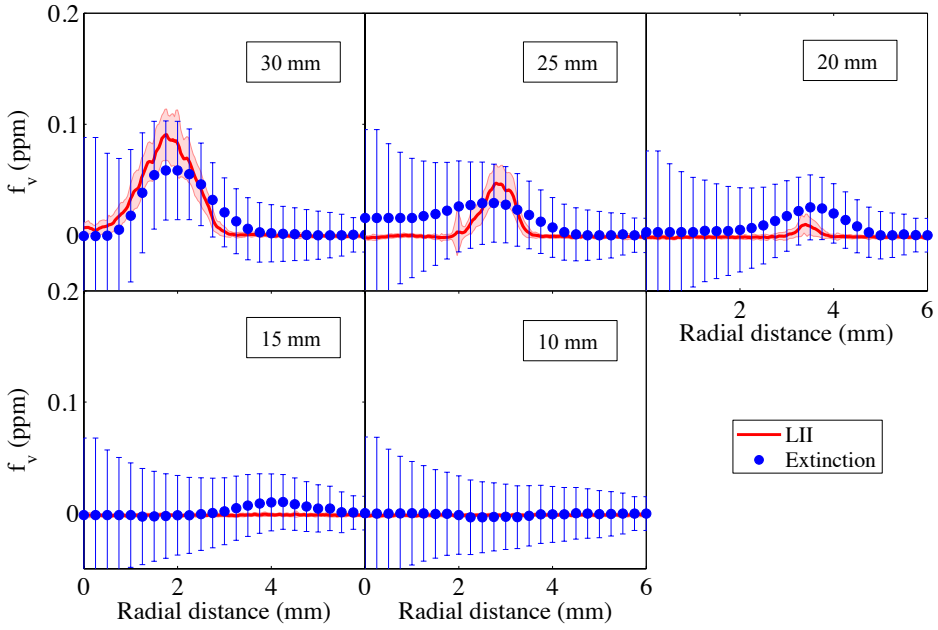

Fig. 3.6 Soot volume fraction f_v measured using cavity extinction (blue circles) and LII (red line) for the flame B0.

3.4.2 Diffusion flame model

The numerically calculated flame temperatures and velocities are verified against experimental data obtained elsewhere. The temperature and flow velocity of a methane flame, case CH4-S-101, with a fuel flow velocity of 10.11 cm/s and co-flow air velocity of 14.6 cm/s, which is very similar to our E0 flame, were obtained from the database provided by Rahul *et al.* on the NIST website [9]. The calculated temperature and velocity of the flame CH4-S-101 are compared with experimental data [9] in Fig. 3.10. Given the relatively simplistic assumptions, the agreements of both temperature and velocity are adequate for the selected profiles. In the flame outer zone, heat diffuses much faster than accounted for in the model, which may be due to the approximations made, including the use of the unity Lewis number, or neglecting axial diffusion. There is also a discrepancy in the region close to the base, most likely due to neglecting the local heat transfer to the base, at around 60 mm, where the temperatures measured appear lower. In this case, it is possible that either the endothermicity of pyrolysis reactions or

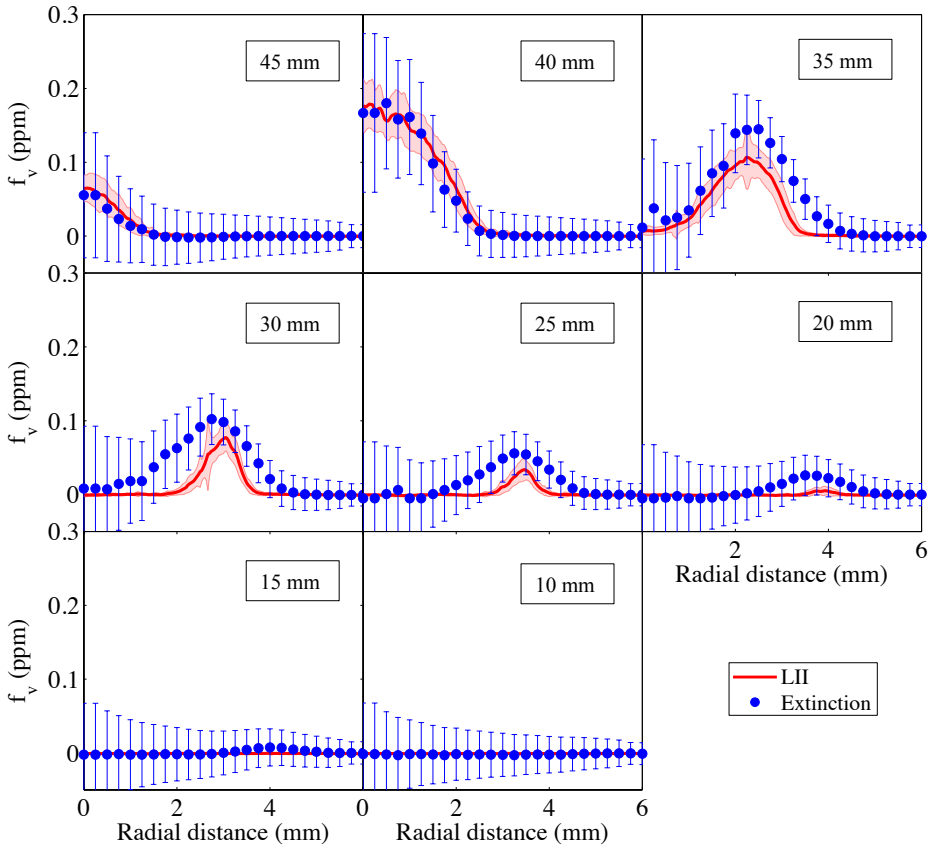

Fig. 3.7 Soot volume fraction f_v measured using cavity extinction (blue circles) and LII (red line) for the flame C0.

radiation losses play an important role. In the present model, we are primarily considering the temperatures and velocities along the symmetry plane, so the discrepancies around the edges are not as relevant. Figure 3.10 (b) shows the calculated flow velocities against measured values obtained from Santoro *et al.* [86]. There is clearly good agreement between the calculated and experimental data for the measured flame heights. Given the reasonable agreement between model and experimental values for temperature and velocity, the model is now used as a basis for further discussion of the findings in the present study.

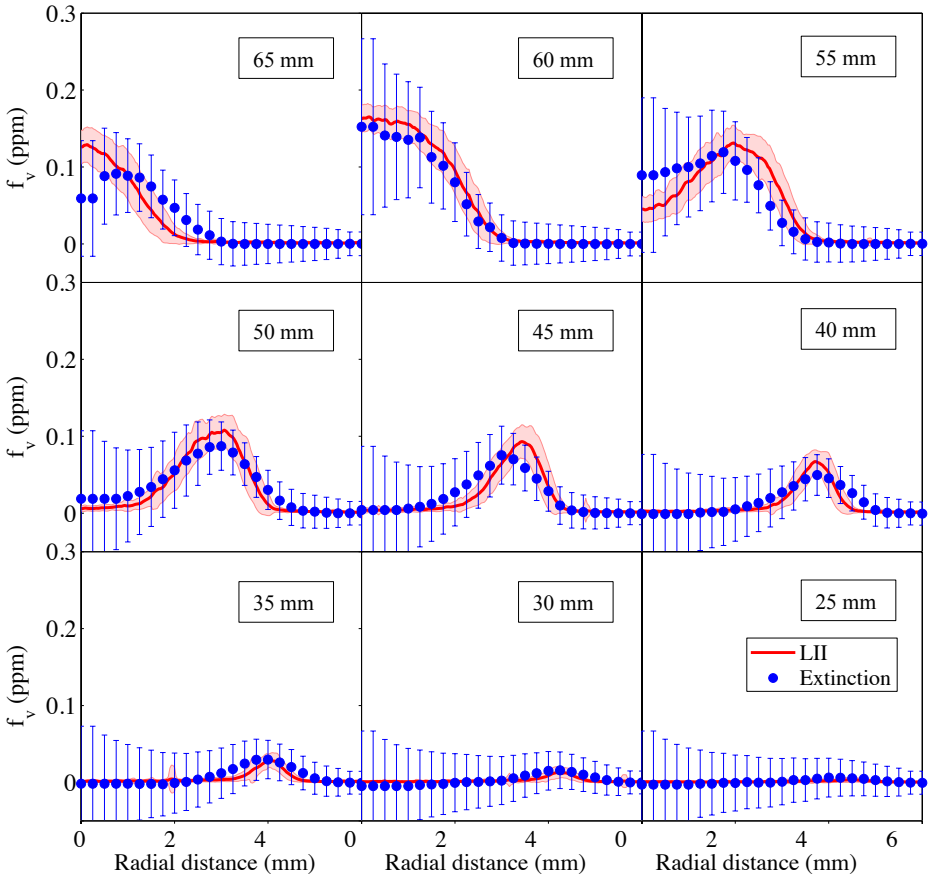

Fig. 3.8 Soot volume fraction f_v measured using cavity extinction (blue circles) and LII (red line) for the flame D1.

3.4.3 Influence of fuel flow rate and nitrogen dilution on soot volume fraction

A) Soot volume fraction and mixture fraction

The experimental results show clearly that dilution by nitrogen reduces the total peak and integrated soot concentrations in these diffusion flames. Figure 3.11 shows how the maximum f_v decreases as a function of the mole fraction of nitrogen in the flow.

The replacement of nitrogen for fuel in the jet at a constant total carbon flow rate has the following effects: (a) a direct effect in reducing the concentration of the fuel mass fraction and thus soot precursors, (b) an indirect effect of lower-

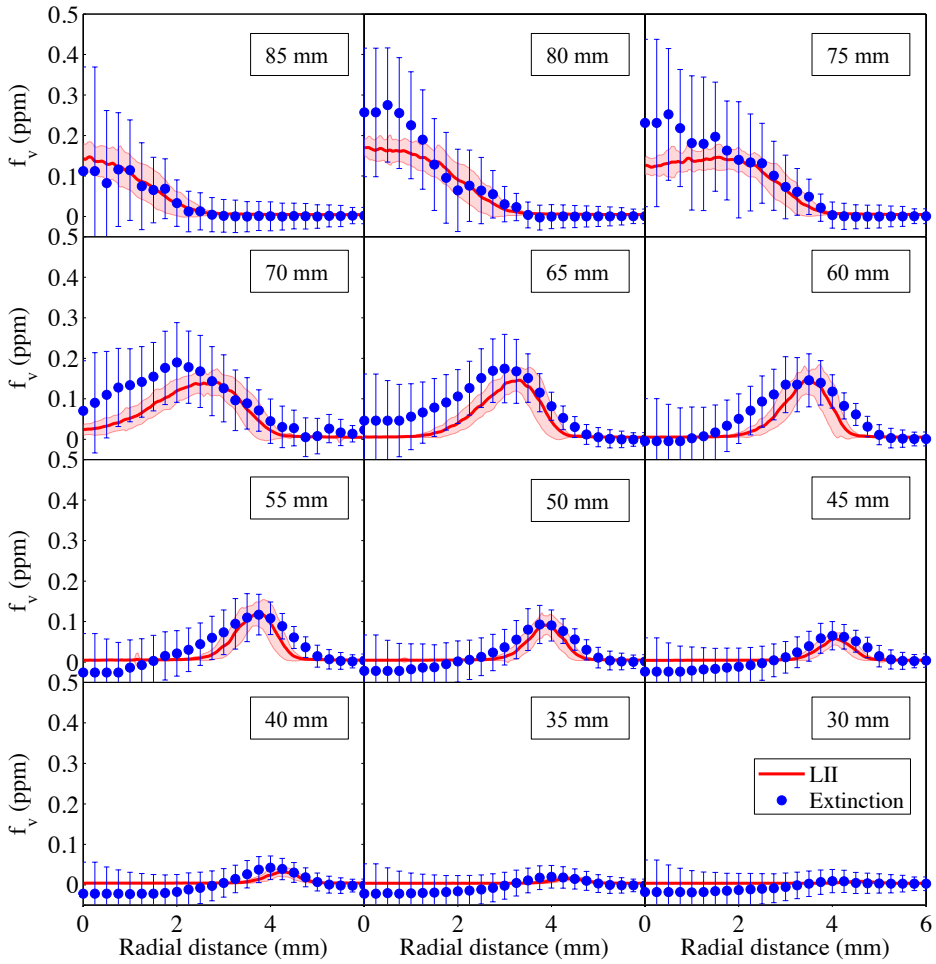

Fig. 3.9 Soot volume fraction f_v measured using cavity extinction (blue circles) and LII (red line) for the flame E1.

ing the temperature, which acts to reduce both the rate of soot formation and oxidation, and (c) a second order effect in reducing the residence time. In order to separate these factors in the analysis, we consider a simplified model for soot formation and oxidation based on a single step reaction, following the approach of Axelbaum *et al.* [154] and Gülder *et al.* [10, 11]. In their studies, the adiabatic temperature of the flames (of varying dilution ratio) was kept constant by adding an external heat source to preheat the fuel and diluent gas. The basic assumption in these studies is that the soot formation rate in diffusion flames is proportional to the product of the first order of the fuel mole fraction in fuel flow and the

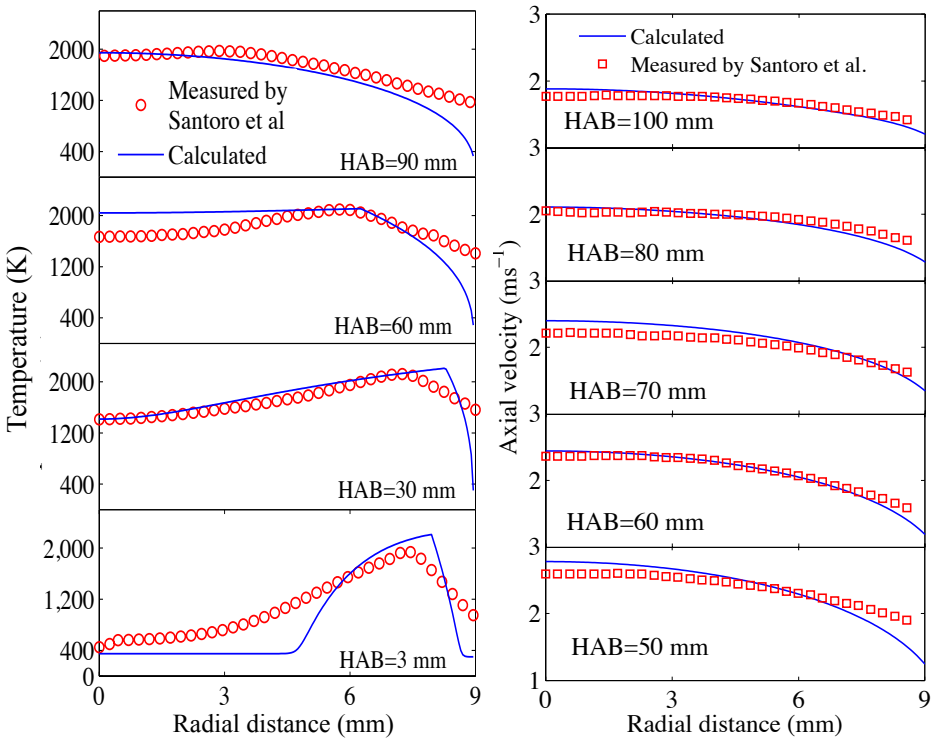

Fig. 3.10 Comparison of flame temperature (left) and flow velocity (right) at different flame heights of a methane flame with a fuel flow velocity of 10.11 cm/s and co-flow air velocity of 14.6 cm/s from [9] (symbols). The calculations are based on identical parameters with the tested flame in [9].

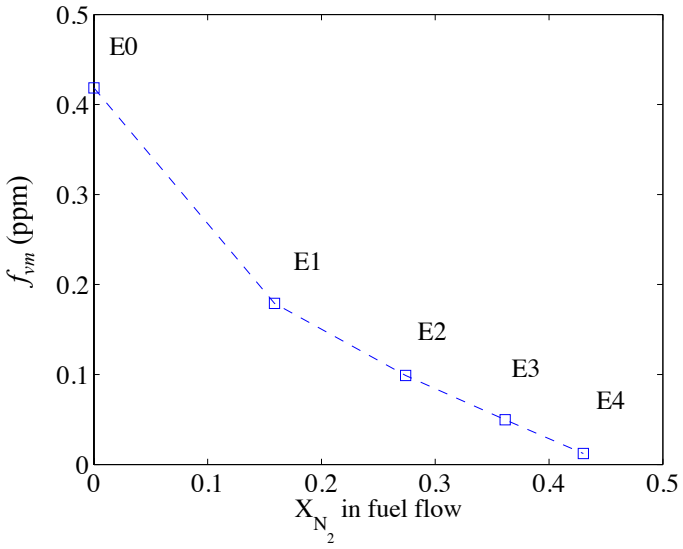

Fig. 3.11 Measured maximum soot volume fraction in group E flames

Arrhenius term determined by the adiabatic temperature:

$$\omega_s = A_p X_{F0} \exp\left(\frac{-E_a}{R_0 T_{ad}(X_{\mathrm{N}_2})}\right) \tag{3.24}$$

where A_p is the proportion coefficient, X_{F0} is the fuel mass fraction in the incoming fuel jet, E_a is the global activation energy, T_{ad} is the adiabatic temperature, which is a function of the mole fraction of nitrogen, $X_{N_2} = 1 - X_{F0}$. Furthermore, Gülder *et al.* [10, 11] assumed that the maximum soot mass fraction f_{vm} is proportional to the product of the rate of reaction in Eq. (3.24) and the total residence time through the reaction zone, τ. In the same study, it is assumed that the residence time scales with the square root of the visible flame height H [10, 11, 148, 153], yielding:

$$f_{vm} = B_p H^{\frac{1}{2}} X_{F0} \exp\left(\frac{-E_a}{R_0 T_{ad}(X_{\mathrm{N}_2})}\right) \tag{3.25}$$

They found that the behaviour of their experimentally measured f_{vm} agreed well with the proposed model [10, 11]. We compare the predictions of such a model with the normalised experimental results in the current study in Fig. 3.12. The adiabatic equilibrium temperature for a stoichiometric mixture T_{ad} is calculated using Cantera with GRI3.0 thermodynamics [155], with results shown on the right-hand side scale. For values of X_{N_2} ranging from 0 to 0.6, there is only a weak dependence of temperature on X_{N_2}, because the reduction in temperature scales with the product of X_{N_2} times the stoichiometric mixture fraction, which is a small number. The effect of X_{N_2} can be isolated by keeping the reaction temperature equal to the undiluted adiabatic temperature $T_{ad}(X_{N_2} = 0)$ (thick blue line in Fig. 3.12). In that case, the effect is linear with X_{N_2} via the decrease in local concentration. Other studies have suggested activation energies for soot formation in methane flames of 2.9×10^5 J/mol [156] and 3.28×10^5 J/mol [157]. Using these values, one can scale the effect of the combined dilution and temperature effects as shown by the dotted line. The overall reaction rate varies

exponentially with the local temperature, as indicated by the green dashed line, for each global activation energy. The two dotted lines are very close, indicating the soot formation is not sensitive to global activation energy in the range from $E_a = 2.9 \times 10^5$ J/mol to 3.28×10^5 J/mol. The global f_{vm} of group C to E flames were normalised by the values of the undiluted flame, as shown by the symbols in Fig. 3.12. The measured decrease of f_{vm} with dilution is steeper than predicted by Gülder *et al.*'s simple scaling. The approximations made in the models in Axelbaum *et al.*'s [154] and Gülder *et al.*'s [10, 11] studies are reasonable attempts to isolate the thermal and diluent effects for soot formation. However, the full effects of temperature variation with dilution along the soot formation path should influence soot formation, but are not taken into account. Furthermore, the approximation for the scaling of residence time with visible height, although reasonable in the case of the highly buoyancy dominated flames [86, 148, 153], the time for soot particle formation should ideally be estimated from the location of the soot inception point to the location of f_{vm} [10]. This is because the particle surface growth, which always takes place in this region, is the greatest contributor to the increase in the soot volume fraction [158]. Finally, the local fuel mole fraction around the soot formation region decreases due to diffusion and conversion into soot. A revised model for soot formation and scaling is proposed in the next section.

Figure 3.13 (a) shows the line-of-sight integral of the soot volume fraction at the flame centre line along the radial direction $\int_0^\infty f_v dr$ for group E flames, based on the measured and calibrated LII data. We chose to compare the LII results, as they offer a higher spatial resolution along the flame height (30 μm) relative to the extinction results (5 mm measurement interval). As shown in the figure, the soot volume fraction decreases significantly with the increase in the nitrogen volumetric fraction in the fuel flow, even though the total flow rate of the methane is kept constant (0.53 slpm for group E flames). This trend can also be observed in Fig. 3.13 (b), which displays the measured local soot volume fraction along

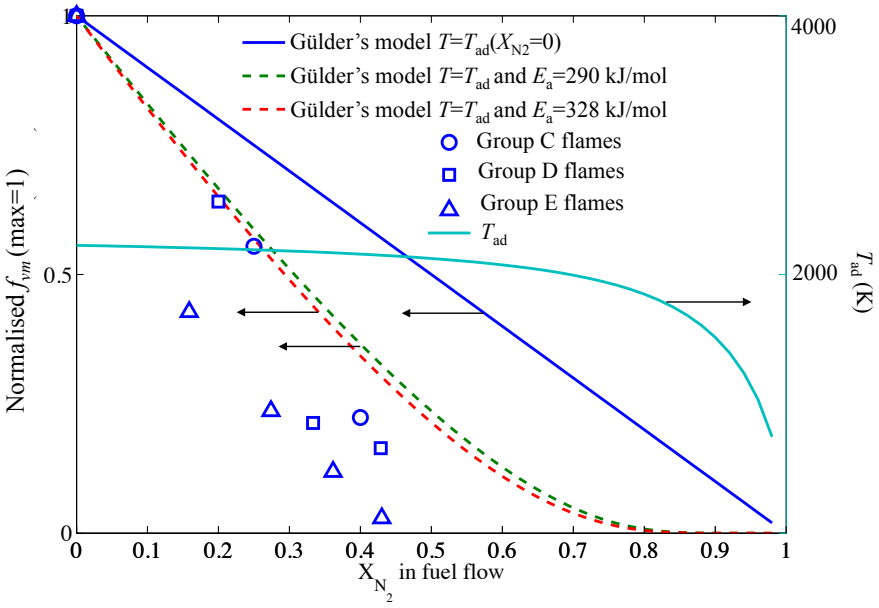

Fig. 3.12 Normalized measured maximum soot volume fraction for group C-E flames (symbols), and predictions using Gülder *et al.*'s model [10, 11] with different global activation energies. The calculated stoichiometric adiabatic temperatures are shown on the right hand side axis. The operational conditions for group C, D and E flames can be found in Table 3.1.

the flame centre line of the group E flames. When X_{N_2} in the fuel flow is as large as 0.43 (flame E4), both the integrated and local soot volume fraction values are close to zero (soot free).

B) Soot formation rate

A species conservation equation of soot in a flame can be written as:

$$\rho u_z \frac{\partial Y_s}{\partial z} + \rho u_r \frac{1}{r} \frac{\partial}{\partial r} (r Y_s) = \frac{1}{r} \frac{\partial}{\partial r} \left(r \rho D_s \frac{\partial Y_s}{\partial r} \right) + \omega_s \tag{3.26}$$

where Y_s is the mass concentration of soot; ω_s is the rate of soot formation in unit volume and D_s is the diffusivity of soot particles. Along the flame centre line, the radial velocity and of species is zero and particle Brownian diffusion is

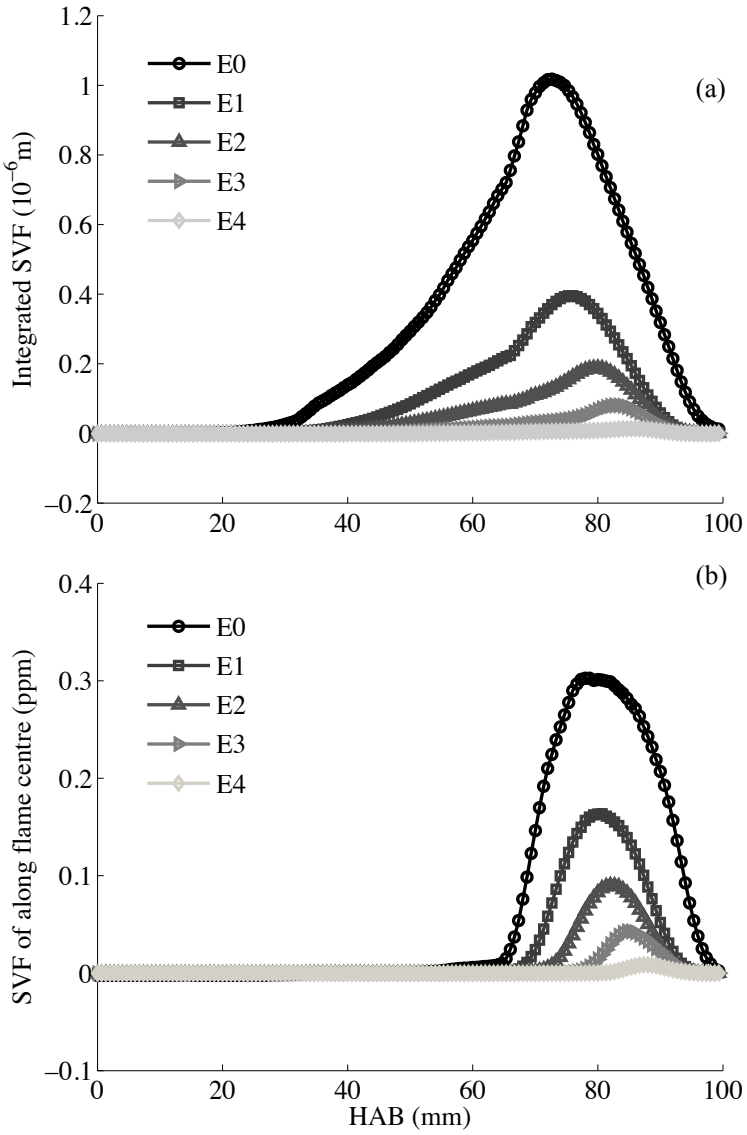

Fig. 3.13 (a) Integrated line-of-sight soot volume fraction $\int_0^\infty f_v \mathrm{d}r$ extracted from LII measurements at the flame centre line along the radial direction for the group E flames; (b) LII measured local soot volume fraction along the flame centre line for case E.

considered to be negligible [145], so that the conservation equation for soot is:

$$\rho u_z \frac{\mathrm{d}Y_s}{\mathrm{d}z} = \omega_s \tag{3.27}$$

Figure 3.14 (a) shows the value of axial ω_s along the flame centre line of undiluted flames A0 to E0; the maximum values of ω_s decrease with increasing

flow rates, which may be because of higher radiant losses in D0 and E0 flames [86]. The results present the same trends as those found in Santoro *et al.*'s study of ethylene flames [86]. For diluted cases, the value of ω_s drops with the diluent ratio due to the low local temperature and shorter residence time for mass growth.

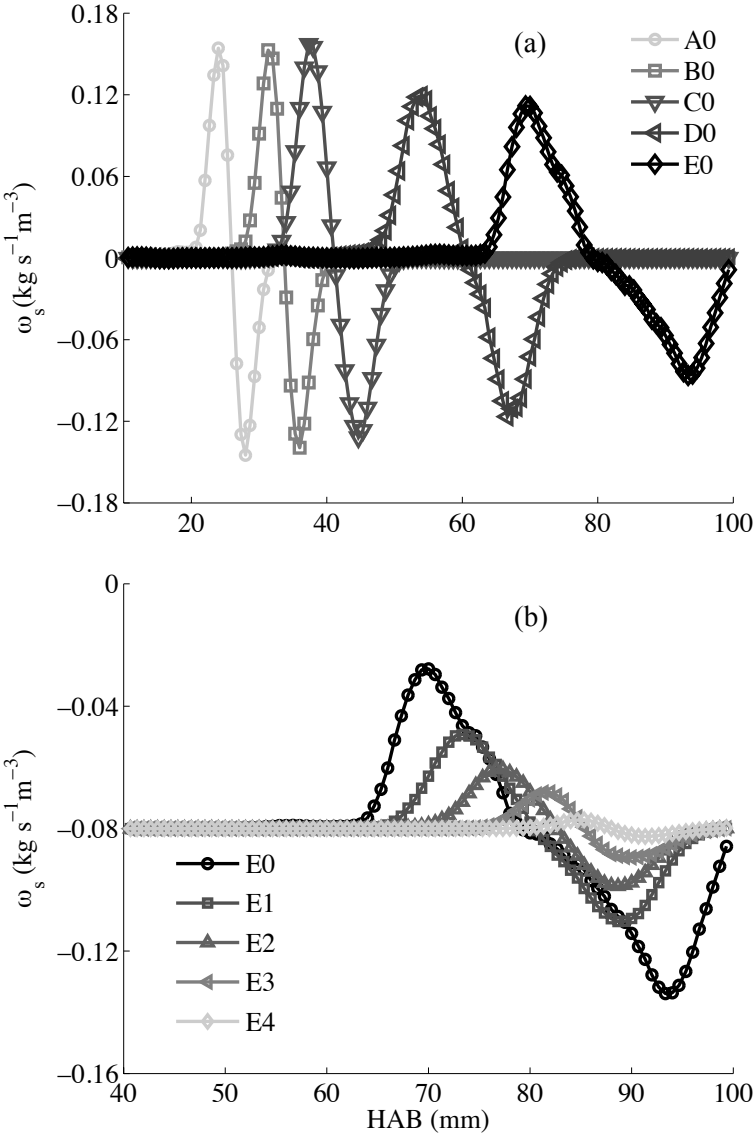

Fig. 3.14 a) measured ω_s along the flame centre line for cases A0 to E0 without nitrogen diluent; b) measured ω_s along the flame centre line of group E flames.

Figure 3.15 shows the measured ω_s in group E flames as a function of temperature and initial fuel mass fraction Y_{F0} along the flame centre line. The result

shows that the soot formation rate is controlled by both fuel concentration and temperature.

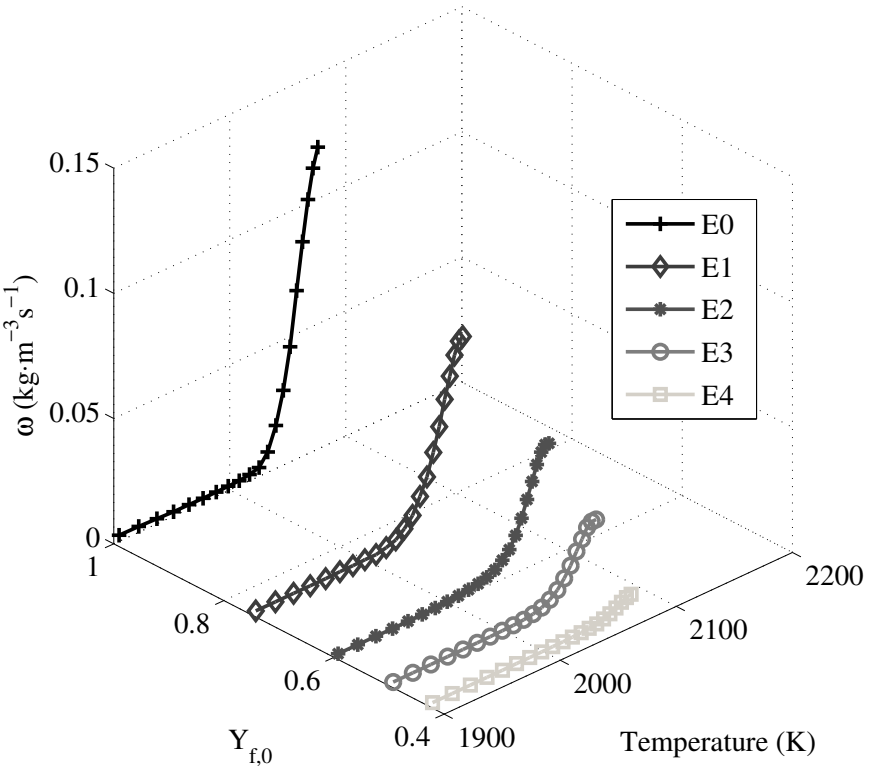

Fig. 3.15 Measured ω_s in group E flames as a function of temperature.

C) Local temperature for soot mass growth

In the present study, the local temperature of a flame is calculated with a mixture fraction based on the state relationship of the diffusion flame as described in section 3.4.2. Figure 3.16 shows that with the increasing dilution rate for flames E0 to E4, the contours of the stoichiometric mixture fraction ξ_{st} move towards the fuel side in the radial direction and downwards towards the jet nozzle in the axial direction (HAB = 67 mm for the E0 flame and 60 mm for the E4 flame). This is consistent with basic mixture fraction theory for diffusion flames. However, for the diluted cases, the positions of the soot formation region (defined as the region

where a soot particle is detectable with LII measurement, as shown by the blue dotted line in Fig. 3.16) show an opposite trend as ξ does, and move upwards to the flame downstream. It is well known that the greatest temperature in a diffusion flame always occurs close to the position of the stoichiometric mixture fraction, ξ_{st}, and the peak temperature can be estimated to be the adiabatic temperature T_{ad} while ignoring the transfer and radiation of heat. For the undiluted case (E0), ξ_{st} equals 0.055 for methane-air combustion. As displayed in Fig. 3.16, the maximum soot volume fraction is also close to the contour of ξ_{st}. However, for diluted cases E1 to E4, while the contour of ξ_{st} moves downwards to the jet nozzle, the soot formation region moves upwards gradually. This means that the soot formation zone is shifted towards the region with a lower temperature than T_{ad}, as shown in Fig. 3.17. This may explain the fact that the measured maximum soot volume fraction f_{vm} is below the predicted value using T_{ad}, as shown in Fig. 3.12.

Figure 3.18 shows the isocontour lines of maximum soot volume fraction f_{vm} for the set of group E flames. With increasing dilution ratio, the isocontour of f_{vm} shifts towards the air side, which is opposite to the shift of ξ_{st}, as well as peak temperature. This trend suggests the idea that, although we can consider the gaseous reactions in flames as one-step reactions, we cannot simplify the formation of soot as one step, otherwise the shift of the isocontour of f_{vm} should be consistent with the calculated shift of ξ_{st} due to the higher temperature in that region. In fact, the formation of soot is far more complicated than the gaseous reactions in flames. Because of the relatively long reaction time required for the inception of the nascent particle, surface growth and coagulation, the introduction of soot in the diffusion flame is determined by the residence time, temperature and local mixture fraction [159]. In the present study, when the total carbon input is kept constant in group E flames (0.53 slpm) while varying the diluent ratio of the fuel (from 0 to 0.4 slpm), the location of soot inception (i.e. where $f_v \geq 0$) shows a reverse shifting trend with ξ_{st}. For example, in the undiluted

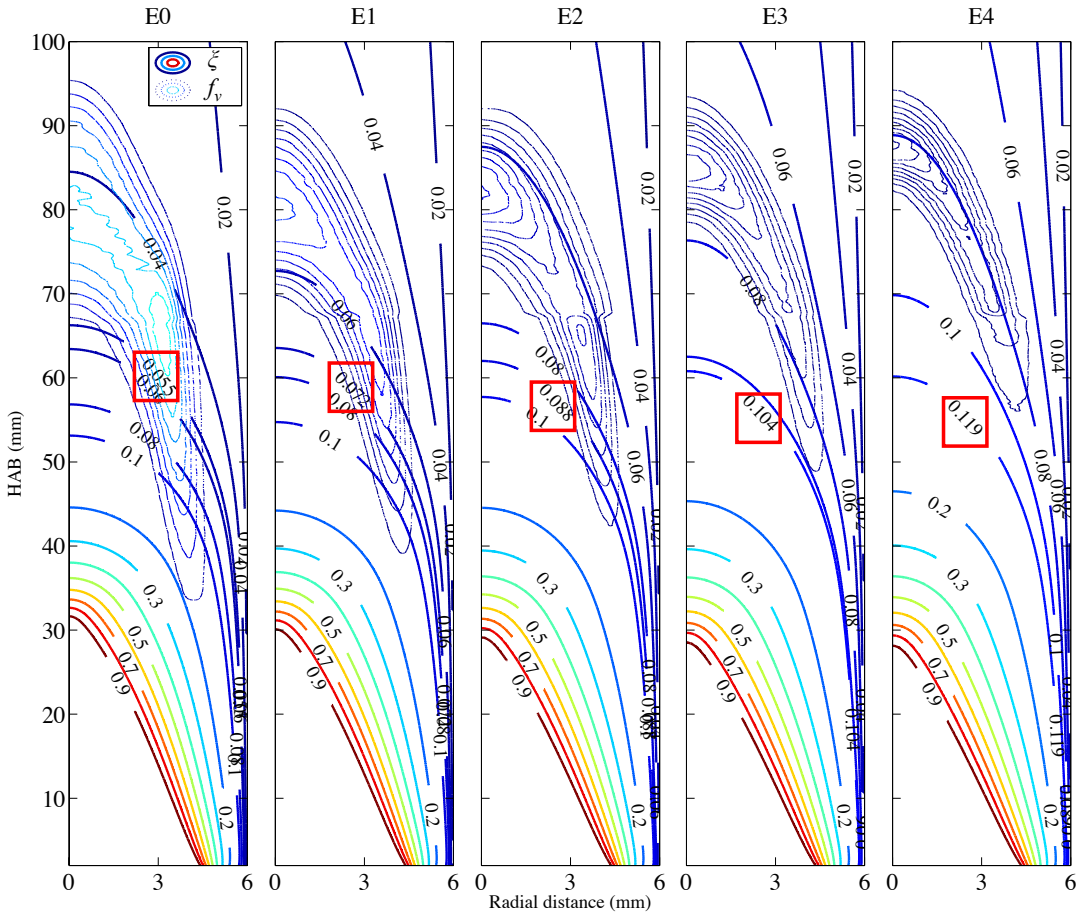

Fig. 3.16 Measured soot volume fraction (thin lines) and calculated mixture fraction ξ (thick lines) for group E flames. The chemical stoichiometric mixture fraction ξ_{st} for each flame is denoted by a red square.

flame E0, the location of ξ_{st} along the flame centre line is at HAB = 67 mm and the soot inception point is located at HAB = 68 mm. However, for flame E4, when the location of ξ_{st} moves to HAB = 60 mm, the soot inception point (where the soot volume fraction starts to be detectable) shifts inversely to HAB = 83 mm. The behaviour of the soot growth region along the flame centre line (from the location of soot inception to the location of f_{vm}) also presents a similar trend, as shown in Fig. 3.16. This indicates that the inception and growth of a soot particle is more residence time dependent than temperature dependent in these flames, as the soot inception point does not shift with the high temperature zone. This argument is supported by Honnery and Kent's [146] study in which

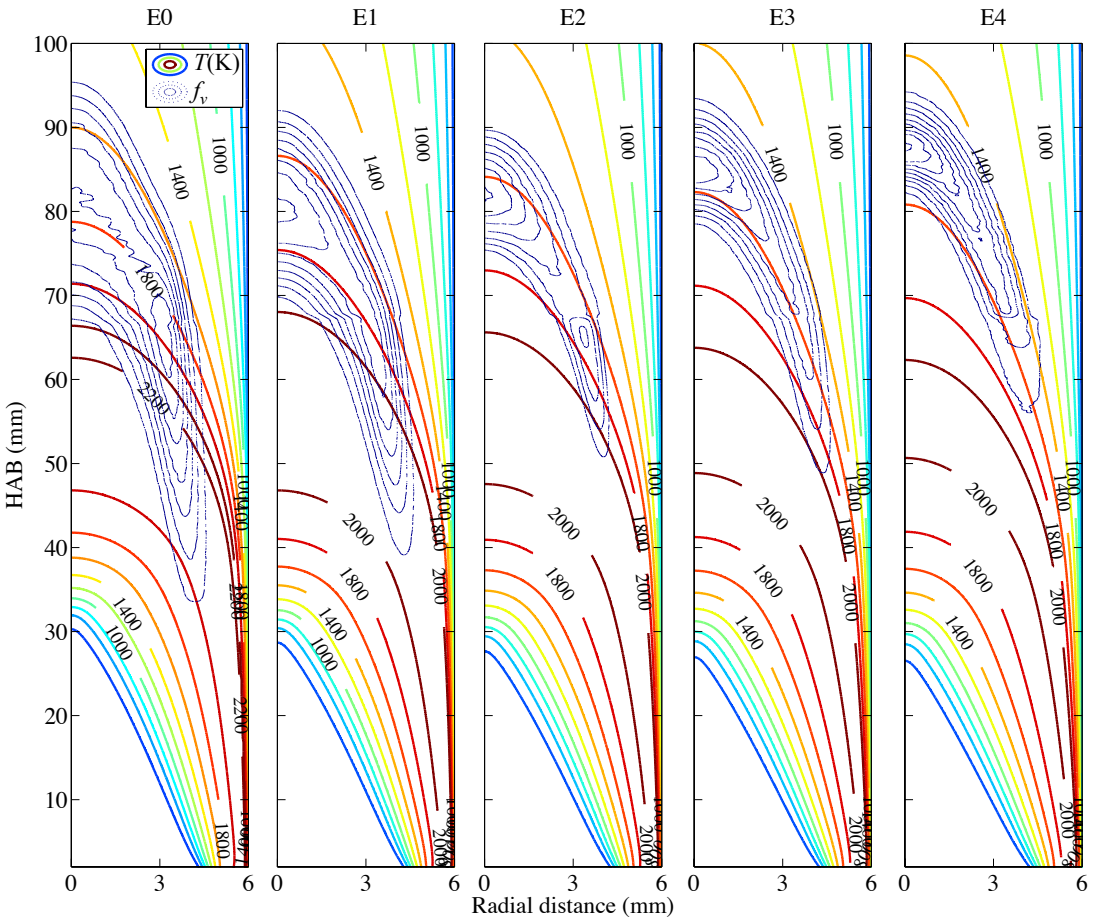

Fig. 3.17 Measured soot volume fraction (thin lines) and calculated temperature (thick lines) for group E flames.

they investigated the soot formation process in long ethylene diffusion flames, and found that the total amount of soot at any height in a flame is only a function of the particle trajectory time from the reaction zone and is independent of the flame length and relative position in the flame. The result indicates that soot particle growth rates averaged across the flame section are not dependent on gas-phase reactions. In this case, given that all of the flames in group E are highly buoyancy dominated, the trajectory time for soot particles should primarily depend on the flame height rather than initial flow velocity due to the large axial buoyancy acceleration [86, 148, 153, 160]. Thus, the soot zone does not shift in the same manner as ξ_{st}.

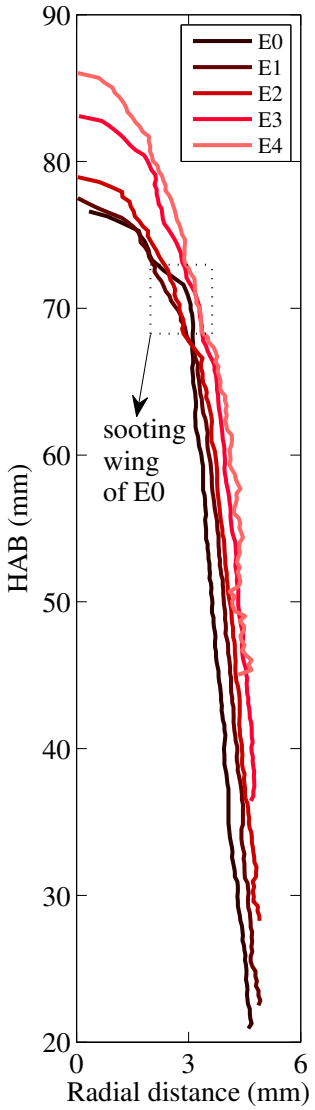

Fig. 3.18 Isocontours of f_{vm} in group E flames.

Furthermore, we observe from the soot volume fraction map (Fig. 3.4) that E0 is the only flame condition tested (from A0 to E4) whose maximum soot volume fraction appears in the annular region rather than at the flame centre line. This is also a result of the effect of the residence time.

Along the flame centre line, an increase in fuel flow rate reduces the rate of

energy transfer of hot products or reactants from the flame front to the flame centre, therefore, the residence time available for the particle remains relatively constant [86]. However, in the annular region of the undiluted flames (A0 to E0), the flame front can provide an energy source to initiate fuel pyrolysis, which is independent of the fuel flow rate. Therefore, with an increased fuel flow rate, the flame height, as well as the available residence time for particle growth, are increased in the annular region, resulting in higher values of the soot volume fraction. When the residence time is longer than that of the flame centre line, the maximum soot volume fraction appears in the annular region rather than along the flame centre line, shifting the maximum soot isocontour as shown in Fig. 3.18, due to the longer oxidation time required to burn out soot. For the diluted cases, the temperature of the flame front in the annular region is reduced by dilution, hence the soot inception in the annular region is delayed and results in a decrease in the residence time in this region.

In the present study, we define a local temperature for soot formation denoted by T_l, which is calculated as the mean temperature in the soot growth region (starting from the location where soot particles first form ($f_v \geq 0$) and ending at the location of the maximum soot volume fraction, as shown in Fig. 3.18). Based on the temperature map shown in Fig. 3.17, the T_l of group E flames is calculated and shown in Fig. 3.19. The results indicate that the actual local temperature T_l for soot growth is below the adiabatic temperature T_{ad}, thus using T_{ad} may underestimate the suppression effect of dilution on soot formation.

D) Residence time for soot mass growth

Gülder *et al.* [10, 11] investigated soot formation in diluted flames and considered the direct influence of the residence time for soot particle growth. However, due to the lack of spatially resolved f_v data, they simply relate the residence time to the square root of the height of the visible flame. However, this may introduce large uncertainty because the actual soot particle does not grow throughout the whole

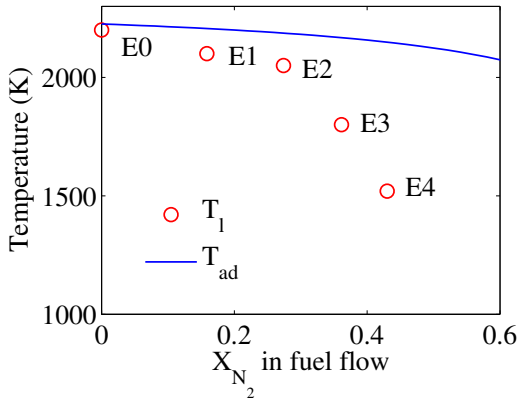

Fig. 3.19 Calculated local temperature for soot growth (circles) compared with the adiabatic temperature (line) for group E flames.

flame. In the present study, the growth distance of the soot particle along the flame centre line is obtained by measuring the distance from the location of $f_v \geq 0$ (where soot particles first form) to f_{vm} (where oxidation becomes dominate) on a 2D soot volume fraction map. When the soot growth distance is obtained, the residence time t_r for particle growth can be calculated using Eq. (3.28) since the axial flow velocity is numerically calculated with the diffusion flame model in Section 3.4.2:

$$t_r = \int \mathrm{d}t = \int_{z_1}^{z_2} \frac{\mathrm{d}z}{u_z\,(z)} \tag{3.28}$$

where z_1 and z_2 are the soot inception and maximum positions, respectively. The residence time calculated for soot mass growth indicates that, when X_{N_2} increases from 0 to 0.43, the residence time t_r decreases by a factor approximately equal to 3.

E) Corrected one-step soot formation model

Following on from the previous discussion, the one-step soot formation model can be corrected by taking the local temperature and the residence time calculated for particle surface growth into account. In the present study, the mean local

temperature for soot growth, T_l, is calculated by averaging the temperature in the sooting zone across the flame. The residence time t_r is calculated using Eq. (3.29). Taking T_l and t_r into Gülder's one-step soot formation model, we obtain:

$$f_{vm} = B_p \int_0^{t_r} X_{F0} \exp\left(\frac{-E_a}{R_0 T_l}\right) \mathrm{d}t \tag{3.29}$$

The calculated f_{vm} is normalised and compared with measured data, as shown in Fig. 3.20. The calculated and measured data show good agreement. This indicates that the use of T_l and t_r can improve the accuracy of the prediction of f_{vm} produced in nitrogen-diluted flames. As shown in Fig. 3.12, calculating f_{vm} using T_{ad} and τ (derived from the flame height) as Gülder *et al.* [10, 11] did, may result in an overestimation of the value. Due to the addition of diluent, the local temperature for soot mass growth, T_l, decreased more than T_{ad}, and the residence time also reduced.

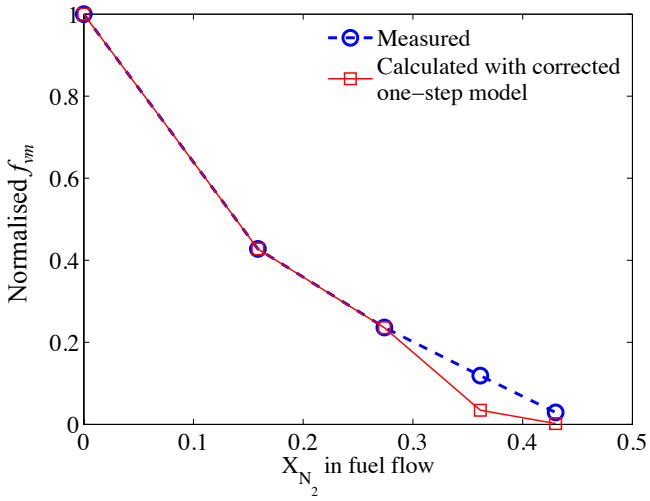

Fig. 3.20 Comparison between normalised measured, and calculated value of f_{vm} using T_l and t_r along the flame centre line in group E flames. All values are normalised by the value of f_{vm} for flame E0.

The various factors affecting soot formation can be isolated individually. If we consider the reaction temperature to take on the value of the undiluted adiabatic temperature T_{ad} ($X_{N_2} = 0$) and we consider the residence time in the undiluted

flame, τ, the characteristic maximum soot volume fraction for an undiluted case (denoted with f_{vm0}) can be calculated as:

$$f_{vm0} = \int_0^{\tau} B_p \exp\left(\frac{-E_a}{R_0 T_{ad}(X_{N_2}=0)}\right) \mathrm{d}t \tag{3.30}$$

where E_a is the global activation energy $E_a = 2.9 \times 10^5$ J/mol for soot formation in methane-air diffusion flames [156]. If we incorporate the influence of X_{N_2} into the calculation, while keeping the reaction temperature to be the undiluted adiabatic temperature T_{ad} $(X_{N_2} = 0)$, we may obtain the soot volume fraction f_{vm,X_F} which is purely affected by dilution, and has a linear relationship with X_{N_2}, as shown in Fig. 3.21 (blue line).

$$f_{vm,X_F} = B_p \int_0^{\tau} (1 - X_{N_2}) \exp\left(\frac{-E_a}{R_0 T_{ad}(X_{N_2}=0)}\right) \mathrm{d}t \tag{3.31}$$

The soot volume fraction $f_{vm,T_{ad}}$ affected by the adiabatic temperature under varying dilution rates can be evaluated using Eq. (3.32) by replacing $T_{ad}(X_{N_2} = 0)$ with the calculated $T_{ad}(X_{N_2})$, as shown in Fig. 3.21 (green line):

$$f_{vm,T_{ad}} = B_p \int_0^{\tau} (1 - X_{N_2}) \exp\left(\frac{-E_a}{R_0 T_{ad}(X_{N_2})}\right) \mathrm{d}t \tag{3.32}$$

Replacing $T_{ad}(X_{N_2})$ in Eq. (3.32) with T_l, the corresponding soot volume fraction f_{vm,T_l} under local temperature can be calculated with Eq. (3.33), and the results are shown in Fig. 3.21 (grey dashed line with circles):

$$f_{vm,T_l} = B_p \int_0^{\tau} (1 - X_{N_2}) \exp\left(\frac{-E_a}{R_0 T_l(X_{N_2})}\right) \mathrm{d}t \tag{3.33}$$

By replacing the characteristic residence time of the undiluted case τ with that of the diluted flame t_r, the resulting f_{vm,t_r} should be close to the true value, as shown in Fig. 3.21 (red dashed line with squares):

$$f_{vm,t_r} = B_p \int_0^{t_r} (1 - X_{N_2}) \exp\left(\frac{-E_a}{R_0 T_l(X_{N_2})}\right) \mathrm{d}t \tag{3.34}$$

The effect of dilution, adiabatic temperature, local temperature and residence time are denoted by $\Delta(d)$, $\Delta(T_{ad})$, $\Delta(T_l)$ and $\Delta(t_r)$, respectively, so that the values can be evaluated using normalised f_{vm0} to f_{vm,t_r} (a subscript 'n' is added), as shown in Eq. (3.35) and Fig. 3.21. This is done so that the various factors affecting soot formation are isolated in a quantitative manner.

$$\begin{cases} \Delta(d) = f_{vm0,n} - f_{vm,X_F,n} \\ \Delta(T_{ad}) = f_{vm,X_F,n} - f_{vm,T_{ad},n} \\ \Delta(T_l) = f_{vm,T_{ad},n} - f_{vm,T_l,n} \\ \Delta(t_r) = f_{vm,T_l,n} - f_{vm,t_r,n} \end{cases} \tag{3.35}$$

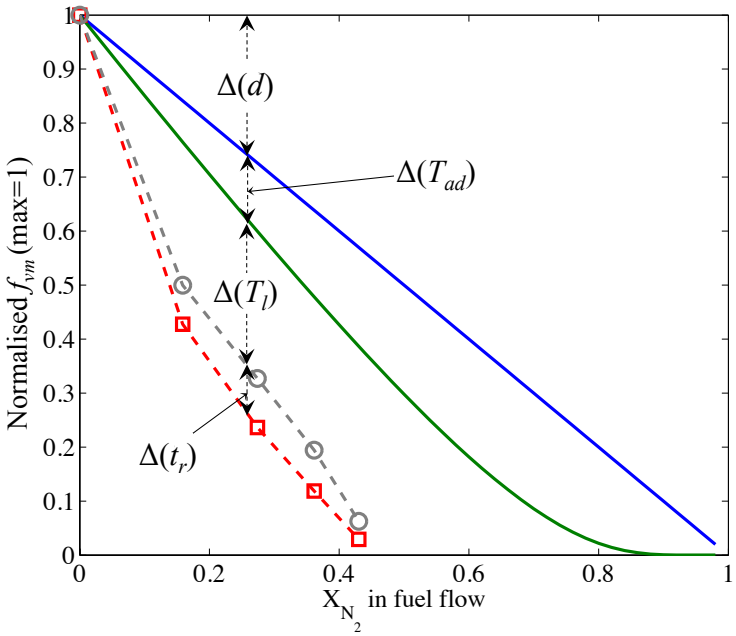

Fig. 3.21 Isolated factors influencing maximum soot volume fraction along the flame centre line in nitrogen-diluted diffusion flames. Blue line: calculated with $T_{ad}(X_{N_2} = 0)$; green line: calculated with T_{ad}; grey dashed line with circles: calculated with T_l; red dashed line with squares: measured data from group E flames. $\Delta(d)$, $\Delta(T_{ad})$, $\Delta(T_l)$ and $\Delta(t_r)$ are effects from dilution, adiabatic temperature, local temperature and residence time, respectively.

3.5 Conclusion

A laser cavity extinction technique with high spatial resolution was developed to measure the soot volume fraction across nitrogen-diluted, low-soot producing laminar methane-air diffusion flames. Comparisons with LII measurements on low sooting flames show good agreement with cavity extinction measurements. Data analysis shows that for a stable measurement target, without flickering, a measurement error of less than 20 ppb can be achieved, resulting in a measurement range of tens of ppbs. A high spatial resolution of 200 μm can be achieved by using concave cavity mirrors in the optical set-up. By comparing the numerically calculated flow field of the diluted flames and the measured soot volume fraction map, the following conclusions were drawn:

1) When keeping the total carbon input constant and varying the dilution of the fuel, the visible flame height of the jet co-flow and the flow velocity in the flame hardly change, indicating the flames are highly buoyancy dominated as opposed to being momentum dominated.

2) The addition of nitrogen into the fuel flow changes the location of the stoichiometric mixture fraction ξ_{st} in the flame. However, the location of the soot inception and growth (region where soot particles are first detected to the point of maximum soot volume fraction along the centreline) do not change with ξ_{st}, and even show a slightly opposite shift to ξ_{st}, indicating that in these flames, the inception and growth of the soot particles may be more dependent on time than temperature.

3) The addition of a nitrogen diluent in a methane flow changes ξ_{st} values and the location of flames with varying diluent ratio. However, the formation and growth region of soot remains in the region where the range of ξ is between 0.04 and 0.08. This means that the soot growth region is located in the zone where the temperature is lower than T_{ad}.

4) Under the present conditions where the total flow of carbon is kept constant,

dilution reduces the residence time for soot mass growth by a factor approximately equal to 3 when X_{N_2} in fuel flow increases from 0 to 0.43. This contributes to soot decrease.

5) The effects discussed in conclusions 3) and 4), combined with the dilution effect, result in a reduction in soot formation in diluted flames. The amount of reduction is more pronounced than estimated with T_{ad} in previous work.

Chapter 4

Planar 2-Dimensional 2-Colour Time-Resolved Laser-Induced Incandescence and Laser Cavity Extinction Measurements of Soot in an Ethylene Diffusion Flame

4.1 Introduction

In time-resolved LII (TiRe-LII), the decay rate of the signal arising from particle cooling, primarily via heat conduction and sublimation, can be used as a marker for the particle size [49, 52, 53, 112]. TiRe-LII has been usually limited to point measurements, where the signal and its decay over hundreds of nanoseconds are collected using photo multiplier tubes (PMTs). The 2D-TiRe-LII technique was first introduced by Will *et al.* [161]. They realised the temporal resolution by capturing two images with a CCD camera at two different times during the cooling of the soot particles. Hadef *et al.* [162] followed the same approach and proposed

a 2D-TiRe-LII method for particle sizing in a steady laminar diffusion ethylene flame, whereby the measurement is resolved in time by shifting the gate time window of an intensified camera along the decay of the LII signal, therefore more than two points can be captured. Sun *et al.* [163] modified the process to allow single shot sizing by using four ICCD cameras to sequentially record the LII decay at four separate time instances after the laser pulse. In all of the studies above, a solution to the energy balance for a single soot particle was used to estimate the maximum particle temperature $T_{\mathrm{p},0}$, and the particle energy absorption is assumed to follow the Rayleigh approximation for particles much smaller than the laser wavelength. The peak temperature estimate requires assumptions about the soot absorption function, $E(m)$. As discussed in Chapter 2, $E(m)$ has uncertainties, which can be as high as 67% (values of 0.18 to 0.30) [141–143, 164], with higher values generally more widely accepted. In addition, the results depend on monitoring the spatial fluence F, as non-uniformities in the resulting temperatures affect the estimation of particle diameter [68, 164].

In the present study, the 2-dimensional 2-colour (2D2C) configuration, which was first proposed by Mewes *et al.* [165], is combined with the 2D-TiRe method. The use of a 2D2C configuration allows experimental estimates of $T_{\mathrm{p},0}$ to be obtained based on Planck's Law (rather than solving the particle energy balance), while minimising the uncertainty arising from estimates of $E(m)$ and F. On the other hand, it is clear that the present approach can also be limited by the signal-to-noise ratio obtained, as well as the averaging effect of the intensifier time window.

In order to eliminate the uncertainty arising from these estimates of $E(m)$ and F, a 2D2C time-resolved LII (2D2C-TiRe-LII) system is developed and tested on a standard ethylene laminar diffusion flame. The local laser intensity profiles are corrected by a shot-to-shot laser sheet measurement, so that no approximation is necessary.

4.2 TiRe-LII model

4.2.1 Energy and mass balance of LII

The energy balance model for LII originally formulated by Melton [85] and refined by a number of researchers over the years [164] includes heat addition by the laser pulse and various cooling terms in the general form:

$$\frac{\mathrm{d}U_{\mathrm{in}}}{\mathrm{d}t} = \dot{Q}_{\mathrm{a}} - \dot{Q}_{\mathrm{s}} - \dot{Q}_{\mathrm{c}} - \dot{Q}_{\mathrm{r}} \tag{4.1}$$

where U_{in}, $\dot{Q}_{\mathrm{a}}$, $\dot{Q}_{\mathrm{s}}$, $\dot{Q}_{\mathrm{c}}$ and $\dot{Q}_{\mathrm{r}}$ represent, respectively, the internal energy, the laser energy absorption rate, the sublimation rate of carbonaceous materials, the rate of heat loss via thermal conduction and the rate of heat loss via thermal radiation. The rate of change in internal energy of a spherical primary particle can be expressed as:

$$\frac{\mathrm{d}U_{\mathrm{in}}}{\mathrm{d}t} = \rho_{\mathrm{s}} c_{\mathrm{s}} \frac{\pi}{6} D^3 \frac{\mathrm{d}T}{\mathrm{d}t} \tag{4.2}$$

where

$$c_s(T) = 1878 + 0.1082\,T - \frac{1.5149 \times 10^2}{T^2} (\mathrm{Jkg^{-1}K^{-1}}) \tag{4.3}$$

The value of density ρ_{s} comes from Michelsen's study [166], which is widely used, with all units in SI and temperature in K. [44, 52, 67, 162, 167]:

$$\rho_s(T) = 2303.1 - 7.3106 \times 10^{-5} T (\mathrm{kgm^{-3}}) \tag{4.4}$$

In the present study, the absorption term $\dot{Q}_{\mathrm{a}}$ is calculated by determining the particle temperature, which can be eliminated with the two-colour technique.

Moreover, below pressure of 1 bar, the radiation heat loss $\dot{Q}_{\mathrm{r}}$ is negligible [164]. Thus, in Eq. (4.1), only $\dot{Q}_{\mathrm{s}}$ and $\dot{Q}_{\mathrm{c}}$ are considered as contributing to the internal energy change of soot particles.

4.2.2 Sublimation

Sublimation is an endothermic phase transition process. Heat loss by sublimation is described by:

$$\dot{Q}_{\mathrm{s}} = -\frac{\Delta H_{\mathrm{v}}}{W_{\mathrm{s}}}\frac{\mathrm{d}M}{\mathrm{d}t} \tag{4.5}$$

where W_s is the molecular weight of solid carbon, and ΔH_V is the enthalpy of formation of sublimed carbon clusters. Beyond the sublimation temperature, gaseous carbon clusters ranging from C1 to C10 start to vaporise from the particle surface [166]. Nevertheless, many models assume that only C3 clusters are sublimed during laser heating [68, 96, 168]. In the present study, for simplicity, we assume the C3 is the only species, which evaporates from the surface of soot particles. The value of ΔH_V for C3 species 7.78×10^5 J/mol, is taken from Melton's data [85].

The term $\mathrm{d}M/\mathrm{d}t$ in Eq. (4.5) is determined by the product of the surface area of soot particles πD^2, the velocity of species C3 evaporating from the surface of the soot particles U_v, and the density of gaseous C3 vapour ρ_v. Maxwellian velocity distribution is applied in the estimation of U_v [164], thus, we have:

$$\frac{\mathrm{d}M}{\mathrm{d}t} = -\pi D^2 \rho_v U_v = -\frac{\pi D^2 W_{\mathrm{v}} \alpha_M P_{\mathrm{v}}}{R_{\mathrm{g}} T}\left(\frac{R_{\mathrm{g}} T}{\pi W_{\mathrm{v}}}\right)^{\frac{1}{2}} \tag{4.6}$$

where α_M is the mass accommodation coefficient, which is taken as 1.00 in the present study [85, 93]; R_{g} is the universal gas constant; W_{v} is the molecule weight of C3, which is 36.033 in the present study; and P_{v} is the partial pressure of sublimed carbon clusters C3, and is given by the Clausius-Clapeyron equation:

$$P_v = P_{\mathrm{ref}} \exp\left[-\frac{\Delta H_v}{R}\left(\frac{1}{T} - \frac{1}{T_{\mathrm{ref}}}\right)\right] \tag{4.7}$$

where P_{ref} is 1 atm and T_{ref} is 3915 K from fits to data by Leider *et al.* [169].

4.2.3 Conduction

Conductive cooling occurs due to the interactions between the particle surface and the surrounding gas molecules. However, the change in the surrounding pressure or temperature may result in different heat conduction regimes. The dimensionless Knudsen number K_n is defined as the ratio of the mean free path of the gas molecules L_{MFP} and the diameter of soot particles D. Liu *et al.* [170] suggested that when $1 < K_n < 10$ (which is the case in the present study), the heat conduction between a soot particle and the surrounding gas can be considered within the transition regime. Based on existing data of soot particles produced in similar flames [96], conductive cooling is assumed to occur in the transition regime and its rate can be calculated with the approach by McCoy and Cha [171]:

$$\dot{Q}_{\mathrm{c}} = \frac{2k_{\mathrm{a}}\pi D^2}{D + GL_{MFP}}(T - T_0) \tag{4.8}$$

where T_0 is the temperature of the ambient gases, k_{a} is the thermal conductivity of the surrounding gases, and L_{MFP} is the mean free path; here we use the values of Melton's model [85] $k_{\mathrm{a}} = 5.83 \times 10^7 (T_0/273)^{0.82}$ W/mK and $L_{MFP} = 2.355 \times 10^{-10} T_0$ m. The heat transfer factor G is given by:

$$G = \frac{8f}{\alpha_{\mathrm{T}}(\gamma + 1)} \tag{4.9}$$

where α_{T} is the thermal accommodation coefficient, which is taken as 0.3 in the present study [67, 166]; γ is the heat capacity ratio for air; and f is the Eucken correction to the thermal conductivity given by:

$$f = \frac{9\gamma - 5}{4} \tag{4.10}$$

4.2.4 Radiative emission and solution

Since the heat loss by radiation is several orders of magnitude lower than other terms, it can thus be neglected in the energy balance equation of soot particles (Eq. 4.1). Moreover, the model can be further simplified by omitting the absorption term by calculating the maximum surface temperature of soot particles using the data from the two-colour LII technique. The two-colour LII measurement detects the LII signal at two different wavelengths λ_1 and λ_2 (each wavelength in the visible spectrum results in a different colour). The maximum surface temperature of soot particles can be deduced by calculating the absolute signal intensity at the two wavelengths by applying Planck's law which describes the electromagnetic radiation by a black body in thermal equilibrium at a specific temperature. By combining Eqs. (4.2) to (4.10), we obtain a differential equation for the particle temperature:

$$\frac{\mathrm{d}T}{\mathrm{d}t} = -\frac{6}{\rho_s c_s \pi D^3}\left(\frac{2k_a \pi D^2}{D + GL_{\mathrm{MFP}}}(T - T_0) + \frac{\Delta H_v}{W_s}\frac{\mathrm{d}M}{\mathrm{d}t}\right) \tag{4.11}$$

The LII signal S_{LII} at a specific emission wavelength λ_{LII} is calculated according to the Planck function:

$$S_{\mathrm{LII}} = \frac{\varepsilon_{\lambda_{\mathrm{LII}}} 2\pi^2 h c^2 D^2}{\lambda^5}\left[\frac{1}{\exp\left(\frac{hc}{\lambda k_B T}\right) - 1} - \frac{1}{\exp\left(\frac{hc}{\lambda k_B T_0}\right) - 1}\right] \tag{4.12}$$

where h is the Planck constant, c is the speed of light, and k_B is the Boltzmann constant. According to Kirchhoff's law [91, 139, 140], absorptivity equates with emissivity, thus the emissivity at a certain wavelegth $\varepsilon_{\lambda_{\mathrm{LII}}}$ is assumed to be:

$$\varepsilon_{\lambda_{\mathrm{LII}}} = \frac{4\pi D E(m)}{\lambda_{\mathrm{LII}}} \tag{4.13}$$

On substituting (4.13) into Eq. (4.12), we obtain:

$$S_{\mathrm{LII}} = \frac{8\pi^3 hc^2 E(m) D^3}{\lambda^6} \left[\frac{1}{\exp\left(\frac{hc}{\lambda k_B T}\right) - 1} - \frac{1}{\exp\left(\frac{hc}{\lambda k_B T_0}\right) - 1} \right] \tag{4.14}$$

At the moment just after the laser pulse, $t = 0$ and all the soot particles in one probe volume are heated up and reach the same peak temperature $T_{\mathrm{p},0}$, then the cooling process starts. By substituting λ_{LII} with λ_1 and λ_2 in Eq. (4.14), the peak particle surface temperature $T_{\mathrm{p},0}$ at $t = 0$ can be calculated by:

$$T_{p,0} = \frac{hc}{k_B} \left(\frac{1}{\lambda_2} - \frac{1}{\lambda_1} \right) \left[\ln \left(\frac{I_1}{I_2} \frac{\lambda_1^6}{\lambda_2^6} \right) \right]^{-1} \tag{4.15}$$

where I_1 and I_2 are the absolute LII signal intensities of soot particles at two wavelengths λ_1 and λ_2, respectively, when $t = 0$. Once the peak temperature of the soot particle is obtained using Eq. (4.15), the differential equation Eq. (5.1) can be solved numerically with the initial condition $T = T_{\mathrm{p},0}$.

4.2.5 Experimental particle sizing with TiRe-LII

In practice, a possible distribution of particle size should be assumed in advance in order to reconstruct the size distribution from the time-resolved LII signal [68]. For a certain particle diameter distribution PDF(D), assuming that the particle number concentration N is constant in the probe volume V_{m} during a single LII event, an integration considering the particle size distribution function PDF(D) yields the total LII signal $J_{\mathrm{LII}}(t)$ at the detector surface:

$$J_{\mathrm{LII}}(t) = C_{\mathrm{det}} N V_{\mathrm{m}} \int_0^\infty \mathrm{PDF}(D) S_{\mathrm{LII}}(t) \mathrm{d}D \tag{4.16}$$

where C_{det} is a constant of the detection system. According to previous research [1, 93, 172], the soot particle size follows a lognormal probability density function,

which can be expressed as:

$$\mathrm{PDF}(D) = \frac{1}{\sqrt{2\pi}D\sigma} \exp\left[-\left(\frac{\ln D - \ln D_\mathrm{m}}{\sqrt{2\pi}\sigma}\right)^2\right] \tag{4.17}$$

where D_m is the count median particle diameter and σ is the standard deviation. The agreement between model and experiment is indicated with the maximum likelihood estimator [162]:

$$\chi^2 = \sum_{i=1}^{N}\left[\frac{J_\mathrm{exp}(t_i) - J_\mathrm{cal}(t_i, D_\mathrm{m}, \sigma)}{\sigma_\mathrm{exp}}\right]^2 \tag{4.18}$$

where $J_\mathrm{exp}(t_i)$ is the experimentally measured temporal LII signal, $J_\mathrm{cal}(t_i, D_\mathrm{m}, \sigma)$ is the model prediction for the fit parameters D_m and σ, N is the number of experimental data points, σ_exp is the experimental standard deviation, and i represents the time steps the of experiment, and accordingly the calculation is based on the temporal resolution of the decay curves. By minimising the value of Eq. (4.18), the lognormal distribution parameters D_m and σ can be fitted.

4.3 Simulation results of the model

A series of calculations were performed with the model and the results are shown in the following sections.

4.3.1 The temperature and LII signal response of a given distribution

A given soot particle distribution D_m = 20 nm and σ = 0.4 is excited with a 532 nm laser pulse. The temporal profile of the laser pulse is assumed to obey a Gaussian distribution with FWHM = 5 ns, which is the same as the laser used in the present study. The mean laser energy fluence is equal to 0.05 J/cm^2. The initial temperature of the particles is set to 1800 K, which is close to

the temperature in the flame. The temporal response of the temperature and LII signal is calculated with the model described in Section 4.2. In the calculation, the absorption function of a soot particle at 532 nm is assumed to be $E(m) = 0.26$, which is the same as the value we used for the extinction measurement. The results of the calculation are shown in Fig. 4.1.

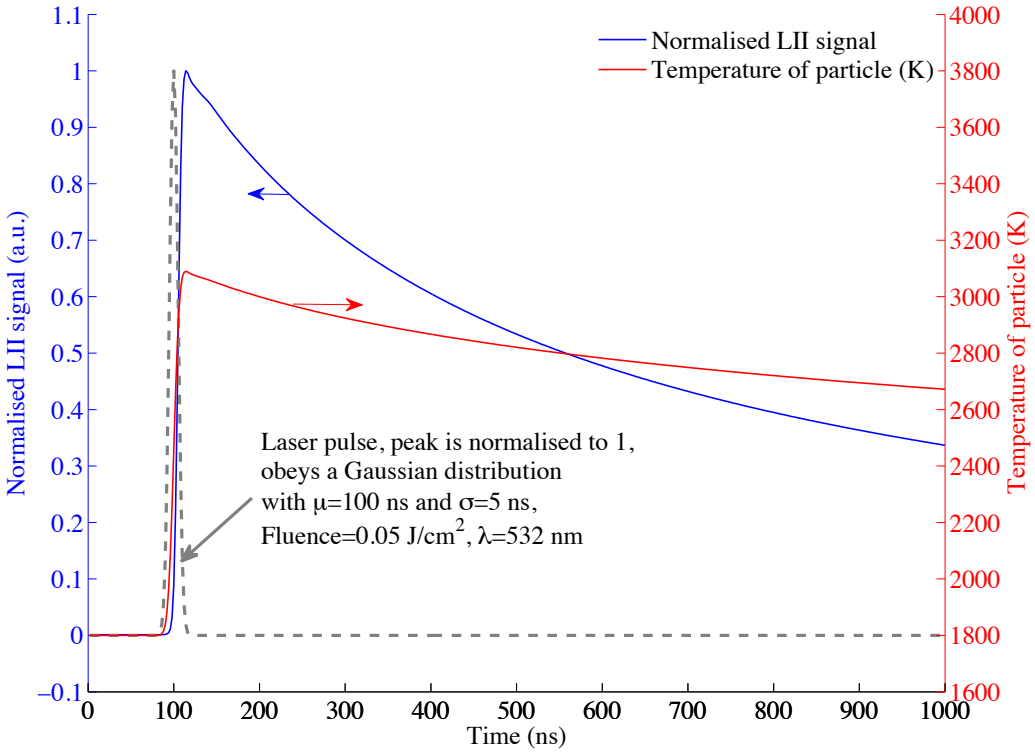

Fig. 4.1 The calculated temperature (red line) and LII (blue line) response of a given soot particle distribution $D_{\mathrm{m}} = 20$ nm and $\sigma = 0.4$ with laser (dashed line) fluence equal to 0.05 J/cm^2

Figure 4.1 shows that both the temperature and LII signal increase rapidly with the arrival of the laser pulse due to the absorption of laser energy. As soon as the laser pulse disappears, the soot particles reach the peak temperature, which is around 3000 K. The maximum temperature is very close to the calculated peak temperature by Michelsen *et al.*'s model [173] using the same laser fluence. Then, the temperature starts to decay due to surface heat conduction, sublimation and radiation. The decay of the LII signal is steeper than the temperature decay,

because the LII radiation intensity is proportional to the fourth power of the temperature [68].

4.3.2 LII signal response of various distributions

The LII signal of different soot particle size distributions (shown in Fig. 4.2) was examined using the model, and each group is assumed to obey a lognormal distribution with a different geometry mean diameter from 10 nm to 60 nm and identical variance σ. The results are shown in Fig. 4.3. It is shown that the modelled LII signal decay of larger particles is slower than for small particles. This trend is qualitatively in accordance with the LII theory.

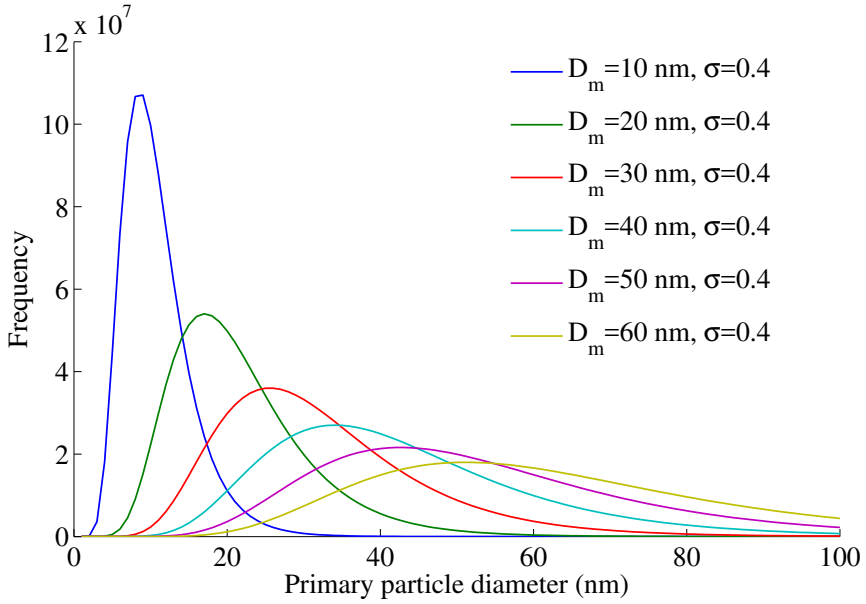

Fig. 4.2 Soot size distribution with D_{m} from 10 nm to 60 nm and $\sigma = 0.2$.

In Fig. 4.4, the variance σ ranges from 0.2 to 1.2. The results shown in Fig. 4.5 indicate that the wider distributed particles have a longer decay time due to the larger number of bigger particles.

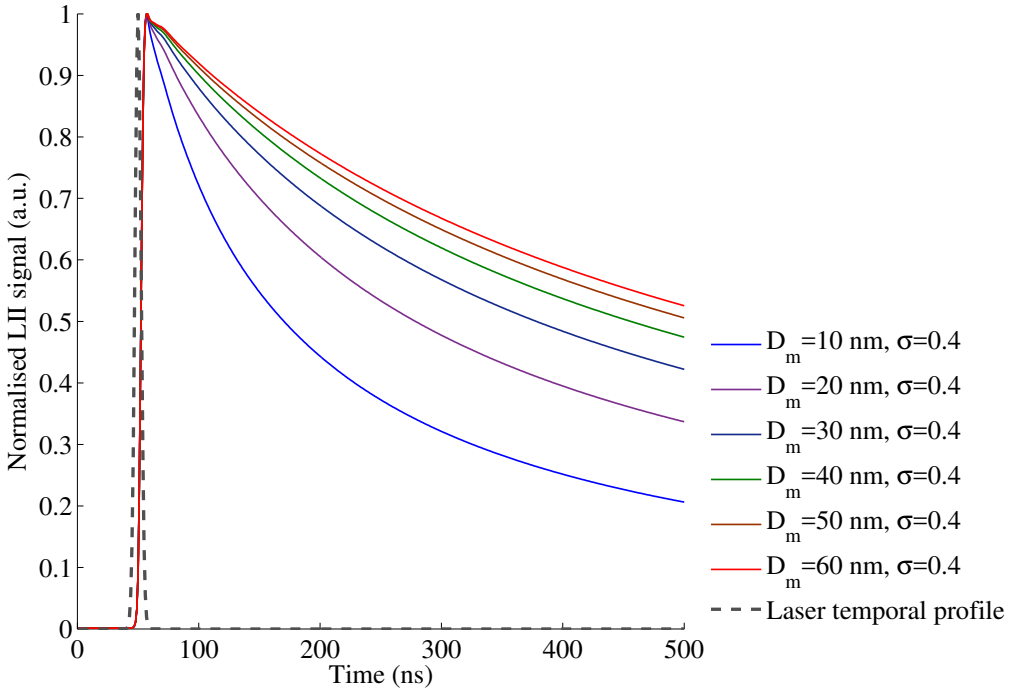

Fig. 4.3 LII response of different soot distributions with laser fluence equal to 0.05 J/cm^2.

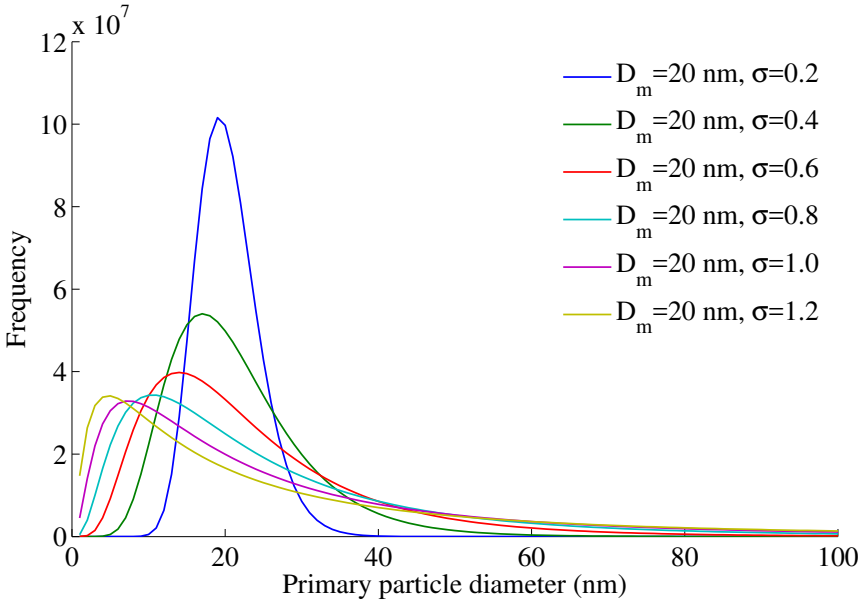

Fig. 4.4 Soot size distribution with $D_{\mathrm{m}} = 20$ nm and σ from 0.2 to 1.2.

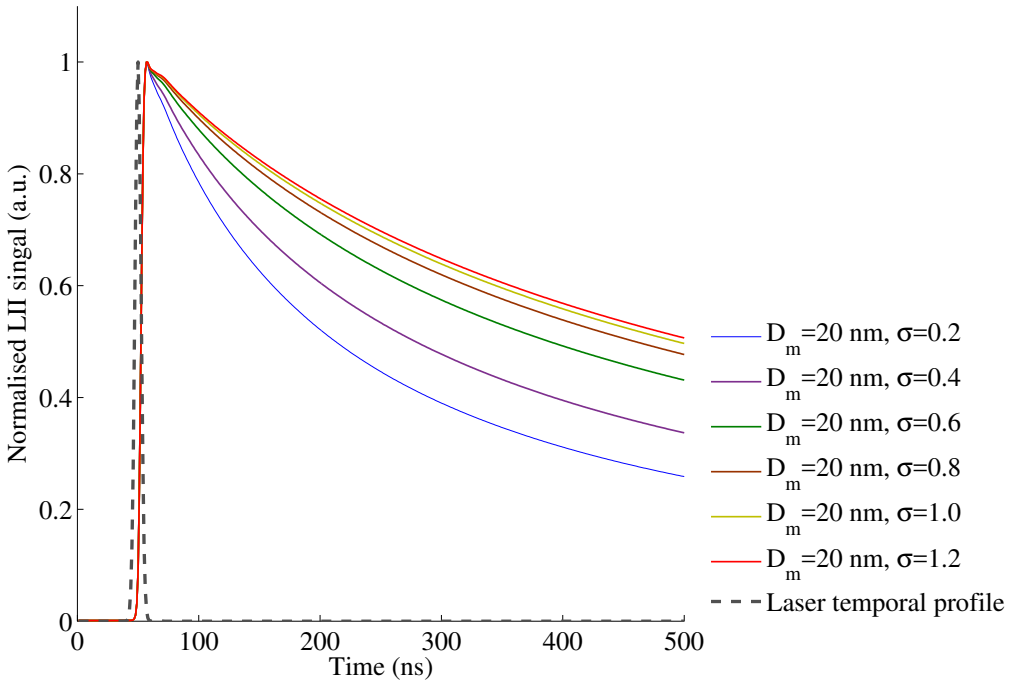

Fig. 4.5 LII response of different soot distributions with laser fluence equal to 0.05 J/cm^2.

4.3.3 The LII signal response of different laser energies

The influence of laser fluence is shown in Fig. 4.6 for two different laser fluences (0.05 J/cm^2 and 0.5 J/cm^2) for soot particles with D_m = 20 nm and σ = 0.4. For a higher laser energy is applied, the normalised LII signal drops dramatically during and after the laser pulse. This may be due to significant sublimation, since the laser fluence 0.5 J/cm^2 is far beyond the sublimation limit at 532 nm, which is smaller than 0.2 J/cm^2 [68].

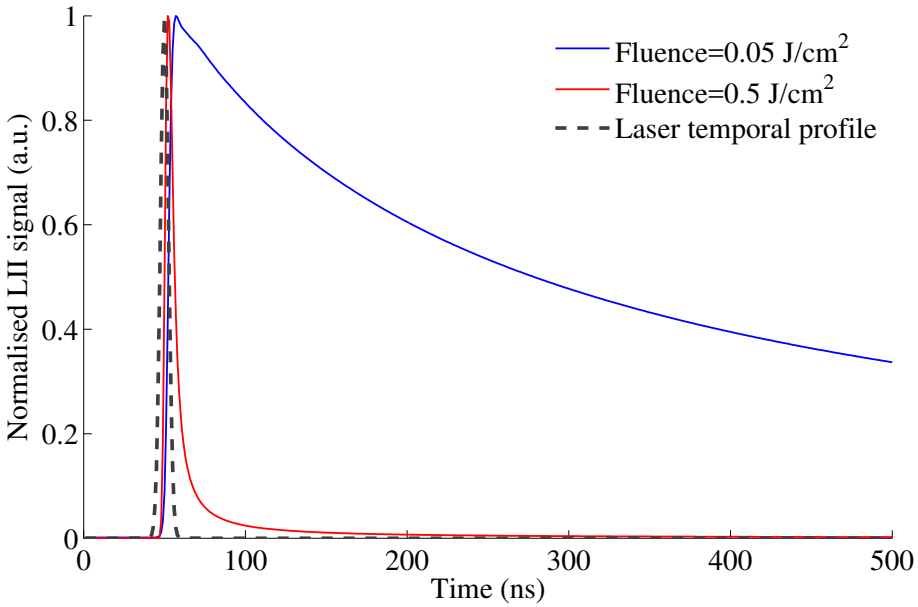

Fig. 4.6 LII response of soot particles (D_m = 20 nm and σ = 0.4) under different laser fluences of 0.05 J/cm^2 (blue line) and 0.5 J/cm^2 (red line)

4.3.4 Energy fraction breakdown

In order to understand how the energy provided by the laser is partitioned, a simulation is performed using laser fluence F = 0.17 J/cm^2 and 30 nm diameter particles. The power associated with absorption, conduction, sublimation and radiation are shown in Fig. 4.7 (top). We can see that conduction is dominant in the cooling process. Radiation is lower than conduction by two to three orders

of magnitude, thus, it is neglected in the present study.

The change of the diameter due to sublimation is also estimated. As shown in Fig. 4.7 (bottom), the diameter reduction is less than 3%, which is small and negligible in the present study.

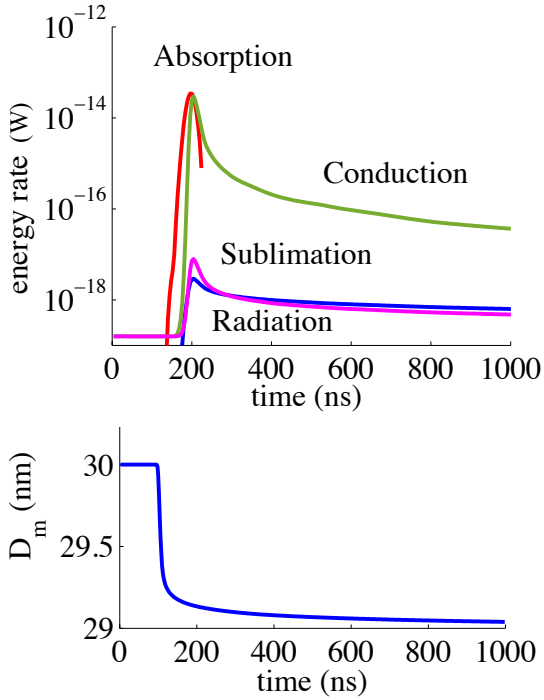

Fig. 4.7 Calculated energy rates of absorption, conduction, sublimation and radiation of a single particle ($F = 0.17$ J/cm^2, $\lambda = 532$ nm, $D = 30$ nm, $T_0 = 1800$ K).

4.4 Experiment

4.4.1 LII setup

The 2D two-colour LII measurement system comprising a Nd:YAG laser (Litron nanoPIV) at 532 nm with a pulsed duration of 8-10 ns and optical components is shown in Fig.4.8. In order to form a parallel, thin sheet with a top-hat spatial profile, a series of cylindrical lenses (Thorlabs, focal lengths of 75, 25 and 100 mm) and a slot were used to expand the collimated laser beam from the Nd:YAG

laser (see Fig. 4.8). The signal detection system consisted of two cameras: an ICCD camera (Lavision Nanostar) equipped a Nikon AF Micro Nikkor 60 mm lens 175 (f/2.8), and a CCD camera (Lavision Pro X 4M) with an intensifier (Lavision IRO9) and with a Nikon AF Micro Nikkor 60 mm lens (f/5.6). In order to detect the LII signal at two different wavelengths, a 400 nm narrow band (NB) filter (Thorlabs FB400-10, central wavelength = 400 ± 2 nm, FWHM = 10 ± 2 nm) and a 450 nm NB filter (Thorlabs FB450-10, central wavelength = 450 ± 2 nm, FWHM = 10 ± 2 nm) were installed in front of the objectives on the ICCDs.

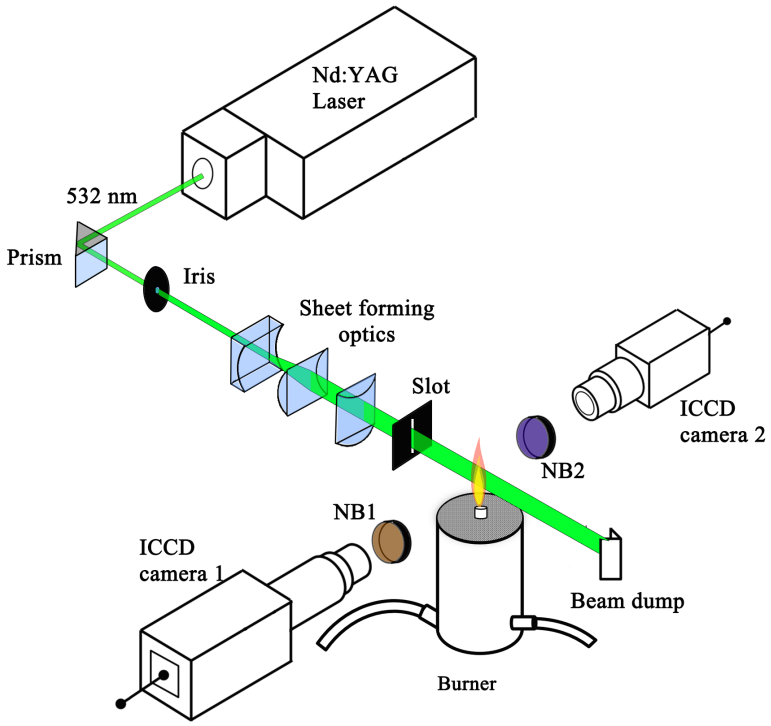

Fig. 4.8 Schematic of 2D-2C-TiRe-LII measurement set-up (B1: 400 ± 5 nm band filter; NB2: 450 ± 5 nm band filter).

To minimise uncertainties, a top-hat profile of the laser sheet was carefully calibrated using the method described in Chapter 2. The intensity profile of the laser sheet was obtained by using the laser sheet to excite the fluorescent dye (Rhodamine 6G in ethanol solvent) in a cuvette placed on top of the burner's central tube. Figure 4.9 shows the normalised laser intensity profile averaged over 500 images in which the intensity variance is represented by the thickness of

the shaded region in green. According to the results, the fluctuation of the local intensity was no higher than 2.5% of the averaged intensity.

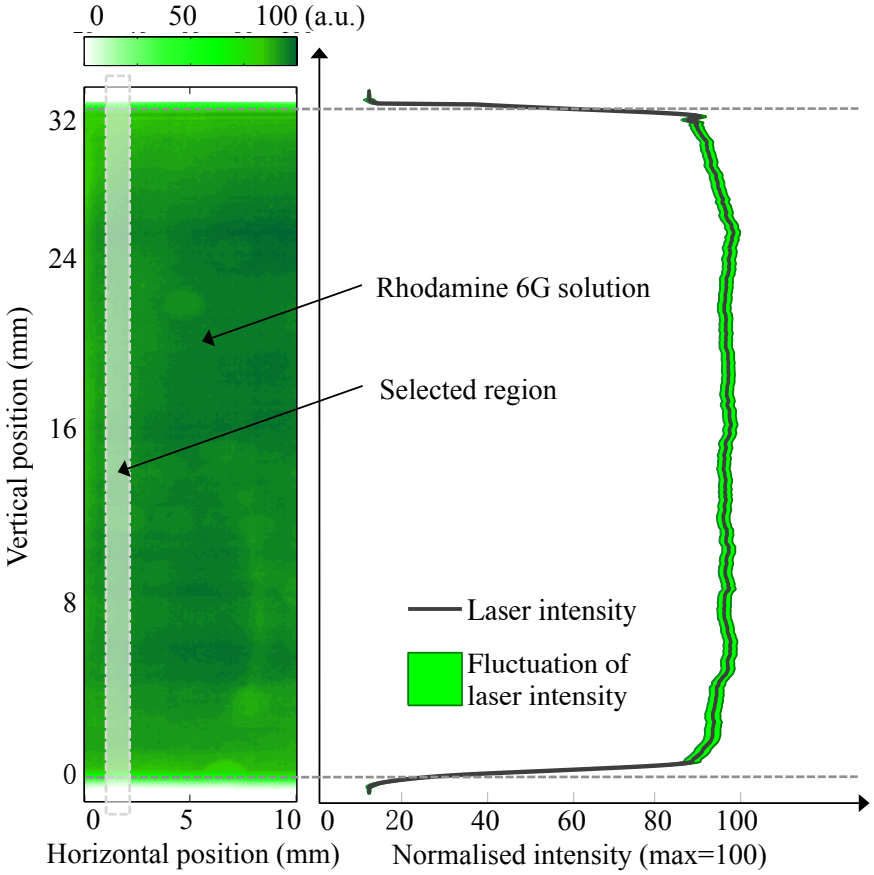

Fig. 4.9 Normalised intensity profile of the laser sheet for the LII measurement. Left: Rhodamine 6G fluorescence excited by the laser sheet; right: profile of the integrated fluorescent signal intensity over the region shown in the selection rectangle.

A laser fluence of 0.17 J/cm^2 is used for LII signal excitation to optimise the signal-to-noise ratio and avoid significant sublimation. Background images are collected 20 ns before the laser pulse reaches the flame, for the minimum possible gate interval of 20 ns. A total of 50 LII images are recorded between times $t = -20$ ns to $t = 2060$ ns. The results are averaged over 200 images, with the flame luminosity background subtracted. The maximum signal-to-noise ratio (peak signal counts to dark signal counts) is around 300. The spatial resolution in the diameter analysis corresponds to 0.1 $\times$ 0.1 mm^2, with a laser sheet thickness

of 0.3 mm. The value of C_1/C_2 was obtained using a tungsten lamp (Thorlabs QTH10B) and the details of the calibration are shown in the following sections. LII signals from this flame have also been used to determine f_v after calibration using extinction measurements, as described by Tian *et al.* in [12]. The resulting measurements are quoted further on in the discussion.

The ethylene flame case B described in Chapter 2 is tested with the 2D2C-TiRe-LII system. The fuel flow is 0.22 slpm and air flow is 38.2 slpm.

4.4.2 Quantitative calibration of cameras

As shown in Eq. (4.15), the ratio of absolute intensity of the LII signal at two wavelengths I_1/I_2 needs to be obtained to calculate the peak temperature of a soot particle. Here we assume the linear collection coefficients of the filter+ICCD set-up are C_1 and C_2 for cameras 1 and 2, respectively, thus, the signal detected by cameras 1 and 2, which are denoted with S_1 and S_2, can be expressed with the product of the absolute signal and the collection coefficient:

$$\begin{aligned} S_1 &= C_1 I_1 \\ S_2 &= C_2 I_2 \end{aligned} \tag{4.19}$$

hence, we have:

$$\frac{I_1}{I_2} = \frac{C_2}{C_1}\frac{S_1}{S_2} \tag{4.20}$$

The value of C_1/C_2 can be measured by following the calibration procedure:

a) Choose a light source with a known emission spectrum, such as a tungsten lamp, which has a very wide emission spectrum. The spectrum of the lamp can be expressed as a function of the wavelength $L(\lambda)$, thus we have:

$$\frac{I_1}{I_2} = \frac{\int_{\lambda_{1-}}^{\lambda_{1+}} L(\lambda)d\lambda}{\int_{\lambda_{2-}}^{\lambda_{2+}} L(\lambda)d\lambda} \tag{4.21}$$

where $\lambda_{i\pm}$ are the collection upper/lower limit of the NB-filter.

b) Mount the NB filters (400 nm, 450 nm) on the two ICCD cameras, and set the camera with the same parameters to be used for soot measurement. Take two images of the lamp simultaneously with the two ICCDs to obtain two images of the lamp at two wavelengths.

c) Calculate the value and the ratio of the mean intensity of the region of the lamp on the two images, S_1 and S_2, directly from the images to obtain:

$$\frac{C_1}{C_2} = \frac{I_2}{I_1}\frac{S_1}{S_2} \tag{4.22}$$

In the measurements of soot, we can apply the value of C_1/C_2 in Eq. 4.20 to obtain the value of I_1/I_2. This procedure is based on the correct assumption that the response of the ICCD to light intensity is linear. However, the response of the ICCD on the gain value is highly non-linear, thus we need to choose a suitable gain value, which will remain unchanged, to conduct both the calibration and measurements.

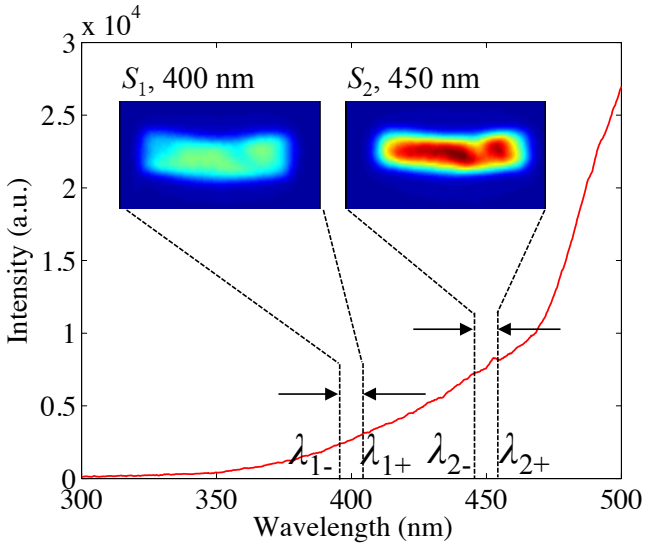

Fig. 4.10 Tested spectrum of the tungsten lamp (red line), and the measured luminosity of the lamp at two different wavelengths (two colour maps).

4.4.3 Flame temperature

In order to account for the TiRe-LII signal so as to extract the information for the particle size distribution, a knowledge of the local gas temperature distribution is essential. Figure 4.11 (left) shows the spatial temperature distribution as a function of the height above burner (HAB) and the flame radius calculated from the diffusion flame model described in Chapter 3. According to the colour map, the peak temperature region around 2250 K can be found to appear in a thin shell from where the combustion occurs. The heat generated from this zone dissipates in both radial and axial directions, which leads to the formation of a thick high-temperature zone. The temperature gradients within this region are small compared with elsewhere, while sharp temperature gradients can be seen from the flame bottom where the cool fuel stream encounters hot combustion products.

The ethylene flame data from the current model was compared with the published flame data measured by Santoro *et al.* [9] as shown in Fig. 4.11 (right). Their measurements were carried out on a similar laminar flame burner consisting of two concentric brass tubes of 11.1 mm (inner) and 101.6 mm (outer), respectively. The calculation is conducted with the same parameters used by Santoro *et al.*. The ethylene flow has a velocity of 3.98 cm/s (3.85 cc/s) while the air co-flow has a velocity of 8.66 cm/s (694 cc/s). According to the comparison shown in Fig. 4.11 (right), the modelling results are generally in good agreement with the published experimental data, although a noticeable deviation is found at HAB = 20 mm, near the rim of the central tube, where the deviation grows to 20%. Nevertheless, this model still provides a good estimate of local flame temperatures.

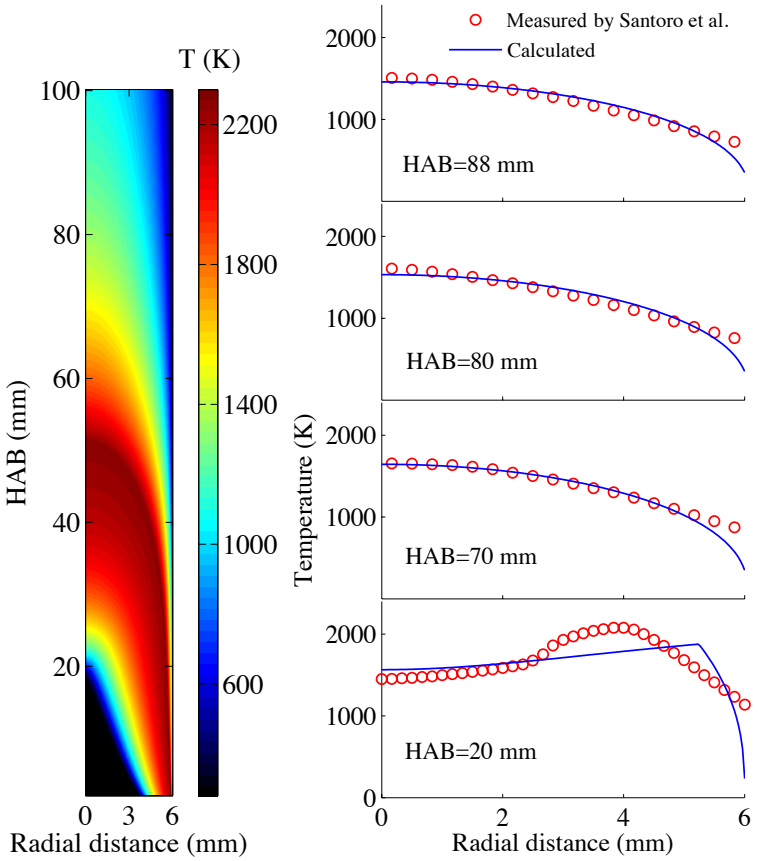

Fig. 4.11 Diffusion flame modelling and validation results. Left: temperature distribution as a function of HAB and radial distance of the ethylene flame. Right: validation of the diffusion flame model against data from Santoro *et al.* (the Santoro file C2H4NS-T [9]).

4.5 Results and discussion

The temporal profile of the LII signal from the middle of the diffusion flame (33 mm-66 mm) is shown in Figs. 4.12 and 4.13. It should be noted that the signal intensities shown in the figures are relative intensities which have not yet been calibrated. The calibration procedure of the cameras is described in Section 4.4.2, and the calibrated signal intensities were then used to calculate the peak surface temperature of the soot particles using Eq. (4.15). Similar to our previous study on the same ethylene diffusion flames, the soot concentration is reflected by the relative LII signal intensity peaks in the annular region at intermediate HABs adjacent to the central area of the flame. This is due to the higher temperatures close to the flame front that contribute to fuel pyrolysis and soot formation. At a specific HAB for both wavelengths, the LII signal intensity first increases with increasing radius up to a region where the maximum soot intensity is reached before sharply diminishing as the radius approaches the flame boundary. The heat generated due to combustion diffuses back to the central area, which creates a temperature gradient. As a result, unburned ethylene fuel decomposes into smaller hydrocarbon fragments, mostly PAHs, due to the ever-increasing temperature in the radial direction. These PAHs are the precursors to soot, which have strong high-temperature resistance. Moreover, the rate of formation of these nascent PAHs are highly kinetically controlled [1], which leads to a rapid formation of primary particles and subsequent soot agglomeration at higher temperatures. In the present study, soot agglomerates were assumed to have similar structures in which primary particles are loosely in point contact. Therefore, the measurement of LII signals at a certain spatial location directly reflects the local volume fraction of soot. Moreover, the shielding effect on heat conduction of soot aggregates due to their structure was assumed to be negligible according Liu *et al.*'s findings [137].

As shown in Figs. 4.12 and 4.13, the peak LII signals measured at 400 nm and

450 nm both appear at 20 ns rather than 0 ns, which is in accordance with Hadef *et al.*'s study [162]. This is due to the gate time limit of the cameras (minimum 20 ns) used in the study, which was insufficient to resolve the sharp and rapid increase of the LII signals (the LII signals normally reach the peak temperature within 10 ns) after the starting point of the laser pulse. From Figs. 4.12 and 4.13, one can deduce that the laser pulse reaches the flame between 0 ns and 20 ns. Within this period of time, soot particles were heated by the laser and their temperatures increase dramatically. However, although the laser pulse is as short as 8-10 ns, the residual laser energy may still affect the decay process. Since the two-colour LII method in the present study makes it possible to calculate the peak temperature of soot particles without using the absorption term, the data measured at 0 ns was not included in the data interpretation. Moreover, abnormal cooling processes usually take place during the initial period of time (tens of nanoseconds from the starting point of laser excitation) [49], and one should avoid using the data collected during this period of time to fit the LII model. The reason for the abnormal cooling is still unclear [25]. As a result, the starting point used to fit the model in the present study was chosen to be 20 ns i.e. the integrated LII signals from 20 ns to 40 ns. As the time span for soot particle cooling is normally several hundreds to several thousands of nanoseconds, and the peak temperature for all particles is assumed to be the same, the temperature difference of particles with various sizes at 40 ns is ignored in the present study, and the peak temperature for all soot particles after the laser pulse is calculated with the two-colour LII signals is also between 20-40 ns.

In order to evaluate the particle size distribution over the 2D diffusion flame, a square mesh grid (0.1 mm $\times$ 0.1 mm) was used. Hence, the temporal evolution of the LII signal averaged over all pixels constituting the standard square unit can be determined. In the present work, two locations were chosen to evaluate the primary particle size: A and B. Location A was chosen at HAB = 38 mm and r = 2.2 mm where the maximum soot volume fraction appeared, while location B was

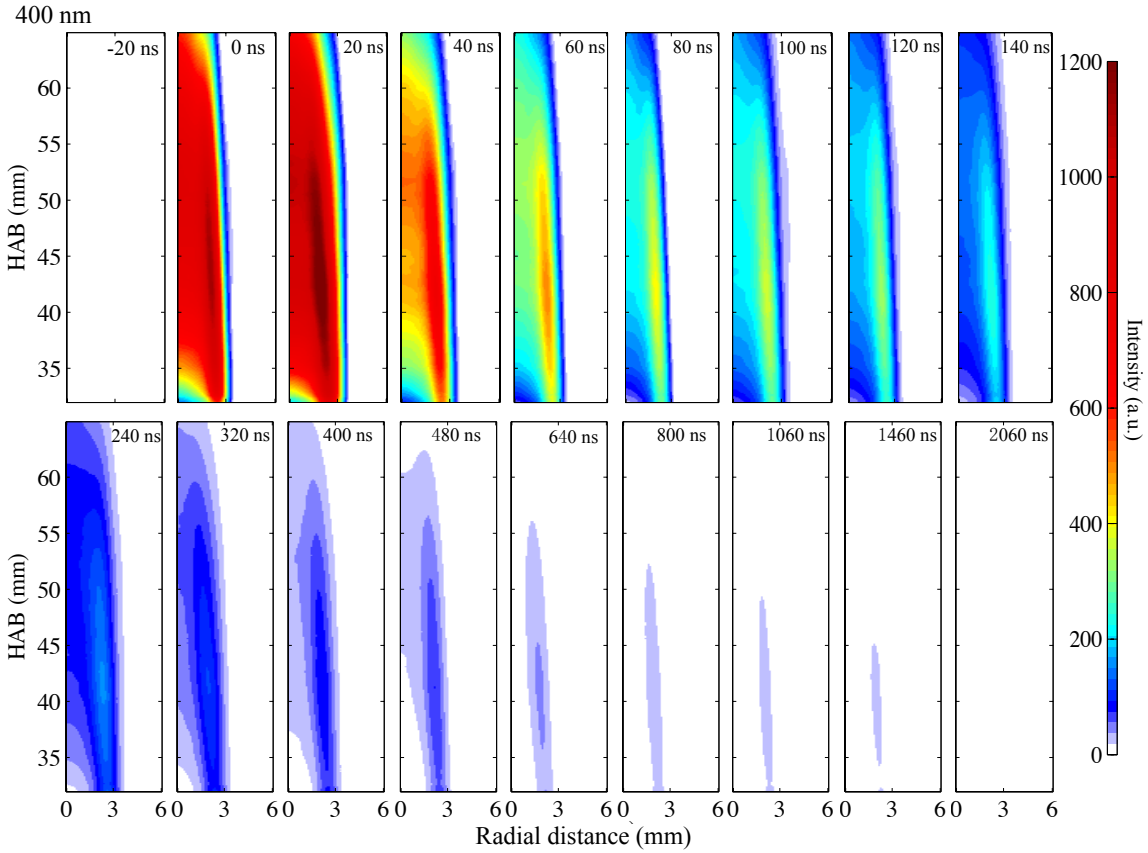

Fig. 4.12 Temporal evolution of the LII signal at 400 nm

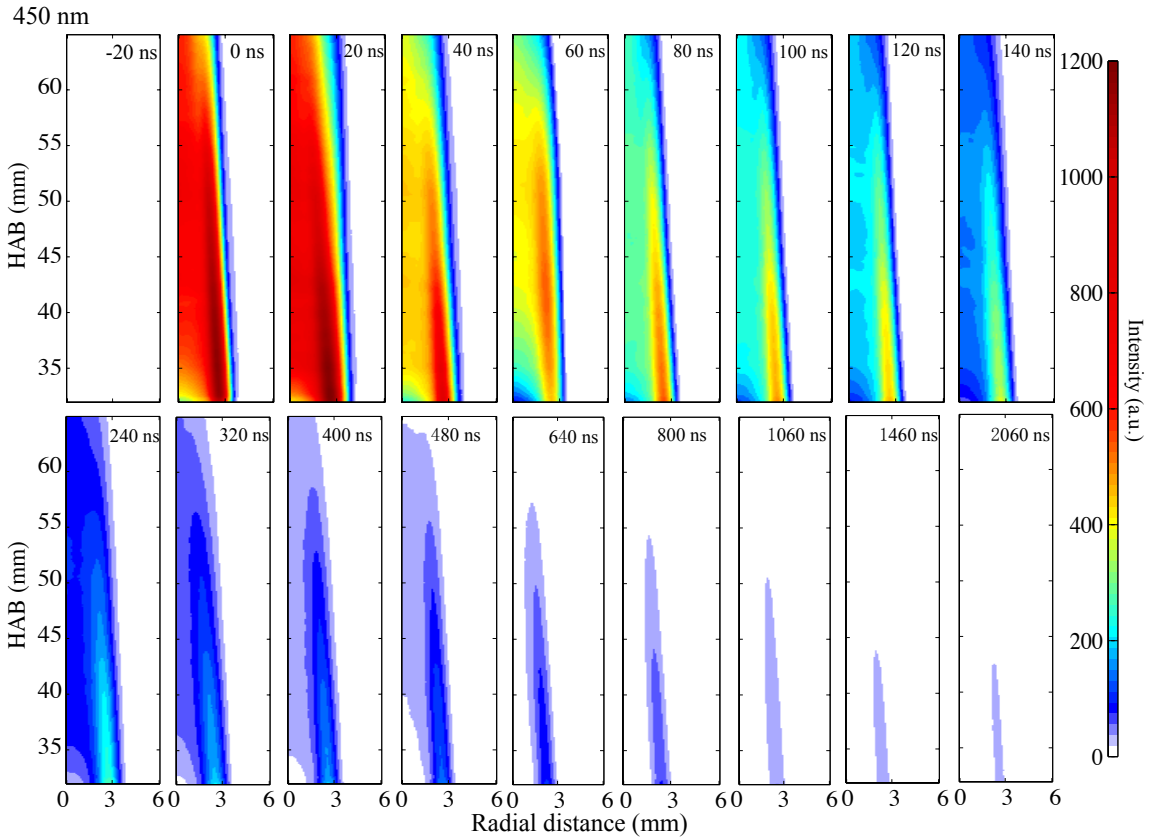

Fig. 4.13 Temporal evolution of the LII signal at 450 nm

chosen at HAB = 42 mm and r = 0 mm for the reason that this is one of the well characterised standard locations for this flame [162]. The minimum error fit was performed from 20 ns to 1060 ns for both locations A and B at the wavelength of 400 nm. The fit was based on the assumption that the diameter distribution of soot particles at each probe volume obeys a lognormal distribution as discussed in section 4.4.1. Thus, the particle size at each location can be described by a pair of parameters D_{m} and σ. The two-parameter fit was conducted by minimising the χ^2-value. At the locations A and B, the estimation of σ covered the whole range from 0.01 to 1, with a 0.01 step, while for D_{m}, the range for location A was chosen from 0 to 50 nm with a 1 nm step, and from 0 to 200 nm with a 2 nm step for location B. The range selection for D_{m} at the different locations was based on previous studies [1, 49, 162, 174].

Figure 4.14 shows the results of the 2D data fitting for locations A and B. According to these false colour maps of the χ^2-distribution over the whole σ range, each pixel represents the level of data fitting (χ^2 values) with a value indicated by the colour bar. A minimising 'valley' of χ^2 can be observed in each map, which is indicated with dashed white line.

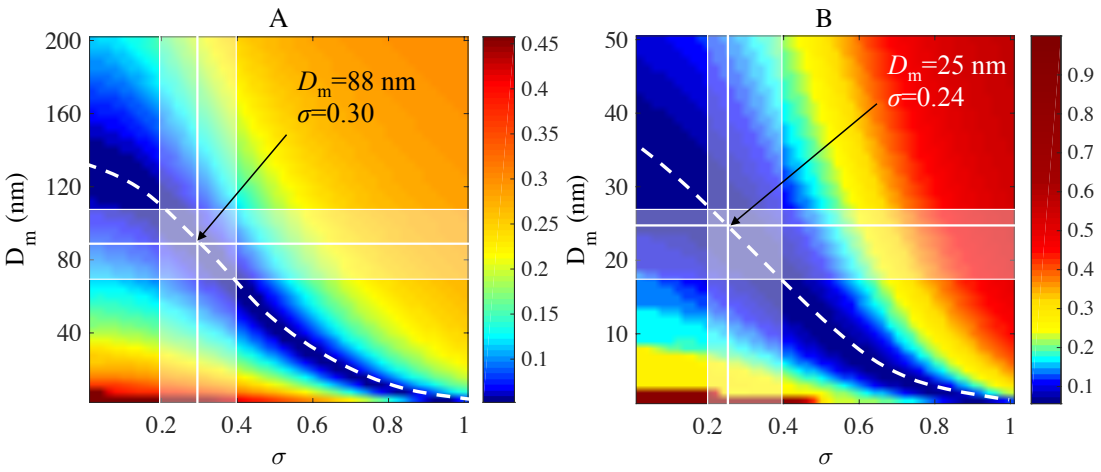

Fig. 4.14 Colour maps of the maximum likelihood estimators χ^2 value as a function of the distribution width σ, and the median diameter D_{m} for location A: HAB = 38 mm and r = 2.2 mm and B: HAB = 42 mm and r = 0 mm. The best fit value is shown in each figure.

Unique mathematical minimum χ^2-values as a function of D_m and σ are found along each 'valley', which are ($D_\mathrm{m} = 88$ nm, $\sigma = 0.30$) for location A and ($D_\mathrm{m} = 25$ nm, $\sigma = 0.24$) for location B. This shows that the best fit is thus determined. However, it should be noted that all of the values of χ^2 are very close and the corresponding pairs of (D_m, σ) can give almost idential reconstructed LII decay curve, as show in the Fig. 4.15. Here we selected some (D_m, σ) pairs (including two most extreme cases $\sigma = 0.2$ and $\sigma = 0.4$) in the 'valley' to reconstruct the LII signal decay and the curves are indistinguishable.

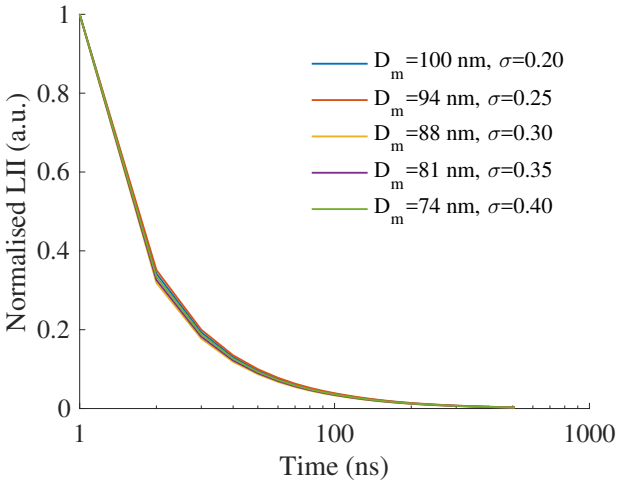

Fig. 4.15 Reconstructed LII signal with selected (D_m, σ) pairs in the 'valley' of minimising values.

This is because all of the solutions of (D_m, σ) in the 'valley' share a narrow distribution of Sauter mean diameters D_{32} [175, 176], which is defined as:

$$D_{32} = \frac{\int_0^\infty D^3 P(D) \mathrm{d}D}{\int_0^\infty D^2 P(D) \mathrm{d}D} = D_\mathrm{m} e^{\left[\frac{5}{2}\sigma^2\right]} \tag{4.23}$$

The value of D_{32} is the key parameter required to determine the decay curve of the LII signal. The value of χ^2 along the valley in location A is shown in both 3D and 2D plots in Fig. 4.16. In this case, all of the values of (D_m, σ) along the

'valley' should be considered as potential solutions for particle sizing besides the best fit value, since the values of D_{32} are close to the best fit values.

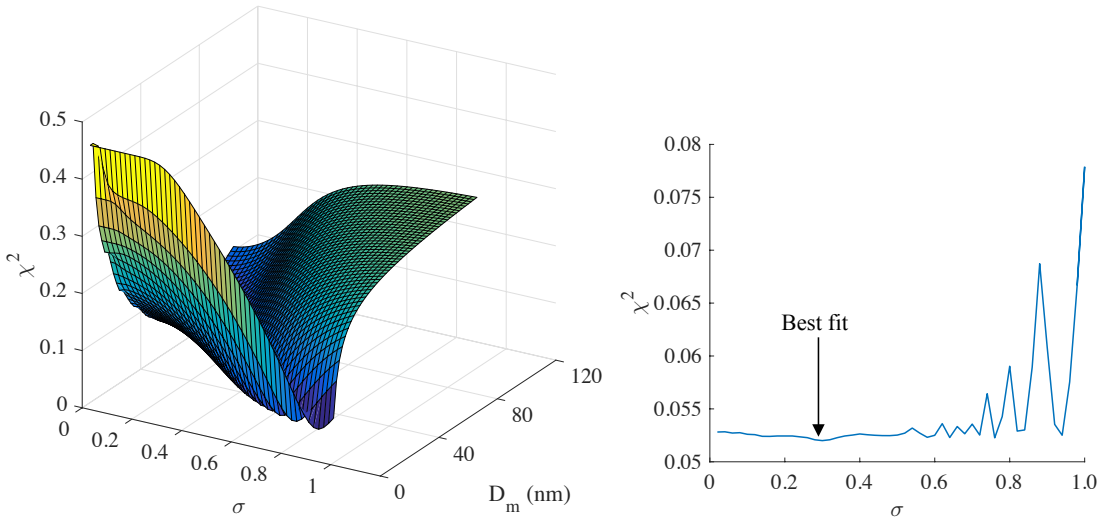

Fig. 4.16 Left: 3D plot of χ^2 for location A; right: value of the minimised χ^2 along the 'valley'.

To obtain a well-difined range of solutions amongst the potential solutions besides the best fit value, Liu *et al.* developed an approach to estimate the particle size distribution based on the decay of the effective temperature. They identified that the initial temperature decay rate of a soot particle ensemble at the moment of the $T_{p,0}$ is inversely proportional to D_{32} for the poly-disperse primary soot particles. The value of σ can then be determined from the decay at later points in time [25, 176].

However, this approach is not suitable to the present study because the SNR is low at the late points in time along the decay, so the effetive temperature cannot be accurately estimated. An alternative method for narrowing down the range of solutions is to use a sensible range of σ to confine the range of D_m, since the distribution of flame-generated soot particle size is quite narrow and the value of σ is typically within the range of 0.2 to 0.4 [25, 177, 178]. Thus, the range of D_m can be determined along the 'valley' correspondingly. The estimated best fit value and range of potential solutions at locations A and B are shown in Table

Table 4.1 Best fit value and range of D_m and σ at locations A and B

Locations	Best fit	Range of Dm (nm)	Range of sigma
A	Dm=88 nm, sigma=0.30	74-100	0.20-0.40
B	Dm=24 nm, sigma=0.24	18-26	0.20-0.40

4.1 and Fig. 4.14.

In Fig. 4.17, the variations of LII signal versus time for the two locations are plotted. The discrete points are measurement results ranging from 40 ns to 1080 ns after initiating the laser pulse. As discussed at the beginning of this chapter, the laser pulse lasts only 8-10 ns, therefore choosing a 40 ns delay as the starting point for the data fitting allows us to apply the simplified LII model as the laser absorption is absent. As a result, the best-fit curves against the experimental data for the two locations are plotted based on the optimal χ^2 value shown in Fig. 4.14.

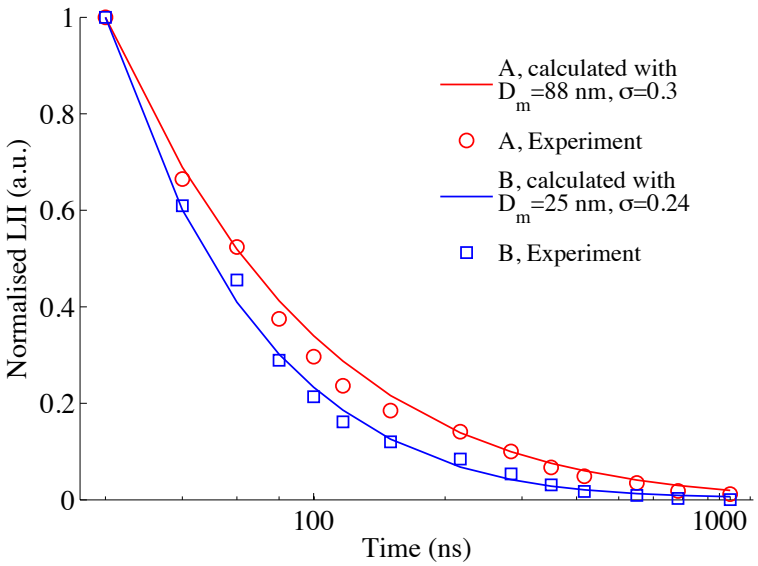

Fig. 4.17 Normalised LII signal as a function of time at flame locations A and B. The best fit of experimental LII signals at the two different locations was found by 2-parameter fitting.

According to the plot, the decay rates of the LII signal at HAB = 38 mm and r = 2.2 mm (location A) are slower than at HAB = 42 mm and r = 0 mm (location

B), which indicates that particles at the former location are larger than those at the latter due to the fact that larger particles cool more slowly than small ones. The reason is that large particles have a smaller surface area to volume ratio than small particles, therefore, temperatures decrease more slowly by conduction to the surrounding environment. Based on the LII model and the calculation of the χ^2 value, the geometric mean of soot particle diameter D_{m} is determined to be as large as 88 nm, which is more than three times that at lower HAB. Such a phenomenon can be explained by the temperature profile shown in Fig. 4.11; the higher temperature at HAB = 38 mm and $r = 2.2$ mm may play a dominant role in rapidly decomposing the unburnt ethylene fuel into small PAHs and promoting their subsequent agglomeration.

The results of the LII signal modelled as a function of time for the optimal parameter are shown in Fig. 4.18 as a solid line. There is clearly good agreement between model and experiment (shown as circles). An alternative method of particle temperature calculation is to use the 2C method itself to estimate the local temperature throughout the signal decay. Although this should in principle be identical to the model case, poor signal-to-noise ratios as the temperatures decrease mean that this is not an ideal method, because when the signal is weak after 400 ns, the ratio of the signals at the two wavelengths will yield large uncertainties, as shown in Fig. 4.18.

Figure 4.19 (left) shows the map for the peak temperature, $T_{\mathrm{p,0}}$, calculated for the flame tested using the 2C method. Some lines are omitted in the $T_{\mathrm{p,0}}$ map due to the low signal intensity at the edge of the laser sheet, and the soot particles in the region are not sufficiently heated. The $T_{\mathrm{p,0}}$ map indicates large variations in the peak temperature T_{p} throughout the flame, which arise from the different particle sizes and consequent implicit absorption rate. The highest apparent temperatures appear at the edges of the flame, and the lowest at the centre line. These findings are consistent with previous work using 2D auto-compensating LII (2D-AC-LII) in diffusion flames [55], and can be explained by the greater heat

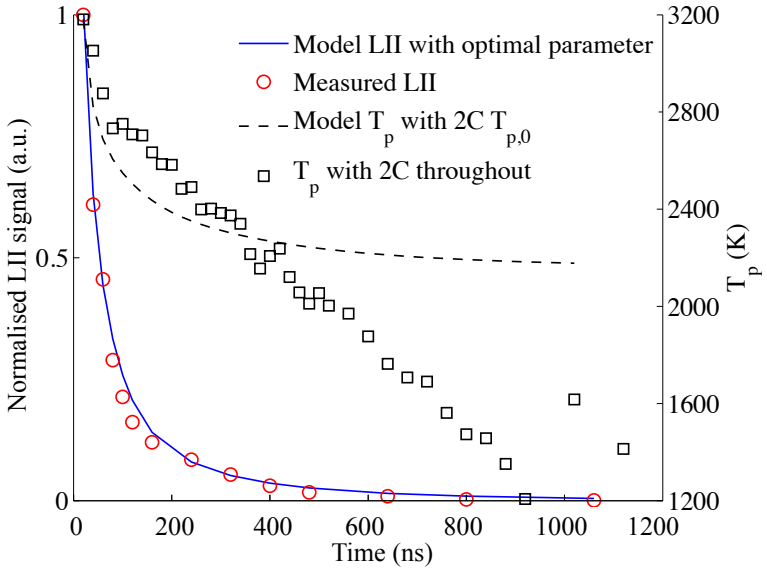

Fig. 4.18 T_{p} and the normalised LII signal as a function of time. Circles: measured LII signal; solid line: modelled LII signal for the optimal parameters, with the 2C method for peak; triangles: measured T_{p} with the 2C method throughout; dashed line: modelled T_{p} with the 2C peak measurement $T_{\mathrm{p,0}} = 3181$ K.

loss via surface heat conduction of smaller particles during the heating process. Figure 4.19 also shows the optimum mean diameter D_{m} calculated across the whole flame, assuming the peak temperature values obtained from the 2C method. The smallest estimated diameters are in the region surrounding the flame: at the inner edge, the particles grow via pyrolysis into larger particles; at the outer edge, the particles oxidise into smaller particles. These measurements are consistent with prior work by Hadef *et al.* [162]. The database of D_{m} distribution across the flame can be found in the supplementary material of the thesis in Section F.3. The distribution of f_v (shown in Fig 4.19 (right)), which was obtained in a previous study [12] shows a similar spatial distribution as the particle size.

Figure 4.20 shows a strong correlation between the soot volume fraction and particle size. This is because the particle surface growth is the greatest contributor to the increase in the soot volume fraction [158].

The SNR of the particle size measurements in some edge regions is very low. This is because: a) the particles are very small and the signal decay is very

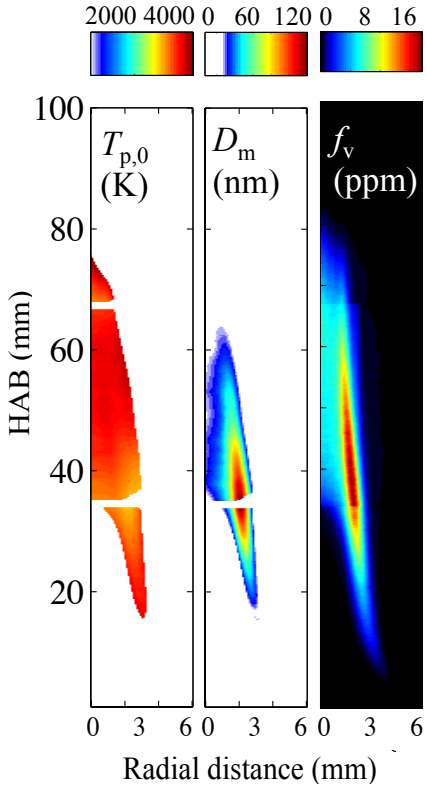

Fig. 4.19 Calculated T_p with the 2C method (left); estimated D_m with the 2-parameter fit (middle); measured f_v of soot in the tested flame (right) [12].

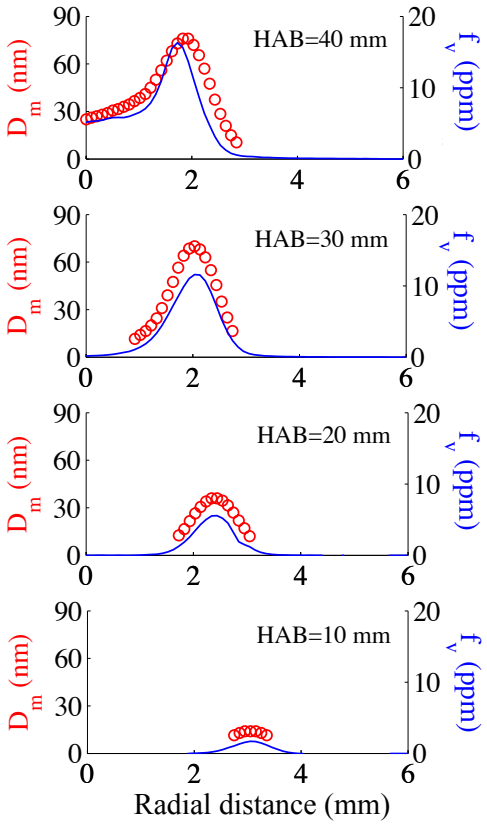

Fig. 4.20 D_{m} and f_v at different HABs.

sharp, making it difficult to resolve by the detectors with limited minimum gate time, or b) the signal intensity is low [162]. In the present study, particle size measurements in regions with SNR < 3 are excluded. Overall, the lower size limit with the present system is 10 nm.

The effect of choosing the 2C method to obtain the peak temperature instead of the usual solution of the energy balance is illustrated in Fig. 4.21 (a), at HAB = 42 mm at the centre line. The energy balance method yields $D_{\mathrm{m}} = 34$ nm and $\sigma = 0.3$, and the 2C method results in a minimum error at $D_{\mathrm{m}} = 25$ nm and $\sigma = 0.24$. The temporal evolution of the particle temperature is reconstructed using the optimal values for D_{m} and σ. The value of $T_{\mathrm{p,0}}$ calculated at 20 ns is 3451 K for the energy balance using $E(m) = 0.26$ of soot, laser fluence $F = 0.17$ J/cm^2 and laser duration 8 ns. This $T_{\mathrm{p,0}}$ is significantly higher than the 2C estimate of $T_{\mathrm{p,0}} = 3181$ K, yet the normalised signals are not significantly affected, in both cases giving good agreement because of the combination of the larger temperature gradient between particle surface and ambient gas for larger particles. Although the absolute intensity of the signal would be different, the decay rate is similar after normalisation. The corresponding temperature history curves T_{p} for the different $T_{\mathrm{p,0}}$ from each method are also shown in Fig. 4.21 (b). As in the case of the LII signal, the shape of the T_{p} curves are similar, yet the absolute values are disparate.

4.6 Conclusion

In this chapter, we have combined the 2D-TiRe-LII technique with the 2C-LII technique to allow both peak temperature and soot primary particle sizes to be determined in a ethylene diffusion flame. The temporal resolution of the LII decay curve is achieved by shifting the delay time of the ICCD cameras in 20 ns steps. The results were employed to determine the particle sizes in sub-ppm, low sooting ethylene flames for the first time, and the agreement with particle sizes

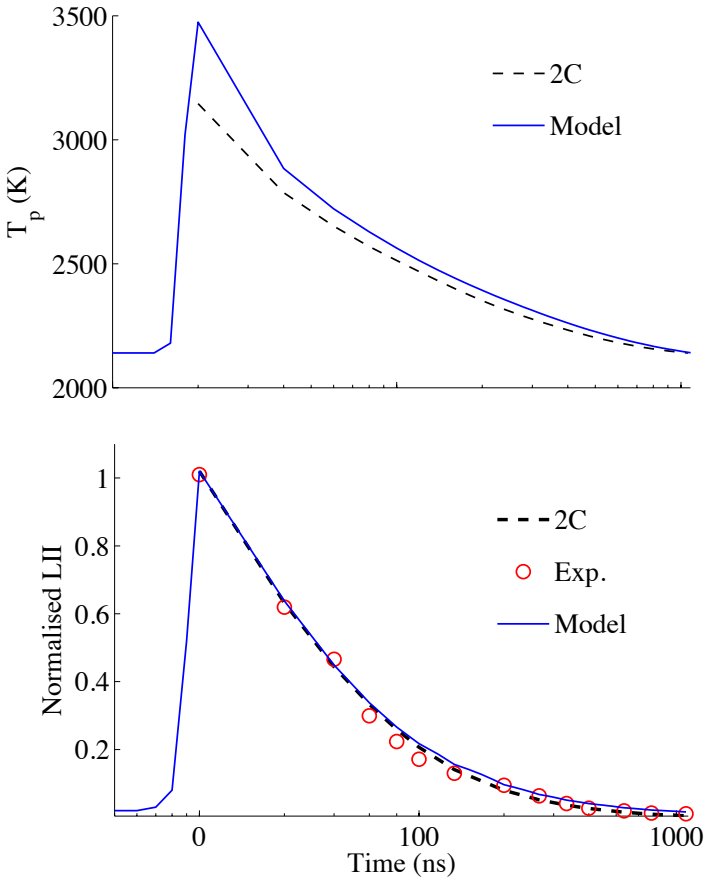

Fig. 4.21 LII (upper) and T_p (bottom) evolution of a particle at HAB = 42 mm and r = 0 mm. Circles: measured LII signal; solid line: modelled LII signal (blue) and T_p (black) with 2C obtained $T_{\mathrm{p},0}$ and optimal D_m = 25 nm and σ = 0.24; dashed line: modelled LII signal (blue) and T_p (black) with $T_{\mathrm{p},0}$ obtained via energy balance and optimal D_m = 34 nm and σ = 0.3.

measured by TEM is very good. Besides the best fit size, a range of possible solutions are also estimated based on the sensible value of distribution width. The use of the 2C method can significantly improve the accuracy of LII particle sizing by avoiding uncertainties which relate to the energy model associated with the absorption function of soot particles and losses via *e.g.* sublimation. The map of T_{p} measured with 2C pyrometry indicates that even when a near top-hat profile laser sheet is used, the variance of the peak temperatures achieved by the incandescing particles within the flame may be as large as 1000 K. This large discrepancy can directly translate into inaccuracies in diameter estimate. The 2D distribution allows both size and diameter to be assessed over the image. In this particular case, the overlap in profiles of f_v and particle size implies that soot particle surface growth rather than inception plays an important role in f_v growth.

Chapter 5

2D 2-colour Time-resolved Laser-induced Incandescence Sizing of Ultra-fine Soot Particles in Methane Diffusion Flames

5.1 Introduction

In this chapter, we demonstrate the use of the 2D2C-TiRe-LII technique using a methane flame. Measurements in methane flames are more challenging than in other fuels as these flames produce very small soot particles. The temperature, velocity and f_v data in this standard methane flame have been studied intensively [7, 23, 89], but particle sizing has not. The present study serves both as a validation of the proposed 2D2C method, and adds to the database of soot formation and growth mechanisms in methane diffusion flames.

Table 5.1 Values for model calculations. *T in K

Variable	Units	Value*
ΔH_{v}	J/mol	7.78×10^5 at 3915 K [85]
W_{s}	kg/mol	0.01201
W_{v}	kg/mol	0.03603
ρ_{s}	kg/m^3	$2303.1 - 7.3106 \times 10^{-5} T$ [44, 67, 167]
c_{s}	J/kg K	$1878 + 0.1082\ T - 151.49 T^{-2}$ [93]
α_{T}	-	0.3 [67, 166]
κ_{a}	W/m K	$5.83 \times 10^7 (T_0/273)^{0.82}$ [85]

5.2 Method

The LII model and particle size estimation calculation were introduced in Chapter 4. The values used for all the relevant variables can be seen in Table 5.1.

5.3 Experiment

The methane flames, cases A and B introduced in Chapter 2 are tested. The details of the burner and operating conditions of the flames can be found in Section 2.3.1.

The experimental set-up is similar to that in Chapter 4, however, due to the relatively shorter decay time of soot particles in a methane flame compared to in an ethylene flame, a different camera timing strategy is applied. The total recording time span is from -20 ns to 500 ns, which is half that in the ethylene flame. Background images are collected 20 ns before the laser pulse reaches the flame, for the minimum possible gate interval of 20 ns. A total of 27 LII images are recorded between times $t = -20$ ns to $t = 500$ ns at 20 ns intervals, with gate times of 20 ns. The results are averaged over 200 images, with the flame luminosity background subtracted. The maximum signal-to-noise ratio (peak signal counts to dark signal counts) is around 200. In order to cover the whole flame, the experiment was repeated three times to cover vertical regions in 33 mm height segments. Given the good symmetry of the flame, only one

half of the flame is presented. The spatial resolution in the diameter analysis corresponds to 0.1×0.1 mm^2, with a laser sheet thickness of 0.46 mm. The value of C_1/C_2 was obtained using a tungsten lamp (Thorlabs QTH10B) with the method described in Section 4.4.2. LII signals from this flame have also been used to determine f_v after calibration using extinction measurements, as described in Chapter 2. The resulting measurements are quoted further on in Section 5.4. Another difference with the experiment on the ethylene flame is the amplification of the ICCD camera, due to the relatively weaker signals in methane flames, a higher gain value of the ICCD cameras is applied.

The gas temperature of the flames is calculate with the diffusion flame model described in Chapter 3. Figure 5.1 (a) shows the calculated and measured temperature profiles for various heights above the burner (HAB) for a standard flame case (Santoro *et al.* CH4#2-T [9]). The temperature differences between model and measurement are less than 200 K within the flame zone. Most of the disagreement appears near the tip of the flame, where neglecting axial diffusion may not hold.

5.4 Results and discussion

The evolution of the LII signal collected in the middle region of the diffusion flame for cases A and B (33-66 mm) at two wavelengths is shown in Fig. 5.2 and 5.3. The time −20 in the images represents 20 ns prior to the arrival of the LII laser pulse. The images collected between 20-40 ns after the laser's arrival are used to estimate the initial temperature $T_{\mathrm{p},0}$ reached by the soot particles prior to the signal decay by cooling.

A two-parameter search was conducted to minimise the χ^2-value, as described in Chapter 4. Results are shown in Fig. 5.4 for the point of maximum LII signal (HAB = 65.3 mm, r = 3.3 mm), for which the 2C temperature measured is $T_{\mathrm{p},0}$ = 3384 K, and the model calculation for the local gas temperature T_0 is 2153

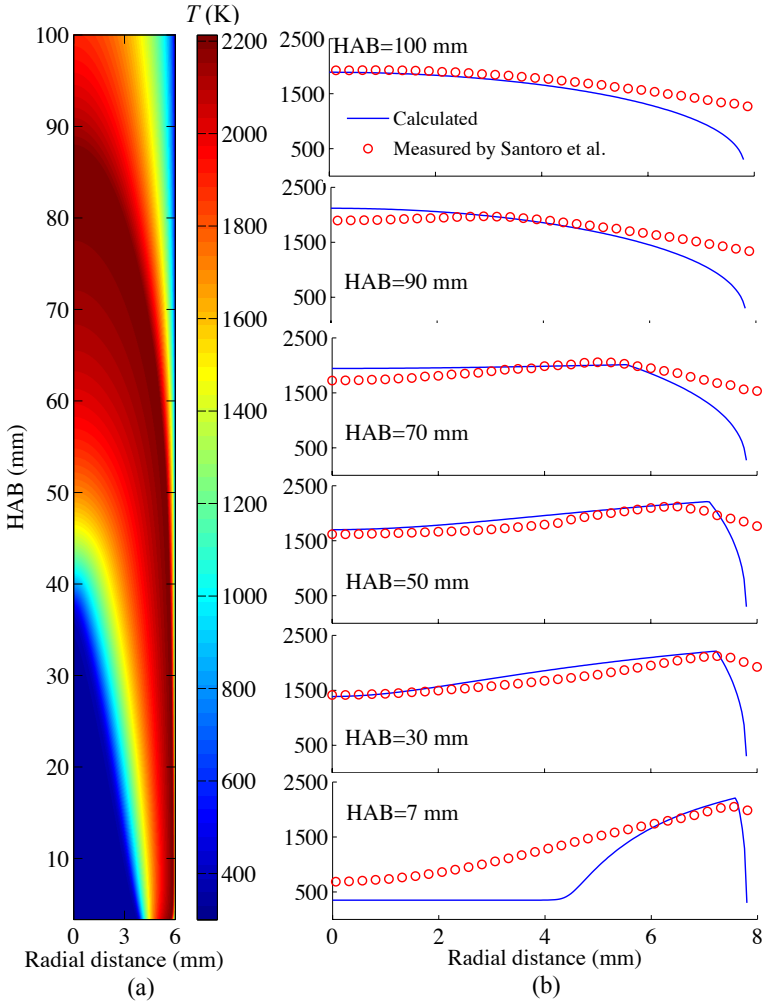

Fig. 5.1 T_0 profile for different HAB. Lines: model; circles: experiment (Santoro *et al.* CH4#2-T [9]).

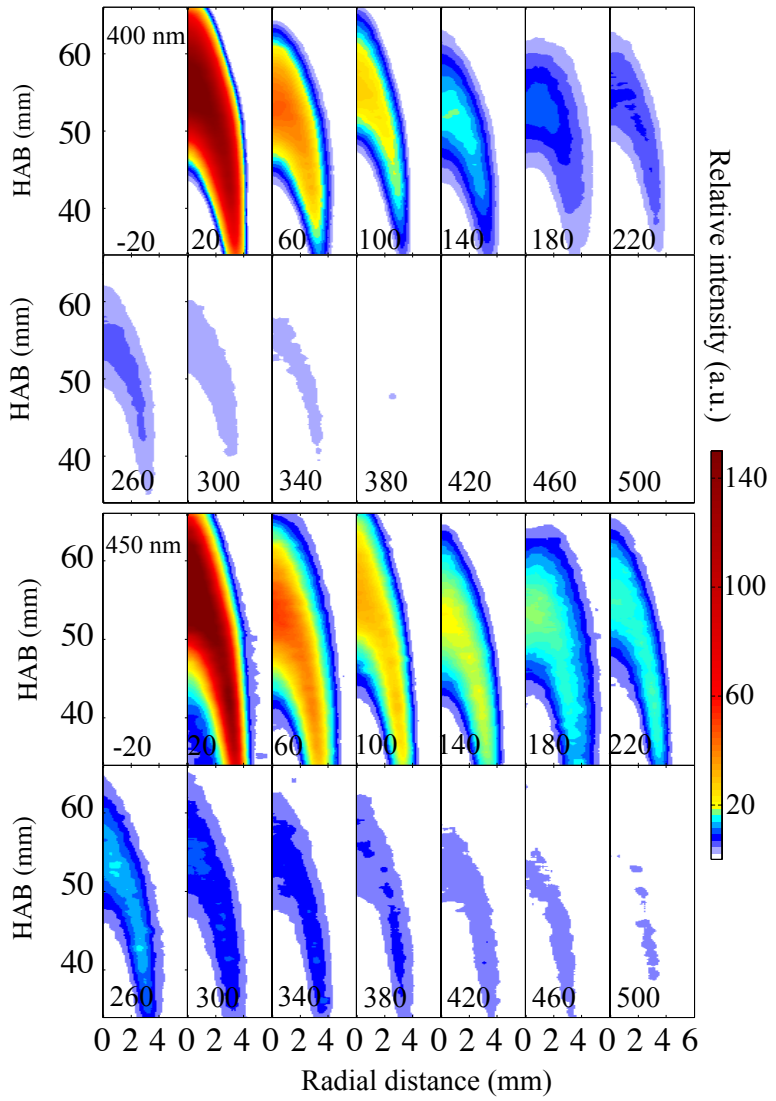

Fig. 5.2 LII signal measured at 400 nm (top) and 450 nm (bottom) of flame case A. Numbers show the intensifier gate time relative to the laser pulse. All images collected at a gate interval of 20 ns. Images at each 40 ns are shown.

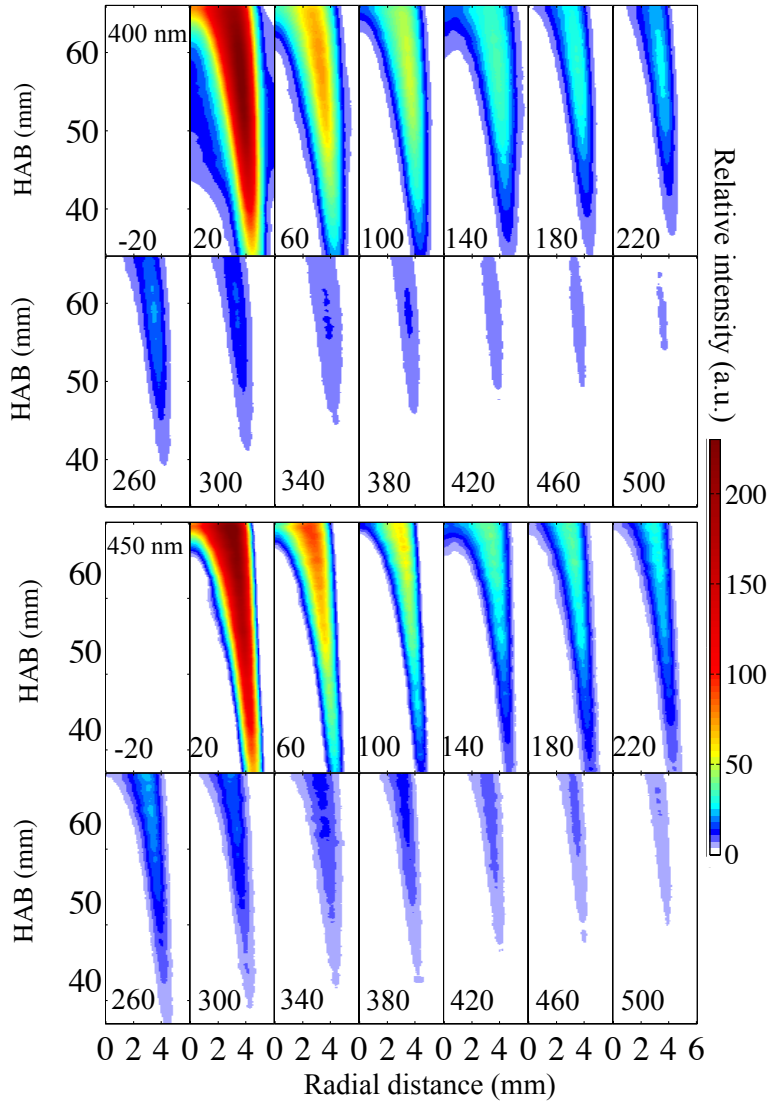

Fig. 5.3 LII signal measured at 400 nm (top) and 450 nm (bottom) of flame case B.

K. The domain of the search covered $0 < D_{\mathrm{m}} < 30$ nm in steps of 0.5 nm and $0.01 < \sigma < 1$ in steps of 0.01, resulting in the unique value at the minimum point of D_{m}=15 nm with a variance σ=0.34 and the parameter of lognormal distribution corresponding to an arithmetic mean diameter of 15.1 nm.

As discussed in Chapter 4, a 'valley' of minimising values around the best fit value is found in the χ^2 map. Thus, with the same method we used in the Chapter 4, a range of potential solution of D_m is defined based on the range of σ = 0.2 to 0.4. At the analysed location (HAB = 65.3 mm, r = 3.3 mm), the range of D_m is 13nm to 21 nm.

The measured mean diameter is very close to the value of 14.2±1.5 nm measured using TEM from particles sampled at the maximum f_v position in a similar diffusion methane flame [59]. The results of the model LII signal as a function of time for the optimal parameter are shown in Fig. 5.4 as a solid line. There is clearly good agreement between model and experiment (shown as circles). An alternative method of particle temperature calculation is to use the 2C method itself to estimate the local temperature throughout the signal decay. Although this should in principle be identical to the model case, poor signal to noise ratios as the temperatures decrease mean that this is not an ideal method, as shown in Fig. 5.4.

Figures 5.5 and 5.6 shows the calculated peak temperature $T_{\mathrm{p,0}}$ map for the tested flames case A and B using the 2C method. The height of the laser sheet in the present study is 33 mm. In order to cover the length of the whole flame, three different series of images were taken, with images connecting at HAB=33 and 66 mm. The $T_{\mathrm{p,0}}$ map indicates large variations in the peak temperature throughout the flame, which arise from the different particle sizes and consequent implicit absorption rate and the low laser intensity at the boundaries of the laser sheet. The highest apparent temperatures appear at the edges of the flame, and the lowest at the centreline. These findings are consistent with previous work using 2D auto-compensating LII (2D-AC-LII) in diffusion flames [55], and can be

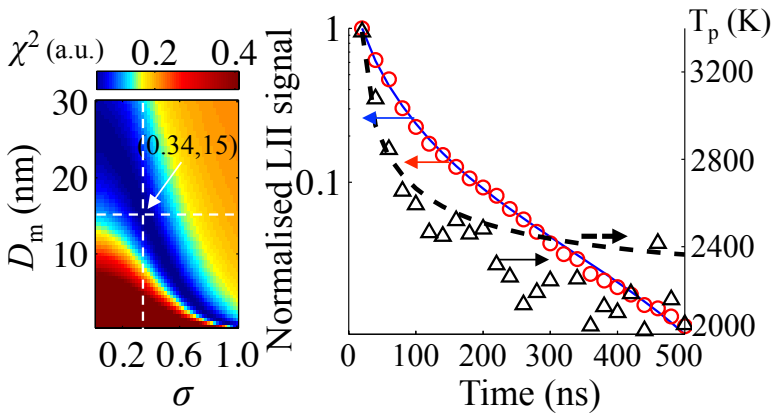

Fig. 5.4 Squared error χ^2 as a function of logarithm standard deviation σ, and mean diameter D_m (left); T_p and normalised LII signal as a function of time (right). Circles: measured LII signal; solid line: model LII signal for the optimal parameters, with 2C method for peak; triangles: measured T_p with 2C method throughout; dashed line: model T_p with 2C peak measurement $T_{\mathrm{p},0}$=3384 K.

explained by the greater heat loss via surface heat conduction of smaller particles during the heating process. It is notable that the $T_{\mathrm{p},0}$ at HAB = 66 mm, where two images combine together, is relatively lower, which may be due to the very sharp decreasing of laser intensity at the edge of the laser sheet. Even the top-hat profile of the laser sheet is well-characterised; the very sharp intensity drop at the sheet's boundary is inevitable. Figure 5.5 also shows the calculated optimum mean diameter D_m across the whole flame, assuming the peak temperature values obtained from the 2C method. The smallest estimated diameters are in the region surrounding the flame: at the inner edge, the particles grow via pyrolysis into larger particles; at the outer edge, the particles oxidise into smaller particles. These measurements are consistent with prior work by Hadef *et al.* [162]. The distribution of f_v (shown in Figs. 5.5 and 5.6 right), which was obtained in a previous study [12] shows a similar spatial distribution as the particle size. This is expected in a situation in which particle surface growth is the main mechanism for an increase in f_v [158].

In a similar way to the ethylene flame shown in Chapter 4, the SNR of the particle size measurements in some edge regions is very low even though the gain

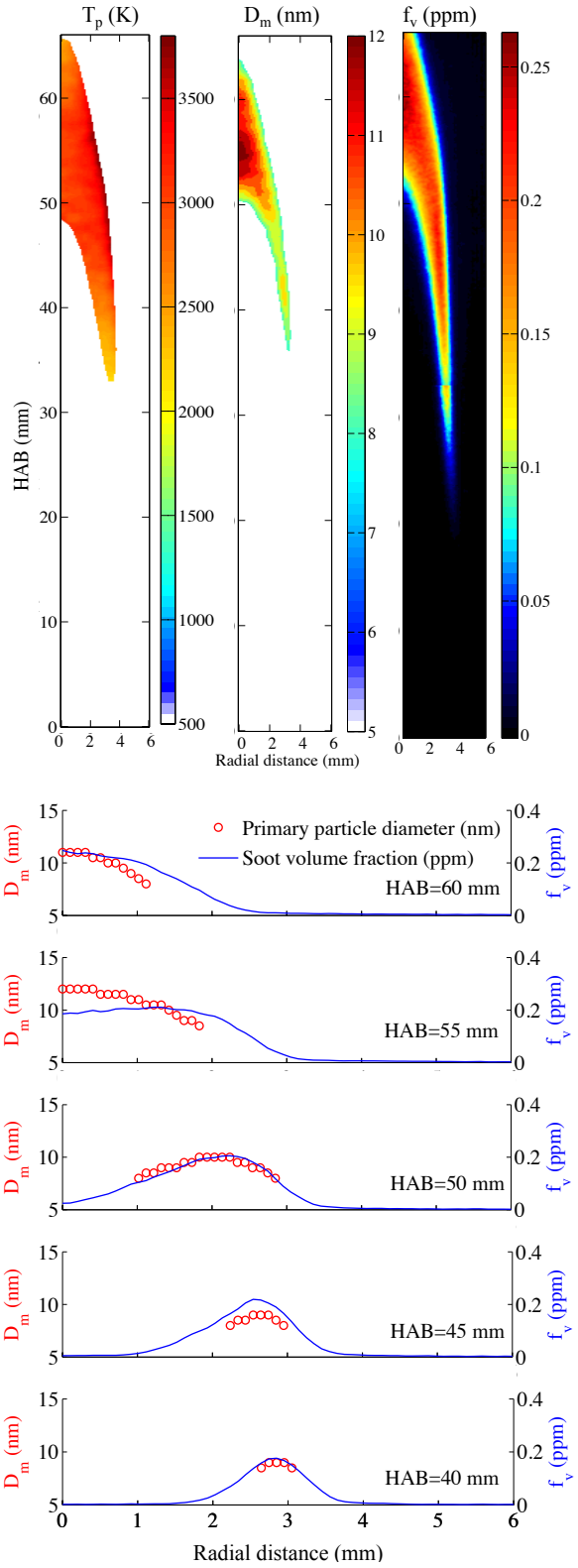

Fig. 5.5 Case A: (a) calculated Tp with two-colour method; (b) estimated Dm with 2-parameter fitting; (c) measured f_v of soot in tested flame; (d) plotted Dm and f_v at various HABs.

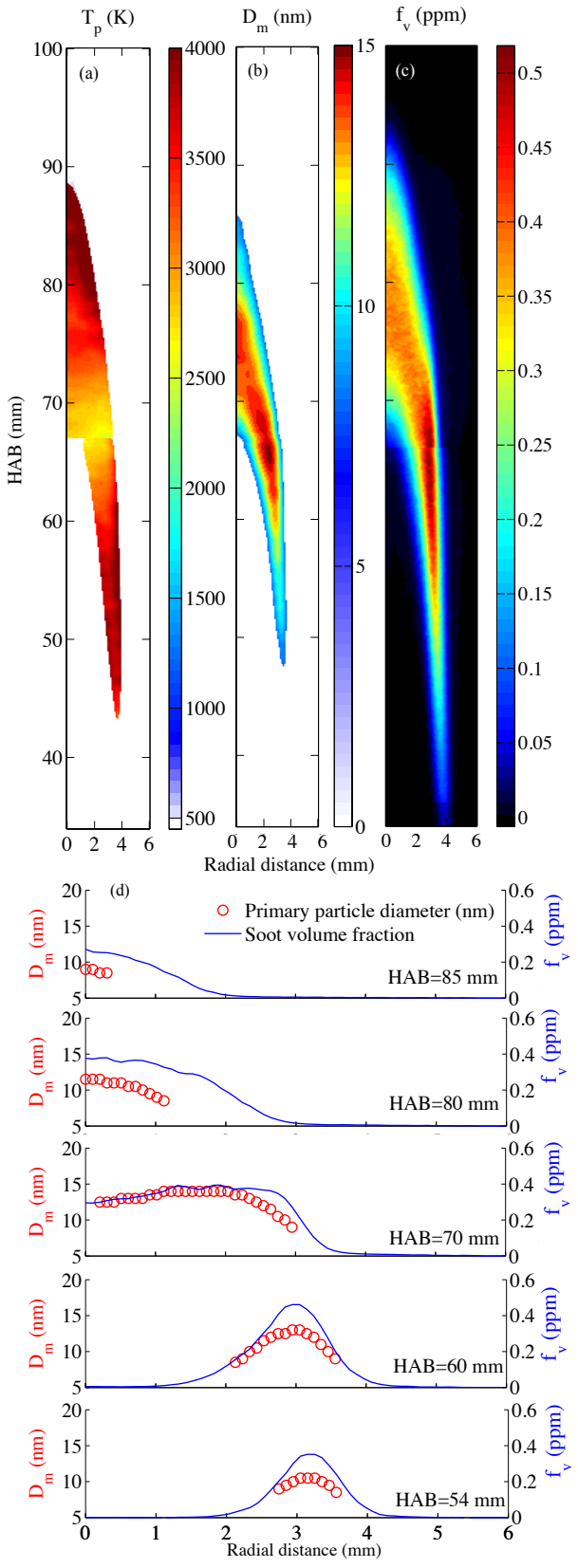

Fig. 5.6 Case B: (a) calculated Tp with two-colour method; (b) estimated Dm with 2-parameter fitting; (c) measured f_v of soot in tested flame; (d) plotted Dm and f_v at various HABs.

value of the ICCD cameras is higher than that for the ethylene flame. This is because of the low signal intensity. In the region around HAB $\leq$ 47 mm, the f_v is still detectable, but the SNR for the LII is too low to be resolved. Overall, the lower size limit with this system applied on a methane flame is 8 nm.

The effect of choosing the 2C method for obtaining the peak temperature instead of the usual solution of the energy balance is illustrated in Fig. 5.7, at HAB = 68.2 mm at the centerline of flame case B. The energy balance method yields D_m = 16 nm, σ = 0.24, and the 2C method results in a minimum error at D_m = 8 nm, σ = 0.15. The temporal evolution of the particle temperature is reconstructed using the optimal values for D_m and σ. The calculated $T_{\mathrm{p},0}$ at 20 ns is 3296 K (while at 0 ns T_{max} is 3971 K) for the energy balance using $E(m) = 0.26$ of soot, laser fluence $F = 0.17$ J/cm^2 and laser duration FWHM = 5 ns. This $T_{\mathrm{p},0}$ is significantly higher than the 2C estimate of $T_{\mathrm{p},0}$ = 2738 K. Yet the normalised signals are not significantly affected, in both cases giving good agreement because of the combination of the larger temperature gradient between particle surface and ambient gas for larger particles. Although the absolute intensity of the signal would be different, the decay rate is similar after normalisation. The corresponding temperature histories curves T_p under the different $T_{\mathrm{p},0}$ from each method are also shown in Fig. 5.7. As in the case of the LII signal, the shape of the T_p curves are similar, yet the absolute values are disparate.

5.5 Conclusions

In this chapter, the 2D2C-TiRe-LII system is employed to determine the very small particle sizes in sub-ppm, low sooting methane flames for the first time, and the agreement with particle sizes measured by TEM is very good. The use of the 2C method can significantly improve the accuracy of LII particle sizing by avoiding uncertainties associated with the energy model associated with the absorption function of soot particles and losses via *e.g.* sublimation. The map

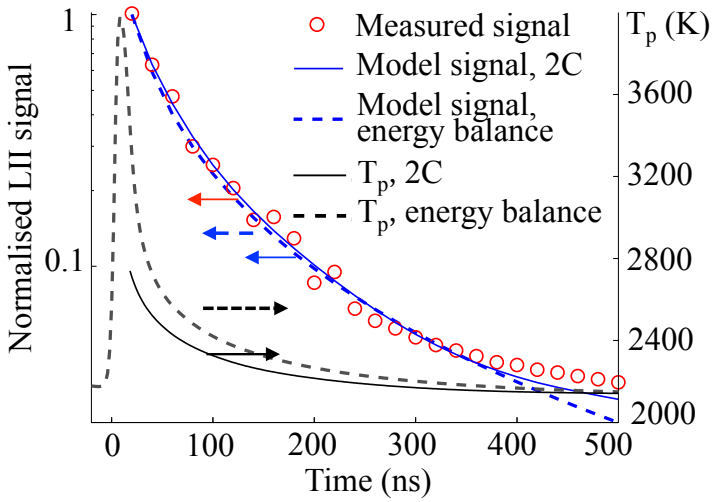

Fig. 5.7 LII and T_p evolution of particle at HAB = 68.2 mm and $r = 0$ mm. Circles: measured LII signal; solid line: model LII signal (blue) and T_p (black) with 2C obtained $T_{\mathrm{p},0}$ and optimal $D_m = 8$ nm and $\sigma = 0.15$; dashed line: model LII signal (blue) and T_p (black) with $T_{\mathrm{p},0}$ obtained via energy balance and optimal $D_m = 16$ nm and $\sigma = 0.24$.

of T_p measured with 2C pyrometry indicates that even when a near top-hat profile laser sheet is used, the variance of the peak temperatures achieved by the incandescing particles within the flame may be as large as 1000 K. This large discrepancy can directly translate into inaccuracies in diameter estimate. The 2D distribution allows both size and diameter to be assessed over the image. In this particular case, the overlap in profiles of f_v and particle size implies that soot particle surface growth rather than inception plays an important role in f_v growth. Further developments in the technique might include the use of high speed 2D2C-TiRe-LII for unsteady flows using split filters.

Chapter 6

Conclusions and future work

6.1 Conclusions

In the present study, comprehensive laser-based in-situ diagnostic techniques for flame-generated soot particles were developed and tested in various hydrocarbon diffusion flames.

1) A high spatial resolution laser cavity extinction technique has been developed. The configuration of the continuous wave laser cavity allowed for quantitative ppb levels of soot volume fraction detection with a spatial resolution of around 200 μm. The high sensitivity was obtained through multiple reflections of the beam through highly reflective mirrors, and the fine spatial resolution of the cavity system was obtained with the use of concave mirrors. A detailed uncertainty analysis of the measurements was also performed. The system was used to measure the soot volume fraction in a series of methane, ethylene and propane flames, and the results show good agreement with LII measurements. The extinction coefficient of the 638 nm laser beam in these flames is supplied as supplementary material (see Appendix F.1), which excludes uncertainty from the absorption parameter $E(m)$, and hence is easy for other researchers to use and refer to.

2) The laser cavity extinction technique with high spatial resolution is used

to measure the soot volume fraction across nitrogen-diluted, low-soot producing laminar methane-air diffusion flames. Comparisons with LII measurements show good agreement. By comparing the numerically calculated flow field of the diluted flames and the soot volume fraction map, the formation of soot and the effects of dilution were investigated. It was found that the addition of nitrogen in the fuel flow can change the location of the stoichiometric mixture fraction ξ_{st} in the flame. However, the location of the soot inception and growth does not change with ξ_{st} , and even shows a slight opposite shift trend to ξ_{st} , indicating that in these flames, the inception and growth of the soot particles is more time dependent than temperature dependent. Furthermore, dilution can also reduce the residence time for soot mass growth dramatically. The combination of the effects results in a reduction in soot formation in diluted flames. The amount of reduction is more pronounced than estimated with T_{ad} in previous work. The K_e value of flames A0 to E4 can be found in Appendix F.2.

3) To achieve 2-dimensional soot particle size measurements in a laminar diffusion ethylene flame, we combined the 2D-TiRe-LII technique with the 2C-LII technique to form the 2D2C-TiRe-LII technique. The configuration allows both peak temperature and soot primary particle sizes to be determined in a stable flame. The temporal resolution of the LII decay curve was achieved by shifting the delay time of the ICCD cameras in 20 ns steps. The results were employed to determine the size of ultrafine particles in the low-soot ethylene and methane flames, and the agreement with particle sizes measured by TEM is very good. The use of the 2C method can significantly improve the accuracy of LII particle sizing as it avoids the uncertainties associated with the energy model relating to the absorption function of soot particles and losses via, *e.g.* sublimation. The D_m map of the flames tested can be found as supplementary material in Appendices F.3 to F.5.

6.2 Future work

A number of interesting opportunities for future work exist, based on the current research on soot particles.

6.2.1 Laser diagnostics of non-soot condensed-phase particles (CPPs) in flame

Combustion synthesised non-soot condensed-phase nanoparticles (CPPs), such as SiO_2, Al_2O_3, TiO_2 and Fe_2O_3 have been used in a number of industrial sectors for decades [1]. These CPPs are produced commercially of the order of millions of tons per year. Moreover, these silicon and metal oxides are important components of $PM_{2.5}$ in the atmosphere. Therefore, developing low-cost and highly accurate diagnostic methods for CPPs would be valuable.

Based on the current progress on soot, studies on the aforementioned CPPs have become possible, since the two processes have many similarities. They are all formed in flames in the form of aerosols and the formation processes are quite similar [1, 179].

In fact, the LII technique has been applied to these CPPs in preliminary measurements [15, 97, 110–112, 180–182]. These works provide important fundamentals to conduct quantitative LII measurement on CPPs, such as important optical parameters, the excitation and collection wavelength etc. In future, quantitative LII on CPPs can be conducted with extinction calibration measurements. We can choose TiO_2 particles as the first step since more reference data is available for comparison.

A diffusion flame [183–185] fuelled with nitrogen-diluted methane/hydrogen may be selected to produce the particles. Dilution of nitrogen can help prevent interference from soot. However, now that we have data for the soot volume fraction in diluted methane flames, we may subtract the soot in the data processing. Four typical reactors for flame-based particle synthesis are shown in Fig.

6.1. The configuration can affect the product particle size by up to an order of magnitude. Titania particles, TiO_2, produced in a double (inverted) diffusion flame with a primary particle diameter <10 nm (Flame A) were up to 10 times smaller than particles produced in a single (classic) diffusion flame (Flame D), where even non-agglomerated particles of a diameter of about 100 nm were made, as proven by small-angle X-ray scattering [13].

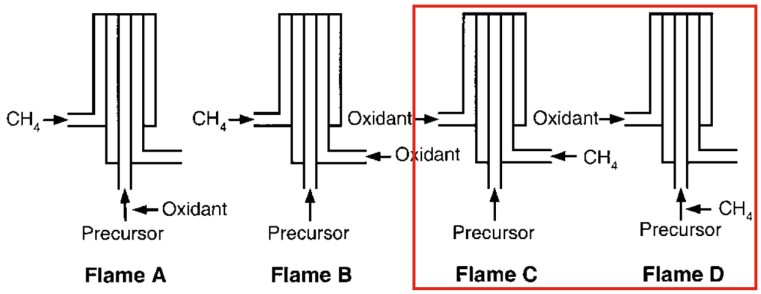

Fig. 6.1 Reactant mixing configurations for a double or inverted (Flames A and B) and single or classic (Flames C and D) diffusion flame reactor [13].

Titanium(IV) isopropoxide (TTIP) has been used for TiO_2 particle synthesis in flames [111]. The structure of TTIP is shown in Fig. 6.2.

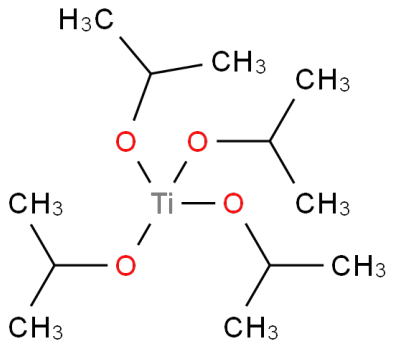

Fig. 6.2 Titanium(IV) isopropoxide (TTIP). Source: Sigma-Aldrich.

The complex refractive index $m = n \pm ki$ for titania can be found in a recent

Table 6.1 Prices for TTIP of different purities

Chemical	Purity	Pack	Price	Storage
TTIP	97%	500 ml	55.10 GBP	glass bottle
TTIP	97%+	500 ml	73.00 GBP	glass bottle
TTIP	99.999%	100 ml	238.50 GBP	glass bottle

publication by Egerton [14] as shown in Fig. 6.3. The value of $E(m)$ can be deduced by the values of n and k as:

$$E(m) = \frac{6nk}{\left(n^2 - k^2 + 2\right)^2 + (2nk)^2} \tag{6.1}$$

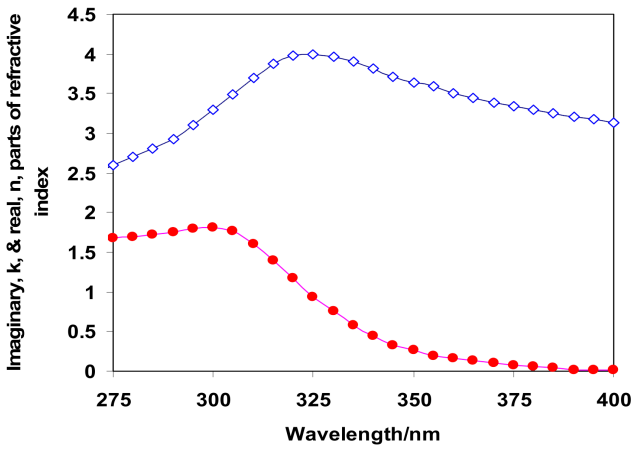

Fig. 6.3 Variation of the real (blue diamonds) and imaginary (red circles) components of the refractive index of rutile between 275 and 400 nm. Above 400 nm the imaginary component, which controls light absorption, is negligible even though the real component is not. Pure rutile crystals are transparent in the visible region of the spectrum but can scatter visible radiation [14].

The Rayleigh approximation may still be valid for the experiment of TiO_2. In order to develop quantitative measurements of TiO_2 particles, extinction measurements are essential.

The cross section of scattering and absorption of small particles within the

Rayleigh region can be expressed as:

$$\sigma_{\text{sca}} = \left(\frac{N\pi}{6} \int_0^{\infty} P(D) D^3 \mathrm{d}D \right)^2 \cdot \sigma_{\text{sca-}i} \tag{6.2}$$

and

$$\sigma_{\text{abs}} = \frac{N\pi}{6} \int_0^{\infty} P(D) D^3 \mathrm{d}D \cdot \sigma_{\text{abs-}i} \tag{6.3}$$

Therefore, we have:

$$\int_0^{\infty} P(D) D^3 \mathrm{d}D = \overline{D}^3 \tag{6.4}$$

Substituting Eq. (6.4) into Eqs. (6.2) and (6.3), gives:

$$\sigma_{\text{sca}} = \left(\frac{N\pi}{6} \overline{D}^3 \right)^2 \cdot \sigma_{\text{sca-}i} \tag{6.5}$$

and

$$\sigma_{\text{abs}} = \frac{N\pi}{6} \overline{D}^3 \cdot \sigma_{\text{abs-}i} \tag{6.6}$$

According to the established Mie scatter theory, the cross section of scattering is inversely proportional to the fourth power of the wavelength, while that of absorption is proportional to the first power of the wavelength, thus we have:

$$\sigma_{\text{sca-}i}(\lambda) = \sigma_{\text{sca-0}} \frac{\lambda_0^4}{\lambda^4} \tag{6.7}$$

and

$$\sigma_{\text{abs-}i}(\lambda) = \sigma_{\text{abs-0}} \frac{\lambda_0}{\lambda} \tag{6.8}$$

Substituting Eqs. (6.7) and (6.8) into Eqs. (6.5) and (6.6) respectively, we

have:

$$\sigma_{\text{sca}}(\lambda) = \left(\frac{N\pi}{6}\overline{D}^3\right)^2 \cdot \sigma_{\text{sca-0}}\frac{\lambda_0^4}{\lambda^4} \tag{6.9}$$

and

$$\sigma_{\text{abs}}(\lambda) = \frac{N\pi}{6}\overline{D}^3 \cdot \sigma_{\text{abs-0}}\frac{\lambda_0}{\lambda} \tag{6.10}$$

From the solution of the Maxwell equations, we have:

$$N^2\lambda_0^4\sigma_{\text{sca-0}} = 24\pi^3\left|\frac{m^2-1}{m^2+2}\right|^2 \tag{6.11}$$

and

$$N\sigma_{\text{abs-0}}\lambda_0 = 6\pi\,\text{Im}\left(\frac{m^2-1}{m^2+2}\right) \tag{6.12}$$

Substituting Eqs. (6.11) and (6.12) into Eqs. (6.9) and (6.10) respectively, we have:

$$\sigma_{\text{sca}}(\lambda) = \frac{2}{3}\frac{\pi^5\overline{D}^6}{\lambda^4}\left|\frac{m^2-1}{m^2+2}\right|^2 = d^6\frac{2}{3}\frac{\lambda^2}{\pi}\left|\frac{m^2-1}{m^2+2}\right|^2 \tag{6.13}$$

and

$$\sigma_{\text{abs}}(\lambda) = \pi^2\overline{D}^3\frac{1}{\lambda}\,\text{Im}\left(\frac{m^2-1}{m^2+2}\right) = d^3\frac{\lambda^2}{\pi}\,\text{Im}\left(\frac{m^2-1}{m^2+2}\right) \tag{6.14}$$

where d is a non-dimensional parameter defined as $\pi D/\lambda$. Thus, we can calculate the portion of absorption of the total extinction:

$$\frac{\sigma_{\text{abs}}(\lambda)}{\sigma_{\text{sca}}(\lambda)+\sigma_{\text{abs}}(\lambda)} = \frac{1}{\left(d^3\frac{2}{3}\left|\frac{m^2-1}{m^2+2}\right|^2\right)/\left(\text{Im}\left(\frac{m^2-1}{m^2+2}\right)\right)+1} = \frac{1}{d^3\frac{2F(m)}{3E(m)}+1} \tag{6.15}$$

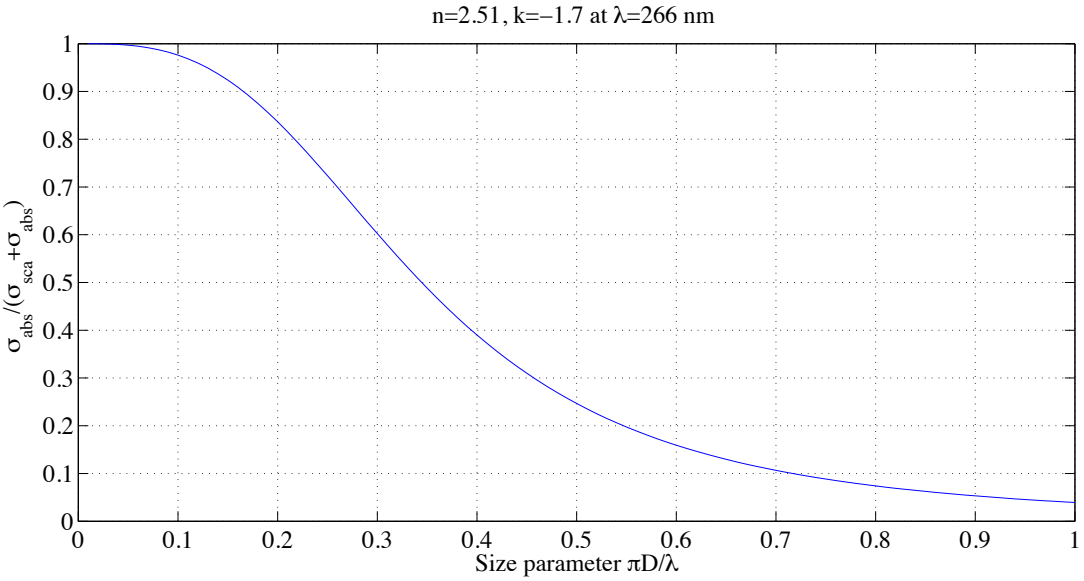

Fig. 6.4 Calculation of the single-absorption ratio for a refractive index of $2.51 - 1.7i$ as a function of particle size parameter $d = \pi D/\lambda$.

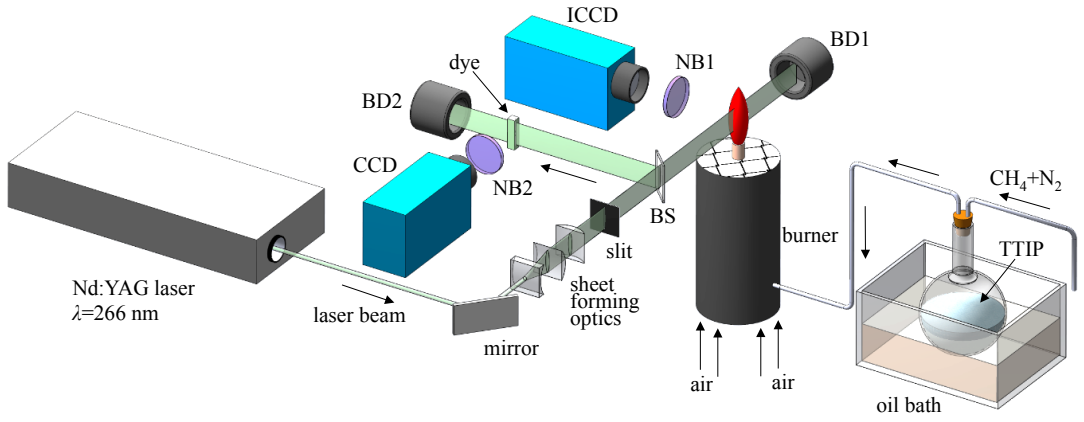

Fig. 6.5 Schematic of TiO_2 measurement experimental apparatus

Volume fraction measurement: based on Vander Wal *et al.*'s study [110], the intensity of laser-induced incandescence is proportional to the volume fraction of metal/metal oxides nanoparticles.

Gating time: random laser-induced emissions can contaminate LII signals [110, 111], and a longer delay time (tens of nanoseconds) can help to avoid irregular laser-induced emissions.

Excitation Wavelengths: the excitation wavelength used is the 4th harmonic of a Nd: YAG laser, $\lambda = 266$ nm. The spectral absorption cross section of nanoparticles can be accurately predicted using the complex index of refraction of the bulk material.

Fluence: this is similar to soot measurement. Considering the response and sublimation limit; smaller fluence can significantly reduce the noise from irregular laser-induced emissions [111]. Thus, 0.02 J/cm^2 might be the optimal fluence for LII measurements.

Collection wavelength: in order to avoid the noise from PAH fluorescence, a shorter wavelength (UV range) should be selected.

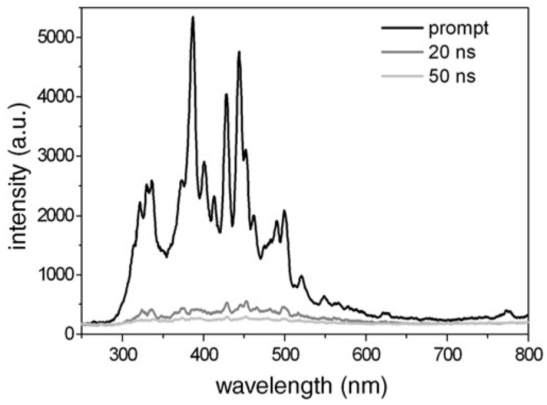

Fig. 6.6 Prompt and delayed laser-induced emissions (LIE) spectra at a fixed height (fluence 600 mJ/cm^2) [15].

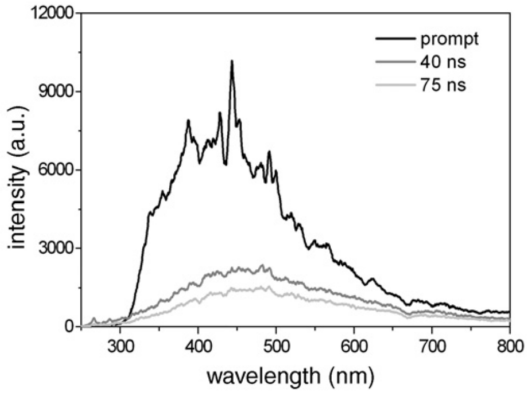

Fig. 6.7 Prompt and delayed laser-induced emissions (LIE) spectra at a fixed height (fluence 20 mJ/cm^2) [15].

Time-resolved LII: similar experiments have been performed on soot particles [162]. Whilst normal ICCDs cannot temporally resolve the whole decay process of the LII signal, the time resolution is achieved by shifting the camera gate along the LII decay from several nanoseconds after the laser pulse to more than 1,000 nanoseconds, subsequently mapping out the soot particle sizes across the flame, which can then be extracted by the method described in Section 4.2.

Qualitative LII measurements have been applied to titania particles during the flame synthesis process [15, 111], and traditional single-point TR-LII measurements were applied to silica [175], iron [186, 187], nickel [112], manganese oxide [97] and molybdenum [188]. However, as far as we know, no experiments have been performed with 2D-TR-LII for titania particles sythesised in a flame.

6.2.2 Optical properties of soot

As discussed in Chapter 1, the wavelength dependence of the absorption function $E(m)$ of soot particles produced in a flame still remains a controversial topic. For simplicity, the most accepted value of m is $m = 1.57 - 0.56i$, which was proposed by Dalzell *et al.*, who measured the value with an *ex-situ* reflectometry technique [143]. Therefore the value of $E(m)$ is 0.26, based on the value of m. However, in Mie theory, the soot particles were considered to be spherical, with a uniform

diameter [142]. TEM analysis shows that soot particles are actually aggregates of primary spheres [1]. Thus, the Rayleigh-Debye-Gans theory for fractal aggregates (RDG-FA) was developed to describe the interference of light with aggregated or larger soot particles [134, 142]. Dobbins *et al.* [189] found that RDG-FA was more accurate than the Mie model in the prediction of light extinction. However, the RDG-FA theory needs more precise knowledge regarding both the geometry and optical properties of soot particles. Therefore, many measurements of the soot complex refractive and $E(m)$ index have been conducted, with particular attention to the spectral behaviour of the refractive index of soot. However, a consensus has not yet been reached on the issue. Krishnan *et al.* [135] and Köylü *et al.* [190] suggested that $E(m)$ was shown to increase within the wavelength range from 380 nm to 750 nm. However, other studies [143, 191] showed contrary results, which indicated that $E(m)$ was decreasing in the visible range and increasing in the range larger than 800 nm. The disagreement regarding those results indicates that further investigation of $E(m)$ is necessary.

Moreover, the aforementioned research is based on *ex-situ* measurements. During the process of sampling the particles into absorption cells, aggregation will inevitably be present and influence the result, although there is dilution to prevent it. At the same time, another method was developed to investigate the wavelength dependence of $E(m)$ by using two-colour LII, which is based on the assumption that the intensity of the LII signal of soot is proportional to the absorbed energy. Therssen revealed that the ratio between $E(m)$ at 532 nm and 1064 nm is nearly 1 in a methane diffusion flame [81]. However, the two-colour technique cannot give an absolute value of $E(m)$.

In the future, some tunable continuous wave light sources may be utilised to investigate the spectral absorption behaviour of the absorption function $E(m)$ of soot particles produced in a methane diffusion flame. This is an *in-situ* measurement, so the influence of aggregation can be eliminated. Moreover, the spatial resolution of the present study is better than sampling with *ex-situ* methods.

6.2.3 Ultrafine soot measurements in inverted diffusion flames

Inverse diffusion flames (IDFs) may provide another potential direction for research. IDFs composed of a central oxidizer injected into an abundance of co-flowing fuel have been studied for many years. Arthur *et al.* [192] first compared the flame structures of IDF and normal diffusion flames (NDFs) experimentally with gaseous (CH_4, C_2H_2, C_3H_8) and liquid (benzene) hydrocarbon fuels. Their work showed that flame characteristics (*i.e.* relative stability, radiation luminosity, carbonaceous deposits, response to additives, *etc.*) are dependent on the manner in which the diffusion combustion is carried out. Wu *et al.* [193] identified six different types of flames in the mapping of methane IDFs, and found regions of high CO and H_2 concentration downstream of each flame, which is a phenomenon that is not expected in NDFs. Sidebotham *et al.* [194] investigated the transition from near to slightly sooting flames and the effects of flame temperature, fuel concentration, and fuel structure. The results suggest that the formation of the aromatic ring is an important controlling parameter in the formation of soot in IDFs and soot inception is observed only when the local temperature exceeds a critical value in a region sufficiently far from the oxidation zone. They then investigated the effect of oxygen addition to identical IDFs and found that the addition of oxygen to the fuel decreased concentrations of the pyrolytic species. This indicates that fuel pyrolysis rates were not enhanced by oxygen addition to the fuel in non-sooting IDFs.

Kaplan *et al.* [195] simulated the flow-field effect on soot formation in co-flow methane-air IDFs. The results suggest that the surface growth rate of IDFs is very small along the particle path line, which eventually results in lower soot production in IDFs, relative to NDFs. Their results are bolstered by Belvin *et al.*'s study [196], where poorly developed soot particles were found in the exhaust of IDFs. Other comparative research on IDFs and NDFs show that soot

particles are transported without passing through the highly reactive oxidation zone [197, 198]. Such studies indicate that IDFs may be applied in the study of early forming soot particles, as Leonard *et al.* predict in their study of under-ventilated combustion [199]. In the past, very few studies have been conducted on soot in IDFs using LOSE or LII. Yamamoto *et al.* [92] use the LII technique to investigate a triple port diffusion flame, which has a similar configuration to that of an IDF (the outer co-flow is air, not inert sheath gas as in normal IDFs). Results show that the triple port configuration can significantly reduce soot production. Shaddix *et al.* conducted a similar test of 2-D planer IDFs and NDFs on a Wolf hard-Parker slot burner [200]. In this case, results indicate that the soot signals are similar in the two types of flame, while many other works suggest that IDFs yield much less soot than NDFs. Mikofski *et al.* measured the soot volume fraction in ethylene-air IDFs using the single pass LOSE method [201] and Macko *et al.* conducted qualitative LII measurements on the same burner [69]. An investigation into mapping out a quantitative evaluation of the soot volume fraction in an annular IDF is required for an enhanced understanding of IDF combustion. With the techniques that we have available and the IDF burner [202], there are some potentially interesting topics worth investigating:

1) Quantitatively mapping the soot volume fraction of IDFs using LII and cavity extinction, in particular for low-sooting methane IDFs would be valuable. The advantage of cavity LOSE measurements is that they can be used due to the low concentration of soot in the IDFs. Although the UC-Berkeley group has previously performed relatively similar work [69] , their LII measurements are not quantitative and extinction data was collected on ethylene flames only.

2) Use the TiRe-LII technique to explore the relationship between the geometric mean diameter (D_m) and the co-flow nitrogen flow rate, since the GMDs can be varied by changing the nitrogen flow rate and hence changing the residence time of the soot particles in IDFs. As far as the author is aware, this is a new area waiting to be explored.

References

[1] H. Wang. Formation of nascent soot and other condensed-phase materials in flames. *Proceedings of the Combustion Institute*, 33(1):41–67, 2011.

[2] Mohammad Reza Kholghy, Armin Veshkini, and Murray John Thomson. The core-shell internal nanostructure of soot - A criterion to model soot maturity. *Carbon*, 100:508–536, 2016.

[3] Ian M. Kennedy. The health effects of combustion-generated aerosols. *Proceedings of the Combustion Institute*, 31(2):2757 – 2770, 2007.

[4] Satya B. Sardar. Seasonal and spatial variability of the size-resolved chemical composition of particulate matter (PM 10) in the Los Angeles Basin. *Journal of Geophysical Research*, 110(D7):D07S08, 2005.

[5] Long-path absorption. http://crf.sandia.gov/combustion-research-facility/diagnostics/gas-phase-diagnostics/long-path-absorption/. Accessed: 2016-01-30.

[6] Béla Tuzson, Markus Mangold, Herbert Looser, Albert Manninen, and Lukas Emmenegger. Compact multipass optical cell for laser spectroscopy. *Optics letters*, 38(3):257–9, February 2013.

[7] C. R. Shaddix and K. C. Smyth. Laser-induced incandescence measurements of soot production in steady and flickering methane, propane, and ethylene diffusion flames. *Combustion and Flame*, 107(4):418–452, 1996.

[8] C. R. Shaddix, J. E. Harrington, and K. C. Smyth. Quantitative measurements of enhanced soot production in a flickering methane/air diffusion flame. *Combustion and Flame*, 99(3-4):723–732, 1994.

[9] http://www.nist.gov/el/fire_research/flamereduc/diffusion_notesb.cfm, 2012. Accessed: 2013-01-01.

[10] O. L. Gulder and D. R. Snelling. Influence of nitrogen dilution and flame temperature on soot formation in diffusion flames. *Combustion and Flame*, 92(1-2):115–124, 1993.

[11] Ömer L Gülder. Effects of oxygen on soot formation in methane, propane, and n-butane diffusion flames. *Combustion and Flame*, 101(3):302–310, 1995.

[12] Bo Tian, Yi Gao, Saravanan Balusamy, and Simone Hochgreb. High Spatial Resolution Laser Cavity Extinction and Laser Induced Incandescence in Low Soot Producing Flames. *Applied Physics B*, 120(3):469–487, 2015.

[13] F.Einar Kruis, Heinz Fissan, and Aaron Peled. Synthesis of nanoparticles in the gas phase for electronic, optical and magnetic applicationsa review. *Journal of Aerosol Science*, 29(5-6):511–535, June 1998.

[14] Terry A Egerton. UV-AbsorptionThe Primary Process in Photocatalysis and Some Practical Consequences. *molecules*, 19:18192–18214, 2014.

[15] F. Cignoli, C. Bellomunno, S. Maffi, and G. Zizak. Laser-induced incandescence of titania nanoparticles synthesized in a flame. *Applied Physics B: Lasers and Optics*, 96:593–599, 2009.

[16] R. F. Service. Study Fingers Soot as a Major Player in Global Warming. *Science*, 319:1745, 2008.

[17] Susan Solomon, Gian-Kasper Plattner, Reto Knutti, and Pierre Friedlingstein. Irreversible climate change due to carbon dioxide emissions. *Proceedings of the National Academy of Sciences of the United States of America*, 106(6):1704–9, 2009.

[18] Jonathan A. Patz, Howard Frumkin, Tracey Holloway, Daniel J. Vimont, and Andrew Haines. Climate Change Challenges and Opportunities for Global Health. *Clinical Review & Education*, 312(15):1565, 2014.

[19] D. Dodman. Blaming cities for climate change? An analysis of urban greenhouse gas emissions inventories. *Environment and Urbanization*, 21(1):185–201, 2009.

[20] Jan Brogger, T. Eagan, G. E. Eide, P. Bakke, and A. Gulsvik. Bias in retrospective studies on trends in asthma incidence. *European Respiratory Journal*, 23(2):281–286, 2004.

[21] Maria Eugenia Monge, Barbara D'Anna, Linda Mazri, Anne Giroir-Fendler, Markus Ammann, D J Donaldson, and Christian George. Light changes the atmospheric reactivity of soot. *Proceedings of the National Academy of Sciences of the United States of America*, 107(15):6605–6609, 2010.

[22] Henning Bockhorn. *Soot Formation in Combustion: Mechanisms and Models*. Springer Berlin Heidelberg, 1994.

[23] R. J. Santoro, H. G. Semerjian, and R. A. Dobbins. Soot particle measurements in diffusion flames. *Combustion and Flame*, 51:203–218, 1983.

[24] R. J. Santoro and H. G. Semerjian. Soot formation in diffusion flames: Flow rate, fuel species and temperature effects. *Symposium (International) on Combustion*, 20(1):997–1006, 1985.

[25] H.a. Michelsen, C. Schulz, G.J. Smallwood, and S. Will. Laser-induced incandescence: Particulate diagnostics for combustion, atmospheric, and industrial applications. *Progress in Energy and Combustion Science*, pages 1–47, 2015.

[26] P Roth. In situ ultrafine particle sizing by a combination of pulsed laser heatup and particle thermal emmission. 27(1):95–104, 1996.

[27] M. Frenklach, D.W. Clary, T. Yuan, Jr. Gardiner, W.C., and S.E. Stein. Mechanism of soot formation in acetylene-oxygen mixtures. *Combustion Science and Technology*, 50(1-3):79–115, 1986. cited By 20.

[28] M. Frenklach and J. Warnatz. Detailed modeling of pah profiles in a sooting low-pressure acetylene flame. *Combustion Science and Technology*, 51(4-6):265–283, 1987. cited By 248.

[29] K. H. Homann. Fullerenes and Soot Formation New Pathways to Large Particles in Flames. *Angewandte Chemie International Edition*, 37(18), 1998.

[30] Michael Frenklach and Hai Wang. Detailed modeling of soot particle nucleation and growth. *Symposium (International) on Combustion*, 23(1):1559–1566, 1991.

[31] Henning Richter, Timothy G. Benish, Oleg A. Mazyar, William H. Green, and Jack B. Howard. Formation of Polycyclic Aromatic Hydrocarbons and their Radicals in a Nearly Sooting Premixed Benzene Flame. *Proceedings of the Combustion Institute*, 28(2):2609–2618, 2000.

[32] Angela Violi. Modeling of soot particle inception in aromatic and aliphatic premixed flames. *Combustion and Flame*, 139(4):279–287, 2004.

[33] J. S. Lighty, J. M. Veranth, and A. F. Sarofim. Combustion aerosols: Factors governing their size and composition and implications to human health. *Journal of the Air and Waste Management Association*, 50(9):1565–1618, 2000.

[34] T. C. Bond, S. J. Doherty, D. W. Fahey, P. M. Forster, T. Berntsen, B. J. Deangelo, M. G. Flanner, S. Ghan, B. Kärcher, D. Koch, S. Kinne, Y. Kondo, P. K. Quinn, M. C. Sarofim, M. G. Schultz, M. Schulz, C. Venkataraman, H. Zhang, S. Zhang, N. Bellouin, S. K. Guttikunda, P. K. Hopke, M. Z. Jacobson, J. W. Kaiser, Z. Klimont, U. Lohmann, J. P. Schwarz, D. Shindell, T. Storelvmo, S. G. Warren, and C. S. Zender. Bounding the role of black carbon in the climate system: A scientific assessment. *Journal of Geophysical Research Atmospheres*, 118(11):5380–5552, 2013.

[35] Douglas W Dockery, C. Arden Pope, Xiping Xu, John D Spengler, James H Ware, Martha E Fay, Benjamin G. Ferris, and Frank E Speizer. An Association between Air Pollution and Mortality in Six U.S. Cities. *New England Journal of Medicine*, 329(24):1753–1759, 1993.

[36] Wen-cai Zhang, Yan-ge Wang, Zheng-feng Zhu, Fang-qin Wu, Yu-dong Peng, Zhu-yue Chen, Jin-hua Yang, Jing-jing Wu, Yi-tian Lian, Mei-an He, Tang-chun Wu, and Long-xian Cheng. Regulatory T Cells Protect Fine Particulate Matter-Induced Inflammatory Responses in Human Umbilical Vein Endothelial Cells. *Mediators of Inflammation*, 2014:1–14, 2014.

[37] Byeong Jae Lee, Bumseok Kim, and Kyuhong Lee. Air pollution exposure and cardiovascular disease. *Toxicological Research*, 30(2):71–75, 2014.

[38] Marie S. O'Neill, Aristidis Veves, Antonella Zanobetti, Jeremy A. Sarnat, Diane R. Gold, Panayiotis A. Economides, Edward S. Horton, and Joel Schwartz. Diabetes enhances vulnerability to particulate air pollution-associated impairment in vascular reactivity and endothelial function. *Circulation*, 111(22):2913–2920, 2005.

[39] http://www.eea.europa.eu/data-and-maps/indicators/emissions-of-primary-particles-and-5/assessment-3, 2015. Accessed: 2016-10-11.

[40] E. M. Dannenberg. Carbon black dispersion and reinforcement. *Rubber Chemistry and Technology*, 25(4):843–857, 1952.

[41] Merton L. Studebaker. The chemistry of carbon black and reinforcement. *Rubber Chemistry and Technology*, 30(5):1400–1483, 1957.

[42] A. I. Medalia. Effect of carbon black on dynamic properties of rubber vulcanizates. *Rubber Chemistry and Technology*, 51(3):437–523, 1978.

[43] A. N. Gent, J. A. Hartwell, and Ginger Lee. Effect of carbon black on crosslinking. *Rubber Chemistry and Technology*, 76(2):517–532, 2003.

[44] Nils-Erik Olofsson, Jonathan Johnsson, Henrik Bladh, and Per-Erik Bengtsson. Soot sublimation studies in a premixed flat flame using laser-induced incandescence (LII) and elastic light scattering (ELS). *Applied Physics B*, 112(3):333–342, May 2013.

[45] B. Axelsson, R. Collin, and P. E. Bengtsson. Laser-induced incandescence for soot particle size and volume fraction measurements using on-line extinction calibration. *Applied Physics B*, 72(3):367–372, 2001.

[46] G. Cléon, T. Amodeo, a. Faccinetto, and P. Desgroux. Laser induced incandescence determination oftheratio ofthesoot absorption functions at 532nm and 1064nm inthenucleation zone of a low pressure premixed sooting flame. *Applied Physics B*, 104(2):297–305, February 2011.

[47] M Commodo and S Violi. Soot and nanoparticle formation in laminar and turbulent flames. *Combustion science ...*, (November 2012):37–41, 2007.

[48] H.-H. Grotheer, K. Wolf, and K. Hoffmann. Photoionization mass spectrometry for the investigation ofcombustion generated nascent nanoparticles and their relation tolaser induced incandescence. *Applied Physics B*, 104(2):367–383, February 2011.

[49] S. Maffi, S. Iuliis, F. Cignoli, and G. Zizak. Investigation on thermal accommodation coefficient and soot absorption function with two-color Tire-LII technique in rich premixed flames. *Applied Physics B*, 104(2):357–366, May 2011.

[50] M. Hofmann, B. F. Kock, T. Dreier, H. Jander, and C. Schulz. Laser-induced incandescence for soot-particle sizing at elevated pressure. *Applied Physics B*, 90(3-4):629–639, December 2007.

[51] P. Desgroux, X. Mercier, B. Lefort, R. Lemaire, E. Therssen, and J. F. Pauwels. Soot volume fraction measurement in low-pressure methane flames by combining laser-induced incandescence and cavity ring-down spectroscopy: Effect of pressure on soot formation. *Combustion and Flame*, 155(1-2):289–301, 2008.

[52] H. Bladh, J. Johnsson, N.-E. Olofsson, a. Bohlin, and P.-E. Bengtsson. Optical soot characterization using two-color laser-induced incandescence (2C-LII) in the soot growth region of a premixed flat flame. *Proceedings of the Combustion Institute*, 33(1):641–648, 2011.

[53] A. E. Karata and Ö. L. Gülder. Soot formation in high pressure laminar diffusion flames. *Progress in Energy and Combustion Science*, 38(6):818–845, 2012.

[54] Stephan Schraml, Stefan Dankers, Katharina Bader, Stefan Will, and Alfred Leipertz. Soot temperature measurements and implications for time-resolved laser-induced incandescence (TIRE-LII). *Combustion and Flame*, 120(4):439–450, March 2000.

[55] B. M. Crosland, M. R. Johnson, and K. a. Thomson. Analysis of uncertainties in instantaneous soot volume fraction measurements using two-dimensional, auto-compensating, laser-induced incandescence (2D-AC-LII). *Applied Physics B*, 102(1):173–183, July 2010.

[56] F Goulay, P Schrader, L Nemes, M Dansson, and H Michelsen. Photochemical interferences for laser-induced incandescence of flame-generated soot. *Proceedings of the Combustion Institute*, 32(1):963–970, 2009.

[57] J. M. Headrick, F. Goulay, P. E. Schrader, and H. a. Michelsen. High-vacuum time-resolved laser-induced incandescence offlame-generated soot. *Applied Physics B*, 104(2):439–450, March 2011.

[58] Y. Kobayashi, T. Furuhata, K. Amagai, and M. Arai. Soot precursor measurements in benzene and hexane diffusion flames. *Combustion and Flame*, 154(3):346–355, August 2008.

[59] R. L. Vander Wal, TM Ticich, and A Brock Stephens. Can soot primary particle size be determined using laser-induced incandescence? *Combustion and flame*, 116(116):291–296, 1999.

[60] Hyun I. Joo. *Soot Formation in Non-Premixed Laminar Flames at Subcritical and Supercritical Pressures*. Phd thesis, University of Toronto, 2010.

[61] N. H. Qamar, Z. T. Alwahabi, Q. N. Chan, G. J. Nathan, D. Roekaerts, and K. D. King. Soot volume fraction in a piloted turbulent jet non-premixed flame of natural gas. *Combustion and Flame*, 156(7):1339–1347, 2009.

[62] Seong-Young Lee, Stephen R. Turns, and Robert J. Santoro. Measurements of soot, OH, and PAH concentrations in turbulent ethylene/air jet flames. *Combustion and Flame*, 156(12):2264–2275, December 2009.

[63] M. Köhler, K. P. Geigle, W. Meier, B. M. Crosland, K. A. Thomson, and G. J. Smallwood. Sooting turbulent jet flame: characterization and quantitative soot measurements. *Applied Physics B*, 104(2):409–425, 2011.

[64] Y. Xin and J. P. Gore. Two-dimensional soot distributions in buoyant turbulent fires. *Proceedings of the Combustion Institute*, 30(1):719–726, 2005.

[65] K. Frederickson, S. P. Kearney, and T. W. Grasser. Laser-induced incandescence measurements of soot in turbulent pool fires. *Applied optics*, 50(4):A49–59, 2011.

[66] J ZHANG and K SONG. Tunable Diode Laser Absorption Spectroscopy System for Trace Ethylene Detection. *Spectroscopy and Spectral Analysis*, 32(10):2875–2878, 2012.

[67] H. Bladh, J. Johnsson, and P.-E. Bengtsson. On the dependence of the laser-induced incandescence (LII) signal on soot volume fraction for variations in particle size. *Applied Physics B*, 90(1):109–125, 2007.

[68] C. Schulz, B. F. Kock, M. Hofmann, H. Michelsen, S. Will, B. Bougie, R. Suntz, and G. J. Smallwood. Laser-induced incandescence: recent trends and current questions. *Applied Physics B*, 83(3):333–354, 2006.

[69] K Macko, MA Mikofski, and C Fernandez-Pello. Laser Extinction in Laminar Inverse Diffusion Flames. *Combustion Processes Laboratories, UC Berkeley*, 2005.

[70] M. P. B. Musculus and L. M. Pickett. Diagnostic considerations for optical laser-extinction measurements of soot in high-pressure transient combustion environments. *Combustion and flame*, 141(4):371–391, 2005.

[71] H. Zhao and N. Ladommatos. Optical diagnostics for soot and temperature measurement in diesel engines. *Progress in Energy and Combustion Science*, 24(3):221 – 255, 1998.

[72] D. R. Snelling, K. A. Thomson, G. J. Smallwood, and O. L. Gülder. Two-dimensional imaging of soot volume fraction in laminar diffusion flames. *Applied optics*, 38(12):2478–85, April 1999.

[73] Javis a Nwaboh, Olav Werhahn, Pascal Ortwein, Detlef Schiel, and Volker Ebert. Laser-spectrometric gas analysis: CO 2 TDLAS at 2 m. *Measurement Science and Technology*, 24(1):015202, January 2013.

[74] D. Mazzotti and G. Giusfredi. High-sensitivity spectroscopy of CO_2 around 4.25 μm with difference-frequency radiation. *Optics and Lasers in Engineering*, 37:143–158, 2002.

[75] Hai-bo Qian, David Turton, PW Seakins, and MJ Pilling. Dynamic frequency stabilization of infrared diode laser for kinetic studies. *Chemical Physics Letters*, (May):57–64, 2000.

[76] C. G. Tarsitano and C. R. Webster. Multilaser Herriott cell for planetary tunable laser spectrometers. *Applied optics*, 46(28):6923–6935, 2007.

[77] A. Manninen, B. Tuzson, H. Looser, Y. Bonetti, and L. Emmenegger. Versatile multipass cell for laser spectroscopic trace gas analysis. *Applied Physics B*, 109(3):461–466, 2012.

[78] a O'Keefe, D a G Deacon, and a Okeefe. Cavity Ring-Down Optical Spectrometer for Absorption measurements using pulsed laser sources. *Review of Scientific Instruments*, 59(12):2544, 1988.

[79] Y. Bouvier, C. Mihesan, M. Ziskind, E. Therssen, C. Focsa, J. F. Pauwels, and P. Desgroux. Molecular species adsorbed on soot particles issued from low sooting methane and acetylene laminar flames: A laser-based experiment. *Proceedings of the Combustion Institute*, 31(1):841–849, 2007.

[80] C. Schoemaecker-Moreau, E. Therssen, X. Mercier, J. F. Pauwels, and P. Desgroux. Two-color laser-induced incandescence and cavity ring-down spectroscopy for sensitive and quantitative imaging of soot and PAHs in flames. *Applied Physics B*, 78(3-4):485–492, 2004.

[81] E. Therssen, Y. Bouvier, C. Schoemaecker-Moreau, X. Mercier, P. Desgroux, M. Ziskind, and C. Focsa. Determination of the ratio of soot refractive index function E(m) at the two wavelengths 532 and 1064nm by laser induced incandescence. *Applied Physics B*, 89(2-3):417–427, 2007.

[82] R. L. Vander Wal. Calibration and comparison of laser-induced incandescence with cavity ring-down. *Symposium (International) on Combustion*, 27(1):59–67, 1998.

[83] R. L. Vander Wal and T. M. Ticich. Cavity ringdown and laser-induced incandescence measurements of soot. *Applied optics*, 38(9):1444–1451, 1999.

[84] R. Engeln, G. Berden, R. Peeters, and G. Meijer. Cavity enhanced absorption and cavity enhanced magnetic rotation spectroscopy. *Review of Scientific Instruments*, 69(11):3763, 1998.

[85] L. A. Melton. Soot diagnostic based on laser heating. *Applied Optics*, 23(13):2201–2208, 1984.

[86] R J Santoro, T T Yeh, J J Horvath, and H G Semerjian. The Transport and Growth of Soot Particles in Laminar Diffusion Flames, 1987.

[87] D. R. Snelling, G. J. Smallwood, F. Liu, Ö. L. Gülder, and W. D. Bachalo. A calibration-independent laser-induced incandescence technique for soot measurement by detecting absolute light intensity. *Applied optics*, 44(31):6773–6785, 2005.

[88] R. L. Vander Wal and K. J. Weiland. Laser-induced incandescence: Development and characterization towards a measurement of soot-volume fraction. *Applied Physics B Laser and Optics*, 59(4):445–452, 1994.

[89] Rahul Puri, Robert J. Santoro, and Kermit C. Smyth. The oxidation of soot and carbon monoxide in hydrocarbon diffusion flames. *Combustion and Flame*, 97(2):125–144, 1994.

[90] F. Liu and G. J. Smallwood. Relationship between soot volume fraction and LII signal in AC-LII: effect of primary soot particle diameter polydispersity. *Applied Physics B*, 112(3):307–319, 2013.

[91] S. De Iuliis, F. Migliorini, F. Cignoli, and G. Zizak. 2D soot volume fraction imaging in an ethylene diffusion flame by two-color laser-induced incandescence (2C-LII) technique and comparison with results from other optical diagnostics. *Proceedings of the Combustion Institute*, 31(1):869–876, 2007.

[92] K. Yamamoto and M. Takemoto. Measurement of PAH and soot of diffusion flames in a triple port burner. *Fuel Processing Technology*, 107:99–106, 2013.

[93] B Kock, B Tribalet, C Schulz, and P Roth. Two-color time-resolved LII applied to soot particle sizing in the cylinder of a Diesel engine. *Combustion and Flame*, 147(1-2):79–92, October 2006.

[94] a.V. Eremin, E.V. Gurentsov, M. Hofmann, B.F. Kock, and C. Schulz. TR-LII for sizing of carbon particles forming at room temperature. *Applied Physics B*, 83(3):449–454, April 2006.

[95] K.J. Daun, B.J. Stagg, F. Liu, G.J. Smallwood, and D.R. Snelling. Determining aerosol particle size distributions using time-resolved laser-induced incandescence. *Applied Physics B*, 87(2):363–372, February 2007.

[96] M. Charwath, R. Suntz, and H. Bockhorn. Constraints of two-colour TiRe-LII at elevated pressures. *Applied Physics B*, 104(2):427–438, mar 2011.

[97] Thilo Lehre, Rainer Suntz, and Henning Bockhorn. Time-resolved two-color LII: size distributions of nano-particles from gas-to-particle synthesis. *Proceedings of the Combustion Institute*, 30(2):2585–2593, jan 2005.

[98] B Axelsson, R Collin, and P E Bengtsson. Laser-induced incandescence for soot particle size measurements in premixed flat flames. *Applied optics*, 39(21):3683–90, July 2000.

[99] R. W. Weeks. Aerosol particle sizes from light emission during excitation by TEA CO2 laser pulses. *Journal of Applied Physics*, 45(10):4661, 1974.

[100] Stefan Will, Stephan Schraml, Katharina Bader, and Alfred Leipertz. Performance characteristics of soot primary laser-induced incandescence. *Applied Physics B*, 37(24), 1998.

[101] Stefan Will, Stephan Schraml, Katharina Bader, and Alfred Leipertz. Performance Characteristics of Soot Primary Particle Size Measurements by Time-Resolved Laser-Induced Incandescence, August 1998.

[102] Jun Hayashi, Hiroaki Watanabe, Ryoichi Kurose, and Fumiteru Akamatsu. Effects of fuel droplet size on soot formation in spray flames formed in a laminar counterflow. *Combustion and Flame*, 158(12):2559–2568, December 2011.

[103] C Allouis and A D'ALESSIO. Time resolved laser induced incandescence for soot and cenospheres measurements in oil flames. *Combustion science and ...*, (October 2012):37–41, 2000.

[104] C Allouis, F Rosano, F Beretta, and a D'Alessio. A possible radiative model for micronic carbonaceous particle sizing based on time-resolved laser-induced incandescence. *Measurement Science and Technology*, 13(3):401–410, March 2002.

[105] H.a. Michelsen. Laser-induced incandescence of flame-generated soot on a picosecond time scale. *Applied Physics B*, 83(3):443–448, April 2006.

[106] BF Kock, T Eckhardt, and P Roth. In-cylinder sizing of Diesel particles by time-resolved laser-induced incandescence (TR-LII). *Proceedings of the Combustion Institute*, 2002.

[107] Barbara Menkiel, Arjan Donkerbroek, Renate Uitz, Roger Cracknell, and Lionel Ganippa. Measurement of in-cylinder soot particles and their distribution in an optical HSDI diesel engine using time resolved laser induced incandescence (TR-LII). *Combustion and Flame*, 159(9):2985–2998, September 2012.

[108] Jongil Park, Hoon Chul Ryoo, Hong Sik Chun, Soonho Song, Jae Won Hahn, and Kwang Min Chun. A Study on Time-Resolved Laser Induced Incandescence Analysis Method for the Measurement of Primary Particle Size in Diesel Exhaust. *JSME International Journal Series B*, 49(4):1351–1357, 2006.

[109] C Tornatore, S S Merola, and B M Vaglieco. Particle and nanoparticle characterization at the exhaust of internal combustion engines. *Proceedings of the Institution of Mechanical Engineers, Part D: Journal of Automobile Engineering*, 222(11):2195–2217, November 2008.

[110] R L Vander Wal, T M Ticich, and J R West. Laser-induced incandescence applied to metal nanostructures. *Applied optics*, 38(27):5867–5879, 1999.

[111] S. Maffi, F. Cignoli, C. Bellomunno, S. De Iuliis, and G. Zizak. Spectral effects in laser induced incandescence application to flame-made titania nanoparticles. *Spectrochimica Acta - Part B Atomic Spectroscopy*, 63:202–209, 2008.

[112] K J Daun, J T Titantah, and M Karttunen. Molecular dynamics simulation of thermal accommodation coefficients for laser-induced incandescence sizing of nickel particles. *Applied Physics B*, 107(1):221–228, feb 2012.

[113] G. Yang, T. Steven, P. Kent, and I.M. Kennedy. Synthesis of an ultrafine iron and soot aerosol for the evaluation of particle toxicity. *Aerosol Science and Technology*, 35(3):759–766, 2001.

[114] J. V. Pastor, J. M. García, J. M. Pastor, and J. E. Buitrago. Analysis of calibration techniques for laser-induced incandescence measurements in flames. *Measurement Science and Technology*, 17(12):3279–3288, 2006.

[115] A. Fuentes, G. Legros, H. El-Rabii, J. P. Vantelon, P. Joulain, and J. L. Torero. Laser-induced incandescence calibration in a three-dimensional laminar diffusion flame. *Experiments in Fluids*, 43(6):939–948, 2007.

[116] J. Zerbs, K. P. Geigle, O. Lammel, J. Hader, R. Stirn, R. Hadef, and W. Meier. The influence of wavelength in extinction measurements and beam steering in laser-induced incandescence measurements in sooting flames. *Applied Physics B*, 96(4):683–694, 2009.

[117] K. A. Thomson and M. R. Johnson. Diffuse-light two-dimensional line-of-sight attenuation for soot concentration measurements. *Applied Optics*, 5(47):694–703, 2008.

[118] T.C. Williams, C.R. Shaddix, K.a. Jensen, and J.M. Suo-Anttila. Measurement of the dimensionless extinction coefficient of soot within laminar diffusion flames. *International Journal of Heat and Mass Transfer*, 50(7-8):1616–1630, apr 2007.

[119] K. Krzempek, M. Jahjah, R. Lewicki, P. Stefaski, S. So, D. Thomazy, and F. K. Tittel. CW DFB RT diode laser-based sensor for trace-gas detection of ethane using a novel compact multipass gas absorption cell. *Applied Physics B*, 112(4):461–465, 2013.

[120] W. Cai and C. F. Kaminski. Multiplexed absorption tomography with calibration-free wavelength modulation spectroscopy. *Applied Physics Letters*, 104(15):154106, 2014.

[121] L. Ma, J. Ye, P. Dubé, and J. L. Hall. Ultrasensitive frequency-modulation spectroscopy enhanced by a high-finesse optical cavity: theory and application to overtone transitions of C_2H_2 and C_2HD. *Journal of the Optical Society of America B*, 16(12):2255–2268, 1999.

[122] S. Gersen, A. V. Mokhov, and H. B. Levinsky. Extractive probe/TDLAS measurements of acetylene in atmospheric-pressure fuel-rich premixed methane/air flames. *Combustion and Flame*, 143(3):333–336, 2005.

[123] T. Cai, G. Wang, Z. Cao, W. Zhang, and X. Gao. Sensor for headspace pressure and H_2O concentration measurements in closed vials by tunable diode laser absorption spectroscopy. *Optics and Lasers in Engineering*, 58:48–53, 2014.

[124] S. Basu, D. E. Lambe, and R. Kumar. Water vapor and carbon dioxide species measurements in narrow channels. *International Journal of Heat and Mass Transfer*, 53(4):703–714, 2010.

[125] T. Le Barbu, I. Vinogradov, G. Durry, O. Korablev, E. Chassefière, and J. L. Bertaux. TDLAS a laser diode sensor for the in situ monitoring of H_2O, CO_2 and their isotopes in the Martian atmosphere. *Advances in Space Research*, 38(4):718–725, 2006.

[126] G. Durry, L. Joly, T. Le Barbu, B. Parvitte, and V. Zéninari. Laser diode spectroscopy of the H_2O isotopologues in the 2.64μm region for the in situ monitoring of the Martian atmosphere. *Infrared Physics & Technology*, 51(3):229–235, 2008.

[127] S. Wagner, B. T. Fisher, J. W. Fleming, and V. Ebert. TDLAS-based in situ measurement of absolute acetylene concentrations in laminar 2D diffusion flames. *Proceedings of the Combustion Institute*, 32(1):839–846, 2009.

[128] J. Ropcke, L. Mechold, M. Kaning, W. Y. Fan, and P. B. Davies. Tunable Diode Laser Diagnostic Studies of H_2 -Ar-O_2 Microwave Plasmas Containing Methane or Methanol. *Plasma Chemistry and Plasma Processing*, 19(3):395–419, 1999.

[129] D. Tree and J. Dec. Extinction measurements of in-cylinder soot deposition in a heavy-duty DI diesel engine. *SAE Technical Paper*, 2001-01-1296, 2001.

[130] K. Song, Y. Lee, and T. Litzinger. Effects of emulsified fuels on soot evolution in an optically-accessible DI diesel engine. *SAE Technical Paper*, 2000-01-2794, 2000.

[131] J. H. Lambert. *Photometria, sive, De mensura et gradibus luminis, colorum et umbrae (Photometry, or On The Measure and Gradations of light, Color, and Shade),Augsburg, Germany.* Eberhardt Klett, 1760.

[132] H. W. Beer. Bestimmung der absorption des roten lichts in färbigen flüssigkeiten (determination of the absorption of red light in coloured liquids). *Annalen der Physik und Chemie*, 86:78 – 88, 1852.

[133] Michael F. Modest. *Radiative Heat Transfer.* Academic Press, 2003.

[134] T L Farias, U Ö Köylü, and M G Carvalho. Range of validity of the Rayleigh-Debye-Gans theory for optics of fractal aggregates. *Applied optics*, 35(33):6560–7, November 1996.

[135] S. S. Krishnan, K. Lin, and G. M. Faeth. Extinction and Scattering Properties of Soot Emitted From Buoyant Turbulent Diffusion Flames. *Journal of Heat Transfer*, 123(2):331, 2001.

[136] J. Johnsson, H. Bladh, N.-E. Olofsson, and P.-E. Bengtsson. Influence of soot aggregate structure on particle sizing using laser-induced incandescence: importance of bridging between primary particles. *Applied Physics B*, 112(3):321–332, February 2013.

[137] F. Liu, K. A. Thomson, and G. J. Smallwood. Numerical investigation of the effect of signal trapping on soot measurements using LII in laminar coflow diffusion flames. *Applied Physics B*, 96(4):671–682, 2009.

[138] C. J. Dasch. One-dimensional tomography: a comparison of Abel, onion-peeling, and filtered backprojection methods. *Applied optics*, 31(8):1146–52, 1992.

[139] S. De Iuliis, F. Migliorini, F. Cignoli, and G. Zizak. Peak soot temperature in laser-induced incandescence measurements. *Applied Physics B*, 83(3):397–402, 2006.

[140] M. I. Mishchenko, L. D. Travis, and A. A. Lacis. *Scattering, Absorption, and Emmision of Light by Small Particles*. 2002.

[141] A. D'Alessio, A. Di Lorenzo, F. Beretta, and C. Venitozzi. Optical and chemical investigations on fuel-rich methane-oxygen premixed flames at atmospheric pressure. *Symposium (International) on Combustion*, 14:941–953, 1973.

[142] J. Yon, R. Lemaire, E. Therssen, P. Desgroux, A. Coppalle, and K. F. Ren. Examination of wavelength dependent soot optical properties of diesel and diesel/rapeseed methyl ester mixture by extinction spectra analysis and LII measurements. *Applied Physics B*, 104(2):253–271, 2011.

[143] W. H. Dalzell and A. F. Sarofim. Optical constants of soot and their application to heat-flux calculations. *J. Heat Transfer*, 91:100–104, 1969.

[144] K. C. Smyth and C. R. Shaddix. The elusive history of $m \approx 1.57 - 0.56i$ for the refractive index of soot. *Combustion and Flame*, 107(3):314–320, 1996.

[145] J. H. Kent and D. R. Honnery. A soot formation rate map for a laminar ethylene diffusion flame. *Combustion and Flame*, 79(3-4):287–298, 1990.

[146] D. R. Honnery and J. H. Kent. Soot formation in long ethylene diffusion flames. *Combustion and Flame*, 82(3-4):426–434, 1990.

[147] Stephen Turns. *An Introduction to Combustion: Concepts and Applications Second Edition [2/Ed]*. McGraw-Hill Science/Engineering/Math, second edition, 2001.

[148] F.G. Roper. The prediction of laminar jet diffusion flame sizes: Part I. Theoretical model. *Combustion and Flame*, 29:219–226, 1977.

[149] R. M. Williams and A. A. Westenberg. *Flame Structure*. McGraw-Hill, New York and London, 1965.

[150] W. M. Haynes. *CRC Handbook of Chemistry and Physics*. CRC Press, New York, 95 edition, 2014.

[151] W. Sutherland. The viscosity of gases and molecular force. *Philosophical Magazine*, S. 5.(36):507–531, 1893.

[152] Crane. *Flow of fluids through valves, fittings, and pipe. Technical Paper No. 410 (TP 410)*. USA, 2009.

[153] F.G. Roper, C. Smith, and a.C. Cunningham. The prediction of laminar jet diffusion flame sizes: Part II. Experimental verification. *Combustion and Flame*, 29:227–234, 1977.

[154] RL Axelbalim, WL Flower, and CK Law. Dilution and temperature effects of inert addition on soot formation in counterflow diffusion flames. *Combustion science and technology*, 61:51–73, 1988.

[155] Goldenberg M Smith G, Golden D, Frenklach M, Moriarty N, Eiteneer B. GRI 3.0.

[156] S. Venkatesh and K. Saito. Estimates on the Effect of Chlorine on the Global Soot Production Rates in Laminar Hydrocarbon-Air Diffusion Flames. *Combustion Science and Technology*, 85(1-6):297–311, sep 1992.

[157] P.a. Tesner and S.V. Shurupov. Some physico-chemical parameters of soot formation during pyrolysis of methane and methane-acetylene and methane-benzene mixtures. *Symposium (International) on Combustion*, 25(1):653–659, 1994.

[158] Hongsheng Guo, Fengshan Liu, Gregory J. Smallwood, and Ömer L. Gülder. Numerical study on the influence of hydrogen addition on soot formation in a laminar ethylene-air diffusion flame. *Combustion and Flame*, 145(1-2):324–338, 2006.

[159] B. M. Kumfer, S. a. Skeen, and R. L. Axelbaum. Soot inception limits in laminar diffusion flames with application to oxy-fuel combustion. *Combustion and Flame*, 154(3):546–556, 2008.

[160] K Oh, U Lee, H Shin, and E Lee. The evolution of incipient soot particles in an inverse diffusion flame of ethene. *Combustion and Flame*, 140(3):249–254, feb 2005.

[161] Stefan Will, Stephan Schraml, and Alfred Leipertz. Two-dimensional soot-particle sizing by time-resolved laser-induced incandescence. *Optics Letters*, 20(22):2342–2344, 1995.

[162] Redjem Hadef, Klaus Peter Geigle, Jochen Zerbs, Robert a. Sawchuk, and David R. Snelling. The concept of 2D gated imaging for particle sizing in a laminar diffusion flame. *Applied Physics B*, 112(3):395–408, May 2013.

[163] Z.W. Sun, D.H. Gu, G.J. Nathan, Z.T. Alwahabi, and B.B. Dally. Single-shot, Time-Resolved planar Laser-Induced Incandescence (TiRe-LII) for soot primary particle sizing in flames. *Proceedings of the Combustion Institute*, 35(3):3673–3680, 2015.

[164] H.a. Michelsen, F. Liu, B.F. Kock, H. Bladh, A. Boiarciuc, M. Charwath, T. Dreier, R. Hadef, M. Hofmann, J. Reimann, S. Will, P.-E. Bengtsson, H. Bockhorn, F. Foucher, K.-P. Geigle, C. Mounaïm-Rousselle, C. Schulz, R. Stirn, B. Tribalet, and R. Suntz. Modeling laser-induced incandescence of soot: a summary and comparison of LII models. *Applied Physics B*, 87(3):503–521, April 2007.

[165] B. Mewes and J.M. Seitzman. Soot volume fraction and particle size measurements with laser-induced incandescence. *Applied optics*, 36(3):709–17, 1997.

[166] H. A. Michelsen. Understanding and predicting the temporal response of laser-induced incandescence from carbonaceous particles. *The Journal of Chemical Physics*, 118(15):7012–7045, 2003.

[167] Thomas Blacha, Massimiliano Di Domenico, Peter Gerlinger, and Manfred Aigner. Soot predictions in premixed and non-premixed laminar flames using a sectional approach for PAHs and soot. *Combustion and Flame*, 159(1):181–193, January 2012.

[168] T. Dreier, B. Bougie, N. Dam, and T. Gerber. Modeling of time-resolved laser-induced incandescence transients for particle sizing in high-pressure spray combustion environments: a comparative study. *Applied Physics B*, 83(3):403–411, apr 2006.

[169] H. R. Leider, O. H. Krikorian, and D. a. Young. Thermodynamic properties of carbon up to the critical point. *Carbon*, 11(5):555–563, 1973.

[170] F. Liu, K. J. Daun, D. R. Snelling, and G. J. Smallwood. Heat conduction from a spherical nano-particle: Status of modeling heat conduction in laser-induced incandescence. *Applied Physics B: Lasers and Optics*, 83(3):355–382, 2006.

[171] B.J. McCoy and C.Y. Cha. Transport phenomena in the rarefied gas transition regime. *Chemical Engineering Science*, 29(2):381–388, 1974.

[172] K. J. Daun, T. A. Sipkens, J. T. Titantah, and M. Karttunen. Thermal accommodation coefficients for laser-induced incandescence sizing of metal nanoparticles in monatomic gases. *Applied Physics B*, 112(3):409–420, May 2013.

[173] H. a. Michelsen, M. a. Linne, B. F. Kock, M. Hofmann, B. Tribalet, and C. Schulz. Modeling laser-induced incandescence of soot: enthalpy changes during sublimation, conduction, and oxidation. *Applied Physics B*, 93(2-3):645–656, September 2008.

[174] a. D'Anna, a. Rolande, C. Allouis, P. Minutolo, a. D'Alessio, and Christopher Shaddix. Nano-organic carbon and soot particle measurements in a laminar ethylene diffusion flame. *Proceedings of the Combustion Institute*, 30 I(1):1449–1456, 2005.

[175] T. a. Sipkens, R. Mansmann, K. J. Daun, N. Petermann, J. T. Titantah, M. Karttunen, H. Wiggers, T. Dreier, and C. Schulz. In situ nanoparticle size measurements of gas-borne silicon nanoparticles by time-resolved laser-induced incandescence. *Applied Physics B: Lasers and Optics*, pages 1–14, 2013.

[176] F. Liu, B. J. Stagg, D. R. Snelling, and G. J. Smallwood. Effects of primary soot particle size distribution on the temperature of soot particles heated by a nanosecond pulsed laser in an atmospheric laminar diffusion flame. *International Journal of Heat and Mass Transfer*, 49(3-4):777–788, February 2006.

[177] H. Oltmann, J. Reimann, and S. Will. Single-shot measurement of soot aggregate sizes by wide-angle light scattering (WALS). *Applied Physics B: Lasers and Optics*, 106(1):171–183, 2012.

[178] F. Xu, P. B. Sunderland, and G. M. Faeth. Soot formation in laminar premixed ethylene/air flames at atmospheric pressure. *Combustion and Flame*, 108(4):471–493, 1997.

[179] Paul Roth. Particle synthesis in flames. *Proceedings of the Combustion Institute*, 31 II:1773–1788, 2007.

[180] Catherine B. Almquist and Pratim Biswas. Role of Synthesis Method and Particle Size of Nanostructured TiO2 on Its Photoactivity. *Journal of Catalysis*, 212(2):145–156, 2002.

[181] Boris F. Kock, Can Kayan, Jörg Knipping, Hans R. Orthner, Paul Roth, Daniel Rosner, and Stefan Will. Comparison of LII and TEM sizing during synthesis of iron particle chains. *Proceedings of the Combustion Institute*, 30 I:1689–1697, 2005.

[182] Yoshinori Murakami, Tsuyoshi Sugatani, and Yoshio Nosaka. Laser-induced incandescence study on the metal aerosol particles as the effect of the surrounding gas medium. *Journal of Physical Chemistry A*, 109:8994–9000, 2005.

[183] Hsiao-Kang Ma and Hsiung-An Yang. A comparative study of TiO2 nanoparticles synthesized in premixed and diffusion flames. *Journal of Thermal Science*, 19(6):567–575, 2010.

[184] N.S. Karan, a. Agrawal, P.K. Pandey, P. Smitha, S.J. Sharma, D.P. Mishra, and N.S. Gajbhiye. Diffusion flame synthesis of hollow, anatase TiO2 nanoparticles. *Materials Science and Engineering: B*, 163:128–133, 2009.

[185] Pratap M. Rao and Xiaolin Zheng. Flame synthesis of tungsten oxide nanostructures on diverse substrates. *Proceedings of the Combustion Institute*, 33(2):1891–1898, 2011.

[186] E. V. Gurentsov and a. V. Eremin. Size measurement of carbon and iron nanoparticles by laser induced incadescence. *High Temperature*, 49(5):667–673, 2011.

[187] a. Eremin, E. Gurentsov, E. Popova, and K. Priemchenko. Size dependence of complex refractive index function of growing nanoparticles. *Applied Physics B*, 104(2):285–295, feb 2011.

[188] T. Sipkens, G. Joshi, K. J. Daun, and Y. Murakami. Sizing of Molybdenum Nanoparticles Using Time-Resolved Laser-Induced Incandescence. *Journal of Heat Transfer*, 135(May 2013):052401, 2013.

[189] RA Dobbins, GW Mulholland, and NP Bryner. Comparison of A Fractal Smoke Optics Model With Light Extinction Measurements. *Atmospheric Environment*, 28(5):889–897, 1994.

[190] ÖÜ Köylu and GM Faeth. Spectral Extinction Coefficients of Soot Aggregates From Turbulent Diffusion Flames. *Journal of Heat Transfer*, 118(2):415–421, 1996.

[191] H. Chang and T. T. Charalampopoulos. Determination of the wavelength dependence of refractive indices of flame soot. *Proceedings: Mathematical and Physical Sciences*, 430(1880):577–591, 1990.

[192] JR Arthur and DH Napier. Experimental characterization of methane inverse diffusion flame. *Symposium (International) on Combustion*, (5):303–316, 1955.

[193] KT Wu and RH Essenhigh. Mapping and structure of inverse diffusion flames of methane. *Symposium (International) on Combustion*, pages 1925–1932, 1984.

[194] G Sidebotham and I Glassman. Flame temperature, fuel structure, and fuel concentration effects on soot formation in inverse diffusion flames. *Combustion and Flame*, 90(3-4):269–283, sep 1992.

[195] C.R Kaplan and K Kailasanath. Flow-field effects on soot formation in normal and inverse methaneair diffusion flames. *Combustion and Flame*, 124(1-2):275–294, jan 2001.

[196] Linda G. Blevins, Robert a. Fletcher, Bruce a. Benner, Eric B. Steel, and George W. Mulholland. The existence of young soot in the exhaust of inverse diffusion flames. *Proceedings of the Combustion Institute*, 29(2):2325–2333, jan 2002.

[197] D. B. Makel and I. M. Kennedy. Soot Formation In Laminar Inverse Diffusion Flames. *Combustion Science and Technology*, 97(4-6):303–314, may 1994.

[198] KT Kang, JY Hwang, SH Chung, and W Lee. Soot zone structure and sooting limit in diffusion flames: Comparison of counterflow and co-flow flames. *Combustion and Flame*, 281:266–281, 1997.

[199] S Leonard, GW Mulholland, R Puri, and RJ Santoro. Generation of CO and smoke during underventilated combustion. *Combustion and Flame*, 98:20–34, 1994.

[200] Christopher R. Shaddix, Timothy C. Williams, Linda G. Blevins, and Robert W. Schefer. Flame structure of steady and pulsed sooting inverse jet diffusion flames. *Proceedings of the Combustion Institute*, 30(1):1501 – 1508, 2005.

[201] MA Mikofski, TC Williams, Christopher R Shaddix, and Linda G Blevins. Effect of varied air flow on flame structure of laminar inverse diffusion flames. In *International Symposium on Combustion, Abstracts of Works-in-Progress Posters*, page 362, 2004.

[202] Marc E. J. Stettler, Jacob J. Swanson, Steven R. H. Barrett, and Adam M. Boies. Updated Correlation Between Aircraft Smoke Number and Black Carbon Concentration. *Aerosol Science and Technology*, 47(11):1205–1214, nov 2013.

Appendix A

Calibration of the cavity mirrors

The reflectances of the two mirrors, r_1 and r_2, are important parameters in the experiment, thus a precise calibration of the mirrors was performed. In the calibration, the incident and reflected powers were measured by a Thorlabs Digital Optical Power and Energy Meter PM100D and S310C sensor.

The intensities of the incident and reflected beam were measured with the setup shown in Fig. A.1.

The results are shown in Fig. A.2.

Assuming I_0 is the total laser beam intensity; I_{r1} is the reflected beam power by mirror 1, and I_{r2} is the reflected beam power by mirror 2,
we have:

$$\begin{cases} r_1 = \dfrac{\overline{I_{r1}}}{\overline{I_0}} = \dfrac{0.074991}{0.076436} = 98.11\% \\ r_2 = \dfrac{\overline{I_{r2}}}{\overline{I_0}} = \dfrac{0.075055}{0.076436} = 98.19\% \end{cases} \tag{A.1}$$

The standard deviation determined for the measurement was approximated as the sum of the uncorrelated:

$$\begin{cases} {\sigma_{r1}}^2 = \left(\dfrac{1}{I_0}\right)^2 {\sigma_{Ir1}}^2 + \left(\dfrac{I_{r1}}{{I_0}^2}\right)^2 {\sigma_{I0}}^2 \\ {\sigma_{r2}}^2 = \left(\dfrac{1}{I_0}\right)^2 {\sigma_{Ir2}}^2 + \left(\dfrac{I_{r2}}{{I_0}^2}\right)^2 {\sigma_{I0}}^2 \end{cases} \tag{A.2}$$

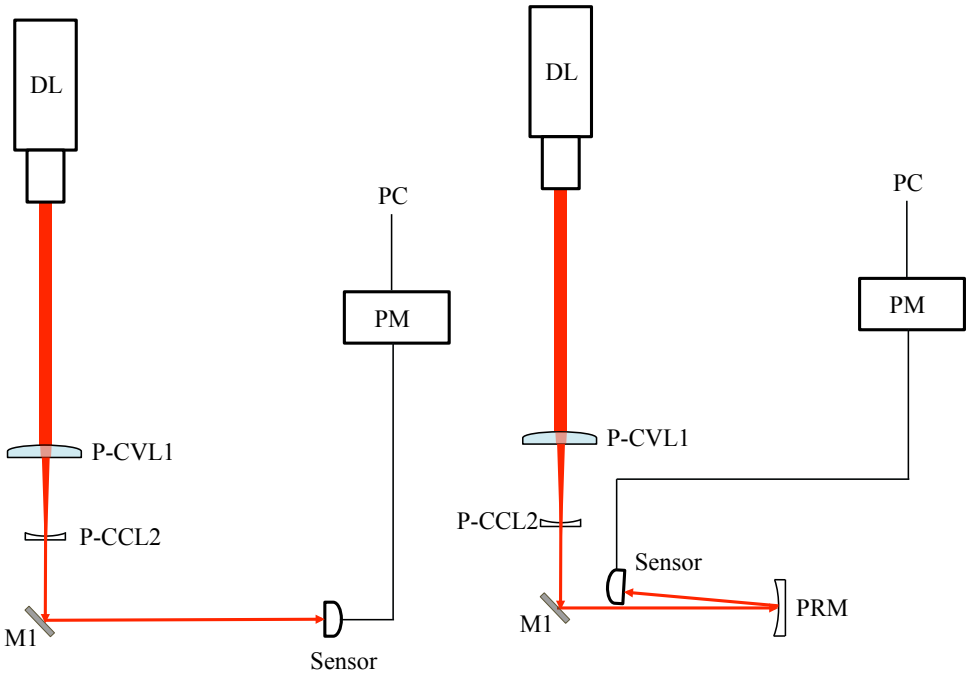

Fig. A.1 Setup for mirror calibration. The incident and reflected powers were measured with the setup in the left and right, respectively. (DL: Diode laser; M: mirror; CVL: convex lens; CCL: concave lens; PRM: partially reflective mirror; PM: powermeter).

where σ_{r_1}, σ_{r_2}, σ_{I_0}, $\sigma_{I_{r1}}$ and $\sigma_{I_{r2}}$ are the standard deviations of r_1, r_2, I_0, I_{r1} and I_{r2}, respectively. The calculated values for σ_{r_1} and σ_{r_2} are:

$$\begin{cases} \sigma_{r1} = 0.0020 = 0.20\% \\ \sigma_{r2} = 0.0019 = 0.19\% \end{cases} \tag{A.3}$$

Thus, the values of r_1 and r_2 are:

$$\begin{cases} r_1 = 98.11\% \pm 0.20\% \\ r_2 = 98.19\% \pm 0.19\% \end{cases} \tag{A.4}$$

Using the same method, we measured t_1 and t_2 for the two cavity mirrors and

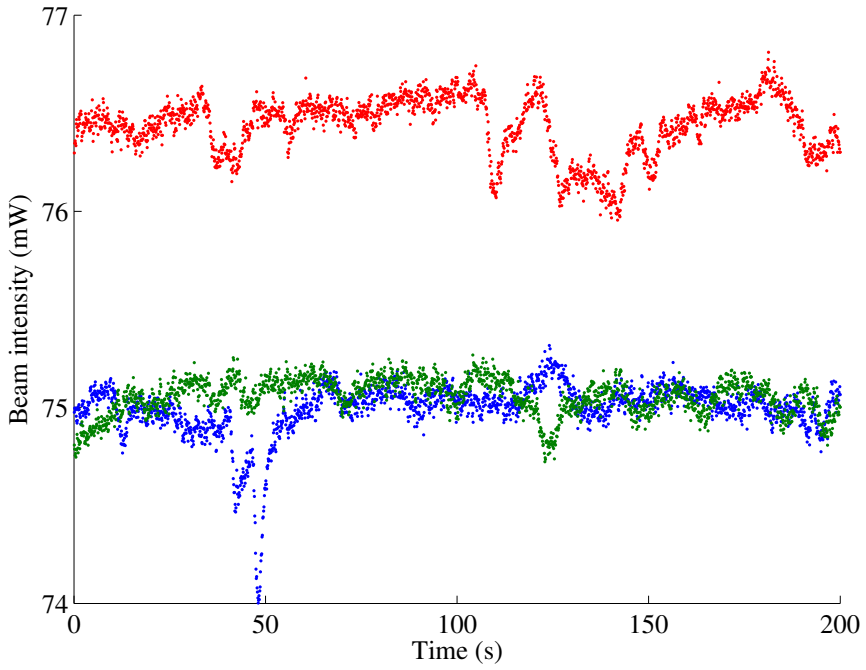

Fig. A.2 Original laser power (red spots), reflected beam power of laser of mirror 1 (green spots), and mirror 2 (blue spots).

obtained:

$$\begin{cases} t_1 = 1.53\% \pm 0.15\% \\ t_2 = 1.54\% \pm 0.16\% \end{cases} \tag{A.5}$$

Appendix B

Matlab program of Abel transform

```
% load data
load abeltest

% set the interval of two point (Unit: m)
delr=0.5*10^-3;

% set the start height (Unit: mm)
bottom=40;

%set the height interval (Unit:mm)
delh=10;

% set the finish height (Unit:mm)
top=70;

% set the series of height
```

```
HAB=bottom:delh:top;

% get the range of VLF
R = numel(VLF);

% set the value of E(m)
Em=0.26;

% set the wavelength of laser
Wavelength=6.38e-7;

%calculate all basic values
VF=mean(data(:,1));
VB=mean(data(:,2));
VL=mean(data(:,3));
VLF=mean(data(:,4));
Vref1=mean(data(:,5));
Vref2=mean(data(:,6));
Vref3=mean(data(:,7));

%assign the value of C
C=0.496

%set the height
h=40

%calculate the P
kint=-(0.25)*log(R)
```

```
%==========================================
%set the wavelength
lambda=600*10^(-9);
%==========================================

%set the tested interval
d=0.25*10^(-3);

%get the value of integrated fv at 40mm
fvint=((sum(data041(:,(1+((h-30)/10))))).*(10^(-6))).*d

%calculate E(m)
Em = (kint.*lambda)./(fvint*6*3.1415927);

% set the amplifier constant
C = 0.496;

% Calculate Kacc
Kacc=zeros(1,R+1)
for i=1:R
Kacc(i)=-(log(10))*(((10^(VLF/C))/(10^(VL/C)))*((1+(10^((
    Vref3-Vref2)/C))-(10^((Vref1-VB)/C))-(10^((VF+Vref3-
    Vref2-VLF)/C)))/(1-(10^((Vref1-VL)/C)))));
end

syms x;
ii = R;
jj = R;
I0 = zeros(ii,jj);
```

```
I1 = zeros(ii,jj);

for i=1:R
    for j=i:R
        if j==i
            I0(i,j)=(int(1./sqrt((2*j+x)^2-4*(i^2)),x,0,1)
                )./(2*pi);
            I1(i,j)=(int(x./sqrt((2*j+x)^2-4*(i^2)),x,0,1)
                )./(2*pi);
        else
            I0(i,j)=(int(1./sqrt((2*j+x)^2-4*(i^2)),x
                ,-1,1))./(2*pi);
            I1(i,j)=(int(x./sqrt((2*j+x)^2-4*(i^2)),x
                ,-1,1))./(2*pi);
        end
    end
end

KextCt=zeros(1,R);
for i=2:R
    for j=i:R
        KextCt(i) = KextCt(i)+(I1(i,j)-I0(i,j)).*Kacc(j-1)
            -2.*I1(i,j).
        *Kacc(j)+(I1(i,j)+I0(i,j)).*Kacc(j+1);
    end
    KextC(i,(HAB(k)-bottom)/10+1)=KextCt(i)
    KextC(1,(HAB(k)-bottom)/10+1)=KextCt(2)
end
end
```

```
Kext1=KextC.*(-1./delr);

% calculate Fv at each point
FvC=Kext1.*(Wavelength./(6*pi*Em));
```

Appendix C

Matlab program of LOSE uncertainty calculation

```
%input the number of samples
n=30000;

%assign the value of C
C_n=0.496;

%calculate all basic values
VF_n=mean(data(:,1));
VB_n=mean(data(:,2));
VL_n=mean(data(:,3));
VLF_n=mean(data(:,4));
Vref1_n=mean(data(:,5));
Vref2_n=mean(data(:,6));
Vref3_n=mean(data(:,7));
```

```
%define the symbols
syms VF VB VL VLF Vref1 Vref2 Vref3 C

%expression of P
P=log(((10^(VLF/C))/(10^(VL/C)))*((1+(10^((Vref3-Vref2)/C))-(10^((Vref1-VB)/C))-(10^((VF+Vref3-Vref2-VLF)/C)))/(1-(10^((Vref1-VL)/C)))));

%calculate the differetiation
dPdVL=diff(P,'VL');
dPdVLF=diff(P,'VLF');
dPdVB=diff(P,'VB');
dPdVF=diff(P,'VF');
dPdVref1=diff(P,'Vref1');
dPdVref2=diff(P,'Vref2');
dPdVref3=diff(P,'Vref3');
dPdC=diff(P,'C');

%calculate the differetiation value
dPdVL_n=subs(dPdVL,{VL,VLF,VB,VF,Vref1,Vref2,Vref3,C},{VL_n,VLF_n,VB_n,VF_n,Vref1_n,Vref2_n,Vref3_n,C_n});
dPdVLF_n=subs(dPdVLF,{VL,VLF,VB,VF,Vref1,Vref2,Vref3,C},{VL_n,VLF_n,VB_n,VF_n,Vref1_n,Vref2_n,Vref3_n,C_n});
dPdVB_n=subs(dPdVB,{VL,VLF,VB,VF,Vref1,Vref2,Vref3,C},{VL_n,VLF_n,VB_n,VF_n,Vref1_n,Vref2_n,Vref3_n,C_n});
dPdVF_n=subs(dPdVF,{VL,VLF,VB,VF,Vref1,Vref2,Vref3,C},{VL_n,VLF_n,VB_n,VF_n,Vref1_n,Vref2_n,Vref3_n,C_n});
dPdVref1_n=subs(dPdVref1,{VL,VLF,VB,VF,Vref1,Vref2,Vref3,C},{VL_n,VLF_n,VB_n,VF_n,Vref1_n,Vref2_n,Vref3_n,C_n});
```

```
dPdVref2_n=subs(dPdVref2,{VL,VLF,VB,VF,Vref1,Vref2,Vref3,C
    },{VL_n,VLF_n,VB_n,VF_n,Vref1_n,Vref2_n,Vref3_n,C_n});
dPdVref3_n=subs(dPdVref3,{VL,VLF,VB,VF,Vref1,Vref2,Vref3,C
    },{VL_n,VLF_n,VB_n,VF_n,Vref1_n,Vref2_n,Vref3_n,C_n});
dPdC_n=subs(dPdC,{VL,VLF,VB,VF,Vref1,Vref2,Vref3,C},{VL_n,
    VLF_n,VB_n,VF_n,Vref1_n,Vref2_n,Vref3_n,C_n});

%calculate P
P_n=subs(P,{VL,VLF,VB,VF,Vref1,Vref2,Vref3,C},{VL_n,VLF_n,
    VB_n,VF_n,Vref1_n,Vref2_n,Vref3_n,C_n});

%calculate the std of Vs
S=std(data);

%define the squence
D=[dPdVF_n,dPdVB_n,dPdVL_n,dPdVLF_n,dPdVref1_n,dPdVref2_n,
    dPdVref3_n,dPdC_n];
u=[S,0.0088];

%calculate the combined uncertainty of P
uP=(sum((D.^2).*(u.^2)))^0.5;

%calculate the combined uncertainty of R
uR=exp(P_n)*uP

%calculate the uncertainty of E(m)
uEm = (uP*lambda)./(fvint*6*3.1415927);
```

Appendix D

Matlab program of 2D flame simulation

D.1 Governing equations

```
function [c,f,s] = pdex3pde(x,t,u,DuDx)

%input value
Xf0 = 1;
Yf0 = 16*Xf0/(28*(1-Xf0)+16*Xf0);
Yox0 = 0.233;
S = 3.989;
Tox0 = 300;
Tf0 = 350;
Q = 45*10^6;
cp = 1300;

ust = (Yox0/S)/(Yf0+Yox0/S);
```

```
Tf = Yf0*ust*Q/cp-(Tox0-Tf0)*ust+Tox0;

%values need to asign
D0 = 0.2*10^-4;
T0 = 300;
den_inf = 1.225;
mu0 = 0.65*10^-5;
ag = 9.8;
MW_air = 28.97;
MW_nitrogen = 28;
MW_CH4 = 16;
MW_ox = 32;

if (0<=u(1)) && (u(1)<ust);
    T = (Tf-Tox0)*(u(1)/ust)+ Tox0;
    Yf = 0;
    Yox = S*Yox0*((ust-u(1))/(1-ust));
else
    T = (Tf-Tf0)*((1-u(1))/(1-ust))+Tf0;
    Yox = 0;
    Yf = Yf0*((u(1)-ust)/(1-ust));
end

%den = den0*(T0/T);
den = den_inf*(T0/T)*(1/MW_air)/(Yox/MW_ox+Yf/MW_CH4+(1-
    Yox-Yf)/MW_nitrogen);

D = D0*power(T/T0,1.67);
mu = mu0*((0.555*T0+80)/(0.555*T0+80))*((T/T0)^1.5);    %
```

```
    Sutherland's formula (Crane, 1988)
c = [1,0,0;
    0,2*den,0;
     0,0,2*den];
f = [D*DuDx(1)-u(1)*u(3);mu*DuDx(2);mu*DuDx(3)];
s = [0; ag*(den_inf-den)-den*u(3)*DuDx(2); -mu*u(3)/(x^2)
    ];
```

D.2 Main program

```
clear all;

% x = [0 0.005 0.01 0.05 0.1 0.2 0.5 0.7 0.9 0.95 0.99
    0.995 1].*(2*10^-2)
% t = [0 0.005 0.01 0.05 0.1 0.5 1 1.5 2].*10^-1;
x = linspace(0,0.006,180);
t = linspace(0,0.09,600);
m = 1;
sol = pdepe(m,@pdex3pde,@pdex3ic,@pdex3bc,x,t);

u1 = sol(:,:,1);
u2 = sol(:,:,2);
u3 = sol(:,:,3);

i = 1;
j = 1;
[m,n] = size(u1);
```

```
Xf0 =    0.5699;
Yf0 = 16*Xf0/(28*(1-Xf0)+16*Xf0);
Yox0 = 0.233;
S = 3.989;
Tox0 = 300;
Tf0 = 350;
Q = 45*10^6;
cp = 1300;

ust = (Yox0/S)/(Yf0+Yox0/S);
Tf = Yf0*ust*Q/cp-(Tox0-Tf0)*ust+Tox0;



for i = 1:m
    for j = 1:n
        if (0<= u1(i,j))&&(u1(i,j)<ust)
            T(i,j) = (Tf-Tox0)*(u1(i,j)/ust)+ Tox0;
        else
            T(i,j) = (Tf -Tf0)*((1-u1(i,j))/(1-ust))+Tf0;
        end
    end
end

T_all=[fliplr(flipud(T)),flipud(T)];
U_all=[fliplr(flipud(u2)),flipud(u2)];
z=zeros(m,1);
for ii=1:m;
    for jj=1:ii;
        z(ii)=z(ii)+(u2(jj,1)*(t(2)-t(1)));
```

```
    end;
end;

r=[-fliplr(x),x];
subplot(1,2,1);
imagesc(r,z,T_all);
subplot(1,2,2);
imagesc(r,z,U_all);
```

D.3 Boundary conditions

```
function[pl,ql,pr,qr] = pdex3bc(xl,ul,xr,ur,t)
pl = [0;0;ul(3)];
ql = [1;1;0];
pr = [ur(1);ur(2)-0.14;ur(3)];
qr = [0;0;0];
```

D.4 Initial conditions

```
function u0 = pdex3ic(x)
if (0<=x)&&(x<=0.005)
    u0 = [1;0.11125;0];
else
    u0 = [0;0.14;0];
end
```

Appendix E

Matlab program of LII modelling

E.1 Energy balance equations

```
%LII energy balance equations copyright of Reacting Flow
    Group @ Cambridge
function dy=monodisperse(t,y)

dy=zeros(5,1);

%================value of quantities==================
pi=3.14159;      %Value of Pi
q_laser=1;       %Integrated laser to unity, a constant
Rp=8.3145;   %Universal gas constant
Rm=8.3145;   %Universal gas constant
H=7.78E5;    %Sublime enthalpy, J/mol
Ws=12/1000;  %Molecule weight of solid, kg/mol
Wv=36/1000; %Molecule weight of gaseous, kg/mol
F=2600; %Laser fluence, J/m^2
lambda_laser=532E-9;  %Wavelength of laser
gamma= 1.3;   %cp/cv of gas
```

```
rhos=1860;      %Density of soot, kg/m3
cs=1900;        %Heat capacity of soot, J/kgK
ka=0.1;  %Thermal conductivity of surrounding gases
T0=2140;  %Ambient temperature
L= (2.355E-10)*T0; %Mean free path
am=1;  %Mass accommodation coefficient
at=0.3;     %Thermal accommodation coefficient
Em=0.26;     %Absorption function
%================value of quantities================


%================Time quantities================
qt = normpdf(t, 30*10^-9, 5*10^-9);    %Temporal profile of
    laser
%================Time quantities================


%================T dependent quantities================
pv=1E5*exp(-(37500/y(4))+9.579);  %Partial pressure of
    sublimed clusters
%================T dependent quantities================

%Absorption=y(1)
dy(1)=(pi^2*y(5)^3*Em*F*qt)/(lambda_laser*q_laser);

%Sublimation=y(2)
dy(2)=(H/Ws)*((pi*y(5)^2*Wv*am*pv)/(Rp*y(4)))*(((Rm*y(4))
    /(2*Wv))^0.5);
```

```
%Conduction=y(3)
f=(9*gamma-5)/4;
G=(8*f)/(at*gamma+1);
dy(3)=((2*ka*pi*y(5)^2)*(y(4)-T0))/(y(5)+G*L);

%Final equation of temperature, T=y(4)
dy(4)=(6/(pi*y(5)^3*cs*rhos))*(dy(1)-dy(2)-dy(3));
```

E.2 Solving program

```
%clear all;
%load('M53_3366_grid.mat');

%================value of quantities==================
h=6.626E-34;  %Plank constant
kb=1.38E-23;  %Boltzmann constant
c=3E8; %Speed of light m/s
Em=0.26;      %Absorption function
Copt=1;%Optical system constant
Np=1; %Number density of particles
Vm=1; %Probe volume
%L1=400E-9; %detection wavelength of Nanostar
%L2=450E-9; %detection wavelength of IRO
%================value of quantities==================


%Calculation of Tmax
%Inputs
%==================input position=======================
```

```
zz=9;  %mm, between 0-33, height want to investigate
rr=0; %mm, between 0-6, r want to investigate
%=========================================================

% S1=NS3366((330-10*zz),(10*rr+1),3)
% S2=IRO3366((330-10*zz),(10*rr+1),3)

%calibration
% Rc=2.42;  %C1/C2
% Rs=(S1/S2)/Rc;

%calculate and plot the temperature
%Tmax=(h*c/kb)*(1/L2-1/L1).*((log(Rs.*(L1/L2)^6)).^-1)

%Calculation of T0
%load('M53_temperature');
%T0=M53t(2000+zz*30,rr*30+1)  %Ambient temperature
T0=2140;

%Inputs
% Dm=30E-9;  %Median diameter of particles
% sigma_g=0.16;  %Std of lognormal distribution
timeinteval=1080E-9; %Time span to simulate
lambda_lii=400E-9; %Determine which wavelength to detect

%==========input fitting parameters==========
Dsc=20; %counts of tested Dm
sigmac=10; %counts of tested sigm
Ds=4; %nm
```

```
sigmas=0.1;
X=zeros(Dsc,sigmac);
%==========================================

%set size parameter
Dmin=1; %nm
Dmax=100; %nm
Dstep=1; %nm

for i=1:Dsc;
    Dm=i*Ds*10^-9;
    for j=1:1:sigmac;
        sigma_g=sigmas*j;

LIImono=zeros(timeinteval*1E9/2,((Dmax-Dmin)./Dstep)); %
    Creat the matrix of LII
Tmono=zeros(timeinteval*1E9/2,((Dmax-Dmin)./Dstep)); %
    Creat the matrix of T

d=((Dmin:Dstep:Dmax).*1E-9);
        Dall=lognpdf(d,log(Dm),sigma_g);
        for ii=1:(Dmax/Dstep);
            D=d(ii);
[tt,TT] = ode15s('enerybalance_EB',[0 timeinteval],[0; 0;
    0; T0; D]);

St=(8*pi^3*D^3*h*c^2*Em)./(lambda_lii^6*(exp((h*c)./(
    lambda_lii*kb.*TT(:,4)))-1))-(8*pi^3*D^3*h*c^2*Em)./(
    lambda_lii^6*(exp((h*c)./(lambda_lii*kb.*T0))-1));
```

```
Ttt=TT(:,4);



tttt=(2:2:timeinteval*1E9).*1E-9;
LIImono(:,ii)=interp1(tt,St,tttt, 'spline').*Dall(ii).*1E
    -9;
Tmono(:,ii)=interp1(tt,Ttt,tttt, 'spline').*Dall(ii).*1E
    -9;

Jt=sum(Copt*Np*Vm*LIImono,2)./max(sum(Copt*Np*Vm*LIImono
    ,2));
Tt=sum(Copt*Np*Vm*Tmono,2);
          end;

time
    =[40,60,80,100,120,140,180,260,340,420,500,660,820,1080].*1
    E-9;
Jtm=interp1(tttt,Jt,time, 'spline');
Jtm=Jtm/max(Jtm);

S1crr=[NS3366((330-10*zz),(10*rr+1),3);
      NS3366((330-10*zz),(10*rr+1),4);
      NS3366((330-10*zz),(10*rr+1),5);
      NS3366((330-10*zz),(10*rr+1),6);
      NS3366((330-10*zz),(10*rr+1),7);
      NS3366((330-10*zz),(10*rr+1),8);
      NS3366((330-10*zz),(10*rr+1),10);
      NS3366((330-10*zz),(10*rr+1),14);
      NS3366((330-10*zz),(10*rr+1),18);
```

```
    NS3366((330-10*zz),(10*rr+1),22);
    NS3366((330-10*zz),(10*rr+1),26);
    NS3366((330-10*zz),(10*rr+1),31);
    NS3366((330-10*zz),(10*rr+1),35);
    NS3366((330-10*zz),(10*rr+1),40);
    ];

S1cr=(smooth(S1crr))';
S1c=S1cr/max(S1cr);
X(i,j)=(sum((Jtm-S1c).^2))^0.5;
    end;
end;

plot(time,S1c);
```

Appendix F

List of supplementary material

F.1 Extinction coefficient K_e of undiluted methane, ethlyene and propane flames (conditions are listed in Table 2.2)

Download: https://www.dropbox.com/s/yw0tutig4oi60hu/Ke.txt?dl=0

F.2 Extinction coefficient K_e of diluted methane flames A0 to E4 (conditions are listed in Table 3.1)

Download: https://www.dropbox.com/s/8o0a4zlkqwb0zfh/Ke_A0_E4.txt?dl=0

F.3 D_m measured in an ethylene flame

Download: https://www.dropbox.com/s/81rppsksc2twdiy/Dm_C2H4.xlsx?dl=0

F.4 D_m measured in a methane flame case A

Download: https://www.dropbox.com/s/j1yf9q5rhr35mx1/Dm_CH4_A.xlsx?dl=0

F.5 D_m measured in a methane flame case B

Download: https://www.dropbox.com/s/pmu4ag4tma51mw8/Dm_CH4_B.xlsx?dl=0